Kinetic Monte Carlo Simulations of Solid Electrolyte Interphase Formation on Lithium Metal Electrodes

Zur Erlangung des akademischen Grades einer
Doktorin der Ingenieurwissenschaften (Dr.-Ing.)
von der KIT-Fakultät für Elektrotechnik und Informationstechnik des
Karlsruher Instituts für Technologie (KIT)

angenommene
Dissertation
von

Janika Wagner-Henke, M.Sc.,
geboren in Rotenburg (Wümme)

Tag der mündlichen Prüfung:	19. September 2025
Hauptreferentin:	Prof. Dr.-Ing. Ulrike Krewer
Korreferentin:	Prof. Dr. Perla B. Balbuena

Kurzfassung

Angesichts des weltweit fortschreitenden Klimawandels gewinnen die Elektrifizierung unseres Verkehrs sowie die Energieerzeugung aus erneuerbaren Quellen stetig an Bedeutung. Bei dieser Transformation nehmen Energiespeicher eine wichtige Schlüsselrolle ein. In den vergangenen Jahrzehnten wurde die Lithium-Ionen-Batterie als wichtige Energiespeichertechnologie etabliert und bis dicht an ihre theoretischen Limits optimiert. Eine weitere wesentliche Steigerung der Energiedichte erfordert daher fundamental neue Zellchemien. Diesbezüglich gelten Lithium-Metall-Anoden aufgrund ihrer hohen gravimetrischen Kapazität als besonders vielversprechend. Allerdings wird ihre praktische Verwendung derzeit noch stark durch ihre hohe Reaktivität gegenüber dem Elektrolyten sowie einer niedrigen Zyklenfestigkeit eingeschränkt. Diese Herausforderung könnte durch die gezielte Ausbildung einer schützenden Solid Electrolyte Interphase (SEI) an der Lithium/Elektrolytgrenzfläche überwunden werden.

In dieser Dissertation werden neuartige *ab initio*-informierte kinetische Monte Carlo (kMC) Modelle entwickelt, welche ein mechanistisches Verständnis der SEI-Bildung sowie eine Identifikation makroskopischer Einflussfaktoren ermöglichen und somit zur Stabilisierung der Grenzfläche an Lithium-Metall-Anoden beitragen können. Ein besonderer Fokus wird dabei auf die Erhöhung der erreichbaren Simulationszeit bis in den Sekundenbereich gelegt, sodass die initiale Phase der Schichtbildung abgedeckt ist. Dies verfolgt insbesondere das Ziel die Lücke zwischen atomistischen Simulationen im Piko- bis Nanosekundenbereich und experimentellen Untersuchungen zu schließen und gleichzeitig eine molekulare Auflösung beizubehalten. Ein weiterer methodischer Schwerpunkt liegt darüber hinaus auf der Implementierung elektrostatischer Wechselwirkungen zur Sicherstellung der lokalen Elektroneutralität. Dazu werden geeignete Transportgleichungen aus der Literatur abgeleitet und Methoden zur Berücksichtigung des Einflusses der Solvathülle, zur Vermeidung des Selbstwechselwirkungsfehlers sowie zur Wahl geeigneter Randbedingungen entwickelt und diskutiert. Basierend auf einem Vergleich verschiedener Modellansätze wird schließlich der 1D-Poisson Ansatz als bester Kompromiss hinsichtlich Genauigkeit und Effizienz für den Einsatz in den entwickelten SEI-Modellen identifiziert. Die kMC-Modelle werden angewendet, um die spontane SEI-Bildung in dem weit verbreiteten Elektrolytsystem aus Ethylencarbonat, Kohlensäureethylmethylester und $LiPF_6$ sowie den Einfluss des Additivs Vinylencarbonat zu untersuchen. Die Ergebnisse der Studien zeigen, dass sich eine erste Passivierungsschicht an Lithium-Metall sehr schnell innerhalb der ersten

Mikrosekunde nach dem Kontakt mit dem flüssigen Elektrolyten einstellt. Ohne Additiv bildet sich in dieser Zeitspanne eine mehrere Nanometer dicke, geschichtete anorganische SEI aus Li_2CO_3 und LiF aus. Diese lässt sich insbesondere durch eine Variation der Salzkonzentration innerhalb der Löslichkeitsgrenzen beeinflussen, wobei höhere Konzentrationen zu einer schnelleren Passivierung, einem höheren LiF-Anteil und einer insgesamt dünneren SEI führen. Zusätzlich wird gezeigt, dass die Kinetik der Schichtbildung und die resultierende Struktur und Zusammensetzung maßgeblich von der lokalen Solvatationsumgebung und Li^+ Konzentration beeinflusst werden. Diese initiale Schichtbildung wird durch das Additiv Vinylencarbonat (VC) kaum beeinflusst. Allerdings führt VC innerhalb weniger Millisekunden zur Ausbildung einer darüber liegenden Polymerschicht. Da die Ausbildung dieser Schicht im Gegensatz zur übrigen SEI-Bildung hauptsächlich chemisch verläuft, wird die Oberfläche dadurch ohne den kontinuierlichen Verbrauch von aktivem Lithium, Lösungsmittel und Leitsalz passiviert. Eine Änderung der VC-Konzentration wirkt sich vor allem auf die Geschwindigkeit der Passivierung sowie auf die Additivmenge aus, welche nach der initialen Schichtbildung im Elektrolyten verbleibt. Es wird erwartet, dass sich dies im späteren Betrieb der Zelle auf Reparaturmechanismen der Passivierungsschicht und somit auf die Lebensdauer der Zelle auswirkt.

Insgesamt trägt diese Arbeit essentiell zur Erweiterung des mechanistischen Verständnisses der spontanen SEI-Bildung an Lithium-Metall-Anoden sowie zur Identifikation makroskopischer Einflussfaktoren bei. Darüber hinaus werden innovative Simulationsmethoden entwickelt, welche sich auch über die durchgeführten Fallstudien hinaus auf zahlreiche weitere Elektrolytsysteme und Zellchemien übertragen lassen. Diese Arbeit schafft somit wichtige Grundlagen für das zukünftige modellbasierte Design der SEI und erleichtert somit die Entwicklung stabilerer Lithium-Metall Batterien.

Abstract

As global climate change progresses, the electrification of our transport sector and the transition to renewable energy sources are becoming increasingly important. Energy storage systems play a key role in this transformation. Over the past decades, today's state of the art lithium-ion batteries have been optimized close to their theoretical limits. A further significant increase in energy density thus requires new cell chemistries. In this regard, lithium metal anodes are considered particularly promising due to their high gravimetric capacity. However, their practical application remains severely limited by their high reactivity with the electrolyte and low cycle stability. This challenge could be addressed by the targeted design of a protective solid electrolyte interphase (SEI) at the lithium metal/electrolyte interface.

In this dissertation, novel *ab initio*-informed kinetic Monte Carlo (kMC) models are developed to provide a mechanistic understanding of SEI formation and to identify macroscopic influencing factors, thus contributing to the stabilization of the interface at lithium metal anodes. Particular emphasis is placed on extending the accessible simulation timescales into the second range, to enable the investigation of the initial phase of layer formation. This approach specifically aims to bridge the gap between atomistic simulations in the pico- to nanosecond range and experimental investigations, while keeping a molecular resolution. Another methodological focus is the implementation of electrostatic interactions to ensure local electroneutrality. For this purpose, consistent transport rate equations are derived from the literature, and methods for accounting for solvation effects, preventing the self-interaction error, and selecting suitable boundary conditions are developed and discussed. Based on a comparison of different electrostatic interaction models, the 1D-Poisson approach is identified as the best compromise between accuracy and efficiency for implementation in the developed SEI models. The kMC models are applied to study spontaneous SEI formation in an electrolyte system consisting of ethylene carbonate, ethyl methyl carbonate and $LiPF_6$, as well as the influence of the film-forming additive vinylene carbonate. The results show that a first passivation layer on lithium metal forms very quickly within the first microsecond after contact with liquid electrolyte. In the additive-free electrolyte, a layered inorganic SEI composed of Li_2CO_3 and LiF with a thickness of several nanometers forms within this time frame. Its formation can be particularly influenced by a variation in salt concentration within solubility limits, with higher concentrations resulting in faster passivation, increased LiF content and an overall thinner SEI. Furthermore, the kinetics of layer formation, as well as the resulting

structure and composition of SEI are shown to be significantly influenced by the local solvation environment and Li^+ concentration. The initial layer formation is not significantly affected by the additive vinylene carbonate (VC), but leads to the formation of an overlying polymer layer starting within a few milliseconds. Unlike the remaining reduction-driven SEI formation processes, this polymerization process is predominantly chemical, passivating the surface without continuous consumption of active lithium, solvent, or conductive salt. A change in the VC concentration mainly affects the polymer growth rate and the amount of additive remaining in the electrolyte after initial layer formation. This is expected to affect the repair mechanisms of SEI during operation and hence the overall lifetime of the cell.

Overall, this dissertation significantly advances the mechanistic understanding of spontaneous SEI formation on lithium metal anodes and identifies key macroscopic influencing factors. In addition, it introduces innovative simulation methods that are applicable to a wide range of electrolyte systems and cell chemistries beyond the examples studied in this work. These contributions provide a sound foundation for future model-based SEI design, facilitating the development of more stable lithium metal batteries.

Acknowledgements

This dissertation presents the main research results from my time as a research associate at the Institute of Energy and Process Systems Engineering (InES) at the Technical University of Braunschweig and at the Institute for Applied Materials – Electrochemical Technologies (IAM-ET) at the Karlsruhe Institute of Technology. This period has been formative and full of learning, but also challenging at times. I would like to take this opportunity to express my gratitude to all those who accompanied me along the way and without whose support this work would not have been possible.

My deep thanks go first to my doctoral advisor, Prof. Dr.-Ing. Ulrike Krewer, for giving me the great opportunity to work on this exciting and challenging topic, and for her continuous support and guidance throughout this project. I am also very grateful for the trust she placed in me by assigning me the leadership of the battery research group at IAM-ET – a responsibility that has allowed me to grow as a person and gain invaluable experience.

I would also like to thank my second examiner, Prof. Dr. Perla B. Balbuena, for the excellent and long-standing collaboration. I am particularly grateful to her for the opportunity to conduct a research stay in her group at Texas A&M University, despite the challenges posed by the COVID-19 pandemic – an experience that contributed greatly to both my academic and personal development.

A special thanks also go to my fellow group leaders Dr.-Ing. Florian Baakes and Julian Ulrich for the outstanding and trusting collaboration. It was a great experience to jointly lead and develop the battery research group. I would also like to thank both of them for many insightful technical discussions. I am additionally grateful to Florian Baakes for proofreading this manuscript.

For the good scientific collaboration, I would especially like to thank my first group leader, Prof. Dr.-Ing. Fridolin Röder, for his guidance and the many insightful discussions on the kinetic Monte Carlo method. My sincere thanks also go to Dacheng Kuai for the countless discussion about reaction mechanisms and for carrying out the DFT calculations included in this work. I would also like to thank my co-authors and all the motivated students I had the pleasure to work with and who supported me throughout various stages of this work.

Good research is not possible without a well-functioning technical and administrative infrastructure. I would therefore like to express my sincere thanks to Torsten Johannsen, who always found timely solutions to any IT problem, as well as to Elke Sénégas-Rouvière, Marika Schäfer, Ina Schunke and Martina Wagner, who supported me reliably in all administrative matters.

I further gratefully acknowledge the financial support provided by the Federal Ministry of Education and Research (BMBF) for both my research at INES and IAM-ET and my stay at Texas A&M University as part of the publicly funded projects Lillint (03XP0225F) and Lillint2 (03XP0511C).

I would like to thank all of my colleagues at InES and IAM-ET for the supportive working atmosphere and the many enriching conversations throughout the years. My special thanks goes to my colleagues from the battery group: Michelle Allion, Lars Bläubaum, Walter Cistjakov, Sebastian Frentzen, Michail Gerasimov, Dr. Kie Hankins, Simone Holzmann, Jakub Jambrich, Leon Schmidt, Dr. Somayeh Toghyani, Aravind Unni, Jorge Valenzuela, Dion Wilde und Daniel Witt. I truly enjoyed our collaboration and the many scientific and non-scientific conversations that helped me through even the most challenging phases of this project.

Finally, I would like to express my heartfelt gratitude to my parents Heike and Norbert Wagner, who have supported and encouraged my academic path from the very beginning, and to my husband Felix Henke, whose unwavering support, encouragement and patience gave me the strength to complete this dissertation.

Karlsruhe, June 2025 *Janika Wagner-Henke*

Publications within the Scope of this Dissertation

Journal publications

First author

1. **J. Wagner-Henke**, S. Frentzen, M.-J. Anton, J. Ulrich, U. Krewer, "Comparative analysis of electrostatic interaction models for kinetic Monte Carlo simulations of liquid electrolytes", *in preparation*, 2026
2. **J. Wagner-Henke**, D. Kuai, P. B. Balbuena, U. Krewer, "Understanding the Effect of Vinylene Carbonate on SEI Formation, Morphology and Stability on Lithium Metal Anodes", *Energy Storage Materials*, vol. 81, p. 104434, 2025
3. **J. Wagner-Henke**, D. Kuai, M. Gerasimov, F. Röder, P. B. Balbuena, and U. Krewer, "Knowledge-driven design of solid-electrolyte interphases on lithium metal via multiscale modelling," *Nature Communications*, vol. 14, no. 1, p. 6823, 2023

Co-author

1. K. Hankins, M. H. Putra, **J. Wagner-Henke**, A. Groß, and U. Krewer, "Insights on SEI Growth and Properties in Na-Ion Batteries via Physically Driven Kinetic Monte Carlo Model," *Advanced Energy Materials*, vol. 2401153, pp. 1-13, 2024
2. M. Gerasimov, F.A. Soto, **J. Wagner**, F. Baakes, N. Guo, F. Ospina-Acevedo, P. B. Balbuena, and U. Krewer, "Species Distribution During Solid Electrolyte Interphase Formation on Lithium Using MD/DFT-Parameterized Kinetic Monte Carlo Simulations," *The Journal of Physical Chemistry C*, vol 127, no. 10, pp. 4872-4886, 2023

3. G. D. Wehinger, M. Ambrosetti, R. Cheula, Z.-B. Ding, M. Isoz, B. Kreitz, K. Kuhlmann, M. Kutscherauer, K. Niyogi, J. Poissonnier, R. Réocreux, D. Rudolf, **J. Wagner**, R. Zimmermann, M. Bracconi, H. Freund, U. Krewer, and M. Maestri, "Quo vadis multiscale modeling in reaction engineering? - A perspective," *Chemical Engineering Research and Design*, vol. 184, pp. 39-58, 2022

Conference contributions

1. **J. Wagner-Henke**, D. Kuai, P. B. Balbuena, and U. Krewer, "Bridging the Scales of Solid Electrolyte Interphase Formation On Lithium Metal with Kinetic Monte Carlo Models", Oxford Battery Modelling Symposium, Oxford, April 15-16, 2024 **(Poster)**

2. **J. Wagner-Henke**, D. Kuai, P. B. Balbuena, and U. Krewer, "Einsichten in SEI-Formierung und Design von SEI-Morphologie mittels Multiskalen-Modellierung", Batterieforum, Berlin, January 21-23, 2024 **(Poster)**

3. **J. Wagner-Henke**, D. Kuai, M. Gerasimov, F. Röder, P. B. Balbuena, and U. Krewer, "Knowledge-driven design of solid-electrolyte interphases on lithium metal via multiscale modelling", Battery Modelling Webinar Series, Online, December 19th, 2023 **(Invited Talk)**

4. **J. Wagner**, D. Kuai, P. B. Balbuena, and U. Krewer, " How does vinylene carbonate affect the formation of initial surface passivation layers on lithium metal? - A model-based analysis", Advanced Battery Power, Aachen, April 27-28, 2023 **(Talk)**

5. **J. Wagner**, D. Kuai, P. B. Balbuena, and U. Krewer, "Model-based Investigation of the Influence of the Electrolyte Additive VC on the initial SEI formation on lithium metal", 33rd ISE Topical Meeting, Santiago de Chile, November 27-30, 2022 **(Talk)**

6. **J. Wagner** and U. Krewer, "Mechanistic comprehension of SEI formation on lithium metal using "ab-initio" kMC simulations", 773. Heraeus-Seminar, Bad Honnef, October 23- 27, 2023 **(Poster with award)**

7. **J. Wagner**, D. Kuai, P. B. Balbuena, and U. Krewer, "Mechanistic comprehension of SEI formation on lithium metal using "ab-initio" kMC simulations", Electrochemistry, Berlin, September 27-30, 2022 **(Poster)**

8. **J. Wagner**, M. Gerasimov, F. Röder, P. B. Balbuena, and U. Krewer, "Revealing the impact of chemistry on SEI formation on Li metal by multi-scale modelling", ISE 72nd Annual Meeting, Online/Jeju Island, August 29 - September 03, 2021 **(Talk)**

9. **J. Wagner**, M. Gerasimov, F. Röder, P. B. Balbuena, U. Krewer, "Unvravel SEI Formation on Li Metal Interfaces By Mechanistic Multi-Scale Modelling", 240th ECS Meeting, Online, October 10-14, 2021 **(Talk)**

Contents

1 Introduction[1,2]

1.1 Motivation

According to the recent publication from the Copernicus Climate Change Service of the European Union [3], 2024 was the first year in which the global temperature exceeded a 1.5 °C increase compared to pre-industrial levels and hence surpassed the target which was set in the Paris Agreement of 2015 [4]. This development underlines the importance of climate protection measures and of the rapid reduction of greenhouse gas emissions. A key step in this direction is the European Green Deal [5], which aims at reducing the greenhouse gas emissions by 2030 by 55% compared to the level of 1990 and making Europe the first climate-neutral continent by 2050. As of today, already more than 50% of the electricity in Germany is generated from renewable sources such as wind and solar power [6]. However, as these energy sources are subject to strong fluctuations, efficient energy storage solutions such as stationary batteries or hydrogen are required to ensure a reliable power supply, while simultaneously further increasing the share of renewable energy in the electricity mix [6]. Additionally, the transport sector, accounting for 22% of greenhouse gas emissions in Germany [7], offers significant potential for emissions reduction. Here, one important strategy is the transition from combustion engine vehicles towards fully electric vehicles that promise significant reduction of greenhouse gas emissions over their entire lifecycle [8]. This transition, however, as well requires reliable and secure energy storage systems with a high energy density.

The current state-of-the art battery technology is the lithium-ion battery (LIB), which is applied in both, stationary energy storage systems and battery electric vehicles [9, 10]. Modern LIB cells can provide gravimetric energy densities of around 250 Wh kg^{-1}, which is very close to their theoretical limit [11]. Consequently, applications such as battery electric propulsion in aviation, which would require a minimum of 500 Wh kg^{-1}, are still out of reach [12] and a

[1] During the preparation of this dissertation, the generative language model ChatGPT was applied in order to improve readability and language of the manuscript. The author has thoroughly reviewed and edited the content and takes full responsibility for the final version of this dissertation.

[2] Parts of this chapter have been published in J. Wagner-Henke et al., *Nat. Commun.* 14, 6823, 2023 [1], licensed under CC BY 4.0. Further parts of this chapter have been published in J. Wagner-Henke et al., *Energy Storage Mater.* 81, 104434, 2025 [2], licensed under CC BY 4.0.

further increase of gravimetric energy density in existing applications is limited. The 'holy grail' in terms of energy density are lithium metal anodes [9]. They combine a specific gravimetric capacity of 3860 mAh g^{-1}, which is ten times more compared to conventional graphite anodes, with a very low electrode potential of -3.04 V against the standard hydrogen electrode (SHE) [11]. Depending on the applied cathode material these properties allow for a significant increase in accessible practical energy densities compared to LIB [11].

1.2 Current State and Objective

When it comes to application, the high reactivity of lithium metal causes challenges that prevent its widespread application in rechargeable battery cells. It makes the lithium metal/electrolyte interface difficult to control and may cause uncontrolled electrolyte degradation including thermal runaway, ongoing loss of active material and dendrite growth [13, 14]. One important strategy to solve this is the control and stabilization of the interfacial layer between the lithium metal electrode and the liquid electrolyte. Introduced by Peled [15], this Li-ion conductive layer is usually referred to as solid electrolyte interphase (SEI). In order to prevent uncontrolled SEI and dendrite growth, the SEI needs to show a wide range of properties: Electrical insulation and simultaneously good ionic conductivity, low thickness to prevent cyclable Li and capacity loss, prevention of the direct contact of lithium metal and electrolyte, and good mechanical stability to accommodate the large volume changes of the metal electrode [11, 14]. The targeted design of such a beneficial SEI requires a detailed understanding of the fundamental formation mechanisms and the resulting chemical SEI composition and morphology, depending on the electrolyte composition.

In the past both, experimental and theoretical characterization techniques have been applied to study the SEI on the lithium metal/liquid electrolyte interface [16]. Spectroscopy and microscopy techniques provided detailed descriptive insights into the chemical SEI composition and morphology [13, 14, 17]. However, since the spontaneous SEI formation on lithium metal begins immediately upon contact with the liquid electrolyte and many formation processes occur within fractions of seconds, it remains difficult to experimentally determine the underlying formation mechanisms [14, 18, 19]. Atomistic simulation techniques, such as density functional theory (DFT) and (*ab initio*) molecular dynamics (MD), have provided valuable insights into reaction mechanisms, kinetics, and the initial stages of SEI formation [20–23]. However, they are too computationally expensive to model phenomena on extended length- and timescales above a few nanoseconds, as envisioned in this work. On the other end of the scale, continuum models allow to study long-term SEI growth and its impact on cell performance during cycling [24–27]. However, they often lump the SEI formation kinetics and cannot predict the nanomorphology and detailed chemical composition of the SEI.

Kinetic Monte Carlo (kMC) models are a promising mesoscale simulation technique for bridging the gap between atomistic and continuum simulations, as they allow to access larger timescales while keeping detailed molecular information [28]. Simple kMC models for SEI formation on graphite electrodes have been developed since 2011 [29]. Afterwards, the complexity and accuracy of these models continuously increased. Advancements included for example the coupling with continuum models [30–32] and the input of *ab initio*-informed reaction mechanisms and kinetics [33]. However, none of these models can yet model the three-dimensional spontaneous SEI formation on lithium metal on a molecular resolution above the nanosecond timescale. Hence, the governing processes on the mesoscale of SEI formation on lithium metal remain poorly understood.

This thesis aims to develop and apply *ab initio*-informed kinetic Monte Carlo models which are specifically tailored for the simulation of spontaneous SEI formation on lithium metal. By applying these models, a detailed mechanistic understanding of the underlying formation processes up to technologically relevant timescales shall be established. Additionally, the work intends to reveal how the molecular SEI composition can be influenced by macroscopic properties, such as electrolyte composition. Based on these insights the thesis aims to contribute to a knowledge-driven design of the SEI on lithium metal electrodes.

1.3 Scope and Structure of this Work

The following work is structured in five chapters. First, the relevant fundamentals and the current state of research are summarized in Chapter 2. The chapter begins with the very general fundamentals of lithium-based batteries, including their operating principles, as well as the advantages of lithium metal anodes and the challenges associated with them. It then provides an overview of the main characterization methods used to study the SEI, and concludes with a deep-dive into the fundamentals of the kinetic Monte Carlo method and its application in SEI research.

Subsequently, Chapter 3 presents the model development and application on the example of the well-established electrolyte system ethylene carbonate (EC) and ethyl methyl carbonate (EMC) with $LiPF_6$ as conductive salt. Here, particular emphasis is on ensuring local and global electroneutrality, parameterizing the considered reaction mechanisms based on DFT calculations, and extending the accessible timescales into the microsecond range. Based on the developed model, the time evolution of SEI composition and morphology are studied. This allows to identify limiting processes as well as the effects of electrolyte composition and local Li^+ ion concentration on SEI formation.

In the following Chapter 4, the effect of the widely used additive vinylene carbonate (VC) on SEI formation is investigated. For this purpose, the previously developed model is extended

to include polymerization processes. Moreover, the accessible timescale is further extended to the second range, enabling the investigation of SEI formation on technologically relevant timescales. The study provides insights into the main underlying processes of SEI formation in a VC-containing electrolyte and reveals how VC plays its role as film-forming additive on lithium metal anodes.

Eventually, in Chapter 5 the focus is moved towards the methodological analysis of electrostatic interactions in kMC models for liquid electrolytes. Different electrostatic interaction models are implemented and compared in terms of accuracy and efficiency. Based on this evaluation, the most promising approach is selected and implemented into the SEI model presented in Chapter 4. Finally, the results of both models are compared to assess the impact of electrostatic interactions on the predicted SEI formation.

The thesis concludes with a short summary of the key findings and the discussion of potential directions for future research in Chapter 6.

2 Fundamentals

The following chapter provides an overview of the fundamental concepts on which this work is based. It begins with a general introduction to the operating principles of lithium-based battery cells (cf. Section 2.1.1) before focusing on lithium metal anodes and their historical development (cf. Section 2.1.2). Building on this, the chapter delves into the current state of research regarding instabilities at the lithium-electrolyte interface (cf. Section 2.1.3), which constitutes the primary focus of the present work. Subsequently, common experimental (cf. Section 2.2.1) and theoretical methods (cf. Section 2.2.2) for characterizing this interface are summarized. Finally, special attention is given to the basic principles (cf. Section 2.3.1) of the kinetic Monte Carlo method and its application in the investigation of the solid electrolyte interphase (cf. Section 2.3.2).

2.1 Lithium-Based Batteries

2.1.1 Operating Principles

The term "lithium-based batteries" serves as an umbrella for various battery technologies that utilize lithium as their primary electrochemically active element. They all have in common that they are electrochemical energy storage systems that store energy chemically and convert it into electrical energy on demand. They can be classified into primary and secondary cells. In primary cells the conversion of chemical to electrical energy is irreversible. In contrast, secondary cells can be recharged, which means that electrical energy can be converted back into chemical energy [34]. The most well-known and widely used representative of secondary lithium-based batteries is the lithium-ion battery. Based on this example, the following section first explains the fundamental working principle of rechargeable lithium-based batteries. The focus then shifts to lithium metal batteries (LMB), which are the main subject of this work.

The basic structures of a LIB and a LMB are illustrated in Figure 2.1. In both cases, the key components are the negative and positive electrodes, which store and release lithium; the liquid electrolyte composed of one or more solvents, a conducting salt, and optional additives, which acts as ionic conductor between the electrodes; and the electronically insulating separator that

prevents short circuits between the electrodes. Both electrodes are furthermore connected by an external electric circuit.

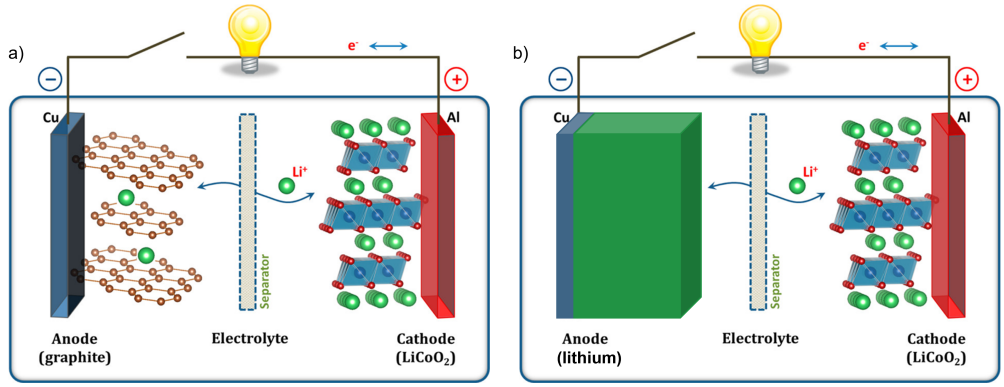

Figure 2.1: Scheme of structure and operating principle of a) Lithium-ion battery cell and b) Lithium metal battery cell adapted with permission from [35]. Copyright 2013, American Chemical Society.

During discharge two separate half cell reactions take place at the two electrodes: (1) At the negative electrode, which is also called anode, an oxidation reaction occurs and (2) at the positive electrode, which is also called cathode a reduction reaction takes place. For the example of a conventional LIB with a graphite anode and a $LiCoO_2$ cathode this leads to the following half cell reactions [34]:

Anode half cell reaction:

$$LiC_6 \rightleftharpoons Li^+ + e^- + 6\,C \tag{2.1}$$

Cathode half cell reaction:

$$2\,Li_{0.5}CoO_2 + Li^+ + e^- \rightleftharpoons 2\,LiCoO_2 \tag{2.2}$$

Once a Li^+ ion was released by the anode half cell reaction, it is solvated in the liquid electrolyte. Driven by concentration and potential gradients it is subsequently transported to the cathode. Simultaneously, the released electron is transferred through the anode current collector into an external circuit where it may power an electrical load and is further transferred to the cathode. Eventually, the cathode half cell reaction takes place at the cathode surface and the Li^+ ion is stored in the cathode crystal structure. All of these processes, including the polarity of the electrodes, are reversed during charging.

For all the mentioned cell components, a wide range of materials is used in state-of-the-art battery cells. A comprehensive overview on this topic can be found in the textbook "Lithium-Ion

Batteries: Basics and Applications" [34] and the reviews by Nitta et al. [36] (electrode materials), Luo et al. [37] (separator materials) and Liu et al. [38] (liquid electrolytes). However, since this thesis focuses specifically on the interfaces at lithium metal anodes, the following will address negative electrode materials exclusively.

Modern LIBs predominantly use graphite as anode material [9]. Graphite electrodes belong to the so-called intercalation electrodes, meaning that Li^+ ions can be reversibly inserted and stored between the graphite layers without being reduced to elemental lithium as illustrated in Figure 2.1. As already pointed out in the anode half cell reaction in Equation 2.1, up to one Li^+ ion can be intercalated per six carbon atoms in graphite. This results in a theoretical gravimetric capacity of graphite anodes of 372 mAh g^{-1} [39]. Overall, graphite combines several advantageous properties, such as high cycling stability and a low electrode potential. Additionally it is readily available and cost-effective [39, 40]. However, its performance has already been pushed very close to the theoretical limits [11]. For instance, Shi et al. [41] reported a synthetic graphite achieving a gravimetric delithiation capacity of up to 369 mAh g^{-1} depending on the discharge current. Hence, to fulfill the market requirements for higher energy density for applications such as long-ranging vehicles or electric propulsion in aviation new anode materials for secondary battery cells need to be considered.

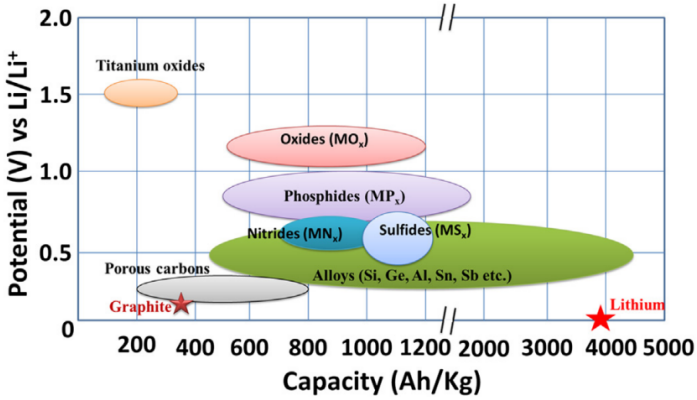

Figure 2.2: Comparison of typical anode materials with respect to potential and theoretical gravimetric capacity, reproduced from [42], licensed under CC BY 3.0.

A comparison of different anode materials in terms of their potential vs Li/Li^+ and their theoretical specific capacity is provided in Figure 2.2. This shows that among the anode materials, graphite offers a favorable low potential but also has a relatively low gravimetric energy density. In contrast, lithium metal exhibits the lowest electrode potential at -3.04 V vs. SHE, paired with a very high theoretical gravimetric capacity of 3860 mAh g^{-1}, more than ten times that of graphite [11]. These properties make lithium metal a very promising candidate for high-energy density

anodes. As visualized in Figure 2.1 b), the lithium metal anode, unlike conventional intercalation electrodes, does not require a host structure. Instead, metallic lithium is directly plated onto the copper current collector during charging. Consequently, the anode half cell reaction transitions to the direct lithium oxidation/reduction reaction as outlined in Equation 2.3.

Lithium metal half cell reaction:

$$\mathrm{Li}^{(0)} \rightleftharpoons \mathrm{Li}^{+} + \mathrm{e}^{-} \tag{2.3}$$

Despite its positive characteristics, the practical implementation of lithium metal in secondary battery cells still faces significant challenges such as dendrite growth, low Coulombic efficiency, and uncontrolled SEI formation [11] (cf. Section 2.1.3). In the following, the historical development and application of LMB is discussed in Section 2.1.2 and a detailed overview on the challenges related to interfacial instabilities and SEI formation is provided in Section 2.1.3.

2.1.2 A Short History of Lithium Metal Batteries

The development of battery cells utilizing lithium metal anodes dates back to the 1970s [11, 43]. Early advancements focused on primary battery cells with a variety of cathode chemistries [44]. Examples include lithium-iodine (Li/I_2) cells and lithium-manganese dioxide (Li/MnO_2) cells, which are used to this day due to their high specific energy densities in the order of 210 to 270 Wh kg^{-1} and long storage capabilities [44, 45]. Typical applications are medical devices such as pacemakers, implantable defibrillators, and electromechanical hearing systems, as well as consumer products like watches and calculators [43–45].

The first secondary LMB was developed only shortly thereafter. By 1972, the general concept of intercalation electrodes on the cathode side was developed [43]. In the late 1970s Exxon Mobil produced the first rechargeable LMB containing a titanium disulfide intercalation cathode developed by Stanley Whittingham [11, 43, 44]. However, the commercialization of this cell was hindered due to uncontrolled dendrite growth (cf. Section 2.1.3) on the lithium metal anode [43]. In the late 1980s the first secondary LMB, combining the lithium metal anode with a molybdenum disulfide (MoS_2) cathode, was commercialized by Moli Energy Ltd. However, the cell had to be withdrawn from the market due to safety concerns stemming from cell fires caused by dendrite formation [11, 44].

With the development and commercialization of graphite as an anode intercalation material by Sony in 1991, safety concerns were effectively addressed, leading to the replacement of lithium metal anodes by graphite electrodes in secondary battery cells [11, 43]. Therefore, in the following years the research focus shifted away from lithium metal anodes towards the optimization of the novel lithium-ion batteries, which can nowadays reach specific energy densities of around

250 Wh kg^{-1} [11]. However, as previously noted, practical LIBs are approaching their theoretical limits [14]. Consequently, the requirement of high-energy-density battery cells has renewed interest in lithium metal as anode material over the last decade [11, 13, 14, 46].

In addition to combining lithium metal anodes with modern intercalation cathodes, which can increase the overall energy to approximately 440 Wh kg^{-1} [11, 47], a special focus of recent research was set on the application in lithium-sulfur and lithium-air batteries [11, 48]. Both promise significantly higher energy densities. In the case of lithium-sulfur batteries the theoretical energy density reaches 2567 Wh kg^{-1} [49] and the practical energy density is estimated between 600 Wh kg^{-1} and 650 Wh kg^{-1} [47, 48]. In this cell, sulfur is utilized as the active cathode material supported by a carbon-based host structure [48]. The cell chemistry is already applied in drones due to its comparatively low weight [48]. Nevertheless, its cycling stability is still low compared to LIB, and challenges such as the poly-sulfide shuttle effect still need to be resolved [44, 48]. The practical energy density of lithium-air batteries is estimated to be even higher with 950 Wh kg^{-1} [11]. In this case, the cathode is usually a porous carbon-structure which is open towards the surrounding atmosphere. During discharge, oxygen is reduced to Li_2O_2 or Li_2O which is reversed during charging [50]. However, this cell chemistry also faces numerous challenges such as complex reaction kinetics, electrolyte stability, safety concerns due to interfacial instabilities on the anode side and poor rate capability [44, 49, 50].

To address the remaining challenges of lithium metal anodes, a significant focus has been placed on electrolyte development with the aim to stabilize interfacial processes and to suppress dendrite growth (cf. Section 2.1.3). In this context also solid-state electrolytes, consisting either of inorganic ceramics or of solid polymers gained increasing interest [11]. They offer a number of advantages such as higher mechanical stability, which could suppress dendrite growth and higher thermal stability [11, 51]. Nevertheless, they come with their own challenges, including potential contact loss between the anode and the solid electrolyte, comparatively low ionic conductivity and instabilities against lithium metal [52]. More details are discussed in the recent review by Janek et al. [51]. In contrast, liquid electrolytes offer high ionic conductivities and better accommodate the large volume changes of the lithium anode during cycling [13]. Therefore, a variety of approaches have been pursued in recent years to improve the performance of LMB with liquid electrolytes. These include the utilization of electrolyte additives, ether-based electrolytes, high-concentrated and locally high-concentrated electrolytes as well as the addition of fluorinated compounds [19]. Based on this, the Coulombic efficiency was increased to more than 99% [53]. Further research efforts were put into the development of protecting surface films, also known as artificial SEI and the design of 3D electrode structures which are supposed to increase the anode surface area and hence reduce local current densities [11, 13].

Nevertheless, secondary LMB still do not meet the requirements for widespread commercialization. In particular, long-term cycling with a capacity retention of 80 to 90 % after 1000 cycles

would require Coulombic efficiencies clearly above 99.95, which remains challenging for current systems [53]. This is primarily due to interfacial instabilities of lithium metal, which lead to SEI formation and dendrite growth, causing a continuous loss of active lithium and significant safety concerns. A detailed understanding of these interfacial processes, and how they can be influenced by macroscopic properties, is therefore crucial for further advancing LMB. The details of interfacial instabilities and SEI on lithium metal are discussed in the following Section 2.1.3. In Chapters 3 to 5 of this work, novel kinetic Monte Carlo models will be developed and applied, providing a mechanistic understanding of the spontaneous SEI formation at lithium metal anodes.

2.1.3 Interfacial Instabilities and Solid Electrolyte Interphase

As outlined in the previous Section 2.1.2, the low Coulombic efficiency of LMB can be mostly attributed to interfacial instabilities of the lithium metal anode, such as dendrite growth and uncontrolled SEI formation. These issues represent the most critical barriers to the widespread commercialization of LMBs [46]. The following section explains these challenges in greater detail, with a particular emphasis on the role and current advancements in understanding the SEI.

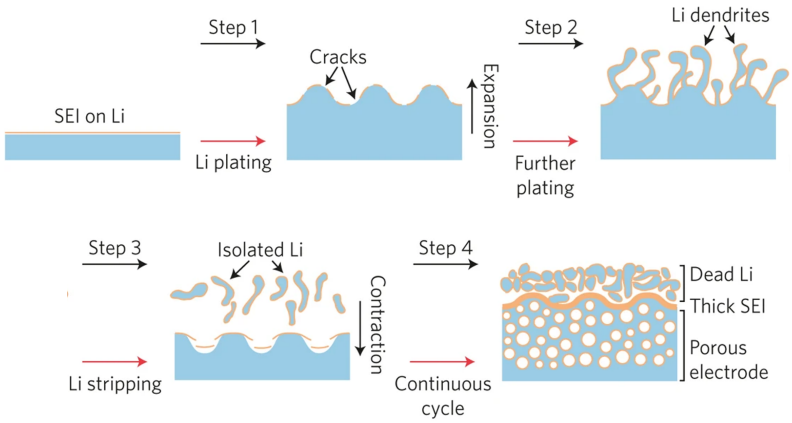

Figure 2.3: Illustration of interfacial processes on lithium metal anodes leading to ongoing SEI formation, dendrite growth and dead lithium adapted with permission from [11]. Copyright 2017, Springer Nature.

Because of the low electrode potential of -3.04 V vs. SHE which lies below the electrochemical stability window of most electrolyte components (cf. Figure 2.4), spontaneous (electro-)chemical

electrolyte degradation reactions occur upon the contact between the lithium anode and the electrolyte [11, 54]. Subsequent precipitation of degradation products leads to the formation of a protective surface layer [14]. This layer is also called solid-electrolyte interphase and was first described by Peled [15]. During cycling, the SEI undergoes further growth and aging, which is strongly related to the lithium stripping and plating behavior as illustrated in Figure 2.3 [11]: Upon charging, lithium is plated onto the anode, which drastically increases the anode's volume. If the SEI lacks sufficient stability and flexibility to accommodate this expansion, cracks can form in the passivating layer, exposing fresh reactive lithium metal to the liquid electrolyte (step 1). This triggers further electrolyte decomposition, leading to the loss of active lithium and promotes inhomogeneous nucleation, which might cause subsequent dendrite growth [11, 13]. Over time dendrites might penetrate the separator and cause hazardous electrical short circuits [54]. In addition, this non-homogeneous plating increases the lithium metal surface, resulting in additional electrolyte decomposition reactions (step 2) [54]. During discharge, lithium is stripped from the lithium metal anode. If lithium is stripped from the bottom of the dendrites, parts of the lithium metal may lose electrical contact with the anode, making it unavailable for further cycling (step 3). This encapsulated lithium is also called 'dead lithium' and drastically decreases the capacity of the cell [11, 13, 54]. It is currently believed that this process is the primary reason for insufficient Coulombic efficiency in LMB [13, 46]. Over the course of many cycles, these processes can result in a highly porous lithium metal anode, also referred to as mossy lithium (step 4) [13]. This porous structure exhibits a highly increased lithium metal surface with a thick SEI and an accumulation of dead lithium [11]. While an initially increased lithium surface area may temporarily even decrease overpotential, the final porous lithium anode causes a significant increase in overpotential caused by slow Li^+ ion transport [13, 14, 54].

An important strategy to overcome the described challenges is the design of a functional SEI that ensures homogeneous nucleation and plating and effectively prevents the growth of dendrites [13]. To achieve this, the ideal SEI must fulfill a comprehensive list of requirements [11, 14]:

- **Electrical insulator** to prevent ongoing reduction of electrolyte components
- **High ionic conductivity** to allow for a fast and homogeneous Li^+ ion transport and reduce internal cell resistance
- **Low thickness** to reduce the loss of active lithium and ensure low internal cell resistance
- **Homogeneous composition** to prevent heterogeneous nucleation and dendrite growth
- **Mechanical stability and flexibility** to accommodate the large volume changes of the metal electrode upon cycling

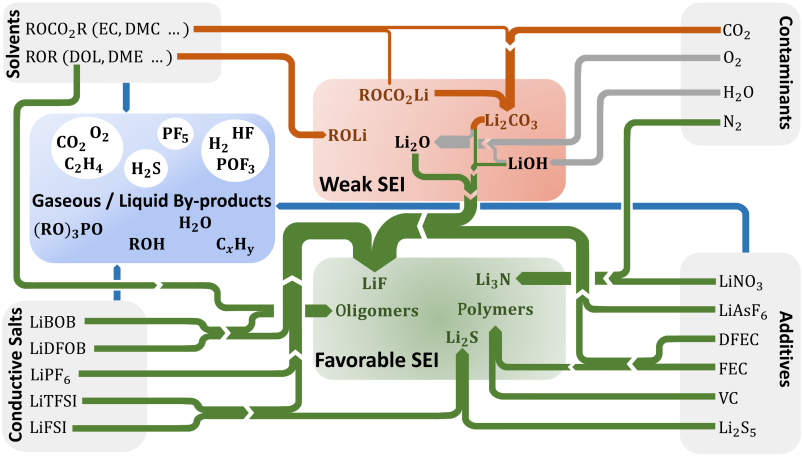

Figure 2.4: Schematic overview of typical SEI species and formation side products derived from various liquid electrolyte components, including solvents, conducting salts, contaminants, and additives. Reproduced from [13], licensed under CC BY-NC 3.0 .

These properties are governed by the chemical composition and morphology of the surface film [13, 16]. Since the SEI originates from the (electro-)chemical decomposition of electrolyte components, including solvents, conducting salts, additives and contaminants, its composition directly depends on the electrolyte chemistry [13, 16, 19]. As illustrated in Figure 2.4, there is a large variety of possible SEI species as well as liquid or gaseous by-products, which depend on the specific reactivity of the electrolyte components. Typical SEI components include inorganic species such as lithium fluoride (LiF), lithium carbonate (Li_2CO_3) and lithium oxide (Li_2O), as well as organic compounds like alkyl carbonates ($ROCO_2Li$) and polymeric species [13, 14, 16, 19]. As indicated in Figure 2.4, these species can be classified into 'favorable SEI' species that are associated with more uniform lithium deposition and a higher mechanical stability of the SEI and 'weak SEI' species, which tend to result in less stable films [13]. However, it should be noted that the mechanistic understanding of the performance of SEI components remains poorly understood [13, 18, 19]. Overall, SEI composition and thus performance can be effectively manipulated by the choice of electrolyte chemistry. However, investigating the correlation between electrolyte composition and SEI properties is particularly challenging due to the extremely thin nature of this interphase on the nanometer scale and its ultrafast formation kinetics. As a result, this topic has already occupied researchers for over 40 years.

As mentioned above, the first SEI model was proposed by Peled in 1979 [15]. In this work, the SEI was described as an electronically insulating and ionically conductive layer that spontaneously forms on lithium metal. This layer was depicted as consisting of crystals of various sizes, with Li^+ ion transport occuring via a Schottky vacancy hopping mechanism. In the following years, pioneering work regarding the composition of SEI in a wide range of different electrolytes

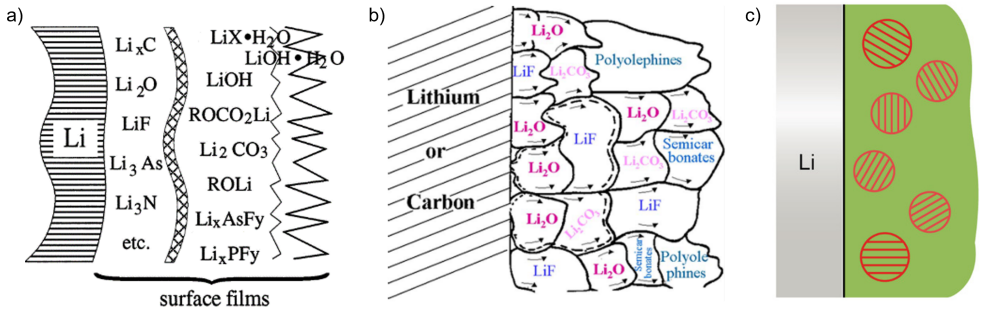

Figure 2.5: Comparison of suggested SEI models from literature. a) Multilayer model by Aurbach [55]. Reproduced with permission from [55]. Copyright 2000, Elsevier. b) Mosaic model by Peled et al. [16, 56]. Reproduced from [16] and [56] by permission of IOP Publishing Ltd., ©The Electrochemical Society. All rights reserved. c) Plum-pudding model. Reproduced with permission from [19]. Copyright 2021, John Wiley & Sons.

and corresponding lithium morphology was conducted by the research groups of Aurbach [55] and Kanamura [57–59]. Based on their in-depth XPS studies, Aurbach et al. eventually suggested the multilayer SEI structure as illustrated in Figure 2.5 a). According to this model, the SEI consists of an inner compact layer, mostly consisting of a mixture of components with low oxidation state and an outer porous layer, rather consisting of a mixture of components of higher oxidation state [16, 55]. Around the same time Peled et al. updated their original SEI model [15] and introduced the mosaic SEI model [56] as illustrated in Figure 2.5 b). In this model, the SEI is described as a heterogeneous mixture of pure mircophases of various insoluble degradation products [16, 18, 19, 56]. Li^+ ion transport is proposed to occur predominantly along the grain boundaries between these microphases [16, 18, 56]. Consistent with the multilayer model of Aurbach [55], the model further suggests a higher concentration of stable, inorganic microphases near the electrode surface and a higher number of less stable, organic microphases closer to the electrolyte [16, 56, 60]. Only recently, Wu et al. [19] introduced the novel "plum pudding" SEI model which is illustrated in Figure 2.5 c). Based on cryogenic transmission electron microscopy measurements they conclude that the SEI mainly consists of amorphous rather than crystalline phases and that only some crystalline microphases are either dispersed within the amorphous SEI or accumulated on the outer layer of the SEI [19].

Overall, the exact structure of the SEI is still under discussion [19]. Although, there is a comprehensive knowledge about the possible degradation products of many different electrolyte systems [13, 16, 18, 19], a full mechanistic understanding of SEI formation is still missing [14, 18, 19]. In particular, a general relationship between the structure, composition and property of the SEI still needs to be established [18, 19]. This knowledge is crucial for the targeted design of an optimized SEI that fulfills all aforementioned requirements and could hence enhance the safety and extend the lifetime of modern LMB. Consequently, SEI research remains a highly relevant field.

The next section provides a brief overview of the most important experimental and theoretical methods that are used for SEI investigation.

2.2 Characterization of Solid Electrolyte Interphase[1]

2.2.1 Experimental Techniques

A wide range of experimental methods is applied to characterize the SEI under a variety of experimental conditions [16]. This section is meant to provide a brief overview of the most important experimental analysis techniques. For more details the reader is referred to the reviews of Verma et al. [17] and Xu et al. [61].

Performance and lifetime data of secondary LMB are comparatively well accessible by cycling experiments, static methods, e.g. differential voltage analysis [62], and dynamic characterization, e.g. via impedance measurements or nonlinear-frequency response analysis [24, 63]. In particular, impedance measurements allow to obtain valuable information on the SEI such as the imposed cell resistance and ionic conductivity. These experiments are non-destructive and can be performed on full battery cells.

In contrast, it is more intricate to investigate the SEI's chemical composition or morphology experimentally, due to its low thickness and high reactivity towards the atmosphere [17, 19]. For the purpose of studying the chemical composition of the SEI, mostly spectroscopy techniques are applied. The two most common techniques are the X-ray photoelectron spectroscopy (XPS) and Fourier transform infrared spectroscopy (FTIR), which have both been applied since the 1990s [18, 19, 60, 64]. XPS allows the analysis of all elements with the exception of H and He [17, 18]. It mainly characterizes the outermost SEI layers, due to its limited penetration depth of up 10 nm [17, 18]. To obtain information on deeper layers, in-depth XPS can be performed by combining XPS measurements with surface sputtering [16, 18, 60, 64]. However, this approach is inherently destructive and may alter the original chemical composition of the SEI [17]. XPS predominately provides information on inorganic compounds [61]. Complementary, FTIR is particularly useful to identify organic compounds [61]. The technique is capable of identifying functional groups and the type of chemical bonds [17, 18] and also allows *in situ* characterization [13, 61]. Further techniques that can be applied to investigate the SEI chemistry comprise Raman spectroscopy, Auger electron spectroscopy, nuclear magnetic resonance and time-of-flight secondary ion mass

[1] Parts of this section have been published in J. Wagner-Henke et al., Nat. Commun. 14, 6823 (2023) [1], licensed under CC BY 4.0.

spectrometry [18, 60, 61]. A combination of these techniques enables a good characterization of SEI chemistry [18].

The analysis of the surface morphology is primarily conducted using microscopy techniques [13]. In this context, morphology comprises properties such as SEI thickness and structure as well as the characteristics of deposited lithium, including porosity and deposition in form of whiskers or dendrites. The most commonly applied methods include optical microscopy, scanning electron microscopy (SEM), and transmission electron microscopy (TEM), listed in order of increasing resolution, with TEM providing sub-nanometer precision [13, 18, 19]. In general, both surface images and cross-section images provide valuable insights into the nature of lithium deposition and SEI morphology. A recent advancement, is the application of cryogenic TEM (cryo-TEM), which allows to study the morphology of electrochemically deposited lithium and the corresponding SEI with great detail in different electrolyte solutions [19, 65, 66]. Another technique is atomic force microscopy (AFM). This method provides insights on the three-dimensional surface structure as well as mechanical properties, such as the Young's modulus [18, 61].

In recent years, increasing efforts have been made to develop methods specifically designed for investigating the spontaneous SEI formation on lithium metal. Kühn et al. [67] introduced a novel cutting technique that enables the reproducible study of SEI formation on pristine lithium metal, eliminating native passivation layers. Additionally, von Holtum et al. [68] developed an approach that periodically disrupts the spontaneously formed SEI, thereby increasing the SEI species concentration in the solid, liquid and gaseous phases. This enables a qualitative and quantitative chemical analysis of the SEI compounds, as well as of the liquid and gaseous byproducts of SEI formation.

Overall, experimental techniques allow comprehensive descriptive insights into the chemical SEI composition and morphology. However, they struggle to identify and understand the underlying mechanisms of SEI formation. It is therefore essential to complement these experimental techniques with theoretical calculations, which will be introduced in the following Section 2.2.2.

2.2.2 Theoretical Techniques

Theoretical calculations allow a complementary and detailed resolution of the governing processes inside a battery, enabling a targeted virtual optimization or tracking of the state of the battery and its components [69, 70]. Battery processes occur across a wide range of temporal and spatial scales, spanning from entire battery packs to individual cells, electrodes, particles, material structures and down to the atomistic level [71]. Due to this large variety, a number of different modeling approaches as well as multiscale models are required to cover the entire system dynamics of a battery cell [71, 72]. A comparison of different approaches with respect

to their typical scales is depicted in Figure 2.6. Models at each scale can be applied either as stand-alone tools, or integrated into a multiscale framework [71, 72]. Multiscale approaches can generally be categorized into sequential and iterative schemes [71]. In sequential multiscale modeling, the output of a lower-scale model – such as reaction energies from quantum chemical calculations – is used as input for a higher-scale model, e.g. a mesoscale or continuum simulation. Iterative models, on the other hand, involve a two-way coupling between different models, where the output of one model is iteratively fed into the other and vice versa [71].

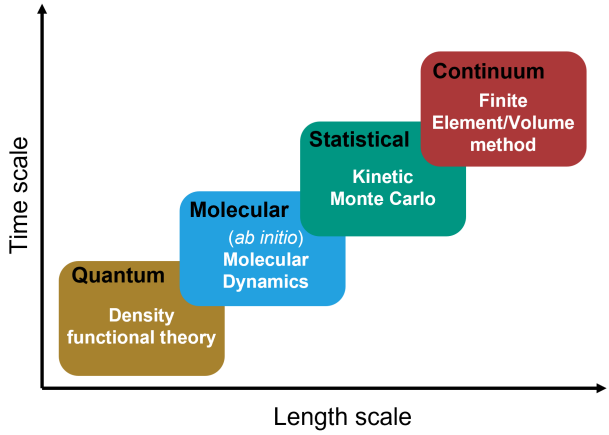

Figure 2.6: Comparison of length- and timescales of different simulation techniques adapted with permission from [73], Copyright 2022, John Wiley & Sons.

In the analysis of phenomena at the electrode/electrolyte interface, including SEI formation, growth and aging, the scales from the cell level downwards are of particular importance. Continuum cell models like Single Particle models [74] or Newman-type pseudo two-dimensional models [75] allow to understand the limiting processes during the cycling of a battery cell. In order to incorporate the effect of the SEI on cell performance with respect to ionic conductivity, thickness and cell resistance, there are some examples in the literature where these models were extended by a mechanistic model for the anodic surface layer [24, 25, 76]. These models also allow identifying SEI properties such as thickness or ionic conductivity, and thus SEI and cell diagnosis, after parametrization to discharge and impedance spectra. Further macroscopic surface models containing a SEI mainly focus on the long-term growth regime and the related charge transport through the SEI. They can predict macroscopic properties such as SEI thickness or porosity depending on applied potential or storage time [26, 77, 78]. Additionally, continuum models can also predict SEI degradation and reformation at elevated temperatures or during the thermal runaway [79, 80]. All of these continuum models have in common that they cannot predict the detailed chemical composition of the SEI or its nanomorphology and mostly neglect or

lump the details of the underlying kinetic processes. These challenges have been partially addressed by the recently published SEI formation model of Weddle et al. [27]. In this sequential multiscale approach, a large *ab initio*-informed reaction network is directly incorporated as input, which allows the prediction of SEI formation and composition on Silicon with a 1D resolution. However, the lack of spatial resolution still prevents the model to predict SEI nanomorphology or to account for local heterogeneities. Moreover, the model requires a constant electrode/SEI surface and can hence not be easily transferred to spontaneous SEI formation on a dissolving lithium metal anode.

On the contrary, atomic-scale theoretical approaches like DFT, *ab initio* MD (AIMD) and ReaxFF MD provide a fundamental understanding of the initial steps of SEI formation. DFT is an *ab initio* method that approximates the solution to the Schrödinger equation by making use of the Hohenberg-Kohn theorem [81] that states that "The ground-state energy from Schödinger's equation is a unique functional of the electron density" [82]. A typical investigated system consists of up to a few hundred atoms and can represent, for example, molecules or crystalline materials [71, 82]. The method enables the calculation of the total energy of the system for a given atomic configuration [82]. Based on the comparison of the energies of different configurations, the reactivity of chemical species such as electrolyte components, as well as relevant decomposition mechanisms and their related reaction energy profiles can be predicted [83]. Since this is of particular interest for the mechanistic understanding of SEI formation, a large number of DFT studies on the decomposition of electrolyte components including solvents [21, 22, 84–90], salts [91, 92] and additives [21, 22, 84, 89, 93, 94] have been reported in literature. These studies provide valuable mechanistic insight into the large variety of SEI formation mechanisms. However, the method is limited to the investigation of elementary reaction mechanisms and can not predict layer formation in larger systems.

To partly overcome this limitation DFT can be coupled with MD. This is a simulation technique that describes the motion of atoms according to classical mechanics, following Newton's laws of motion [82]. When DFT and MD are iteratively coupled, the resulting method is referred to as AIMD. In this approach DFT is used to compute the potential energy after each MD time step, which then serves as the basis for updating the atomic positions in the subsequent MD iteration [82]. Applied to SEI formation, AIMD enables the prediction of electrolyte decomposition reactions and the very initial stages of layer formation in multi-molecular system. However, due to the high computational cost of the frequent DFT calculations, these simulations are typically limited to timescales of up to approximately 20 ps [71]. Despite this constraint, the approach has been successfully applied to a wide range of electrolyte components, including organic [23, 95] and ether-based [96, 97] solvents, conducting salts [23, 96–98], and additives [23, 95, 98].

A more computational efficient approach is the sequential coupling of DFT and MD through the development of reactive force fields. In this approach, force fields are trained based on DFT

calculations to capture not only interatomic interactions but also bond breaking and formation, enabling the simulation of chemical reactions [71, 99]. Since this method, that is commonly referred to as ReaxFF MD, is not directly coupled to *ab initio* calculations, it requires complex, system-dependent parameterization of the force fields and is less accurate than AIMD [20]. However, it significantly extends the accessible timescales up to the nanosecond range and allows to study larger systems as demonstrated in various SEI formation studies [100–102]. A promising hybrid approach that aims to combine the accuracy of AIMD with the efficiency of ReaxFF MD is the recently developed hybrid *ab initio* MD combined with reactive force fields (HAIR) method [97, 103]. This approach allows to increase the simulation time by one order of magnitude compared to AIMD while maintaining higher accuracy than ReaxFF MD, and has yield SEI compositions and structures for different electrolyte systems [97, 103].

Although the wide range of atomistic simulation techniques already covers multiple scales and provides valuable insights into early SEI formation and relevant degradation mechanisms, these methods remain too computationally expensive to access more practically relevant scales, as envisioned in this work. Nevertheless, their predicted reaction mechanisms and associated energies can serve as valuable input for higher-scale modeling approaches within the framework of sequential multiscale simulation [71, 72]. Their output data can either be directly used as input for continuum models, as demonstrated by Weddle et al. [27] or applied to parameterize mesoscale models [72]. As highlighted by previous publications [28, 71] and illustrated in Figure 2.6 the kinetic Monte Carlo method is a key mesoscale approach to bridge the gap between atomistic and continuum scales. This stochastic approach overcomes the scale limitations of atomistic simulations, while keeping detailed molecular information [28]. Beyond their applications in sequential multiscale frameworks with DFT-derived input data, kMC models can also be iteratively coupled with continuum-level models. This bidirectional coupling allows to additionally investigate the interplay of macroscopic properties such as electrode design or charging rates and microscopic film growth across scales [30, 31, 72, 104].

Details on the fundamentals of the kMC method and published kMC models for the simulation of SEI are discussed in the following Section 2.3. For more details on the fundamentals of atomistic and continuum simulation techniques interested readers are directed to the following literature: "Density Functional Theory: A Practical Introduction" by Sholl and Steckel [82] and "Density Functional Theory: An Advanced Cours" by Engel and Dreizler [105] for DFT, " Understanding Molecular Simulation" by Frenkel and Smit [106] and "Statistical Mechanics: Theory and Molecular Simulation" by Tuckerman [107] for MD and "Electrochemical Systems" by Newman and Balsara [108] for continuum cell modeling.

2.3 The Kinetic Monte Carlo Method

As previously discussed, the kMC method is a powerful mesoscale simulation technique that effectively bridges the gap between detailed atomistic simulations and length- and timescales of practical relevance. This section aims to provide a general overview of the method and previous applications in the context of SEI research. Readers seeking more detailed insights into the fundamentals of the kMC approach are directed to the works of Jansen [109], Andersen et al. [110] and Kratzer [111]. The section is divided into two parts: First, the fundamental principles of the kMC technique and the derivation of rate constants from transition state theory are briefly summarized (cf. Section 2.3.1). Second, existing literature on kMC models for SEI formation simulations is reviewed, highlighting key findings, recent methodological advancements, and remaining challenges (cf. Section 2.3.2).

2.3.1 Theoretical Fundamentals

The kMC approach, like all Monte Carlo techniques, is a stochastic simulation method that models the behavior of chemical systems based on random numbers. Its unique feature lies in its ability to describe the dynamic evolution of a system over time, rather than predicting thermodynamic properties at equilibrium such as conventional Monte Carlo approaches [110, 111]. To achieve this, the kMC method models time-dependent processes that move the system from one state of locally minimized energy on the potential energy surface (PES) to the next. In contrast to atomistic simulation techniques such as MD or AIMD, these processes only comprise comparatively slow and rare events. This excludes processes that only result in fluctuations around the same local minimum such as e.g. fast atomic vibrations. This coarse-graining approach allows the kMC method to reach significantly larger length- and timescales while maintaining detailed spatial resolution at the molecular or atomic level [110]. Each of the considered rare events requires a predefined transition rate, which depends on the local configuration of the system. Based on these transition rates, a series of randomly selected processes is carried out with only one event occurring at a time. The waiting time between two consecutive events defines the respective time step of the simulation. Overall this approach results in a Markov process, where each event depends solely on the current configuration of the system and is independent of any previous processes or configurations [111].

A mathematical formulation of this Markov process is given by the so-called master equation (cf. Equation 2.4). This describes the time-evolution of probability P_α to find the system in a

configuration α as a function of the sum of all transition rates of processes that would leave $\Gamma_{\alpha\beta}$ or enter $\Gamma_{\beta\alpha}$ this configuration. [109, 110, 112].

$$\frac{dP_\alpha(t)}{dt} = -\sum_{\beta\neq\alpha}\Gamma_{\alpha\beta}P_\alpha(t) + \sum_{\beta\neq\alpha}\Gamma_{\beta\alpha}P_\beta(t) \tag{2.4}$$

In principle this gives a finite system of differential equations with the number of states corresponding to the number of possible configurations. Since a configuration describes the kind and position of molecules at all locations within the simulation domain, the complexity scales quickly with the number of considered species and the size of the simulation domain, making an analytical solution infeasible [110]. Instead, the stochastic kMC algorithm aims at a numerical solution of this master equation. It starts at an initial configuration and then follows a sequence of randomly selected processes from one configuration to another leading to a stochastic trajectory of the system through time [112]. To further reduce the complexity of the calculations, the investigated physical systems are often mapped onto a lattice with predefined discrete sites that specify the possible locations for all modeled particles [113]. This approach allows to determine the transition rates based on a finite number of possible local configurations [112] and is applied in this thesis.

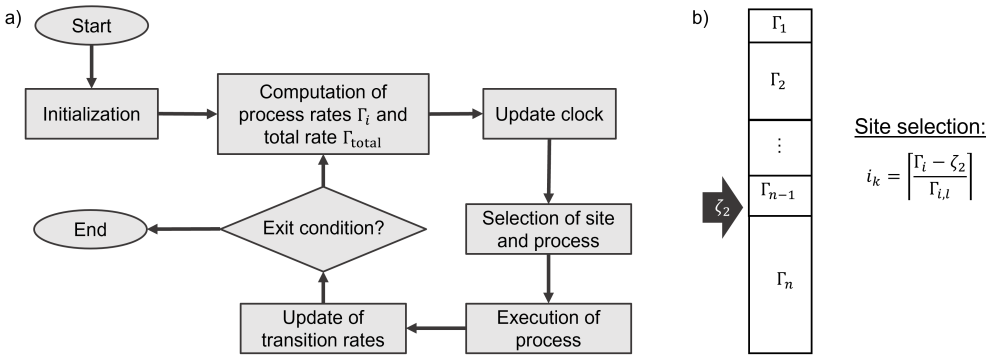

Figure 2.7: Schematic illustration of kinetic Monte Carlo algorithm. a) Flow chart of the Variable Step Size algorithm. b) Selection of process and site following the list-based algorithm of Schulze [114].

For the implementation of the kMC approach, several algorithms have been developed, comprising null-event and rejection-free algorithms, with the latter being usually more efficient and more commonly used in kMC simulations [113, 115]. A widely used rejection-free algorithm is the Variable Step Size Method [109], which goes back to Bortz et al. [116] and Gillespie [117] and is illustrated in Figure 2.7 a). Its main steps can be summarized as follows [31, 109, 110]:

Variable step size algorithm:

1. Initialization of simulation box, set up of initial configuration and precalculation of all transition rates $\Gamma_{i,l}$ for all possible events i on all lattice sites l for given state
2. Computation of process rates $\Gamma_i = \sum_l \Gamma_{i,l}$ and overall rate $\Gamma_{\text{total}} = \sum_i \Gamma_i$
3. Drawing of first random number $\zeta_1 \in (0,1]$, calculation of time step $\Delta t = -\frac{\ln(1-\zeta_1)}{\Gamma_{\text{total}}}$ [118] and update of clock
4. Drawing of second random number $\zeta_2 \in (0, \Gamma_{\text{total}}]$ and selection of process m and site k, such that $\sum_{i=1}^{m}\sum_{l=1}^{k-1}\Gamma_{i,l} < \zeta_2 \leq \sum_{i=1}^{m}\sum_{l=1}^{k}\Gamma_{i,l}$
5. Execution of selected process
6. Update transition rates $\Gamma_{i,l}$
7. If stop condition is not fulfilled (e.g. $t_{\text{KMC}} < t_{\text{end}}$) go back to 2, else stop

In this algorithm, especially the process selection in step 4 and the updating of transition rates in step 6 can be computationally expensive. Therefore, a wide range of efficient searching and updating algorithms has been suggested in literature [113–115]. One example, which is applied in this thesis to accelerate the process selection in step 4, is a list-based algorithm according to Schulze et al. [114]: Usually, the selection process requires two binary searches - one to select a process and a second to select the site on which the process is to be conducted. In case of only a limited number of distinct transition rates the second binary search can be eliminated by precomputing all possible processes on all sites and sort them into lists corresponding to their distinct rates. Once a process with a distinct rate is selected, the site can be directly calculated based on the random number, as the process occurs with equal probability at all sites (cf. Figure 2.7 b)). This is particularly useful if the number of distinct rates is small, as the remaining binary search can then be carried out over a correspondingly short list. Moreover, instead of updating all transition rates in step 6 (global update), it is common to only update the transition rates of all sites, which are affected by the last executed event (local update). Since most transition rates only depend on the next-neighbor configuration of the respective site, this significantly reduces the number of rates that need to be updated in every single kMC iteration [113].

Although, the above kMC algorithm is theoretically exact, its practical accuracy highly depends on the quality of its input parameters. The selection of relevant processes to be considered and the determination of the corresponding transition rates is hence a crucial task when it comes to setting up a kMC model and requires *a priori* knowledge of the investigated system. In principle, processes, which comprise transport and (electro-)chemical reactions, and their rates can

be determined experimentally or theoretically. Experiments are particularly useful in determining transport rates, which can be calculated based on diffusion coefficients as derived by Jansen [109]:

$$\Gamma_D = \frac{D}{\Delta L^2} \tag{2.5}$$

Moreover, they can be used to obtain a general idea of the governing macroscopic reactions in the investigated system. However, it is usually difficult to identify and separate elementary reaction steps in experiment [109]. Therefore, elementary reactions and corresponding transition rate constants are usually derived theoretically [110]. *Ab initio* molecular dynamic calculations can be applied to identify relevant reaction pathways. Transition rates can subsequently be determined using Transitions State Theory (TST) as proposed by Eyring [119]. According to this theory, rates can be calculated by the following expression [110]:

$$\Gamma^{\mathrm{TST}} = \frac{Q^{\ddagger}}{Q_\alpha} \frac{k_B T}{h} \exp\left(-\frac{\Delta G^{\ddagger}}{k_B T}\right) \tag{2.6}$$

Thereby, $Q^{\ddagger}$ and Q_α are partition functions at transition state and at initial state, $\Delta G^{\ddagger}$ is the activation barrier, T represents the temperature and k_B and h stand for the Boltzmann and Planck's constant, respectively.

The general idea of the TST is illustrated in Figure 2.8. Both, the initial and final states correspond to local minima on the PES. These states are separated by an energy barrier that must be overcome to move from one state to the other. The saddle point between these two states represents the transition state (TS), and the energy difference between this transition state and the initial state defines the activation barrier $\Delta G^{\ddagger}$. The transition state is assumed to be in quasi-equilibrium with the initial state.

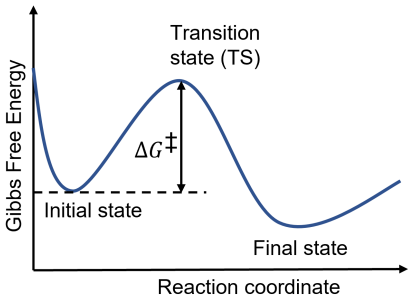

Figure 2.8: Schematic illustration of Transition State Theory.

The activation barrier is typically calculated using DFT. While the prefactor can theoretically also be calculated, its computation is often avoided due to the high computational cost. Instead, it is commonly approximated as a fixed prefactor k_0 within the range of 10^{12} s^{-1} to 10^{13} s^{-1} [110]. This assumption simplifies Equation 2.6 to the following expression:

$$\Gamma = k_0 \exp\left(-\frac{\Delta G^{\ddagger}}{k_B T}\right) \tag{2.7}$$

When calculating the activation energy, the following aspects should be considered: First, it is important to note, that there may be multiple possible TS for a given set of initial and final states. Accurate rate determination requires identifying the energetically most favorable TS, which can be challenging to identify. Furthermore, the calculated Gibbs Free energies are highly sensitive to interactions with the surrounding environment, including coordination with neighboring ions and molecules, interactions with surfaces (e.g. electrodes) and the electrolyte. Additionally, the applied level of theory can significantly impact the computed results. Due to these complexities, calculated reaction energies should always be considered as approximations. To ensure meaningful results, it is important to maintain a consistent framework for the calculation of energy values.

2.3.2 State of the Art: SEI Formation in kMC Simulations[2]

In terms of battery research, kMC models were already applied to a number of different systems [28] such as conventional lithium-ion batteries [29, 31] and next-generation lithium-sulfur [120–122] or lithium-air [123, 124] chemistries. A comprehensive summary of kMC models applied to all different kind of battery processes is given in the review by Gavilan-Arriazu et al. [28]. The focus of the following section is more specific, concentrating on literature that applies kMC models to simulate the formation of the solid-electrolyte interphase.

The application of kMC models to study SEI formation is a relatively novel technique. The first study in this field was published by Methekar et al. and dates back to 2011 [29]. In their study, they apply a two-dimensional kMC model to investigate SEI formation on a graphite anode during cycling. Their considered processes include adsorption, desorption, surface diffusion and a generic SEI formation reaction. All processes are parameterized based on experiment and continuum simulation. This approach allows them to draw conclusions on surface coverage and capacity fade in lithium-ion batteries, but did not allow to get insight on SEI properties such as thickness, porosity or chemical composition. Based on this work Röder et al. [30, 31] developed enhanced multiscale models that couple 2D+1 kMC models with macroscopic Newman-type battery cell models. These models were subsequently applied to evaluate the interplay between molecular growth of the SEI and macroscopic properties. For instance, the impact of particle radius and C-rates on SEI thickness and chemical composition were investigated. The considered reaction networks were relatively simple, considering either EC degradation to Li_2CO_3 and $(CH_2OCO_2Li)_2$ [30] or generic SEI formation mechanisms [31]. The required parameters were

[2] Parts of this section have been published in J. Wagner-Henke et al., Nat. Commun. 14, 6823 (2023) [1], licensed under CC BY 4.0.

either sourced from literature or estimated within plausible ranges. A similar approach was reported by Shinagawa et al. [32], who applied a 2D+1 kMC model coupled with a Single Particle Model to study the evolution of SEI thickness and the capacity fade of a battery cell over the course of several hundred charging cycles as well as the impact of surface defects. Thereby, they considered Li_2CO_3 formation from the EC solvent as the only SEI forming reaction and could hence not draw conclusions on the details of chemical SEI composition.

In parallel, also kMC stand-alone models have further been reported. Ramos-Sanchez et al. [125] developed a coarse-grained 3D kMC model to study the formation of $(CH_2OCO_2Li)_2$ surface films on graphite. They were particularly interested in how the interplay of the reduction rate and the $(CH_2OCO_2Li)_2$ formation rate impacts SEI formation and concluded that EC reduction limits the SEI growth. Additionally, Hao et al. [126] reported on a kMC model predicting capacity fade caused by a generic SEI formation reaction on graphite anodes. Based on this, they demonstrated that SEI formation is highly affected by the Li^+ ion diffusion kinetics through the SEI and that the SEI thickness increases as a square-root function of time.

More recently, an increasing number of kMC models that include more complex SEI formation reaction networks, which are at least partly derived from first principles calculations have been reported. Spotte-Smith et al. [33] presented a homogeneous spatially not resolved kMC model that incorporates an extensive computational reaction network for EC degradation, which was identified and parameterized using *ab initio* calculations and machine learning methods [127]. This model was used to study the competition between different SEI-forming reactions at graphite electrodes during cycling as well as the impact of CO_2 impurities. The approach succeeded to reproduce the often reported SEI structure with an inorganic inner and an organic outer SEI layer [16]. Esameilpour et al. [128] further investigated the root-cause of such layered SEI structures by applying a 2D kMC model which discretizes the graphite anode surface as well as the electrolyte phase. Their simulations suggest that the outer organic SEI forms through a 'solution-mediated pathway' in which intermediate species diffuse into the electrolyte, where they form clusters, which eventually result in a porous outer SEI. The kinetic parameters in this study were mostly taken from first principles calculations from literature and were partly estimated.

Further recent studies focused on the investigation of SEI formation in next-generation batteries: Gerasimov et al. [129] introduced the first full 3-dimensional kMC model covering the spontaneous SEI formation in an EC/$LiPF_6$ electrolyte on lithium metal. The model includes the solvent and salt degradation reactions. The corresponding kinetic parameters were partly derived from first principles calculations and partly estimated based on literature values. The study identified the SEI structure and chemical composition with a full spatial resolution within the first 100 ns after immersion. Another study on SEI formation and lithium deposition dynamics on lithium metal was reported by Perez-Beltran et al. [130]. In this work the authors focused on the effect of a novel fluorinated-ether-based electrolyte with LiFSI as condcuting salt. The considered

reaction pathways and energies were fully derived by first principles calculations in a previous study [92]. Eventually, Hankins et al. [131] studied the SEI formation on hard carbon for Na-ion batteries. In this study as well, the reaction mechanisms and energies were fully derived from first principles. Additionally, the study introduced a novel method for the calculation of the local potential that drives SEI formation and demonstrated the impact of electrolyte composition and external current on the SEI structure and composition.

This literature review reveals the shortage of kMC models for SEI formation on lithium metal, with only two having been developed recently. It is important to note that in contrast to other cell chemistries, SEI formation on lithium metal occurs spontaneously due to its high reactivity and low potential. Moreover, the absence of a stable electrode surface complicates modeling, as the lithium metal anode partially reacts and dissolves during SEI formation. To date, only one model [129] explicitly addresses spontaneous SEI formation, but is limited to a timescale of 100 ns. Key remaining challenges include extending accessible timescales, ensuring both local and global electroneutrality, and expanding the scope of investigated reaction networks and electrolyte chemistries based on first principles calculations.

3 Solid Electrolyte Interphase Formation on Lithium Metal[1]

3.1 Introduction

This chapter aims at the development and application of an advanced *ab initio*-informed kinetic Monte Carlo model to reveal the underlying mechanisms of spontaneous SEI formation on lithium metal, as well as its chemical composition and macroscopic influencing factors. As previously discussed (cf. Section 2.1.3), this knowledge is vital to enable a targeted design of beneficial SEI layers that can stabilize the lithium metal/electrolyte interface and effectively suppress dendrite growth and capacity loss upon cycling.

The presented model builds upon the recently published work of Gerasimov et al. [129]. In their study they published the first 3-dimensional kMC model simulating the spontaneous SEI formation on lithium metal. This study provided a proof-of-concept and identified the SEI structure and chemical composition with a full spatial resolution within the first 100 ns after contact of lithium metal and liquid electrolyte. However, the applied reaction kinetics in this study were only partly derived from first principles and the model could not ensure electroneutrality inside the simulation box. This chapter introduces several significant extensions to this model, substantially improving its predictive capabilities and the accuracy of the results. Additionally, the accessible simulation timescale is extended into the microsecond range. This allows for sound physical conclusions on the SEI formation and represents a first step towards more realistic timescales. As presented in Figure 3.1 these extensions include a multiscale concept, in which the kMC model is coupled with a continuum model after the example of Röder et al. [104] for guaranteeing electroneutrality as well as the use of a consistent set of DFT-based energy parameters of solvent degradation. In this study, an electrolyte consisting of EC, EMC and $LiPF_6$ is chosen as the model system. Due to its widespread application in LIB this electrolyte system is comparatively well studied, simplifying model development while providing insights into SEI formation in a highly relevant electrolyte system.

[1] Parts of this chapter have been published in J. Wagner-Henke et al., *Nat. Commun.* 14, 6823, 2025 [1], licensed under CC BY 4.0.

The presented simulations explicitly track the spatial distribution of electrolyte components, reaction intermediates, SEI components and lithium metal. From this, the time-resolved morphology and chemical composition of the SEI is analyzed and conclusions on the limiting processes of its formation are drawn. This modeling approach allows to take unprecedented steps towards the model-based design of SEI structures by predicting the effect of (local) concentration changes of the liquid electrolyte components EC and $LiPF_6$. This promotes the understanding of the origin of different SEI structures, and enables the suggestion of strategies for the knowledge-driven design of the SEI.

3.2 Methods

The multiscale methodology applied in this study consists of three main parts and is depicted in Figure 3.1: First, DFT calculations are used to identify the energetics of the SEI formation reactions, which are then used as input parameters for the higher-scale models. Second, a three-dimensional kMC model is established, which models the formation processes and the resulting chemical composition of the SEI. This stochastic model is, thirdly, directly coupled with a continuum model to ensure global electroneutrality within the simulation box. The mentioned kMC model is based on a prior work of Gerasimov et al. [129]. Here this model is extended to improve the physical reliability in terms of electroneutrality, ionic conductivity of the SEI and solid-state behavior of the lithium metal anode and incorporated into a multiscale modeling framework. In the following section, first the kMC model is introduced, followed by a description of the coupling to the continuum model. Afterwards, the model initialization and details on the performed DFT calculations are discussed.

3.2.1 KMC Model

As previously discussed in Section 2.3.1, the comparatively high efficiency of the kMC modeling approach primarily originates from the simulations on a molecular instead of an atomic level. Thereby, rare events such as reactions or diffusions are considered while the vibrational motions of atoms are neglected [110]. All considered rare events must be provided as a model input along with their kinetic parameters. Based on this, transition rates for each process are calculated, and the algorithm then stochastically chooses the process to be performed in a random fashion. In this work, an algorithm based on the Variable Step Size Method (cf. Figure 2.7) [109, 111] was applied. It was further modified with the structured list approach suggested by Schulze [114] to increase its efficiency further. Thereby, all possible transition rates are calculated at the start of

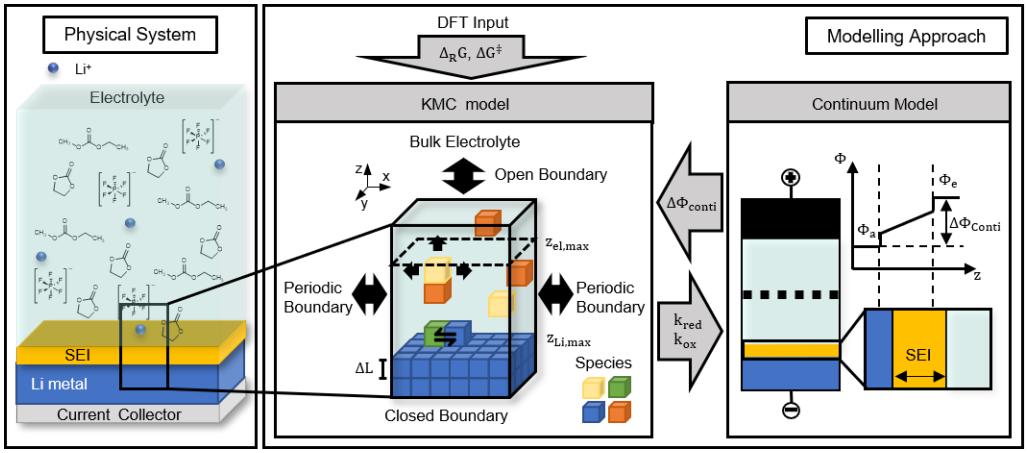

Figure 3.1: Schematic modeling idea of SEI formation on lithium metal. Left: Chemical system under investigation. Right: Multiscale kMC/continuum modeling approach with DFT input. DFT provides the Gibbs free energies $\Delta_R G$ and activation energies $\Delta G^{\ddagger}$ of the considered reactions for the kMC model. The kMC model passes the reaction constants k_{red} and k_{ox} to the continuum model and the continuum model returns the potential $\Delta\Phi_{\text{conti}}$.

the simulation and updated after every time step. More details on the general algorithm can be found in Section 2.3.1 in the Fundamentals.

The overall kMC modeling idea is shown in the middle of Figure 3.1. A section of 5.165 nm $\times$ 5.165 nm of the lithium metal surface in contact with the liquid electrolyte is represented in the kMC box with a height of 25.823 nm. This modeling domain is divided into a fixed three-dimensional cubic lattice. Each lattice site can either be vacant or occupied by a molecule or ion. In this way, the lattice predefines all possible configurations. Based on the occupied and vacant sites in the simulation output, the average SEI thickness $\overline{d_{\text{SEI}}}$ in the z-direction can be calculated as follows:

$$\overline{d_{\text{SEI}}} = \frac{1}{n_x \cdot n_y} \left(\sum_{(x,y)} \left(z^{(x,y)}_{\text{max, SEI}} - z^{(x,y)}_{\text{min, SEI}} \right) + \Delta L \right) \tag{3.1}$$

Thereby, $z_{\text{max, SEI}}$ and $z_{\text{min, SEI}}$ represent the height of the highest and lowest layer in the kMC box occupied by a SEI species, n_x and n_y stand for the number of lattice sites in x- and y-direction and ΔL describes the edge length of the single voxels which is set to 0.3443 nm based on the size of a lithium metal atom [129].

Further, the boundary conditions of the simulation box are defined to be periodic at the lateral walls to allow for free diffusion of species. The top of the box is an open boundary which is

connected with a bulk electrolyte phase of constant composition, and the bottom boundary is closed, so that no species can leave or enter the box through this wall.

For this study, three different types of events were considered: Diffusion of species in the electrolyte with the rate $\Gamma_{\mathrm{D,i}}$, reactions in the solid and liquid phase with the rate $\Gamma_{\mathrm{R,i}}$ and clustering of SEI species to form larger agglomerates with the rate $\Gamma_{\mathrm{Cl,i}}$. In the following sections, their implementation and the respective transition rates are presented. A list of all model parameters can be found in Table A.1 in the appendix.

3.2.1.1 Transport of Species and Charge

The diffusion rate is represented by Γ_{D} and is implemented for all liquid components. This includes electrolyte species and dissolved electrolyte decomposition products. In general, species can hop to vacant sites in their next neighborhood. In order to allow for Li^+ conduction through the SEI, Li^+ is additionally enabled to hop to the next neighbors, which are occupied by clustered SEI species. Next neighbors are connected with the current lattice site with their face (horizontal diffusion), their edge (diagonal diffusion), or their corner. Since diffusion in solid phases such as in lithium metal and in SEI clusters is comparatively slow, it is not expected to have a significant influence on the SEI composition and morphology and is therefore neglected. The respective transition rates for the diffusion in the liquid phase are calculated with the following equations, which are based on Röder et al. [30][2]:

$$\Gamma_{D,\mathrm{face}} = \frac{D_j}{2\,(\Delta L)^2} \tag{3.2}$$

$$\Gamma_{D,\mathrm{edge}} = \frac{D_j}{4\,(\Delta L)^2} \tag{3.3}$$

$$\Gamma_{D,\mathrm{corner}} = \frac{D_j}{6\,(\Delta L)^2} \tag{3.4}$$

D_j represents the macroscopic diffusion coefficient of species j. It is assumed to be the same constant value of $2.27 \cdot 10^{-10}$ $\mathrm{m^2\ s^{-1}}$ for all considered species, which is in the range of previously

[2] The transition rates for diffusion used in this chapter are directly adopted from [30]. For the following Chapters 4 and 5 the transition rates were newly derived for a cubic lattice, following the derivation by Drews et al. [132]. The full derivation can be found in Section B.1.2 of the appendix. As confirmed by a comparative simulation (cf. Section A.2.1 in the appendix), the revised rates only have a minor effect on the results presented in this chapter and do not alter the overall conclusions.

reported values for EC systems [129, 133]. Equation 3.2 is further applied to calculate the transition rate of the clustering processes of SEI species, which were introduced by Gerasimov et al. [129]. These clustering processes describe the precipitation of SEI components from the liquid phase on crystalline or amorphous solid SEI species of the same kind. The underlying driving force is that during the formation of the solid phase, a structural reorientation of neighboring SEI species reduces the total energy of the system, as observed in [134].

The transport of charged species is not purely diffusive, but also depends on the electrostatic forces, which arise from the interaction of all charged species within the simulation box. A full calculation of these interactions is computationally expensive, since the electric field – and consequently the transport rates of all charged species – would need to be updated after every change in the charge carrier configuration within the kMC box [135]. To ensure local electroneutrality while simultaneously enabling efficient simulations and the access to longer simulation times, a simplified approach to model the electrostatic interactions was applied in this chapter. Thereby, only the repelling forces based on the local charge distribution on the next-neighbors of each charged species are considered. Additionally it is assumed that all charges behave like point charges. After the example of Pippig et al. [135], the local electrostatic energy E_n is calculated based on the next-neighbor charges as follows:

$$E_n = -\frac{N_A}{4\pi\varepsilon_0\varepsilon_r\Delta L}\, q_l \sum q_{nn} \tag{3.5}$$

Here, q_l represents the charge of the species on the current site l, and q_{nn} stands for the charges of the species on the neighboring sites. Furthermore, ε_0, ε_r and N_A describe the vacuum permittivity, relative permittivity and Avogadro constant, respectively. Based on this, the transport rate of charged species $\Gamma_{\mathrm{D/C}}$ is given by the applicable diffusion rate $\Gamma_{\mathrm{D,dir}}$ (see Equations 3.2 - 3.4) and, in case of repelling local forces, an exponential dependency on the local electrostatic energy as follows:

$$\Gamma_{\mathrm{D/C}} = \begin{cases} \Gamma_{\mathrm{D,dir}} \cdot \exp\left(-\frac{E_n}{RT}\right) & \text{for } E_n < 0 \\ \Gamma_{\mathrm{D,dir}} & \text{for } E_n \geq 0 \end{cases} \tag{3.6}$$

Thereby, *dir* stands for the respective direction of diffusion, e.g. face, corner or edge. k_B represents the Boltzmann constant, and T the temperature. A comparative analysis on more advanced electrostatic interaction models is provided in Chapter 5. Additionally, the impact of the consideration of electrostatic forces on the predicted SEI formation is discussed there (cf. Section 5.4).

3.2.1.2 Reactions

In the kMC model, one or two reactants can form up to two products per reaction process. Therefore, reactants have to be present on neighboring sites, as can be seen in the middle of Figure 3.1, and products are placed on the reaction site or vacant next neighbor sites. It is assumed that gaseous products are volatile, insoluble and are instantaneously transported away from the surface. Hence, all related reverse reactions are neglected. The transition rate of the chemical reaction process i is calculated based on TST (cf. Section 2.3.1), as shown in Equation 3.7.

$$\Gamma_{R_i} = k_{0,i} \exp\left(-\frac{E_{A,i}}{RT}\right) \tag{3.7}$$

$$E_{A,i,\text{forw}} = \Delta G_i^{\ddagger} \tag{3.8}$$

$$E_{A,i,\text{rev}} = \Delta G_i^{\ddagger} - \Delta_R G_i \tag{3.9}$$

$E_{A,i}$ represents the energy barrier defined by Equations 3.8 and 3.9 for forward and reverse reactions, respectively. Thereby, $\Delta G_i^{\ddagger}$ represents the activation energy, and $\Delta_R G_i$ stands for the free energy of the respective reaction i. The energy values applied in this study have been derived by first principles methods (cf. 3.2.4) and are summarized in Table 3.1. Furthermore, $k_{0,i}$ stands for the frequency factor, which is usually in the range of 10^{12} s^{-1} to 10^{13} s^{-1} [110] and was chosen to be 10^{13} s^{-1} , corresponding roughly to $k_B T/h$, for all reaction processes in this study. Eventually, R describes the ideal gas constant, which is defined as the product of the Boltzmann constant k_B and the Avogadro constant N_A and T the temperature, which is set to be 298.15 K in accordance with the DFT calculations throughout this study. The total activation energy of the oxidation of the only solid reactant lithium metal E_{A,R_1}^{total} accounts in addition for the binding energy E_A^{bond} between the lithium metal atoms:

$$E_{A,R_1,\text{forw}}^{\text{total}} = E_{A,R_1,\text{forw}} + E_A^{\text{bond}} \cdot n_{nn}^{\text{Li}} \tag{3.10}$$

Here, n_{nn}^{Li} stands for the number of directly neighbored lithium metal atoms. A similar approach was e.g. chosen by Callejas-Tovar et al. [136].

The transition rates of electrochemical reactions further depend on the electrical potential $\Delta\Phi_{\text{KMC}}$. Here the electrochemical transition rates as reported by Röder et al. [30, 104] are applied:

$$\Gamma_{R,\mathrm{ox}} = k_{0,i} \exp\left(-\frac{E_{A,i}}{RT}\right) \exp\left(\frac{\alpha \Delta\Phi_{\mathrm{KMC}} F}{RT}\right) \tag{3.11}$$

$$\Gamma_{R,\mathrm{red}} = \kappa(z) k_{0,i} \exp\left(-\frac{E_{A,i}}{RT}\right) \exp\left(-\frac{(1-\alpha)\Delta\Phi_{\mathrm{KMC}} F}{RT}\right) \tag{3.12}$$

This Galvani potential is calculated by the continuum model and transferred to the kMC model as an input in each sequence. Furthermore, α stands for the symmetry factor and F represents the Faraday constant.

Since the movement of single electrons is too fast to be directly considered in the kMC model, an electron transport factor $\kappa(z)$ is defined as a macroscopic approximation for the availability of electrons for reduction reactions (cf. Eq. (12)) depending on the distance $\Delta z = z - z_{\mathrm{Li,max}}$ to the lithium metal anode in z-direction:

$$\kappa(z) = \begin{cases} 1 & \text{for } z \leq z_{\mathrm{Li,max}} + \Delta L \\ \exp\left(\frac{\ln(p_{\mathrm{e^-}})}{z_{\mathrm{e^-,max}}} \cdot \Delta z\right) & \text{for } z_{\mathrm{Li,max}} + \Delta L < z \leq z_{\mathrm{Li,max}} + \Delta L + z_{\mathrm{e^-,max}} \\ 0 & \text{for } z > z_{\mathrm{Li,max}} + \Delta L + z_{\mathrm{e^-,max}} \end{cases} \tag{3.13}$$

Thereby, $p_{\mathrm{e^-}}$ describes the electron probability at the maximum electron tunneling distance $z_{\mathrm{e^-,max}}$, and $z_{\mathrm{Li,max}}$ stands for the height of the kMC-box initially occupied by lithium metal. For this study, $p_{\mathrm{e^-}}$ was chosen to be 0.01 according to [129], and $z_{\mathrm{e^-,max}}$ was set to be 2 nm which is a typical range for electron tunneling already used in previous simulation studies [137]. A detailed derivation of the electron factor is provided in Section A.1 in the appendix.

3.2.2 Continuum Model

Local electroneutrality was already accounted for in the kMC model by Equations 3.5 and 3.6. However, if used as a standalone model, this does not include any control of global electroneutrality. Hence, oxidation and reduction processes can occur independently without consideration of the availability of excess or lack of electrons. Therefore, here the 3-dimensional kMC model is coupled to the following macroscopic charge balance following the MPA2 coupling algorithm developed by Röder et al. [104]:

$$C^{\mathrm{DL}} \frac{d\Delta\Phi_{\mathrm{Conti}}}{dt} = I - v_{el} F \tag{3.14}$$

As shown in Figure 3.1, it is assumed, that the potential drop $\Delta\Phi_{\mathrm{Conti}}$ between the electrode and the liquid electrolyte behaves like an electrochemical double layer over the electrode/electrolyte interface with a capacitance C^{DL}, which is set to 0.2 F m^{-2} [104]. Thereby, only one electron is transferred per electrochemical reaction step. Furthermore, I represents the applied current, which is set to be 0 A m^{-2} in this study. v_{el} refers to the total rate of electrochemical reactions in the system. It is calculated as the difference between the total reduction and oxidation rates $v_{\mathrm{el}} = v_{\mathrm{red}} - v_{\mathrm{ox}}$ which depend on the output of the kMC model according to the following correlations:

$$v_{\mathrm{ox}} = k_{\mathrm{ox}} \exp\left(\frac{\alpha \Delta\Phi_{\mathrm{Conti}} F}{RT}\right) \tag{3.15}$$

$$v_{\mathrm{red}} = k_{\mathrm{red}} \exp\left(-\frac{(1-\alpha)\Delta\Phi_{\mathrm{Conti}} F}{RT}\right) \tag{3.16}$$

The reaction constants k_{red} and k_{ox} are derived from the kMC output by Equations 3.17 and 3.18 for each sequence.

$$k_{\mathrm{ox}} = \frac{\sum \Psi_{\mathrm{ox}}}{t \Delta L^2 n_x n_y N_A} \cdot \frac{1}{\exp\left(\frac{\alpha \Delta\Phi_{\mathrm{KMC}}^{\mathrm{seq}} F}{RT}\right)} \tag{3.17}$$

$$k_{\mathrm{red}} = \frac{\sum \Psi_{\mathrm{red}}}{t \Delta L^2 n_x n_y N_A} \frac{1}{\exp\left(-\frac{(1-\alpha)\Delta\Phi_{\mathrm{KMC}}^{\mathrm{seq}} F}{RT}\right)} \tag{3.18}$$

In these equations, $\sum \Psi_{\mathrm{red/ox}}$ describes the number of reduction/oxidation processes that were performed in the kMC model since time $t = 0$, t is the time simulated by the kMC model, n_x and n_y are the number of lattice sites in x and y direction, and N_A stands for the Avogadro constant. The charge balance in equation 3.14 is solved in each continuum model sequence, which is called after every 1000 kMC iterations, by using the ode15s solver of MATLAB. The resulting potential at the end of the sequence is fed back to the kMC model by $\Delta\Phi_{\mathrm{KMC}}(\mathrm{seq}) = \Delta\Phi_{\mathrm{Conti}}(t^{\mathrm{seq}})$. After computing the next 1000 kMC steps with this potential value, the final number of electrochemical reactions and the simulated time are again transferred to the continuum for determining the next potential.

3.2.3 Choice of reaction network

As a stochastic, mesoscale approach, the kMC model used in this study requires the input of a predefined reaction network as well as the related activation energies $\Delta G^{\ddagger}$ and free energies $\Delta_R G$

(cf. Figure 3.1). The considered reaction network was determined based on literature information and DFT calculations. Thereby, the focus is on electron transport reactions instead of adsorption reactions. This is due to the high reactivity of lithium metal which quickly leads to lithium oxidation and the loss of a distinct lithium metal surface on which electrolyte molecules could adsorb.

The considered reaction network of SEI formation is summarized in Table 3.1 and graphically displayed in Figure 3.2. On the pure lithium metal surface, the lithium atom acts as electron donor, i.e. is oxidized, which promotes reductive electrolyte degradation. The rapid oxidation of Li is reflected in the low electrode potential and is the driving force for the rapid SEI formation on lithium metal. In this study, the electrolyte consists of EC + EMC and $LiPF_6$. Since the degradation of EMC on lithium metal is known to be significantly slower than EC or the conductive salt [89] and is too slow for the maximum simulation time of 1 µs, the degradation of EMC is neglected in this study. In terms of the electrolyte solvent EC, the SEI species LiEDC and Li_2CO_3 are known as the main degradation products since the early work of Aurbach et al. in the 1990s [64, 138, 139]. The related reaction pathways were extensively studied by *ab initio* calculations [87, 88]. The two pathways considered in this chapter were extracted from the paper of Wang et al. [87] and were recently confirmed by the study of Spotte-Smith et al. [33]. Both pathways start with the electrochemical ring-opening of EC, denoted as R2. In a second reduction step, R4, one ethene can be released. The remaining carbonate ion undergoes the chemical reaction, R5, forming Li_2CO_3 with Li^+ from the solution. Alternatively, two ring-opened $(Li^+)EC^{\bullet-}$ can react in R3 to form the organic species LiEDC. Thereby, one ethene molecule is released.

In the absence of water or other contaminants, LiF is considered to be the main degradation product of the conductive salt $LiPF_6$ [100, 139, 140]. Based on the observations of *ab initio* and reactive force-field (ReaxFF) MD calculations from the literature [98, 100] it is assumed that each salt molecule can almost simultaneously release up to three fluoride anions. In order to ensure compatibility with the kMC algorithm, this is divided into the elementary reactions R6-R8, which are summarized in Table 3.1 and have a maximum of two reactants and two products per reaction step. Additionally, the electrochemical nature of these reactions ensures that the degradation processes occur only in the vicinity of the anode surface. Overall, this means that from each salt anion close to the lithium surface, three LiF can be formed. The corresponding reaction energies are adopted from Gerasimov et al. [129], where they were determined using the slow-growth approach.

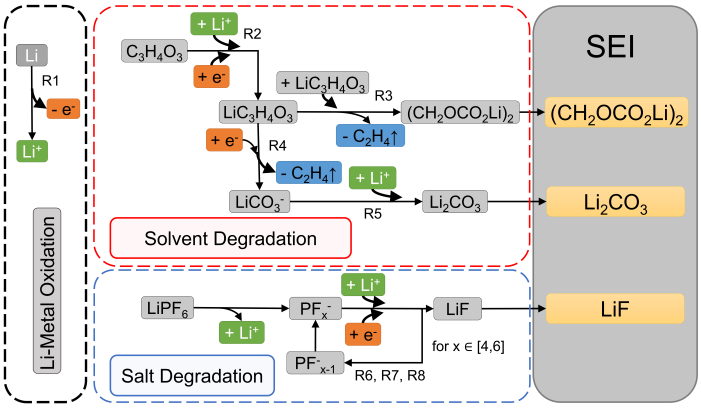

Figure 3.2: Reaction network considered in the multiscale kMC model. It consists of lithium metal oxidation, solvent degradation and salt degradation. Full equations of reactions R1 – R8 are given in Table 3.1.

3.2.4 Density Functional Theory Calculations[3]

Since the accuracy of the model and the predicted system dynamics highly depend on good quality kinetic input data, DFT calculation were performed to identify consistent energy values for the EC degradation under the local conditions at the lithium metal anode. A summary of all reaction energies is shown in Table 3.1[4]. The reaction energies of the salt degradation were already determined in the publication of Gerasimov et al. [129] and were adopted for the reactions R6 - R8. The DFT calculations were conducted with the Gaussian16 package. All the chemical structures were optimized to their local minimum at the B3PW91 level of theory with 6-311G(3df) basis sets [141, 142]. The free energy values were converted from the default 1 atm condition to the standard state of 1M. An implicit solvation model based on density (SMD) was implemented to emulate the solvation environment in cyclic-carbonate-based electrolyte [143]. More details on the performed DFT calculations can be found in Table A.3. It was found that the lithiation relaxation energies vary from species to species. To prevent this phenomenon from influencing the reaction thermochemistry calculation, each elementary reaction step was evaluated based on the electronic energy difference from TS or product to reactant with proper thermal energy corrections to obtain the free energy barrier/change from the total electronic energy value of each species.

In the case of R2, which describes the ring-opening reaction of EC, no unique parameter set could be identified. It was recently shown by Kuai et al. [22], that the activation energy of this

[3] The DFT calculations were performed by Dacheng Kuai, formally Texas A&M University.

[4] For better comparability with the study by Kuai et al. [22], the reaction energies in this thesis are reported in kcal mol^{-1}. All values were converted to the SI unit J mol^{-1} for the conducted computations.

Table 3.1: Summary of implemented reaction processes and corresponding Gibbs free energies $\Delta_R G$ and activation energies $\Delta G^{\ddagger}$. TS represents the transition states. Reaction energies for R2 are given for two cases: with (w/) and without (w/o) lithium coordination of EC.

N_0	Reaction	$\Delta_R G$ / kcal mol^{-1}	$\Delta G^{\ddagger}$ / kcal mol^{-1}
R1	$Li \rightleftharpoons Li^+ + e^-$	-70.22[a]	1.9[a]
R2	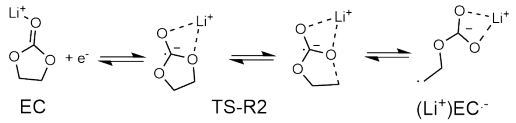	w/o Li^+ -30.43[b] w/ Li^+ -39.17[b]	0[c] 12.05[b]
R3	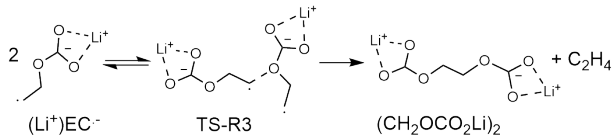	-56.5[b]	2.93[b]
R4	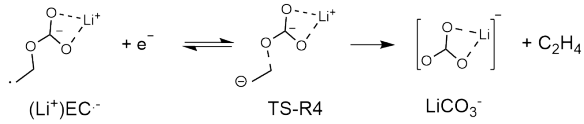	-90.83[b]	0[c]
R5	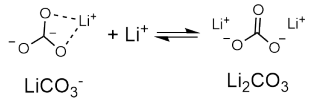	-54.72[b]	0[c]
R6	$Li^+ + PF_6^- + e^- \rightleftharpoons LiF + PF_5^-$	-0.454[d]	3[d]
R7	$Li^+ + PF_5^- + e^- \rightleftharpoons LiF + PF_4^-$	-0.454[d]	3[d]
R8	$Li^+ + PF_4^- + e^- \rightleftharpoons LiF + PF_3^-$	-0.454[d]	3[d]

[a] Assumed energies.
[b] Energies calculated by DFT.
[c] Activation energy manually set to 0 kcal mol^{-1} since the DFT calculations suggested negative values.
[d] Energies adopted from [129]

process is significantly impacted by lithium coordination. When coordinated with one Li^+ ion, the energy barrier was calculated to be 12.05 kcal mol^{-1}. As previously shown in literature [94] this barrier is mostly independent of the exact coordination ratio of EC and Li^+, and also applies if several EC-molecules are coordinated with one Li^+-ion. However, Kuai et al. [22] showed that the ring-opening barrier is significantly different for uncoordinated EC and becomes even negative. Similar declining energy surfaces are found in reactions R4 and R5. To transcribe this into the kinetic information, the activation energies $\Delta G^{\ddagger}$ of the corresponding reactions are assumed to be 0 kcal mol^{-1}. Since the lithium coordination of EC and solvation are evolving

dynamic processes in the electrolyte system, the energy barrier of the EC ring-opening process R2 is not clearly identifiable from the DFT calculations.

3.2.5 Model Initialization

The simulation box is initialized with a clean and pristine lithium metal surface which comes into contact with the pure electrolyte solution without any contaminants being present in the electrode or electrolyte. The first 30 bottom layers of the kMC simulation box, starting from $z = 0$ and ending at $z_{\mathrm{Li,max}}$, are initially completely filled with lithium metal atoms to represent the lithium metal anode. The remaining lattice sites, i.e. $z > z_{\mathrm{Li,max}}$, are randomly occupied by electrolyte molecules or vacant. Thereby, the number of species n_j depends on the chosen salt concentration and solvent composition, which is 1.2M of $LiPF_6$ in EC in the standard case and can be calculated by Equation 3.19.

$$n_j = \left\lfloor N_A c_j \Delta L^3 n_x n_y \left(n_z - \frac{z_{\mathrm{Li,max}}}{\Delta L} \right) \right\rfloor \quad \text{with } j \in \{\mathrm{EC}, \mathrm{PF}_6^-, \mathrm{Li}^+\} \tag{3.19}$$

The concentrations c_j are varied for the modeling studies on the effect of salt and solvent concentrations. After placing the molecules, all possible events and transition rates are determined and saved in the structured lists according to Schulze et al. [114]. In the last step, the electrical potential for the first kMC sequence $\Delta\Phi_{\mathrm{KMC}}(seq = 1) = \Delta\Phi_{\mathrm{Conti}}(t = 0)$ is calculated by minimizing Equation 3.20 in order to balance out the probability of oxidation and reduction processes. Thereby, the index i_{el} stands for the implemented electrochemical reaction processes, and l represents the lattice sites in the kMC box.

$$\min_{\Delta\Phi} \left(\left| \sum_{l} \sum_{i_{\mathrm{el}}} \Gamma^{\mathrm{red}}_{i_{\mathrm{el}},l}(\Delta\Phi) - \sum_{l} \sum_{i_{\mathrm{el}}} \Gamma^{\mathrm{ox}}_{i_{\mathrm{el}},l}(\Delta\Phi) \right| \right) \tag{3.20}$$

The presented multiscale model was implemented in MATLAB, and all simulations were performed using MATLAB Version 2021a. The calculations were performed on an i7-8700 CPU with 16 GB RAM.

3.3 Results and Discussion

3.3.1 Parameter Estimation and the Effect of Local Li^+ Concentration

As previously discussed in Section 3.2.4, the kinetics of the ring-opening reaction of EC (R2) highly depend on the Li^+ coordination and local solvation environment, which are highly dynamic close to the lithium metal surface. Hence, the energy barrier of R2 could not be clearly identified. To estimate the effect of the ring-opening barrier on the resulting SEI structure and to choose a meaningful ring-opening energy for further investigations, a parameter study of the energy barrier $\Delta G^{\ddagger}$ of the EC-ring opening reaction R2 was performed. The parameter was varied in the DFT-proposed parameter range between 0 and 12.05 kcal mol^{-1} (cf. Table 3.1). Thereby, each parameter set represents a different stochastic average of the availability of uncoordinated vs. Li^+-coordinated EC molecules close to the reaction site. Hence, lower energy barriers correspond to a lower and higher energy barriers to a higher local availability of Li^+ ions.

The results are shown in Figure 3.3. In Figure 3.3 a), the final kMC box configurations after a simulated time of 1 µs are shown for different ring-opening energy barriers between 0 kcal mol^{-1} and 12.05 kcal mol^{-1}. In Figure 3.3 b) the corresponding composition of the resulting SEI is plotted. From this, it is observed that the ring-opening energy, and hence the local Li^+ concentration, has a strong effect on the resulting SEI composition and morphology. Low energy barriers lead to a SEI with an inorganic phase close to the lithium metal anode and an organic phase above, closer to the electrolyte phase. The inorganic phase is composed of Li_2CO_3 and LiF, which are arranged in a mosaic-like manner, and the organic phase consists of $(CH_2OCO_2Li)_2$ (LiEDC). Moreover, Li_2CO_3 is strongly dispersed over the SEI, and reaches inside the electrolyte. Relatively higher ring-opening barriers lead to a shift towards more LiF species in the increasingly layered inorganic phase. Moreover, both the organic phase and the dispersed Li_2CO_3 phase become less distinct until they entirely disappear when the ring-opening barrier reaches 12.05 kcal mol^{-1}.

These observations can be explained based on the reaction network shown in Figure 3.2. Since the kinetics of R2, which is the first reaction step of the EC degradation, were tuned in this parameter study, it is reasonable that faster kinetics lead to more solvent-degradation-related products, which include both the inorganic Li_2CO_3 and the organic LiEDC. Vice versa, the increase of LiF quantities with slower EC degradation kinetics follows a complex interplay of diffusion and reaction limitations which is analyzed in detail in Section 3.3.2. In brief, since fewer EC degradation products are formed, the passivation of the lithium metal is slower, which allows the reduction of salt over a longer period of time. From a practical point of view, a high local Li^+ concentration close to the electrode surface stabilizes many EC molecules and consequently

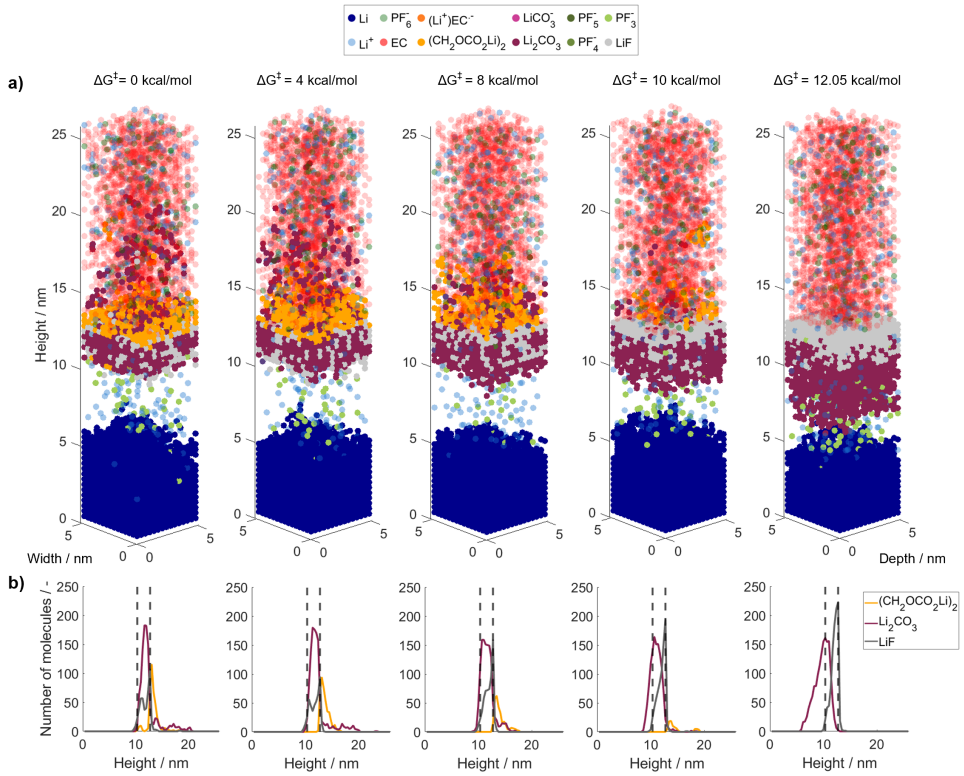

Figure 3.3: SEI composition and structure 1 µs after the initial contact of EC + 1.2M $LiPF_6$ and lithium metal for varying EC ring-opening energies $\Delta G^{\ddagger}$. a) Resulting species distribution in kMC box. b) Number of SEI molecules over the height. The dashed lines represent the initial lithium metal surface (left) and the maximum electron transport distance (right).

leads to less EC degradation products such as LiEDC or Li_2CO_3 and a layered inorganic initial SEI layer. In contrast, a low local Li^+ concentration increases the availability of uncoordinated EC molecules and thus – due to the negligible barrier for uncoordinated EC – facilitates EC degradation. The resulting SEI contains more EC degradation products with a more mosaic-like morphology. These local properties could vastly differ depending on the working conditions. Therefore, SEI formation on pure lithium metal under OCV conditions could be different from e.g. SEI formation during lithium plating or SEI formation on intercalation electrodes in LIB. This could also partly explain the different SEI structures reported in literature (cf. Section 2.1.3) and could be exploited for a rational tuning of the SEI.

In order to better understand which parameter set represents best the conditions at the initial interface between lithium metal and liquid electrolyte, the simulation results are in the following compared with the data of the recent MD study of Ospina-Acevedo et al. [100]. These authors

applied reactive MD simulations with ReaxFF to model the first 20 ns of SEI formation in different electrolytes – among others, the EC + $LiPF_6$ electrolyte, which is considered in this study. Since MD and kMC are very different simulation paradigms, which were applied to the same chemical system with identical time and temperature, the comparison is a good approach for validating and benchmarking the modeling approach in this study. Moreover, comparison shows the low computational costs of the multiscale kMC/continuum approach: According to the authors of the comparative MD study [100] their calculations ran for a couple of weeks on high performance computer clusters in order to reach 20 ns. In contrast the here presented kMC/continuum model only took 29.2 minutes on a personnel computer with an i7-8700 CPU and 16 GB RAM to reach the same time on a 32 times larger length scale.

The comparison of the resulting MD box and the kMC/continuum simulation with a ring-opening energy of 12.05 kcal mol^{-1} after 20 ns is shown in Figure 3.4. Despite the difference in length and timescale of the MD and the kMC/continuum simulations, a qualitative comparison can be made by using a representative section of the lithium metal surface in the kMC box after a simulated time of 20 ns.

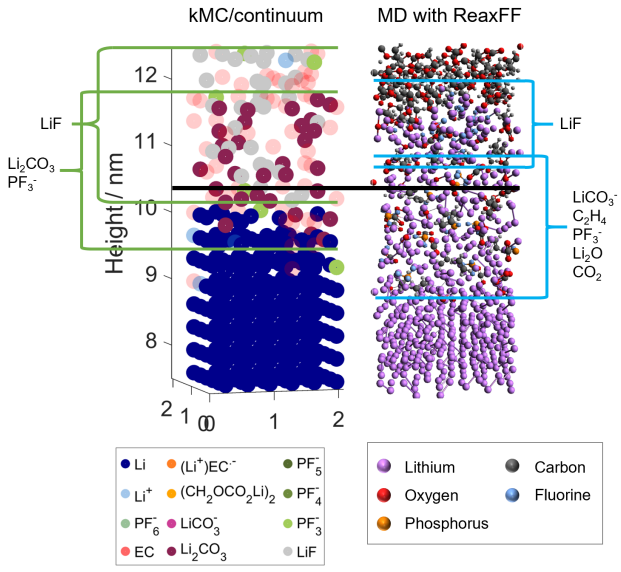

Figure 3.4: Comparison of SEI structure in EC + $LiPF_6$ from kMC-continuum for a ring-opening energy of 12.05 kcal mol^{-1} (left) and ReaxFF MD (right) after 20 ns. The dimensions of both boxes are 2.07 nm x 2.07 nm x 4.96 nm, each. The kMC result is taken as a representative sample from the large-scale simulations of 5.165 nm x 5.165 nm x 25.823 nm. The MD simulations were provided by Ospina-Acevedo et al.[100].

First of all, the MD simulation suggests a layered inorganic SEI. Thereby, below the initial interface carbonate, ethene, LiO_x, PF_3 and CO_2 can be found. Above the initial interface, a LiF layer can be observed. Moreover, no organic species were formed within the simulated time period. It should be noted that in the study of Ospina-Acevedo et al. [100] the salt was initially placed close to the lithium metal surface while it was evenly distributed in the here presented kMC/continuum study. In any case, both the layered structure and the absence of organic SEI components are qualitatively similar to the results of the kMC/continuum model for high EC ring-opening energies of 10 or 12.05 kcal mol^{-1}.

For a more quantitative comparison, the number of released ethene molecules was identified as a good indicator for the EC degradation kinetics. Since it can only be produced as a side product of the EC degradation, it is directly related to the number of reduced EC molecules and can be quantified by the tracked number of the ethene forming reactions R3 and R4. In order to ensure comparability between both simulation approaches, the released gas in the kMC/continuum simulations was scaled by the scaling factor $\nu = \frac{n^{\text{init}}_{\text{EC,MD}}}{n^{\text{init}}_{\text{EC,KMC}}}$, which relates the number of initial EC molecules in the MD $n^{\text{init}}_{\text{EC,MD}}$ simulation box to the number of initial EC molecules within a distance of 2 nm above the lithium metal in the kMC simulation box $n^{\text{init}}_{\text{EC,KMC}}$. In Figure 3.5, the result is plotted over the simulated time. Thereby, only the ethene production for the parameter set with an EC ring-opening energy of 12.05 kcal mol^{-1}, which corresponds to the ring-opening energy with Li^+ coordination, is in the same order of magnitude as the ethene production in the MD simulation. However, the ethene release for this parameter set is still slightly higher than observed from the MD calculations. This effect could have multiple reasons. First of all, all salt ions were placed close to the lithium metal surface in the MD simulation. This could lead to an overestimated LiF production, which quickly passivates the surface and hinders fresh EC molecules from reaching the lithium metal surface. Moreover, the kMC/continuum simulation has an open upper boundary connected with a bulk electrolyte phase, while in the MD simulation box all considered molecules are placed in the initial box. This means that in the case of the kMC/continuum simulation a higher amount of fresh EC is available to be transported towards the lithium metal surface and subsequently decompose.

Overall, the comparison with the MD simulation clearly indicates that the kMC/continuum simulation using the highest EC ring-opening barrier of 12.05 kcal mol^{-1}, which corresponds to strong influence from local Li^+, best reproduces the local conditions at the lithium metal surface within the first 20 ns after contact. Since the lithium metal anode acts as a source of Li^+ ions, which are the cause for the EC ring stabilization, this result is reasonable for the investigated cell chemistry. Therefore, for the following detailed SEI analysis, including the influence of salt and solvent concentration on the SEI, an EC ring-opening barrier of 12.05 kcal mol^{-1} is applied.

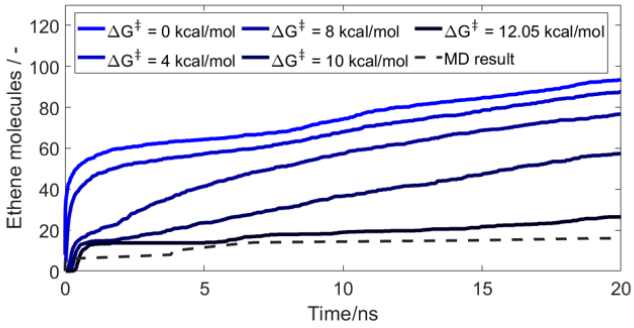

Figure 3.5: Comparison of the number of released ethene molecules over time for varying EC ring-opening energies $\Delta G^{\ddagger}$ with MD simulation performed by Ospina-Acevedo et al. [100]. The number of ethene molecules for the multiscale kMC/continuum simulation is calculated from occurrence of the gas-forming reactions R3 and R4 and is scaled to the amount of EC molecules in the initial MD simulation box.

3.3.2 Temporal Analysis of SEI Formation

The following analysis of the temporal evolution of the SEI formation allows an in-depth understanding of the limiting processes and process interactions which cause the final SEI composition and thickness. The general trends of SEI formation over time are presented in Figure 3.6 which shows several snapshots of the kMC box along with the development of the average SEI thickness over time. Thereby, the SEI thickness shows an asymptotic growth to 5.3 nm, where 50% and 90% of the height is reached after approximately 100 and 200 ns, respectively.

1 ns after the initial contact of lithium metal with the liquid electrolyte, the first intermediate products and SEI species form within 1 nm from the initial surface. This shows the high reactivity of pure lithium metal, which was already described by He et al. [14]: As reduced lithium with a very low open circuit potential is present from time $t = 0$, the SEI formation starts immediately after contact of the electrolyte with the electrode material and does not require any external current. After 10 ns, some more SEI species were formed, and the initiation of the layering of the inorganic phase, with a Li_2CO_3 layer below a LiF layer, can be observed. The two layers of the inorganic phase can be clearly distinguished after 100 ns. It is interesting to note that LiF mainly forms above the initial solid-liquid interface at the height of approximately 10 nm. In contrast, Li_2CO_3 grows into the former lithium metal phase, and is mainly present below the initial interface. In comparison with the SEI after 1 µs, both observed phases are still very porous, and solvent molecules are still present close to the lithium metal surface. Eventually, after 1µs all EC molecules below the newly formed SEI layer are consumed. Moreover, the LiF and the Li_2CO_3 layer became less porous and thicker. Thereby, the LiF layer mainly grows towards the electrolyte, while the Li_2CO_3 layer further grows into the lithium metal phase below the initial interface. As already described above, even after 1 µs, no formation of organic species

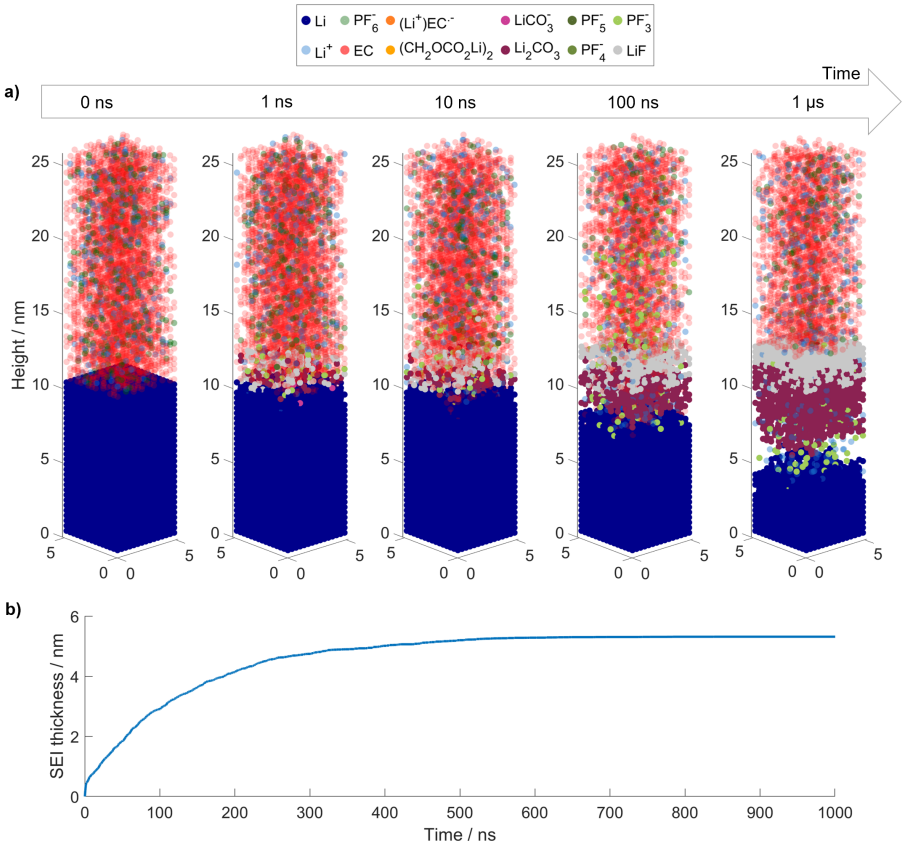

Figure 3.6: Temporal evolution of SEI formation on lithium metal in EC + 1.2M $LiPF_6$ electrolyte. a) Resulting species distribution in kMC box at selected times and b) development of SEI thickness over time. Energy values comprise the case for EC reduction in the presence of Li^+.

can be observed for this parameter set. This suggests that the experimentally observed organic SEI species [14] form only on larger timescales and require an initial inorganic passivation of the lithium metal surface. The same SEI formation and chemical SEI composition were observed when smaller inhomogeneities were introduced to the lithium metal surface, as shown in Figure A.2. This shows the low sensitivity of the SEI layer on structural inhomogeneities. Detailed experimental studies on the initial SEI formation on lithium metal and its resulting composition, especially with a sub-µm resolution, are scarce in literature [14, 19]. To the best of the authors knowledge, there is no experimental study, yet, which was able to reveal the here observed layering of the inorganic SEI. Future advancements in experimental methods may allow to reach a similar resolution and thus provide an experimental validation.

In addition, it is interesting to note that, in comparison to the first nanosecond, the SEI growth within the subsequent 9 ns slowed down significantly. This can also be seen in the thickness evolution in Figure 3.6 b). After a sharp increase within the first ns, the SEI growth continuously slows down until it reaches a maximum thickness of 5.3 nm after approximately 700 ns. This deceleration is caused by the increasing surface passivation constituted by the previously formed SEI species. After 700 ns, the surface becomes completely passivated to further electron tunneling, which is considered the only electron transport process in the presented model. Indeed, this does not mean that no further growth of the SEI is possible. Additional electron transport processes such as solvent diffusion, electron conduction through the SEI or Li-interstitial diffusion [21, 144] or SEI dissolution [131, 145–147] could lead to ongoing SEI growth on significantly larger timescales. These are not considered in the presented model since they are not expected to have a substantial effect during the first µs of SEI formation. Moreover, the cycling current will also lead to changes in and further growth of the SEI. Lastly, the developing electrical double layer could affect the SEI formation. Its effect on the simulation results is analyzed in Section A.2.3 in the appendix.

The obtained Li_2CO_3-LiF-layered SEI partly differ from the observations made in the work of Gerasimov et al. [129]. Despite a reported layered SEI, the order of the inorganic species was different, and a very fast formation of organic species within the first 100 ns after the initial contact of lithium metal and the liquid electrolyte was observed, which cannot be confirmed here. These differences can be mainly attributed to the overestimation of the reaction rate of the EC degradation in [129]: The activation barrier of the EC ring-opening reduction was estimated at 2.7 kcal mol^{-1}, while this work found a barrier of 12.05 kcal mol^{-1} by considering the stabilization effect of Li^+ ions on the EC-ring. This is why the previously predicted SEI is more similar to the here presented results with lower EC ring-opening energies of 0 or 4 kcal mol^{-1}, which can be found in Figure 3.3 on the very left. Another crucial difference is that the more detailed energetic calculations in this work have found that the energy barriers of the possible subsequent degradation reactions are the reverse of what was assumed by the previous study. While in this work the formation of inorganic carbonates was found to be more likely in an electron-rich environment due to lower energy barriers of the carbonate-forming reaction R4 compared to the organic-forming reaction R3, the formation of organic LiEDC was energetically preferred in the former study of Gerasimov et al. [129]. Overall, the inclusion of electroneutrality, including multiscale coupling, the reparameterization and further model extensions done in this work lead to a significant improvement in the accuracy and predictive power of the modeling approach.

In order to understand the underlying processes governing SEI formation, a detailed analysis of the temporal changes in the distribution of reactants and SEI products is presented in Figure 3.7. Since the salt concentration is comparatively low, for better visualization, it is plotted in a separate figure with a zoomed-in y-axis. From these figures, it is well visible that the salt

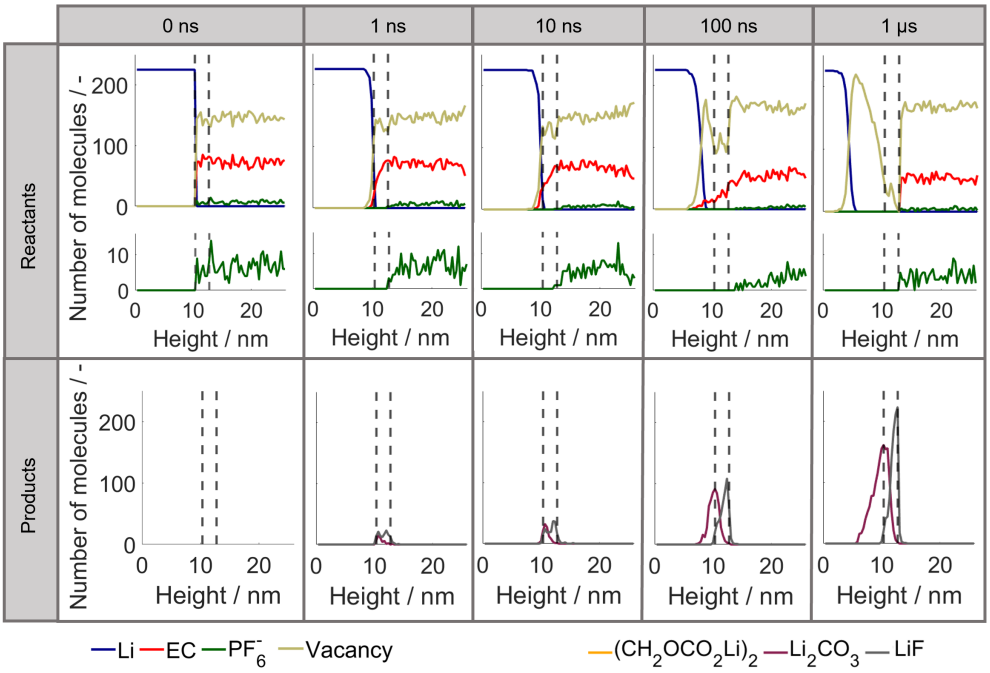

Figure 3.7: Temporal evolution of the species distribution over the height of the kMC box. The first row shows the reactant distribution and second row shows the SEI products distribution at selected time points. The dashed lines represent the initial lithium metal surface (left) and the maximum electron transport distance (right). Energy values comprise the case for EC reduction in the presence of Li^+.

concentration within the electron transport zone (between the dashed lines) quickly drops to 0 within 1 ns. This results from the rapid salt degradation kinetic with an energy barrier of only 3 kcal mol^{-1} (cf. Table 3.1). Since this process is approximately one order of magnitude faster than the salt diffusion, all available salt ions are reduced at their current position. Hence, the degradation product LiF is evenly distributed throughout the electron transport layer at this time point of the simulation. Subsequent diffusion of PF_6^- from the neighboring electrolyte layers to the electrochemically active reaction zone leads to a concentration gradient into the electrolyte zone, as visible for 10 and 100 ns. This indicates that all salt which reaches the electrochemically active zone is immediately consumed. The development of the LiF concentration over time confirms this observation since it develops an increasing concentration peak at the upper end of the electron transport layer. Overall, this shows that the transport rate of the reactant PF_6^- is slower than its decomposition. Hence, it is concluded that LiF production is a diffusion-limited process.

At the end of the simulation, after 1 µs, the concentration gradient above the electron transport zone mostly vanished. This matches the observation made in Figure 3.6 b) that the interphase is thicker than the electron tunneling zone, which blocks the electron tunneling to a negligible

probability. Hence, no new salt above the formed SEI is consumed after 1 µs. The consumption of EC, which is approximately 11 times more numerous in the electrolyte solution, is much slower in comparison. This can be especially observed in the EC concentration profiles. Even after 100 ns, solvent is still present within the electron transport layer. Moreover, it should be noted that EC molecules even exist below the initial interface after 10 and 100 ns. This relatively high stability of EC can be traced back to the energy barrier of the first EC ring-opening step. This barrier was determined to be 12.05 kcal mol^{-1}, which is high compared to the energy barrier of only 3 kcal mol^{-1} for the salt decomposition (cf. Table 3.1). Additionally, in contrast with the salt concentration profiles, no EC-concentration gradient develops above the electron transport layer. From this, we can conclude that the first step of electrolyte degradation is reaction-limited. With regard to the presented mesoscale calculations, this means that the EC molecules have enough time to approach the lithium metal surface without being immediately reduced. This further allows the formation of the Li_2CO_3 peak closer to the lithium metal surface and below the LiF layer.

The reason why Li_2CO_3 is preferably produced over LiEDC can be explained by comparing the kinetics of both EC degradation pathways in R2-R4. As previously pointed out by Yu et al. [88], the second EC reduction step R4 which reduces $(Li^+)EC^{\bullet-}$ to $LiCO_3^-$ is faster than the first EC reduction step R2, which reduces EC to the ring-opened $(Li^+)EC^{\bullet-}$. This is also reflected in the kinetic parameters (cf. Table 3.1), in which the activation barrier of R2 is 12.05 kcal mol^{-1}, and the barrier for R4 is 0 kcal mol^{-1}. Hence, as long as electrons are readily available, which they are close to the Li surface, newly formed $(Li^+)EC^{\bullet-}$ can quickly undergo a subsequent reduction reaction via reaction R4, leading to low $(Li^+)EC^{\bullet-}$ concentrations and significant $LiCO_3^-$ production. In contrast, two $(Li^+)EC^{\bullet-}$ at neighboring sites are required to produce LiEDC (cf. R3). As the $(Li^+)EC^{\bullet-}$ concentration is low, this makes LiEDC production unlikely close to the surface. Hence, the production of LiEDC could only occur in an electron-deficient environment, which prevents the second reduction step. One possibility to obtain this environment is a first passivation layer at the surface which significantly slows down the electron leakage from the lithium metal anode. This explains why the organic SEI species are often observed at the top of the SEI: They require a first passivation layer to be formed. Therefore, the formation of organic species such as LiEDC would be mostly expected on larger timescales.

Meanwhile, Figure 3.7 also answers the question of why the surface is fully passivated against electron tunneling at the end of the simulation. From the reactant distribution after 1 µs, it can be observed that the number of vacancies drops to zero at the upper electron transport limit, i.e. at the interface to the electrolyte. This means that the surface is fully occupied with SEI species. Hence, solvent and salt molecules in the electrolyte phase cannot pass the outer SEI surface and thus are not close enough to the lithium metal to be reduced by electron tunneling. Further, at 1 µs, all reactants inside the electron transport range are consumed. Therefore, no

further SEI formation is possible. Transferring this insight to the actual physical system of 1.2M $LiPF_6$ in EC/EMC, it can be expected that this initial passivation significantly slows down further SEI growth, which could continue only by other, slower transport paths, such as interstitial Li diffusion or electron conduction [21, 144].

3.3.3 Influence of Salt and Solvent Concentration

Having revealed the SEI composition and related governing processes of the SEI formation on lithium metal in EC with 1.2M $LiPF_6$, the model is in the following applied to study how the resulting SEI can be modified by tuning macroscopic properties. An intuitive approach is to vary the concentration of the conductive salt in the electrolyte. Therefore, the SEI formation is studied for four different $LiPF_6$ concentrations from 1M to 2M[5]. In doing so, the same set of kinetic parameters is applied for all salt concentrations and hence possible salt concentration effects on the reaction kinetics are neglected. The results are presented in Figure 3.8.

Overall, the SEI keeps its layered structure across all investigated salt concentrations. Thereby the changes of the salt concentration have only a minor effect on the distribution and quantities of LiF, while the amount of the EC degradation product Li_2CO_3 decreases at higher salt concentrations. Considering the previously analyzed governing processes of the SEI formation, this observation can be explained as follows: We learned that the salt degradation process which produces LiF is diffusion-limited, and that PF_6^- anions which reach the electron transport layer are almost immediately consumed. An increased salt concentration in the electrolyte automatically results in a higher initial salt concentration in the electron transport zone (cf. Table A.2) . These salt species are almost immediately reduced and thus increase the LiF concentration in the electron transport layer. Moreover, the transport of additional salt species from the electrolyte solution towards the lithium metal surface is more frequent in systems with higher salt concentrations. Overall, this leads to a faster production of LiF and hence to a quicker passivation of the lithium metal surface. As a consequence, fewer solvent molecules can approach the electron transport layer before the complete passivation of the surface. This can be confirmed by the ratio of initially present to overall consumed EC, which is summarized in Table A.2 for all parameter sets. This ratio increases from 0.3 for 1M $LiPF_6$ to 0.46 for 2M $LiPF_6$ and hence indicates that fewer EC molecules diffuse to the electron transport zone for high salt concentration. Moreover,

[5] In the original publication [1], salt concentrations of up to 4M $LiPF_6$ were considered for theoretical comparison. However, concentrations of 2M and above exceed the solubility limit of $LiPF_6$ in pure EC and are therefore to be regarded as hypothetical (cf. Figure A.4). In this dissertation, the concentration range is limited to 1-2M $LiPF_6$ in order to reflect more physically realistic conditions. Salt concentrations between 1M and 1.5M $LiPF_6$ are well-established in the literature [68, 101, 148–150]. At 2M first salt precipitation is observed under ambient conditions (cf. Figure A.4). It is hence included as an extreme case, in which the solution remains liquid, although the solubility limit is already exceeded.

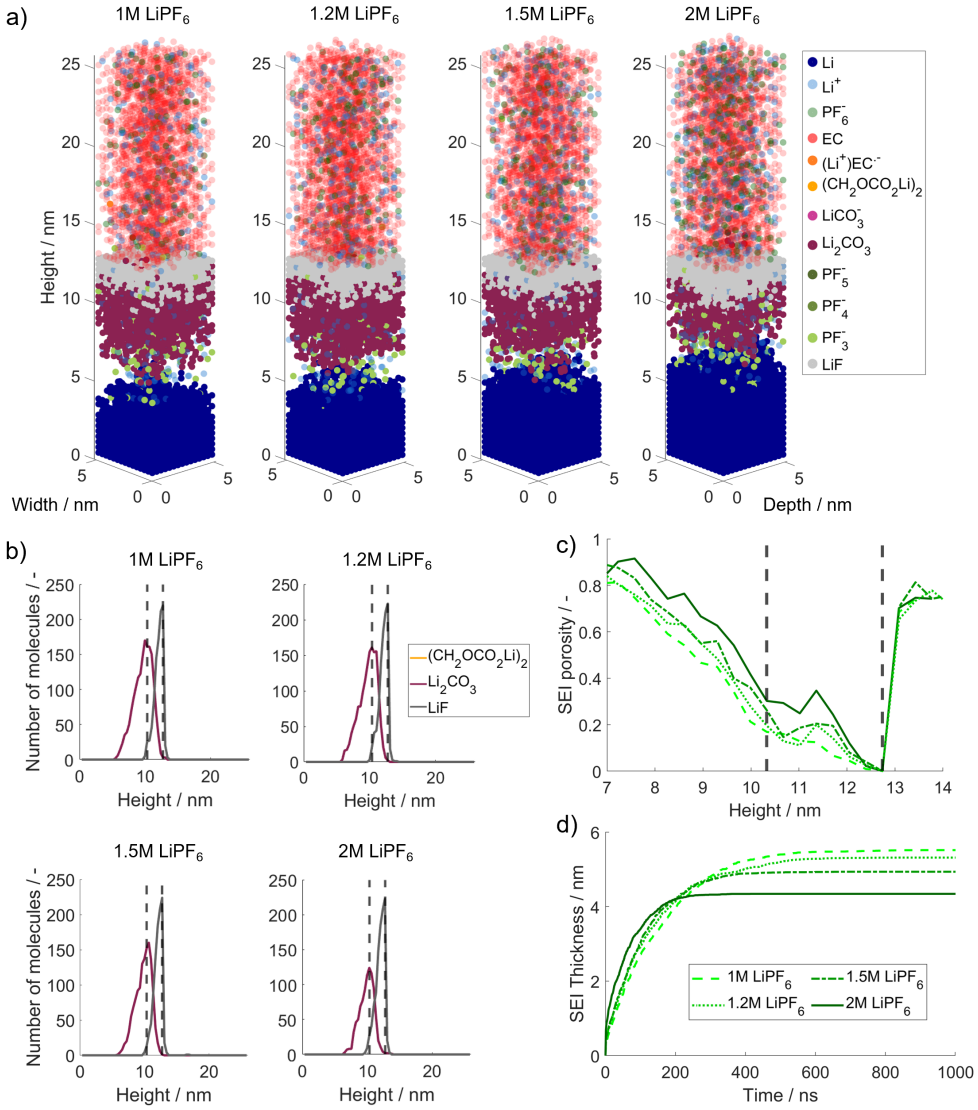

Figure 3.8: Variation of the salt concentration between 1M and 2M $LiPF_6$ in 100 wt.% EC. a) Resulting species distribution after 1 µs. b) Number of SEI molecules after 1 µs over height. The dashed lines represent the initial lithium metal surface (left) and the maximum electron transport distance (right). c) SEI porosity after 1 µs over height. d) SEI thickness evolution within 1 µs

the number of consumed EC molecules decreases from 1686 in the 1M $LiPF_6$ electrolyte to 937 in the 2M $LiPF_6$ electrolyte. This results in the observed reduced amount of the EC degradation product Li_2CO_3. Furthermore, it leads to increased porosity of the inner SEI, which can be seen

in Figure 3.8 c). The described faster passivation of the SEI surface can also be observed in Figure 3.8 d), which compares the SEI thickness evolution for the investigated salt concentrations. Higher salt concentrations lead to steeper growth of the initial SEI layer. At the same time, the final mean SEI thickness decreases with the salt concentration. From the final kMC boxes, which are shown in Figure 3.8 a), it can additionally be concluded that less lithium metal is consumed for the fast formation of this first passivation layer in the case of higher salt concentrations. All of these trends are consistent with those reported in the original publication [1], but less pronounced due to the narrower concentration range considered here.

Overall, by modifying the salt concentration in the electrolyte, the ratio of Li_2CO_3 and LiF in the inorganic layer of the SEI, the thickness of the inorganic layer and the loss of cyclable lithium can be purposefully tuned. From this, it is concluded that higher concentrations of the conducting salt lead to a faster passivation and an increased LiF content, which in turn is reported to improve the self-protection of the SEI and mechanical stability [13, 151].

EC is usually mixed with further, more chemically stable solvents such as EMC or DMC [89, 152]. The effect of adding such a more stable solvent compound to the electrolyte, is in the following investigated with the presented model. For this study, EMC is exemplarily used as the second electrolyte solvent, which dilutes the EC concentration. As discussed in more detail in Section 3.2.3, EMC is not expected to undergo a significant number of degradation reactions within the first microsecond. For this reason, no related degradation reactions were considered. It is further assumed that the second solvent does not have a significant impact on the considered reaction and transport processes and does not chemically interact with the salt or co-solvent in the investigated period of time. Under these assumptions, the following results, which are presented in Figure 3.9, are valid for all electrolyte solvents with a higher or similar chemical stability as EMC on lithium metal.

The simulation results show the following effect of a decreased EC concentration: The LiF distribution in the formed SEI does not change significantly while the amount of formed Li_2CO_3 decreases. Overall, the inorganic SEI keeps a layered structure. Moreover, the thickness of the SEI decreases with decreasing EC concentration. These observations can be mainly attributed to the lower amount of EC molecules initially present close to the lithium metal surface at decreased EC concentrations (cf. Table A.2). Additionally, the transport of fresh reactants towards the electron transport layer is decelerated since fewer EC molecules are available in the electrolyte solution. As a consequence, less Li_2CO_3 can be formed before the surface becomes fully passivated by LiF. In addition, from Figure 3.9 c), it can be observed that the porosity of the inner SEI increases with decreased EC concentrations.

Although these observations seem similar to the effect of the salt variation, it should be noted that in contrast to the sensitivity to salt concentration, the speed of the passivation cannot be

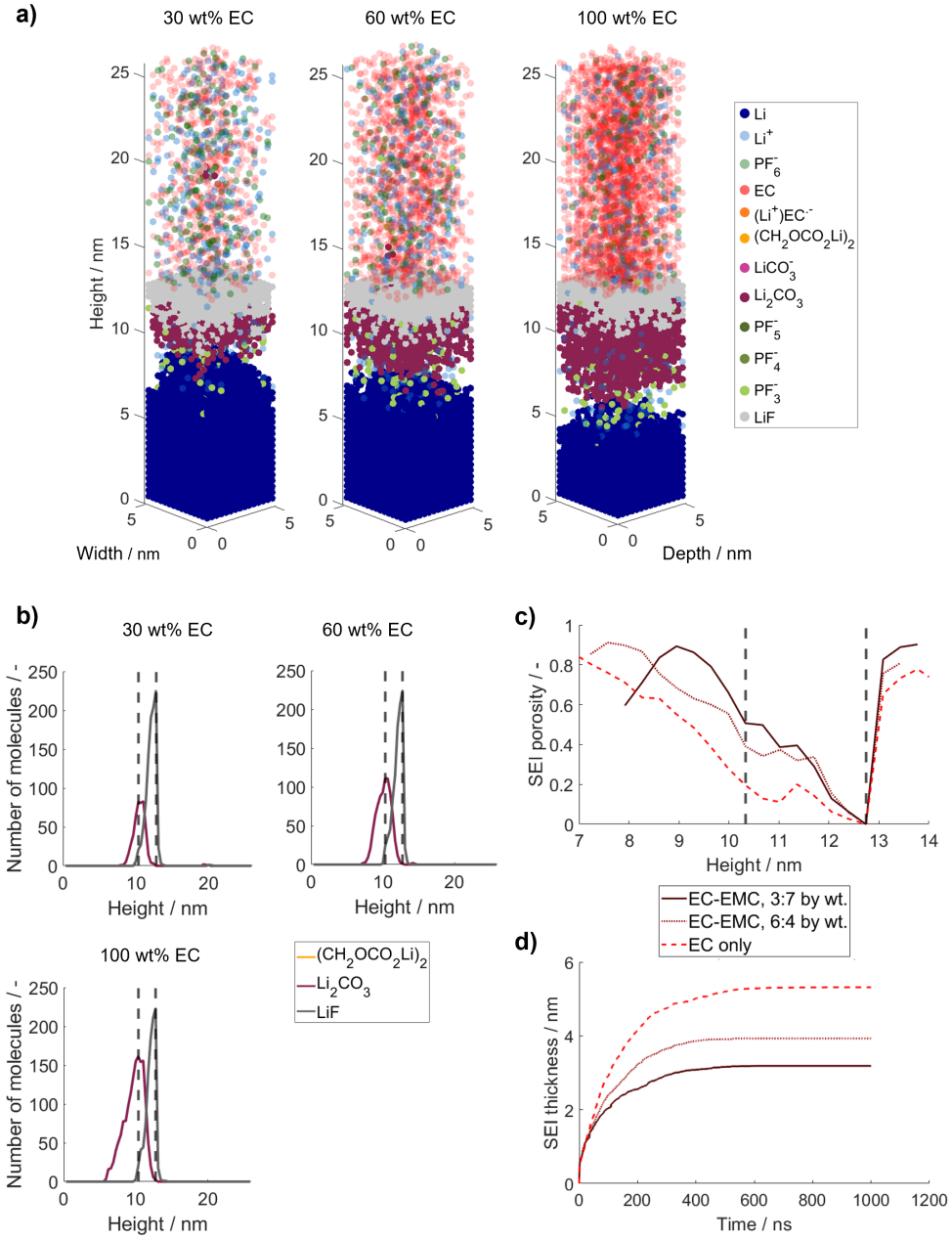

Figure 3.9: Variation of the EC concentration between 30 wt.% and 100 wt.% of the solvent with 1.2M $LiPF_6$. a) Resulting species distribution after 1 µs. b) Number of SEI molecules after 1 µs over height. The dashed lines represent the initial lithium metal surface (left) and the maximum electron transport distance (right). c) SEI porosity after 1µs over height. d) SEI thickness evolution within 1 µs.

tuned by adjustment of the EC concentration. This important difference can also be observed in Figure 3.9 d), which shows that the SEI thickness evolution is consistent for all solvent concentrations within the first nanoseconds. Afterwards, it becomes first limited for low EC concentrations since fewer fresh EC molecules are available in the electron transport zone.

This difference between the effect of the salt and solvent concentration can have some important implications in real systems. In general, real experimental systems are usually more complex than the ideal assumptions in the presented model. Neither the lithium metal anode nor the electrolyte components are perfectly clean. Therefore, impurities within the electrolyte and lithium metal or the often-reported initial surface layer on lithium [153] may cause additional effects and modify the outcome. Furthermore, EMC may also degrade, though slower, leading to additional degradation products. Hence, fast passivation of the lithium metal surface is preferable since it leads to a more controllable SEI formation and could decrease the amount of unwanted side products from impurities. The simulations suggest that faster passivation can be achieved by increasing the salt concentration. However, solubility limits as well as potential downsides, such as slower ion transport, high viscosity and cost need to be considered in order to identify the optimal electrolyte composition.

3.4 Concluding Remarks

Within this chapter a novel kMC/continuum multiscale modeling approach was developed and applied to obtain detailed insight into the procedure of SEI formation on a 50 times larger timescale and a 32 times larger length scale than comparable ReaxFF MD simulations [100]. Thereby, the presented approach is able to track the time-evolution of SEI formation on a molecular resolution and to reveal details of the SEI composition and morphology and on the underlying formation mechanisms, which are presently inaccessible by experiments [14, 19].

During the initial SEI formation, the transport was identified to be the limiting process for the degradation of the conductive salt $LiPF_6$, whereas the decomposition of the electrolyte solvent EC is limited by its reaction kinetics. In this context, the carbonate electrolyte solvent can maintain its chemical integrity for a sub-microsecond timescale when approaching the lithium metal surface. Overall, a complex interplay of electrolyte diffusion, electrolyte degradation and consumption of the lithium metal electrode was revealed, which results in a layered inorganic SEI on the lithium metal surface. Thereby, a Li_2CO_3 layer was observed close to the lithium metal surface and a LiF layer above.

Additionally, it was demonstrated that the Li^+ concentration and solvation environment has a vast impact on the morphology of the formed SEI due to its stabilization effect on the EC solvent [22]. High Li^+ concentrations, which are related to slow EC degradation kinetics, lead to a

layered inorganic SEI. In contrast, low local Li^+ concentrations relate to fast EC degradation kinetics resulting in a more mosaic-like inorganic SEI and a higher amount of organic SEI species. This finding explains parts of the ambivalent literature on the SEI structure and could allow the rational tuning of the SEI based on the local Li^+ concentration. Further analyzed options of SEI tuning included the variation of salt and solvent concentration. In contrast to solvent concentration, increasing the salt concentration led to accelerated surface passivation and a simultaneous increase in the LiF content of the SEI. These trends highlight the potential of salt concentration as a design parameter, provided that solubility limits and potential drawbacks, such as reduced ionic transport and increased viscosity, are carefully considered. In order to reveal the relation between the predicted SEI structures and its performance, in future the predicted structures could either be tested experimentally or by an additional performance model.

Overall, the presented modeling approach gives interesting new insights into the SEI formation on the µs timescale, which is challenging to obtain by MD simulation or *in situ* characterization. It is suitable for studying the mesoscale processes, which bridge the experimental studies and atomistic calculations. The presented model is therefore an important first step towards theoretical prediction of SEI composition and morphology and model-assisted SEI design. In the following Chapter 4 this model is further extended to investigate the impact of vinylene carbonate and polymerization on SEI formation, and to increase the accessible simulation timescale to the order of seconds.

4 Effects of the Film-Forming Additive Vinylene Carbonate[1]

4.1 Introduction

As already introduced in Section 2.1.2, one strategy to stabilize the lithium metal/liquid electrolyte interface is the use of interphase forming electrolyte additives. These can positively alter the properties of the SEI, e.g. making it thinner, more electrically passivating or more mechanically stable against electrode volume changes [13, 61]. A popular additive for both, lithium-ion batteries and LMB is vinylene carbonate [61, 154]. It is well-known to improve the cyclic efficiency of lithium metal batteries [19, 66, 155] and is reported to form a mechanically stable polymeric surface film, which may also increase the internal resistance of the LMB cells [66, 154–156]. In recent years, advanced cryo-transmission electron microscopy (cf. Section 2.2.1) studies could reveal that VC in carbonate-based electrolytes leads to a mosaic-like SEI on electrochemically deposited lithium, consisting of inorganic species embedded in amorphous, organic SEI layers [66]. Furthermore, it was demonstrated that VC has a substantial impact on the initial SEI formation on lithium metal before any external potential is applied, causing an enhanced passivation of the electrode surface and an overall thinner SEI [157]. However, to gain a mechanistic understanding of the specific influence of VC on SEI formation, theoretical studies are required. To date, most contributions in this field apply first principles density functional theory (DFT) and have focused on identifying possible degradation and polymerization pathways [21, 22, 84, 93–95, 158]. Notably, Kuai et al. [22] recently conducted an in-depth DFT investigation of VC decomposition and polymerization in an EC-based electrolyte close to the lithium metal surface. This study provides reaction activation barriers and reaction energies along with possible degradation and polymerization mechanisms and provides a good understanding of the molecular-level interactions between VC, EC and Li^+ ions. However, due to the high computational cost, first principles studies are inherently limited to short timescales and small system sizes. As a result, they cannot capture the full evolution of the SEI layer.

[1] Parts of this chapter have been published in J. Wagner-Henke et al., *Energy Storage Mater.* 81, 104434, 2025 [2], licensed under CC BY 4.0.

To address these limitations, the kMC model introduced in the previous Chapter 3 is particularly well-suited. The mechanistic insights gained from the DFT study of Kuai et al. [22] serve as valuable input for the kMC model, enabling a more comprehensive and computationally efficient investigation of SEI formation under realistic conditions. So far, this model as well as other kMC models from the literature (cf. Section 2.3.2) have primarily focused on relatively simple electrolyte systems and did not consider the effect of additives. Since VC is well known to form polymers [16, 154, 159], an extension of the existing kMC framework by polymerization is required to study its effect on SEI formation. There are examples from polymer-science in which kMC approaches were applied to study different polymer properties such as chain length distribution or the order of copolymers [160–164]. In many cases, the focus was on bulk-phase polymerization, which is why off-lattice approaches were chosen that do not save any configurational information [160–162]. However, some works also focused on surface-initiated polymerization and applied lattice-based kMC approaches [163, 164].

Inspired from these approaches, in this chapter polymerization processes are integrated into the previously developed kMC framework (cf. Chapter 3), leading to the first kMC model of SEI formation that explicitly accounts for polymerization reactions. This allows to reveal the impact of the electrolyte additive VC on the SEI formation on lithium metal beyond elementary reaction steps. The study provides new insights into how VC plays its role as an SEI-forming additive, how it causes a better cycling efficiency and what the major processes of the polymer film formation are. Additionally, the timescale accessible by the kMC model is further extended to seconds, which allows to bridge the scales from the ns range of DFT and MD simulations to more macroscopic scales.

4.2 Methods

4.2.1 Kinetic Monte Carlo Model

For this study an extended version of the previously introduced 3D-kMC model from Chapter 3 is applied. While details of the modeling approach can be found in Section 3.2 of the previous chapter, in the following the main model equations with a focus on the model extensions are briefly summarized. The kMC model is based on the Variable Step Size Method [109, 111] and a structured list approach according to Schulze [114]. Details on the algorithm can be found in Section 2.3.1.

The rare events considered in the presented model are (electro-)chemical reactions, polymerization, transport and clustering processes. The respective rate equations of all processes are summarized in Table 4.1. The description of all symbols may be found in the list of symbols. The

considered radical polymerization processes consist of electrochemical initiation and chemical propagation and termination reactions. The corresponding rates are hence calculated following the rate equations for electrochemical and chemical reactions, respectively. In contrast to the implemented non-polymeric species, polymer species can occupy multiple voxels with each subunit occupying one voxel. The same holds for dimers such as LiEDC. Once a macromolecule covers more than one voxel, its transport is neglected since it is considered to be slow compared to the transport of smaller molecules in the electrolyte. Moreover, radical polymer species are assumed to be only reactive at their active chain end. Hence, further propagation and termination reactions can only occur on the voxel, which was added last to the polymer and therefore represents the active site. This approach is very similar to previous kMC polymerization studies such as the work of Arraez et al. [163, 164], who also applied lattice-based kMC models to investigate surface-initiated polymerization processes. Further assumptions regarding the polymerization processes are that terminated chains cannot be reactivated and that propagation reactions are irreversible.

Table 4.1: Summary of rate equations for all types of implemented rare events.

Process	**Rate Equation**
Chemical reaction[a]	$\Gamma_{R,i} = k_{0,i} \exp\left(-\frac{E_{A,i,\mathrm{dir}}}{RT}\right) \prod_j p_j$
Electrochemical reaction[a]	$\Gamma_{\mathrm{ox},i} = k_{0,i} \exp\left(-\frac{E_{A,i,\mathrm{dir}}}{RT}\right) \exp\left(\frac{\alpha F \eta}{RT}\right) \prod_j p_j$ $\Gamma_{\mathrm{red},i} = \kappa(z) k_{0,i} \exp\left(-\frac{E_{A,i,\mathrm{dir}}}{RT}\right) \exp\left(-\frac{(1-\alpha) F \eta}{RT}\right) \prod_j p_j$
Transport[b]	$\Gamma_D = \frac{3}{13} \frac{D}{l^2} \exp\left(-\frac{E_n}{RT}\right) \exp\left(-\frac{E_A^{\mathrm{bond}}}{RT}\right)$
Clustering	$\Gamma_{\mathrm{Cl},i} = k_{0,i} \exp\left(-\frac{E_{A,i}}{RT}\right)$

[a] With dir = {forw, rev}
[b] The derivation of the prefactor $\frac{3}{13}$ can be found in Section B.1.2 of the appendix.

In the following, further details on the input parameters of the rate equations are provided: The electron transport from the lithium metal anode to the site of reaction in the electrolyte is modeled using an electron transport factor $\kappa(z)$:

$$\kappa(z) = \exp\left(-\beta \cdot (z - z_{\mathrm{Li,max}})\right), \quad \text{for } z > z_{\mathrm{Li,max}} \tag{4.1}$$

Here, β represents the decay factor, $z_{\mathrm{Li,max}}$ is the highest position in the kMC box in which lithium metal is present and z is the height variable of the kMC box. This means, once one layer of lithium metal is entirely consumed, the electron transport factor $\kappa(z)$ is updated, since $z_{\mathrm{Li,max}}$ decreases. In literature, exponential decay functions are very common to model electron tunneling [30, 33, 165]. However, electron tunneling does not reach further than a few nanometers [137, 166], and is hence not sufficient to explain experimentally observed SEI thicknesses. Therefore, a number of further electron transport mechanisms through SEI such as electron conduction [78, 167], neutral lithium diffusion [21, 168] or solvent diffusion through SEI pores is under discussion [77, 166]. For simplification, the exponential decay function in Equation 4.1 is assumed to empirically account for all electron transport processes across the SEI. In contrast to the previously introduced model (cf. Chapter 3), no cutoff distance for the exponential decay is defined in this study.

In the transport rate equation Γ_D (cf. Table 4.1), l represents the diffusion length which equals the size of the lattice sites ΔL in case of face-directed diffusion, $\sqrt{2}\cdot\Delta L$ in case of edge-directed diffusion and $\sqrt{3}\cdot\Delta L$ in case of corner-directed diffusion. The choice of ΔL depends on the size of the smallest explicitly considered species in the simulation box. Its derivation is discussed in Section B.1 in the appendix. Furthermore, the electrostatic energy E_n accounts for repulsive coulombic forces between like-charged neighboring species as given in Equation 3.5, which ensures local electroneutrality. Attracting forces are neglected for the sake of computational efficiency and to prevent numerical artefacts which would be caused by the missing long-range interactions of this approach. Hence, E_n is set to 0 if $E_n \geq 0$. In addition, global electroneutrality throughout the entire simulation box is further ensured by coupling each reduction process with the oxidation of lithium metal and the corresponding release of one Li^+ ion. Additionally, the second exponential term in the transport rate equation accounts for an additional energy barrier E_A^{bond} due to adsorption effects of intermediate species on neighboring solid SEI species. Thereby, the local energy barrier is calculated based on the number n_j, type j and binding energy $E_{A,j}^{\mathrm{bond}}$ of direct neighbors as shown in Equation 4.2.

$$E_A^{\mathrm{bond}} = \sum_j n_j E_{A,j}^{\mathrm{bond}} \tag{4.2}$$

As an extension to Chapter 3, the accessible timescales of the presented calculations are significantly increased. In order to achieve this, the following new assumptions are made: First, implicit electrolyte species are introduced, which are assumed to be homogeneously distributed over the empty voxels of the simulation box, for times beyond 2 µs. This is justified as diffusion is significantly faster than reaction at this timescale (cf. Figure B.4 a) and b)). These species are not explicitly placed on individual voxels in the simulation box, but can still take part in (electro-)chemical reactions. They may be present on each empty voxel with a probability

p_j which is based on their bulk concentration c_j and the lattice site volume ΔL^3 as shown in Equation 4.3.

$$p_j = c_j \cdot \Delta L^3 \cdot N_A \tag{4.3}$$

If implicitly considered species are formed by a reaction, they are not placed in the simulation box, since their concentration is considered to be constant. For explicitly considered species *j*, p_j is 1 for voxels which are occupied by a molecule of species *j*, and 0 for voxels which are empty or covered by another species. In addition, the lithium oxidation process is implicitly considered by assuming that the solid transport of lithium atoms in the lithium metal bulk phase is fast enough to fill voids that arise by lithium oxidation. This assumption is based on the self-diffusion coefficient of solid lithium which is reported to be in the range of 4.82 to 7.78 x 10^{-15} m^2 s^{-1} for a temperature of 298 K [169]. Furthermore, it is assumed that electrolyte decomposition products that are located more than 5 nm away from the upmost layer containing clustered SEI species or lithium metal are dissolved. They are hence removed from the simulation box in order to reduce the number of modeled transport steps of electrolyte decomposition products within the bulk electrolyte phase and to further increase the computational efficiency of the model. This is justified, since interactions with the electrode or SEI surface are not expected beyond this distance.

The long-time calculations are further initialized with a primary, simplified SEI layer. This layer can be adjusted to represent the initial passivation due to the SEI formed within the first microsecond and/or further native or artificial passivation layers. It consists of dense LiF, which was chosen, since it constitutes the topmost layer of the primary inorganic SEI (cf. Figure 4.3). The Li_2CO_3 layer below is hence not expected to impact follow-up reactions at the SEI/electrolyte interface (cf. Figure B.6). The porosity of the primary passivation layer is set to zero, since the short-term calculations indicated a very high density of the LiF-layer in the primary SEI (cf. Figure 4.3 b)). Detailed information on the selection of all parameters is provided in Section B.1 in the appendix.

4.2.2 Identification of Electrolyte Degradation Reactions

This study focuses on the effect of the electrolyte additive VC on the SEI formation in the baseline electrolyte EC + 1.2M $LiPF_6$. Since all electrolyte species may in principle contribute to SEI formation, the major degradation pathways were identified for each electrolyte component based on literature data and DFT calculations. The degradation reactions as well as the related kinetic parameters for the electrolyte solvent EC and the conductive salt $LiPF_6$ were already identified

in the previous Chapter 3 and are kept for this study[2] (cf. Table B.2). The current literature on the degradation of VC on anode surfaces suggests multiple degradation and polymerization mechanisms. The two major possibilities which are frequently reported are the ring-opened polymerization of VC [94, 158, 170] and the polymerization without ring-opening which would lead to the formation of poly(VC) [171–175]. Products of both reaction pathways have been experimentally identified as components of VC-derived SEI layers on graphite anodes [176].

In order to clarify, which mechanism is kinetically preferred, Kuai and Balbuena [22] recently conducted an extensive DFT study for both VC polymerization mechanisms as well as for EC polymerization and EC/VC cross-polymerization between both species and identified the corresponding Gibbs free energies and energy barriers. Based on their results, the suitable VC degradation reactions for this study were selected as follows: First, reasonable reaction mechanisms are expected to have a negative Gibbs free energy $\Delta_R G_i$ to ensure thermodynamic favorability. Second, the corresponding activation energy $\Delta G_i^{\ddagger}$ should be sufficiently low to allow the reaction to proceed in an accessible time. As illustrated exemplarily for a chemical reaction with $k_{0,i} = 10^{13}$ s^{-1} and $p_j = 1$ in Figure B.2, the average reaction time until a process occurs is still well below 1 s for an energy barrier of 15 kcal mol^{-1}, significantly increases when it approaches a barrier of 20 kcal mol^{-1} and hits a reaction time of 1000 s for about 21.8 kcal mol^{-1}. Since no simulation times of up to 1000 s are reached in the presented kMC simulations, all reactions with an energy barrier above 21.8 kcal mol^{-1} are neglected. Kuai and Balbuena [22] demonstrated that the ring-opening mechanism of VC has to overcome a very high energy barrier of at least 38.48 kcal/mol. Similarly, both the self-polymerization of EC and its reaction with VC-derived radicals have been reported to exhibit high energy barriers of more than 50 kcal/mol, respectively. This significantly exceeds the previously defined cutoff energy barrier of 21.8 kcal mol^{-1}. Therefore, these mechanisms were not considered in the kMC model. In contrast, the calculated energy barriers for the poly(VC) formation mechanism (cf. Scheme 4.1 a)) were determined to be well below 21.8 kcal mol^{-1} which makes this reaction mechanism suitable to be studied with the presented kMC framework (cf. Table 4.2). The same holds for the cross-polymerization mechanism (cf. Scheme 4.1 b)), which is induced by an EC-radical species attacking a VC monomer and followed by subsequent VC polymerization without ring-opening.

Kuai and Balbuena [22] additionally showed that the energy barriers of monomer reduction, initiation and polymerization significantly depend on Li^+ coordination (hereafter referred to as 'lithiation' or 'lithiated') of the monomer and polymer species. Since this lithiation heavily depends on the bulk electrolyte composition (cf. Figure B.5), two different parameter sets were

[2] A recent study [91] suggests more complex salt degradation pathways, strongly depending on local Li^+ coordination and the electrolyte's dielectric constant. Since this chapter focuses on the effect of VC, the previously established salt degradation pathways and parameters are maintained. Future studies could investigate the impact of the new results on salt degradation and SEI formation in greater detail.

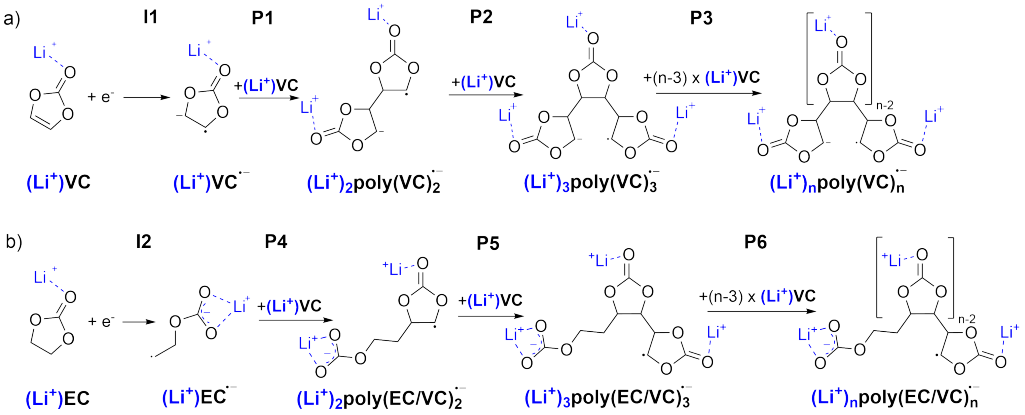

Scheme 4.1: Considered polymerization mechanisms with optional Li^+-coordination shown in blue. a) poly(VC)-formation mechanism. b) Cross-polymerization mechanism with EC radical as initiator.

extracted from their study as input for the kMC simulation studies to account for low and high Li^+ concentration scenarios. The first one considers all monomers to be coordinated with one Li^+ ion and the second accounts for the case without Li^+ coordination. As demonstrated in the previous Chapter 3, the assumption of lithiated electrolyte molecules aligns well with the local conditions on the lithium metal surface during the initial SEI formation on the nanosecond to microsecond scale. Therefore, the lithiated parameter set is applied for all short-term calculations in this study. In case of the long-time calculations, a homogeneous bulk electrolyte phase is considered. Hence, the amount of lithiated and non-lithiated electrolyte molecules can be estimated (cf. Figure B.5). This calculation shows that in a single-solvent EC electrolyte with 1.2M $LiPF_6$ and 5 wt.% VC a high number of non-lithiated electrolyte species exists. Since these are more prone to react compared to their lithiated counterparts (cf. Table 4.2), the non-lithiated parameter set is used for this case. In contrast, most solvent and additive molecules are coordinated with at least one Li^+ ion in case of a mixed EC:EMC (3:7 by wt.) electrolyte with either 1.2M or 3M $LiPF_6$ and 5 wt.% VC (cf. Figure B.5). Therefore, the lithiated parameter set is applied for the corresponding calculations.

The summary of the extracted energy barriers can be found in Table 4.2. Thereby, the energy barriers of the reaction steps I1, I2, P1, P2, P4 and P5 have been directly calculated by DFT. Moreover, all of these steps have negative Gibbs free energies and hence are thermodynamically favorable. Due to computational limitations, the energies for propagation of longer polymer chains (P3 and P6) are not easily accessible by DFT. For this reason the simplifying assumption is made that the energy barriers of propagation steps, forming chains longer than three monomers, are independent of the exact chain length and configuration of the polymer species. Hence, the energy barriers of the corresponding polymerization reactions P3 and P6 are set to the next integer values of the respective second propagation steps (P2 and P5). Since all barriers except of the

non-lithiated case of P5 are close to 14 kcal mol^{-1}, this energy barrier is set for all long-chain propagation steps. In order to assess the possible impact of this assumption the sensitivty of the simulation results towards this parameter was analyzed (cf. Section B.2.6). This shows that neither the chemical composition or morphology nor the growth dynamics are highly affected by the exact energy barrier of the long-chain propagation. However, the parameter significantly influences the duration of layer formation, which hence should be interpreted with caution.

Table 4.2: Activation energies in kcal mol^{-1} for VC and EC degradation (I), VC polymerization, cross-polymerization (P) and termination reactions (T) for the lithiated and non-lithiated case. All energies are derived from first principles calculations. The optional Li^+ coordination is shown in blue.

		$\Delta G_i^{\ddagger}$ / kcal mol^{-1}	
N^0	**Reaction**	**Lithiated**	**Non-lithiated**
I1	$(Li^+)VC + e^- \longleftrightarrow (Li^+)VC^{\bullet-}$	0[c,e]	0[c,e]
I2	$(Li^+)EC + e^- \longleftrightarrow (Li^+)EC^{\bullet-}$	12.05[b]	0[b]
P1	$(Li^+)VC^- + (Li^+)VC \rightarrow (Li^+)poly(VC)_2^{\bullet-}$	9.97[c]	0[c,e]
P2	$(Li^+)poly(VC)_2^{\bullet-} + (Li^+)VC \rightarrow (Li^+)poly(VC)_3^{\bullet-}$	13.54[c]	13.63[c]
P3	$(Li^+)poly(VC)_{n-1}^{\bullet-} + (Li^+)VC \rightarrow (Li^+)poly(VC)_n^{\bullet-}$	14[d]	14[d]
P4	$(Li^+)EC^{\bullet-} + (Li^+)VC \rightarrow (Li^+)poly(EC/VC)_2^{\bullet-}$	13.42[c]	14.31[c]
P5	$(Li^+)poly(EC/VC)_2^{\bullet-} + (Li^+)VC \rightarrow (Li^+)poly(EC/VC)_3^{\bullet-}$	14.1[c]	6.09[c]
P6	$(Li^+)poly(EC/VC)_{n-1}^{\bullet-} + (Li^+)VC \rightarrow (Li^+)poly(EC/VC)_n^{\bullet-}$	14[d]	14[d]
T1	$(Li^+)VC^{\bullet-} + (Li^+)VC^{\bullet-} \rightarrow (Li^+)poly(VC)_2$	0[a,e]	0[a,e]
T2	$(Li^+)VC^{\bullet-} + (Li^+)EC^{\bullet-} \rightarrow (Li^+)poly(EC/VC)_2$	3.97[a]	3.97[a]
T3	$(Li^+)poly(EC/VC)_m^{\bullet-} + (Li^+)poly(EC/VC)_n^{\bullet-} \rightarrow (Li^+)poly(EC/VC)_{m+n}$	17.83[a]	17.83[a]
T4	$(Li^+)poly(EC/VC)_{n-1}^{\bullet-} + (Li^+)EC^{\bullet-} \rightarrow (Li^+)poly(EC/VC)_n$	16.59[a]	0[a,e]
T5	$(Li^+)poly(EC/VC)_{n-1}^{\bullet-} + (Li^+)VC^{\bullet-} \rightarrow (Li^+)poly(EC/VC)_n$	16.78[a]	0[a,e]

[a] Original DFT calculations
[b] Adopted from Wagner-Henke et al. [1]
[c] Adopted from Kuai and Balbuena [22]
[d] DFT calculations for different Li^+ coordinations were averaged and rounded
[e] Manually set to 0 kcal mol^{-1} since the DFT calculations suggested negative values

Besides the aforementioned initiation and propagation mechanisms, termination reactions are an important step of each polymerization process. Based on the radical species present in the studied electrolyte system, namely $(Li^+)VC^{\bullet-}$, $(Li^+)EC^{\bullet-}$, $(Li^+)poly(VC)_n^{\bullet-}$, $(Li^+)poly(EC/VC)_n^{\bullet-}$, the following five recombination processes to be added to the reaction network were identified: The recombination of two VC radicals (T1), the recombination of a VC radical and an EC radical

(T2), the recombination of two active chain ends (T3), the recombination of an active chain end with an EC radical (T4), and the recombination of an active chain end with a VC radical (T5). Additionally, the recombination of two EC radicals is accounted for by the LiEDC forming reaction (R3), which has already been parameterized as part of the previous Chapter 3. The kinetic parameters of the considered termination reactions (cf. Scheme 4.2) could not be found in literature and were hence calculated using DFT as part of this study (cf. Section 4.2.3). Due to computational limitations of DFT, the termination of the active polymer chains is approximated using the values for the corresponding dimers. Thereby, it is assumed that the results are also representative for longer polymer chains and that the type of initiator does not have a significant impact on the termination kinetics. All energies were again calculated for a lithiated and a non-lithiated case. The resulting parameters are summarized in Table 4.2. Details on the calculations can be found in the following Section 4.2.3.

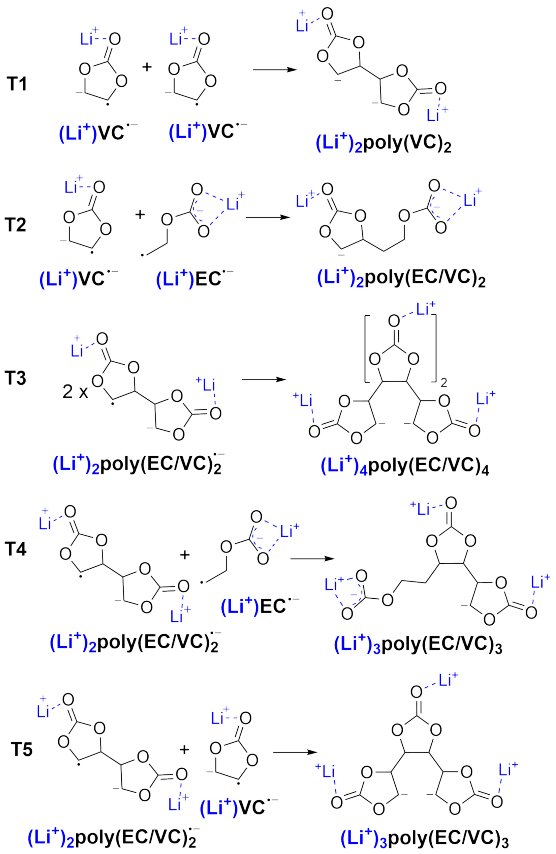

Scheme 4.2: Considered termination reactions with optional Li^+-coordination shown in blue.

4.2.3 Density Functional Theory Calculations[3]

DFT was used to calculate the reaction free energy $\Delta_R G_i$ and the energy barriers $\Delta G_i^{\ddagger}$ of the polymer termination reactions (cf. Section 4.2.2). These kinetic parameters were then provided as an input for the subsequent kMC calculations. The molecular modeling was carried out with Gaussian16 [142] in accordance with the previous publication of Kuai and Balbuena [22]. The B3PW91 level of theory with 6-311g(3df) basis sets [141] was used to optimize all structures. Solvation effects were evaluated based on the SMD. The catalytic effects of lithium metal were neglected, as direct contact with the electrolyte phase is limited to the initial few nanoseconds of the simulation. Grimme dispersion corrections were included in the calculations. All the free energy values were converted to the standard state of 1M.

4.3 Results and Discussion

4.3.1 Primary SEI Formation on the Microsecond Timescale

To analyze the effect of the VC additive on the primary SEI formation on lithium metal in a 1.2M $LiPF_6$/EC electrolyte, 5 wt.% of VC were added to the electrolyte in the initial simulation box. In the previous Chapter 3, it was demonstrated that during the initial SEI formation on the nanosecond to microsecond scale, the assumption of Li^+ coordinated electrolyte molecules aligns well with the local conditions on the lithium metal surface. Consequently, for the subsequent calculations, the parameter set for the lithiated case was applied, which has been primarily extracted from the work of Kuai and Balbuena [22] (cf. Section 4.2). It should be further noted that in the following analysis for simplicity, the term ‘polymer’ refers to all macromolecules composed of at least two VC and/or EC monomers. Moreover, all simulated parameter sets may be found in Table B.5 and are subsequently referred to as cases.

The SEI formed 2 µs after the initial contact of lithium metal and the liquid electrolyte phase is displayed in Figure 4.3. Figure 4.3 a) and b) show the overall species distribution and SEI composition for the electrolyte without (left) and with (right) VC, respectively. The corresponding temporal evolution of SEI composition may be found in Figure B.7 in the appendix. As already revealed in the previous Chapter 3, the primary SEI formed in EC + 1.2M $LiPF_6$ within the first 2 µs is inorganic and consists of two layers: A Li_2CO_3-layer closer to the lithium metal surface and a LiF-layer above. In the VC-containing electrolyte, the additional formation of an organic/polymeric layer above the inorganic SEI is observed. Interestingly, the formed inorganic

[3] The DFT calculations were performed by Dacheng Kuai, formally Texas A&M University.

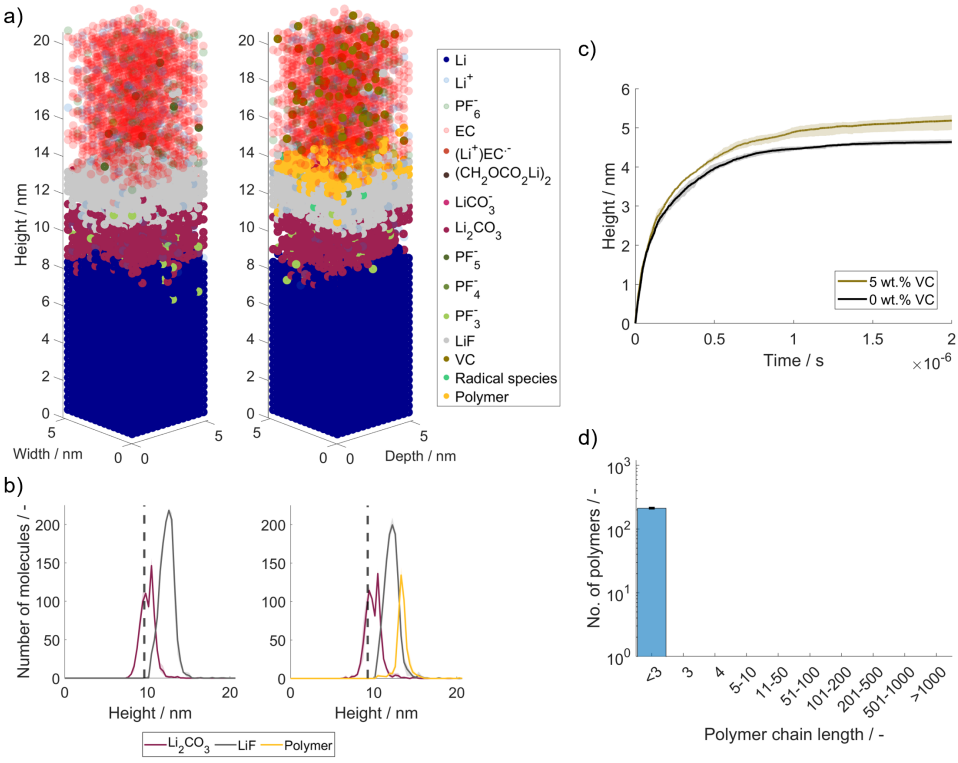

Figure 4.3: SEI formation in carbonate-based electrolyte with (case 1) and without (case 2) 5 wt.% VC after the first 2 µs. The results in a) are based on a single kMC run and the results in b)-d) display the average of three runs with the same parameter set. Deviations from the average are represented as shadings around the average in b) and c). In d), they are illustrated using error bars. a) SEI composition and morphology without (left) and with (right) VC. b) SEI species distribution over height without (left) and with (right) VC. The dashed line represents the upmost layer in which metallic lithium is present after 2 µs. c) Evolution of SEI height up to 2 µs for both cases. d) Polymer chain length distribution in SEI formed in VC-containing electrolyte after 2 µs.

layer barely differs from the layer formed in the additive-free electrolyte. The only significant effect is that the LiF peak in Figure 4.3 b) is slightly decreased for the VC-containing electrolyte case. From this it can be concluded that VC suppresses the salt degradation during the initial SEI formation to a certain extent. Figure 4.3 c) further shows the height evolution of the SEI for the electrolyte compositions with and without VC within the first 2 µs. The overall trajectory of the SEI growth is very similar in both cases with a steep increase of the SEI height within the first nanoseconds and a continuous deceleration of the SEI growth afterwards, which can be attributed to the increasing passivation of the lithium metal surface. However, over time, an increasing spread between the SEI height evolution of both systems is observed, with the VC-containing

electrolyte leading to a slightly thicker primary SEI than the VC-free electrolyte. This can be attributed to the formation of the additional polymer layer. 2 µs after the contact of electrolyte with lithium, the average height of the SEI results in 5.18 nm with VC and in 4.64 nm without VC in the electrolyte. At first glance, this result is not as expected since it contradicts the experimental findings by Weber et al. [157], who investigated the SEI thickness evolution on lithium foil in 1M $LiPF_6$ in EC:EMC (1:1 v/v) with and without 5% VC and found a thicker SEI in the VC-free electrolyte. The authors attribute this to the formation of decomposition species that are only loosely associated with the electrode surface and thus only provide limited surface passivation. However, it is important to note that these experimental measurements were conducted on significantly longer timescales, ranging from minutes to hours and are hence not directly comparable to the presented simulation results on the microsecond timescale. The observed discrepancies may arise from slow processes such as the dissolution of electrolyte decomposition products and secondary reactions of dissolved intermediates, which are likely to contribute to the experimental observations but only occur on longer timescales and are thus not yet captured by the simulation model.

A more detailed analysis of the polymeric layer formed in the VC-containing electrolyte is presented in Figure 4.3 d), which displays the chain length distribution of the polymer species in the VC-containing case. It reveals that the observed organic layer does not consist of actual macromolecules. Instead, within the considered time frame, only dimers have formed. The explanation of this observation is twofold. First, the pristine lithium metal surface, which is present at the beginning of the simulation, is very reactive. This favors many reduction reactions and hence the formation of many VC radicals, which can act as initiators for the subsequent polymer propagation. Yet, due to the high reactivity, the local concentration of these radical species is high, which leads to quick recombination and hence to the formation of inactive dimers. Second, the energy barriers of the propagation reactions P1 – P6 in the lithiated parameter set range between 9.97 and 14.1 kcal mol^{-1} (cf. Table 4.2). This translates to average reaction times of 2 µs up to 2.2 ms, which is higher than the here investigated timescale. It is therefore expected that a significant number of propagation reactions can only be observed on a considerably larger timescale.

Overall, VC only has a minor effect on the SEI formation on the µs-timescale. The slight suppression of salt decomposition and the formation of an additional organic layer might not be sufficient to justify the performance improvement of lithium anodes which is observed experimentally. Furthermore, the observation of an even thicker SEI formed from the VC-containing electrolyte compared to the VC-free electrolyte and the exclusive formation of dimers contradicts experimental findings. It is therefore concluded that the key effects of the VC additive become apparent only on significantly longer timescales. Therefore, in order to understand the actual working principles of the VC additive, an increase of the investigated timescale is required and conducted in the following section.

4.3.2 SEI Formation beyond the Microsecond Timescale

Simulation of SEI growth up to milliseconds or seconds with the same approach as in Chapter 3 and the previous Section 4.3.1, would cause prohibitively high computational costs, and thus runtime. Therefore, in order to reach simulations at much longer timescales and acceptable runtimes, the kMC time steps may be increased by identifying quasi-steady state processes that can be removed from the kMC simulations. The subsequent simulations take advantage of the fact that after the first microsecond, the electrolyte species are homogeneously distributed above the densest SEI layer (cf. Figure B.4 c) and d)). Hence, the further SEI formation is not transport-limited and transport processes can be considered to be quasi-stationary. As a consequence, for timescales exceeding 2 µs all electrolyte species (EC, $LiPF_6$ and VC) are considered implicitly, i.e. through a residence probability derived from their respective bulk concentrations (cf. Equation 4.3). Moreover, in contrast to the short-term calculations, the long-time calculations are further initialized with a reduced initial SEI consisting of a dense LiF-film of varying thicknesses, to represent the primary passivation layer that has been formed upon the first contact of lithium metal with the electrolyte. Details on the assumptions for the long-time calculations may be found in Section 4.2.1 and in Section B.1.6. Overall, this allows to increase the simulation time from the microsecond- up to the second-timescale and above.

Figure 4.4 a) shows the temporal evolution up to 1 s of the SEI composition and morphology in the VC-containing electrolyte EC + 1.2M $LiPF_6$ + 5 wt.% VC. Here, the thickness of the initial passivation layer is set to 3.57 nm. This corresponds to the observed distance between the upmost metallic lithium and the densest layer of the primary SEI after 2 µs (cf. Figure 4.3 b)). For any electrochemical reaction to occur after 2 µs, electrons need to bridge at least this distance. The first box shows the configuration after a total time of 3 µs after the initial contact between lithium and the electrolyte, since the initially placed LiF-layer represents the primary SEI after 2 µs (cf. Subsection 4.3.1). On the microsecond-scale the formation of a comparatively dense layer consisting of a mixture of LiEDC, Li_2CO_3 and different polymeric species and the formation of small Li_2CO_3 clusters above the surface inside the electrolyte phase is observed. The polymer chain length distribution in Figure 4.4 b) demonstrates that up to 3 µs no chain formation with more than three units occurs. This finding is well in line with the previous observation made in the short-term kMC simulation (cf. Subsection 4.3.1). The composition of the dense layer differs from the short-term simulations as a consequence of the comparatively low local Li^+ ion concentration in the bulk phase of the electrolyte. This leads to changed reaction kinetics and the additional formation of the organic LiEDC.

Up to 1 ms, the dense organic layer has slowly grown. Moreover, additional short chains with a chain length up to 3 have formed. Overall, the vast majority of oligomer species still has a chain length of 2 or 3, and only few longer chains with a maximum chain length of 5 – 10 units are

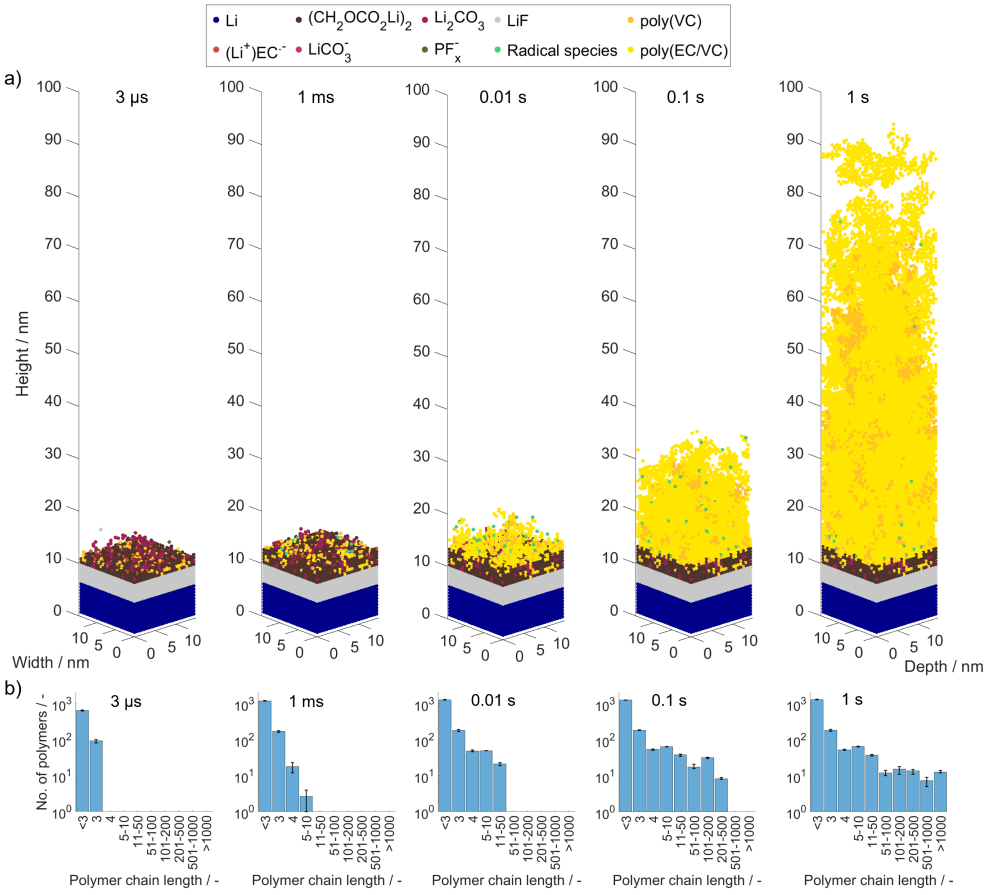

Figure 4.4: Temporal evolution of SEI growth on lithium metal in EC + 1.2M $LiPF_6$ + 5 wt.% VC until 1 s after formation of an initial 3.57 nm thick, dense LiF-based SEI at 1 µs (case 3). a) Spatial morphology and composition of the formed SEI at different times. b) Corresponding chain length distribution of the formed polymer species.

present. The picture changes when further increasing the timescale to multiple ms. 10 ms after the first contact of lithium and electrolyte, an increase in polymeric species can be clearly seen in Figure 4.4 a). Moreover, the corresponding chain length distribution in Figure 4.4 b) indicates the formation of an increasing number of longer chains with more than 10 units. This trend persists on larger timescales. At 0.1 s it becomes apparent that the polymer species have significantly grown towards the electrolyte phase and thereby form a porous polymer layer on top of the initial SEI with increased chain length. The developing polymer layer consists of a mixture of poly(VC) species and poly(EC/VC) species. In the latter, an EC radical species has acted as initiator. Overall, the EC-radical based polymers constitute the majority of the polymeric SEI.

Interestingly, the previously formed Li_2CO_3 clusters close to the surface are gradually encapsulated by the growing polymer phase. This observation aligns well with cryo-TEM measurements reported in literature, which show the formation of inorganic species embedded within organic SEI layers [66].

1 s after the initial contact of lithium and electrolyte, the surface is completely covered with a thick polymer layer consisting of both, poly(VC) and poly(EC/VC) chains. In contrast, the Li_2CO_3- and LiEDC-based SEI layer has not further grown and remains unchanged in its properties. This can be attributed to the passivating and protective properties of the formed polymeric layer. It prevents continuous reductive decomposition of electrolyte components (cf. Figure 4.5) and loss of active lithium, while it itself is formed through a purely chemical process. Moreover, it can be observed that the number of shorter polymer chains with up to 10 units almost remained constant, i.e. they were not reactive and only few chains have grown into long polymer chains with several hundred up to more than 1000 units. An explanation on this phenomenon is provided below in the discussion on Figure 4.6 and Figure 4.7. It can further be concluded that the polymer growth is still ongoing and that, for times longer than 3 µs, the chain propagation represents, by far, the most prevalent process, accounting for over 99% of the occurrences (cf. Figure B.13). As the growth has not yet stopped, it is not possible to conclude on the final thickness of the VC-based SEI. However, the average height of the formed SEI after 1 s can be observed to be quite large with 72.2 nm, which is in the range of experimentally observed SEI thicknesses in VC-containing systems [157] or slightly above [66]. Uncertainties in this result may occur due to the hard-to-determine long chain propagation kinetics. While minor alterations in this rate do not affect the system dynamics in a way that the observed SEI composition or morphology changes, it influences the duration of layer formation (cf. Figure B.16). Hence, while the observed trends are robust, the time-dependent thickness should be interpreted with caution.

A deeper understanding of how VC impacts the SEI formation is gained by comparing the long-time formation in the VC-containing and in the VC-free electrolyte. Figure 4.5 a) shows the formed SEI after 1 s in the VC-free electrolyte. It can be observed that the formed SEI mostly consists of the organic LiEDC mixed with some clusters of Li_2CO_3. Overall, the layer is significantly thinner than the SEI that has formed within the first second in the VC-containing electrolyte (cf. Figure 4.4). The major reason for this is the missing polymer layer. This observation contradicts previous experimental literature, which reported that the VC-containing electrolyte leads to a significantly thinner SEI than the VC-free electrolyte [157].

A closer examination of electrolyte consumption and the number of dissolved species provides a better understanding of these differences between simulation and experiment and the effect of the VC additive. First, Figures 4.5 b) and c) show that a significantly higher amount of the electrolyte solvent EC is consumed within the first second in the VC-free compared to the VC-containing electrolyte. A similar but less distinct trend is observed for $LiPF_6$. Moreover, the consumption

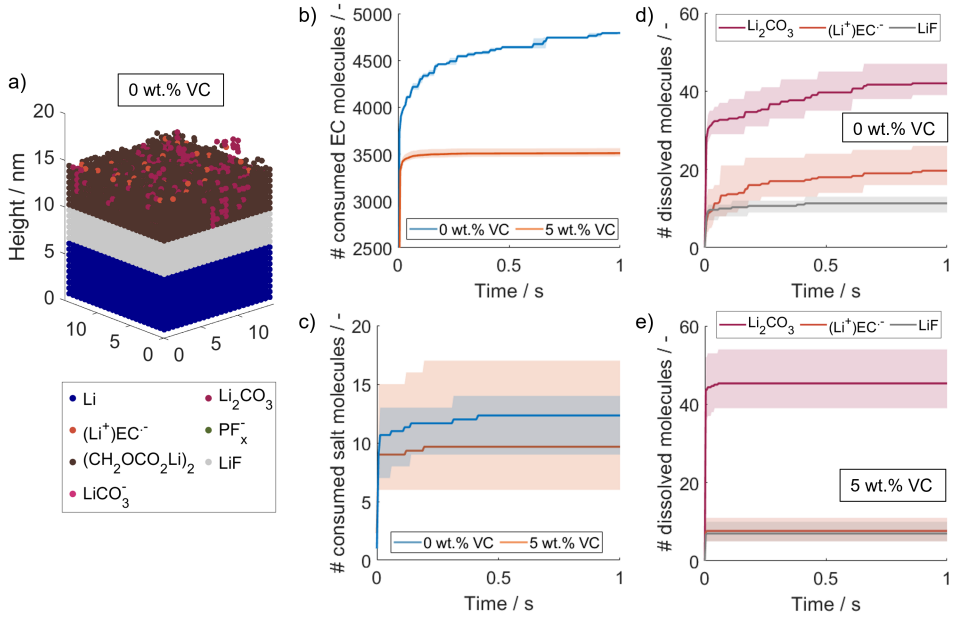

Figure 4.5: Comparison of long-time SEI formation in VC-free (case 4) and VC-containing (case 3) electrolyte. a) SEI composition and morphology in VC-free electrolyte after 1 s. b) Comparison of consumed EC molecules over time. c) Comparison of consumed salt molecules over time. d) Number of dissolved electrolyte decomposition products over time in VC-free electrolyte. e) Number of dissolved electrolyte decomposition products over time in VC-containing electrolyte.

of EC is still ongoing in the VC-free electrolyte case, whereas it has stopped after approximately 0.2 s in the VC-containing electrolyte. A similar trend may be observed in Figure 4.5 d) and e), which show the number of dissolved electrolyte decomposition products over time. Here a dissolved species is defined as a species that either leaves the kMC box through its open upper boundary or that has moved more than 5 nm away from the highest SEI (cf. Section 4.2.1). It should be noted that this does not include the dissolution of previously deposited and clustered SEI species, which is due to the short timescale below 1 s not considered in the presented model. It might, though, play a significant role at much longer times [131] – this holds especially for the VC-free electrolyte. Instead it only refers to not yet deposited electrolyte decomposition products that stay and diffuse in the electrolyte, rather than deposit and cluster on the surface. In both, the VC-free and VC-containing electrolyte, dissolved Li_2CO_3, LiF and $(Li^+)EC^{\bullet-}$ can be observed. However, a significantly higher amount of LiF and $(Li^+)EC^{\bullet-}$ stays in solution in the case of the VC-free electrolyte, while the overall number of dissolved Li_2CO_3 molecules after 1 s is similar. The number of dissolved molecules still increases in the VC-free electrolyte after 1 s, while it remains constant after a few milliseconds in the VC-containing electrolyte. The dissolved electrolyte decomposition products may undergo further subsequent reactions and/or

form solid clusters, which are only loosely connected to the surface. Thus, they could form a porous layer which is still part of the SEI but does not adequately passivate the surface to prevent further reduction of the electrolyte. Similar mechanisms have been previously proposed by other kMC studies for graphite anodes [30, 128] and hard carbon anodes for Na-ion batteries [131]. SEI dissolution on lithium metal anodes has also been observed experimentally for different electrolyte chemistries [145–147]. Although the observed number of dissolved molecules does not quantitatively explain the difference between simulation within the first second and the experimental observations of Weber et al. [157], the simulation results suggest the following qualitative explanation: The VC-free electrolyte does not passivate the lithium metal surface in a way that sufficiently suppresses ongoing electrolyte reduction and dissolution of electrolyte decomposition products. This irreversibly consumes active lithium and electrolyte components. In contrast, VC quickly passivates the surface against ongoing electrolyte decomposition within the first 0.2 s after contact. Importantly, this primarily occurs through chemical propagation rather than electrochemical reactions and hence consumes significantly less active material, i.e. lithium. It is further hypothesized that the formed polymer chains constitute a comparatively stable SEI, which does not dissolve to a significant extent.

Further insights into the effect of the additive VC are subsequently provided by the analysis of the spatial chain length distribution and height-depending porosity of the polymeric SEI. Thereby, the thickness of the initial passivation layer is varied to study the effect of varying degrees of initial passivation, which can e.g. be caused by different native or artificial passivation layers on the lithium metal surface [153, 177–179]. Figure 4.6 a) depicts the height-dependent polymer chain length distribution for a varying thickness of the initial LiF layer between 3.57 and 5.95 nm. Interestingly, many short chains closer to the electrode and a constant increase of the chain length towards the electrolyte phase can be observed independent of the thickness of initial passivation. Thereby, the polymeric phase in close proximity to the lithium metal consists exclusively of dimers. This effect is most distinct for thinner initial passivation layers and diminishes the thicker the initial layer gets. Figure 4.6 b) further shows that this dimeric part of the SEI is completely dense without any porosity. Together with the initial LiF-layer this leads to an overall dense passivation layer with a thickness of approximately 6.55 nm for all investigated cases. Above this height, the porosity of the SEI gradually increases with the distance to the lithium electrode. From this, it is concluded that a minimum passivation of the lithium surface is required before longer polymer chains can form and that the subsequent polymer layer is more porous. The reason is that without sufficient passivation the rate of electron transport through the SEI and subsequent reduction of electrolyte and additive species to radicals is still higher than the propagation rate. Hence, close to the surface the local concentration of radicals is high, which favors recombination reactions and therefore the formation of dimers. It should be noted that the thickness of this dense layer depends on the electron transport through the formed SEI – a better passivating SEI will lead to a thinner dense layer and vice versa.

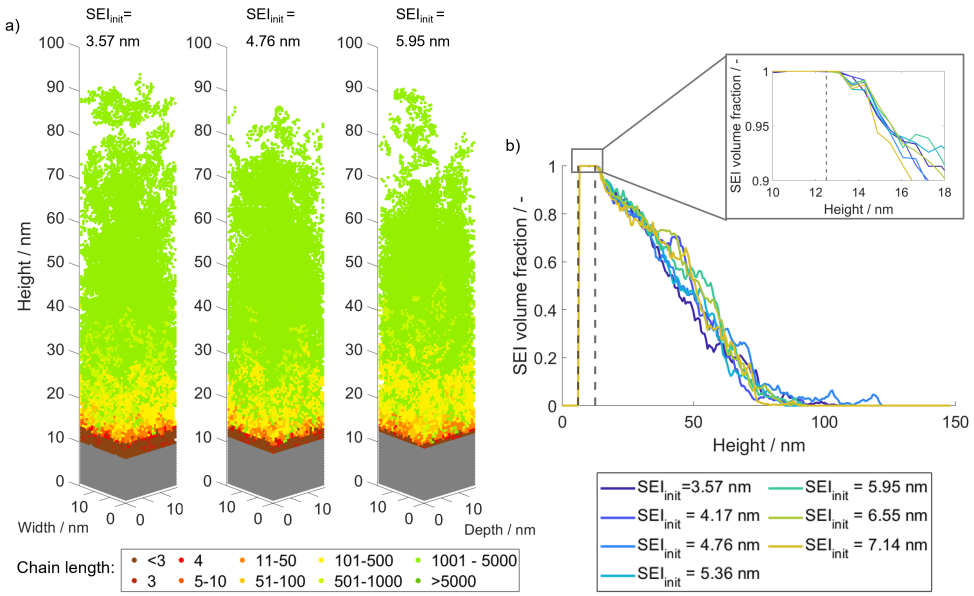

Figure 4.6: Polymeric SEI layer formed after 1 s for varying thicknesses of the initial LiF passivation layer between 3.57 nm and 7.14 nm (cases 3, 5, 6, 7, 8, 9, 10). a) Spatial polymer chain length distribution (cases 3, 6, 8). b) SEI volume fraction over height (cases 3, 5, 6, 7, 8, 9, 10). The dashed line represents the lithium metal surface and the dashed-dotted line the highest completely dense passivation layer.

The previous explanation on spatial polymer chain length distributions is supported by the analysis of the spatial and temporal evolution of radicals and reactive chain ends (summarized as radical species). Figure 4.7 a) displays the number of free and blocked radicals and their sum for an initial passivation layer with a thickness of 3.57 nm. The term 'blocked radicals' describes radical species which are fully embedded inside the polymer layer and hence have a low chance to get in contact and react with fresh monomer species or other radical species. In the presented simulation a radical species is interpreted as blocked, if all neighboring sites are occupied by SEI species. In contrast 'free radicals' refers to radical species which are still capable to further propagate as electrolyte can reach the respective sites.

Most radicals are formed early within the first 0.2 s after the contact with the electrolyte. Subsequently, the total amount of radical species remains almost constant with only minor fluctuations. The reason for this is twofold. First, the increasing surface passivation due to polymer growth limits the number of electron transfer reactions and hence the ongoing electrolyte degradation which would be required for the formation of new radical species. Second, only very few termination reactions occur that could decrease the overall amount of radical species. This is because the number of free radicals steadily decreases over time and slowly approaches zero, while the number of blocked radicals increases and approaches the overall number of radical species. Free

radicals are thus converted into blocked ones, which can no longer reach other radical species and can hence not undergo termination reactions.

The distribution of radicals over height after 1 s in Figure 4.6 b) further reveals that most radical species are located relatively close to the electrode surface, where they were formed through reduction reactions. Only few radical species can be found further away from the electrode. This correlates well with the previous observation that only few long polymer chains grow into the electrolyte phase (cf. Figure 4.6). The major reason for this is that most radicals or reactive chain ends get encapsulated within the polymer phase and hence get shielded from fresh monomer species and from further propagation reactions. Similar effects have been previously reported in studies from polymer-science focusing on surface-induced polymerization [163, 164, 180–184]. They are usually known as confinement effects that shield or hinder initiators [180–182] and reactive chain ends [163, 164, 181] from propagation. Here, to the best of the authors knowledge, this effect is observed for the first time in relation to SEI. This confinement effect leads to an increased number of termination reactions between confined radical species within the polymer layer [180]. In the presented simulations, polymers and thus reactive chain ends cannot move towards each other to recombine. Yet, similarly as the terminated polymers, the hindered chain ends do not participate in further propagation reactions. Thus, the simulation indeed reproduces the shielding effect. Overall, the shielding effect significantly slows down the SEI growth over time (cf. Figure B.13 b)) and hence acts as a major limiting factor of polymer propagation and thus SEI growth.

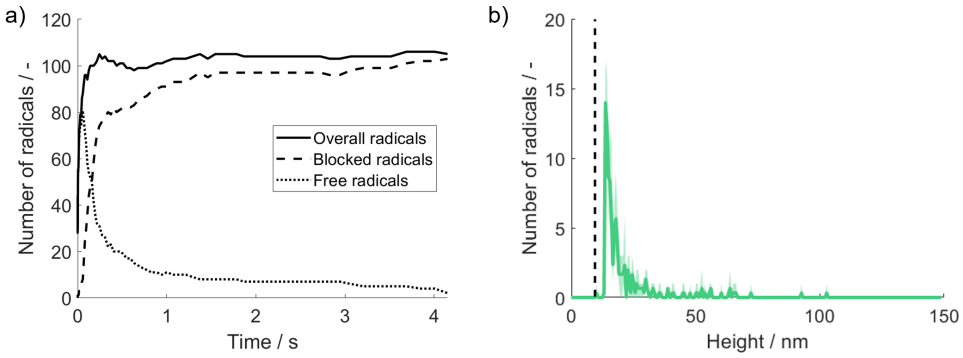

Figure 4.7: Number of radicals and reactive chain ends over time and height for an initial SEI thickness of 3.57 nm (case 3). a) Number of free and blocked radicals, and total number over time. b) Distribution of radicals over the distance from the electrode after 1 s. The dashed line indicates the lithium metal surface. The solid line represents the average of three independent kMC runs with the same parameter set and corresponding shading show the maximum observed deviation within these runs.

Based on this analysis on extended timescales, it can be concluded that VC polymerization primarily occurs on timescales starting from milliseconds. As discussed before, it does not affect the very early inorganic SEI formation. However, with increasing surface passivation, the rate of electron transport and subsequent reduction reactions declines, and after approximately 6 ms, polymer propagation reactions become more likely than reduction reactions (cf. Figure B.13 a)). From there on, the further passivation of the surface is mostly chemically driven via propagation instead of electrochemically driven via electrolyte reduction reactions. The major advantage of this is that the chemical propagation does neither consume further lithium nor electrolyte species and hence prevents ongoing capacity loss in the cell. Furthermore, polymeric layers were reported to have beneficial properties such as a higher flexibility, which might better accommodate the large volume changes of the lithium metal anode in comparison with non-polymeric SEIs [66, 154].

4.3.3 Impact of Electrolyte Composition

After discussing the passivating role of the VC additive on SEI formation in the previous sections, it is subsequently analyzed if and how the SEI formation is sensitive to the electrolyte composition and could thus be optimized by tailoring the concentrations of the electrolyte.

First, the SEI formation up to 1 s in the standard electrolyte consisting of EC, 1.2M $LiPF_6$ and 5 wt.% VC is compared with the binary electrolyte EC:EMC (3:7 by wt.) with 1.2M or 3M $LiPF_6$ and 5 wt.%, respectively. As discussed in Section B.1.6, in this binary electrolyte most EC and VC molecules are expected to be coordinated with at least one Li^+ ion, even at the moderate salt concentration of 1.2M. Therefore, in contrast to the standard electrolyte, the lithiated parameter set (cf. Table 4.2) is applied for the corresponding calculations. Moreover, EMC is assumed to not significantly contribute to SEI formation.

Figure 4.8 illustrates how the chemical composition of the formed SEI changes with the electrolyte composition. As discussed before, in the single-solvent EC electrolyte with 1.2M $LiPF_6$ and 5 wt.% VC, a dense layer of LiEDC with few Li_2CO_3, poly(VC) and poly(EC/VC) species, followed by poly(EC/VC) mixed with fewer poly(VC) and some Li_2CO_3 is observed. In contrast, in the mixed EC:EMC electrolyte with 1.2M $LiPF_6$ and 5 wt.% VC, the formed SEI mostly consists of poly(VC) with very few LiF embedded in the polymer phase close to the surface. Notably, no EC-derived degradation products such as LiEDC, Li_2CO_3 or poly(EC/VC) are observed above the initial passivation layer. This is primarily attributed to the increased ring-opening barrier of lithiated EC species (cf. Table 4.2, I2), which is applied to all EC molecules in the simulations. It should be noted, that in real systems, a fraction of EC may temporarily remain uncoordinated with Li^+, potentially enabling alternative reaction pathways. An increase of salt concentration from 1.2M to 3M $LiPF_6$ does not significantly alter the chemical SEI composition but leads to a

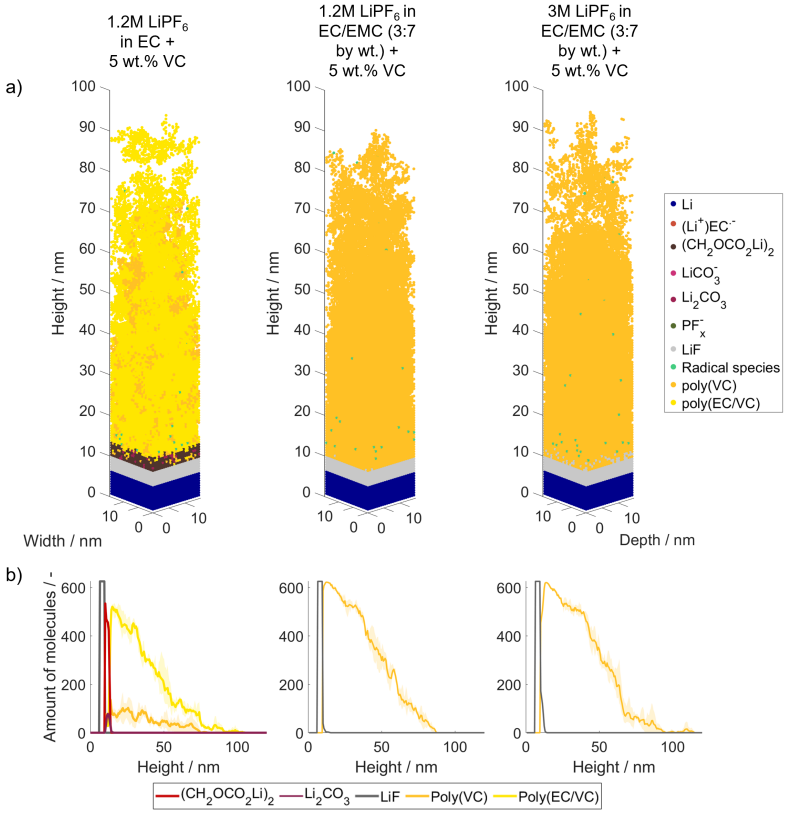

Figure 4.8: Impact of electrolyte composition on SEI formation above the initial LiF passivation layer of 3.57 nm within 1 s. Comparison of EC + 1.2M $LiPF_6$, EC:EMC (3:7 by wt.) + 1.2M $LiPF_6$ and EC:EMC (3:7 by wt.) + 3M $LiPF_6$, each containing 5 wt.% of VC (cases 3, 17, 18). a) Spatial SEI composition and morphology. b) SEI composition over height. Solid lines represent the average of three independent kMC runs with the same parameter set, and corresponding shadings show the maximum observed deviation within these runs.

slightly higher amount of the salt-derived product LiF, which is embedded in the polymer phase close to the electrode surface.

Interestingly, the polymer properties and formation dynamics that have been discussed for the standard electrolyte (cf. Section 4.3.2) are very similar in both mixed electrolytes (cf. Figure B.8 – B.11): Longer polymer chains just start to form above the millisecond timescale, shorter chains may be found closer to the lithium metal surface, and only few longer chains grow into the electrolyte phase. Moreover, the porosity of the polymeric layer increases with height, and the majority of radical species is found near the anode surface. Across all investigated electrolyte systems, a VC-based polymeric layer forms that passivates the surface and suppresses further

electrolyte degradation. These results suggest that VC plays its role as film-forming additive independent of the exact electrolyte composition.

Finally, the impact of varying VC content in the electrolyte is analyzed. The overall structure of the SEI, i.e., a compact inner layer consisting of dimers and Li_2CO_3, followed by an outer polymeric layer, remains qualitatively unaffected by VC concentration. The corresponding three-dimensional SEI composition and morphology can be found in the appendix (cf. Figure B.12). However, a number of quantitative differences in SEI composition and growth behavior are observed: First, as displayed in Table 4.3 the number of EC-derived polymers and oligomers including LiEDC decreases with VC concentration and the volume fraction of poly(VC) within the total polymer phase increases from 5.1% for a VC content of 2.5 wt.% to 16.39% for a VC content of 10 wt.%. Moreover, the VC concentration impacts properties such as the overall number of polymers, the average polymer chain length and the average SEI thickness. These properties are presented as a function of time and concentration in Figure 4.9. For all concentrations, the number of polymers increases steeply within the first milliseconds and stays constant afterwards. Since new polymers are formed only via an electrochemical reduction process (cf. I1 and I2), this clearly shows the quick passivation of the electrode surface within the first few 100 ms. Interestingly, with higher VC concentrations formation of new polymers stops earlier, which indicates a faster surface passivation. This also manifests in the final number of observed polymers after 1 s which is decreasing with VC concentration.

The average polymer chain length after 1 s of contact between lithium and electrolyte shows the opposite trend and increases with VC concentration. This observation can be attributed to the smaller overall number of polymers present in the SEI as well as to the increased propagation rate due to the higher availability of monomers. This higher propagation rate also causes the higher SEI thickness after 1 s. It can be additionally observed that both, the increase in average polymer chain length and SEI thickness, slow down over time for all analyzed concentrations, which is well in line with the previous analysis of the decreasing number of free radical chain ends. Overall, these results show that changing VC-concentration only slightly affects the formation of the spontaneous SEI layer. The faster surface passivation in case of high VC concentration could be an advantage, since it suppresses unwanted side reactions and reduces the consumption of electrolyte species and active lithium. However, the resulting increase in SEI thickness may also contribute to higher resistance, as already previously reported for VC-based SEI layers [66, 154–156] and could thus lead to a worse cell performance.

The presented simulation further allows to estimate the proportion of VC that was consumed within the first second. Assuming a specific electrolyte volume of roughly 8.6 µl cm^{-2} (cf. Section B.1.7) between 0.27% (for 10 wt.% VC) and 0.56% (for 2.5 wt.% VC) of the initial VC molecules have been consumed within the first second (cf. Table 4.3). Hence, only a small fraction of the additive was consumed within the observed timespan. Since a deceleration of polymer

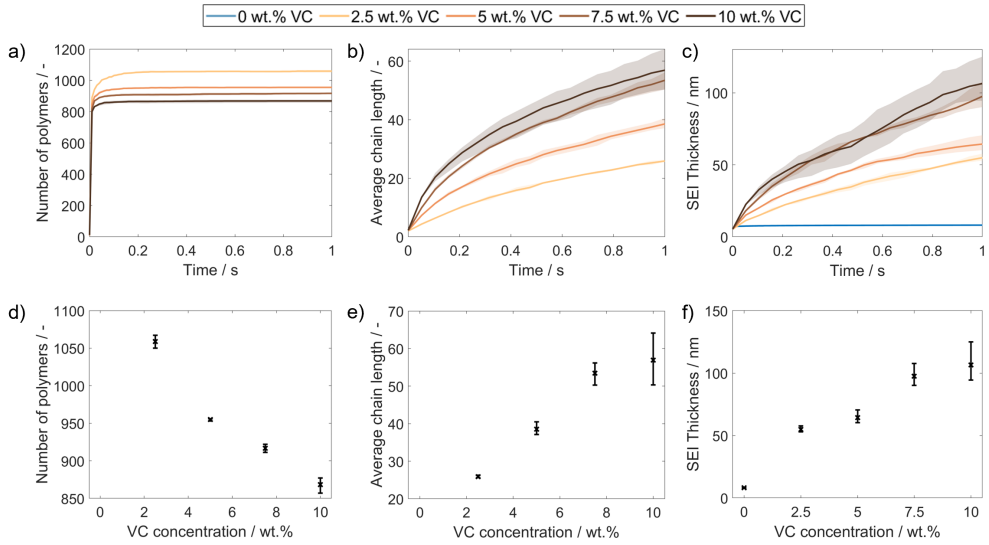

Figure 4.9: Impact of VC concentration on SEI formation and properties (cases 7, 11, 12, 13, 14). a) and d): Number of formed polymers over time and VC concentration. b) and e): Average polymer chain length over time and VC concentration. c) and f): Average SEI thickness over time and VC concentration. Solid lines represent the average of three independent kMC runs with the same parameter set and corresponding shadings show the maximum observed deviation within these runs. Concentration dependent properties are shown after 1 s. Data points indicate the average of three independent kMC runs with the same parameter set and error bars show the maximum observed deviation within these runs.

Table 4.3: Impact of VC concentration on SEI composition and proportion of consumed VC after 1 s. All values represent the average of three independent runs.

VC concentration / wt.%	**2.5**	**5**	**7.5**	**10**
Number of Li_2CO_3 / -	6	28.67	27.67	20
Number of LiEDC / -	768.33	624.33	555	474.33
Volume fraction poly(VC) / %	5.1	10.52	11.09	16.39
Consumed VC after 2 µs / %	0.56	0.39	0.35	0.26

propagation is already observed within this time, it can be expected that a significant proportion of the additive remains in the electrolyte, which aligns well with previous reports for graphite anodes [185, 186]. The remaining additive will then be slowly consumed during cell operation and can quickly repassivate the surface if fresh lithium comes into contact with the electrolyte due to e.g. SEI cracking or dendrite growth. Once all additive has been depleted, this repair mechanism would cease to function, leading to a deteriorating coulombic efficiency and to the end-of-life of the cell. It is therefore anticipated that the VC concentration could play a crucial

role during cycling, particularly towards the end of the cell's life, although other events such as plating and stripping may substantially modify the scenario [130]. A higher VC concentration is expected to contribute to a longer lifespan, as the additive is depleted more slowly. This hypothesis aligns with experimental reports of extended cycle stability at increased VC concentration [155, 187] and may offer a mechanistic explanation for these findings. However, elevated VC concentrations may also lead to an increase in cell internal resistance [66, 156, 176, 187], which could adversely affect rate capability and overall cell performance. This trade-off suggests the existence of an application-dependent optimal VC concentration, which should be subject of future studies.

4.4 Concluding Remarks

In this chapter the previously introduced *ab initio*-informed kMC modeling framework was extended to include polymerization processes and to increase the accessible timescale up to seconds. Based on this the impact of VC on the SEI formation was studied with a molecular resolution and it was elucidated how VC plays its role in enhancing SEI performance and battery lifetime.

It was shown that the addition of VC has only minor impact on the formation of the initial inorganic SEI within the first microsecond. This is attributed to the initial high reactivity of the lithium metal surface which favors electrochemical reactions and the formation of a high number of dimers over the comparatively slow chemical polymerization process. Only at timescales beyond 1 ms longer polymer chains form. Active chain ends get blocked inside the polymer phase, which slows down the SEI growth over time. The presented model further reproduced the experimental finding [66] that inorganic SEI clusters get embedded in the evolving polymeric phase. These SEI formation dynamics were demonstrated to only slightly be impacted by VC-concentration and electrolyte composition. However, mixed electrolytes favor the formation of a polymer layer that solely consists of poly(VC) chains with embedded LiF clusters, while single-solvent EC with 1.2M $LiPF_6$ result in a mixture of poly(VC) and poly(EC/VC) chains with embedded Li_2CO_3 and a dense LiEDC-rich layer close to the anode surface.

Based on the presented findings, the experimentally reported positive impact of VC on SEI and cell performance is attributed to a combination of the following factors: First, apart from the initial radical formation, VC-polymerization is a purely chemical process. Therefore, the passivation layer formation in a VC-containing electrolyte proceeds without continuous consumption of solvent, conductive salt or active lithium. The formed polymeric SEI further prevents ongoing dissolution of electrolyte decomposition products which might further react and cluster in

the electrolyte and eventually result in a porous and poorly passivating SEI. Moreover, the observed polymeric SEIs are expected to be more flexible and hence better accommodating towards the drastic volume changes of the lithium anode during operation [66, 154, 188]. Finally, since only a small fraction of VC is initially consumed, the remaining additive may quickly repair the SEI once new lithium surface becomes exposed to the electrolyte during operation due to e.g. dendrite growth or SEI cracks. In this regard, higher additive concentrations could extend cell lifetime due to slower additive depletion. However, potential increases in internal resistance at elevated concentrations may counteract performance gains, indicating that an optimal balance must be identified in future studies.

The extended model presented in this chapter successfully bridges the gap between isolated *ab initio* reaction mechanisms and their dynamic interplay on technologically relevant timescales in the order of seconds, and provides unique insights into SEI formation dynamics under the influence of the electrolyte additive VC. The governing VC polymerization processes are suggested to only start to occur above the millisecond timescale, whereas atomistic simulation techniques are limited to the nanosecond-scale and below. Once again, this highlights the importance of mesoscale models for understanding the multiscale nature of SEI formation and its interplay with macroscopic properties such as electrolyte composition. Quantitative experimental validation remains challenging due to the molecular resolution and relatively short timescales accessed in the simulations. Nevertheless, the simulation results show qualitative agreement with key experimental trends such as the formation of polymers in VC-containing electrolytes and a layered SEI with more inorganic SEI species close to the electrode and an increasing number of organic species above. To further enhance the predictive power of the presented approach, tailored experiments to specifically validate the predicted SEI structure, e.g. in terms of polymer chain length distribution, would be beneficial.

Overall, the *ab initio*-informed kMC framework developed in Chapter 3 and 4 represents a powerful tool to allow for knowledge-driven SEI design and to pave the way towards the safe application of rechargeable lithium metal batteries with liquid electrolytes. To further enhance its predictive accuracy, the following Chapter 5 focuses on refining the ionic transport in liquid electrolytes by discussing the accurate and efficient consideration of electrostatic interactions within the kMC framework.

5 Comparative Analysis of Electrostatic Interaction Models

5.1 Introduction

In the SEI formation models in the previous chapters, electrostatic interactions between ions were described in a simplified manner, solely considering the repulsion between charge carriers on next-neighbor sites. The same applies to other kMC studies of liquid electrolyte systems reported in literature: Their application ranges from the investigation of local electrochemistry and transport in cathode pores of lithium-O_2 batteries [124], through the mesostructural evolution of carbon/sulfur cathodes [121] and the formation of the solid-electrolyte interphase in different cell-chemistries [30, 129, 131], to ionic transport in high-concentration electrolytes [189]. However, in all of these models, electrostatic interactions are either fully neglected [30, 31, 121, 124, 129, 131] or represented in a highly simplified manner, limited to nearest-neighbor interactions [189].

A major reason for this is the long-range nature of these interactions which causes a substantial number of additional computations and significantly increases the computational cost. However, electrostatic interactions have a significant impact on the ionic transport. Neglecting these interactions can substantially affect the simulation results, particularly with regard to transport limitations and ionic distribution. Moreover, modeling electrostatic interactions is inevitable to describe the formation of an electrical double layer. Hence, its accurate and efficient implementation in kMC simulations of liquid electrolytes is the prerequisite of directly considering electrical double layers in kMC simulations.

The consideration of electrostatic interactions in kMC models is significantly more wide-spread in the field of charge transport in solids. KMC models are e.g. commonly employed to describe the transport of electrons and holes in organic semiconductors [135] for applications such as organic field effect transistors [190, 191], organic photovoltaic [192–196] and organic light-emitting displays [197]. Moreover, they have been applied to study ionic conductivity in oxygen ion conductors [198] as well as ionic transport in solid oxide fuel cells [199–202] and garnet solid electrolytes [203]. Common approaches to compute the potential energy resulting from

electrostatic interactions are cutoff methods [135, 192–195, 198, 202, 204, 205] or the solution of the Poisson equation [190, 191, 196, 197, 206]. Moreover, techniques such as the Ewald sum for periodic systems [135, 193] or the Fast Multipole Method [207, 208] have been applied by a few studies.

Building on this foundation, this comparative study aims to identify efficient and accurate electrostatic interaction models for kMC simulations of liquid electrolyte systems. Furthermore, the respective advantages and limitations of different approaches are discussed to facilitate the choice of the most suitable interaction model depending on the application. Additionally, a special focus is placed on the definition of transport rate equations based on local potential differences as well as on specific characteristics of liquid electrolyte systems. This includes the impact of solvation shells and the comparatively high charge carrier concentration, as well as the definition of accurate boundary conditions. The investigated electrostatic interaction models are examined and discussed with respect to an exemplary EC/EMC + 1M $LiPF_6$ electrolyte system.

To conclude, the most suitable electrostatic interaction model for the previously developed kMC models for SEI formation (cf. Chapters 3 and 4) is selected and integrated into the full SEI model. This step aims to assess the impact of electrostatic interactions on SEI formation, thereby linking the methodological advancements of this study to their practical application in the context of this thesis.

5.2 Methods Development

The method development for considering electrostatic interactions in kMC simulations of liquid electrolyte systems is twofold. First, consistent rate equations need to be established, which allow to calculate the transport rate as a function of the local potential difference caused by electrostatic interactions. This is presented in Section 5.2.1. Second, model approaches need to be developed that enable the efficient and accurate computation of the local coulomb potential based on the ion distribution inside the simulation box. For this purpose, five different approaches are introduced in Section 5.2.2. Subsequently, they are compared based on an example system introduced in Section 5.2.3 and discussed in Section 5.3 of this chapter.

5.2.1 Potential Dependent Rate Equations

The conventional diffusion rate equation is expressed as follows [109]:

$$\Gamma_D = \frac{D}{\Delta L^2} \tag{5.1}$$

It solely depends on the diffusion coefficient D and the edge length of the sites ΔL and is independent of the local potential energy difference (cf. Equation 5.5). Hence, it is not capable of accounting for electrostatic interactions between dissolved ions. In contrast, kMC studies on the charge transport in organic semiconductors frequently account for electrostatic interactions between electrons and holes. For this purpose, the applied rate equations are commonly either based on the Miller-Abraham approach [190, 191, 193, 194, 197, 206, 209, 210] or Marcus theory [194, 204–206, 210–212]. However, both have been derived predominantly for electronic transport and are not directly transferable to the here considered ionic transport in liquid electrolyte systems. Instead, in the following the potential energy dependent transport rate equations developed by Lee et al. [213] are discussed and transferred to electrostatic interactions between ions in liquid electrolytes. The general idea is, that an average effective drift velocity $\mathbf{v}^*$ can be calculated for a given potential difference, which then allows to calculate the average transport rate by migration Γ_M based on Equation 5.2.

$$\Gamma_M = \frac{\mathbf{v}^*}{\Delta L}\hat{\mathbf{e}} \tag{5.2}$$

Here, $\hat{\mathbf{e}}$ represents the unit vector in the direction of one box dimension. The drift velocity can be expressed in terms of the ionic mobility μ_j and the electric field $\mathbf{E}$ and, by applying the Nernst-Einstein equation, in terms of the diffusion coefficient D_j as follows:

$$\mathbf{v}^* = \mu_j \cdot \mathbf{E} = \frac{D_j q_j}{k_B T} \cdot \mathbf{E} \tag{5.3}$$

where q_j is the charge of the moving ion, k_B the Boltzmann constant and T the temperature.

The product of the electric field and the direction vector can be discretized in each direction as shown in Equation 5.4 for the example of the x-direction.

$$\hat{\mathbf{e}}_x \cdot \mathbf{E} = E = \frac{-d\varphi}{dx} \approx -\frac{\Delta\varphi_{lk}}{\Delta L} \tag{5.4}$$

Here, $\Delta\varphi_{lk} = \varphi_k - \varphi_l$ represents the local potential difference between two direct neighbors, which may arise from electrostatic particle interactions or external fields. Based on this local potential difference, the local potential energy difference U_{lk} can be calculated as follows:

$$\Delta U_{lk} = q_j \Delta\varphi_{lk} \tag{5.5}$$

Substituting Equations 5.3, 5.4 and 5.5 into Equation 5.2 yields the following expression for the overall transport rate between two sites l and k as a function of the local potential energy difference U_{lk}:

$$\Gamma_M = -\frac{D_j}{k_B T}\frac{\Delta U_{lk}}{\Delta L^2} \tag{5.6}$$

In the case of kinetic Monte Carlo simulations, distinct forward (along decreasing potential energy difference) and reverse (along increasing potential energy difference) rates need to be defined. Their sum must equal the overall transport rate (cf. Equation 5.7). Moreover, the equilibrium between both rates must follow Equation 5.8 in order to ensure microscopic reversibility [213, 214].

$$\text{Condition 1:} \quad \Gamma_M^{\text{forw}} - \Gamma_M^{\text{rev}} = \Gamma_M \tag{5.7}$$

$$\text{Condition 2:} \quad \frac{\Gamma_M^{\text{forw}}}{\Gamma_M^{\text{rev}}} = \exp\left(-\frac{\Delta U_{lk}}{k_B T}\right) \tag{5.8}$$

Based on these conditions the following expressions for the forward transport rate Γ_M^{forw} and reverse transport rate Γ_M^{rev} can be derived [213]:

$$\Gamma_M^{\text{forw}} = \Gamma_M \frac{\exp\left(-\frac{\Delta U_{lk}}{k_B T}\right)}{\exp\left(-\frac{\Delta U_{lk}}{k_B T}\right) - 1} \tag{5.9}$$

$$\Gamma_M^{\text{rev}} = \Gamma_M \frac{1}{\exp\left(-\frac{\Delta U_{lk}}{k_B T}\right) - 1} \tag{5.10}$$

Figure 5.1 shows both rates as a function of the local potential energy difference for an exemplary diffusion coefficient of 1.5×10^{-10} m^2 s^{-1}, which corresponds to the transport of Li^+ ions in EC/EMC 3:7 by wt. [215] and an edge length ΔL of 0.8 nm, representing the solvation shell (cf. Section 5.2.4.3). For comparison, the corresponding diffusion rate Γ_D, which is independent of the potential energy and based on Equation 5.1 and the same parameters is depicted. The figure illustrates clearly that the forward and reverse transport rates diverge for increasing potential energy differences, but converge toward the diffusion rate as the potential energy difference decreases. Hence, they approach Brownian dynamics for small energy differences:

$$\lim_{\Delta U_{lk} \to 0} \Gamma_M^{\text{forw}} = \Gamma_D = \lim_{\Delta U_{lk} \to 0} \Gamma_M^{\text{rev}} \tag{5.11}$$

Furthermore, it is shown that numerical instabilities occur for very small potential energy differences on the order of 10^{-35} J and below. Hence, for energy differences below this threshold, the forward and reverse transport rates are set to the diffusion rate according to 5.1.

All derived rate equations account for the total transport along a single dimension of the cubic kMC box. In each direction they may move towards the face, edge and corner neighbors. The total rate is therefore distributed among nine neighboring sites in each direction leading to a distance-depending scaling factor of $\frac{3}{13}$ for direct, $\frac{3}{26}$ for diagonal and $\frac{1}{13}$ for corner neighbors [132].

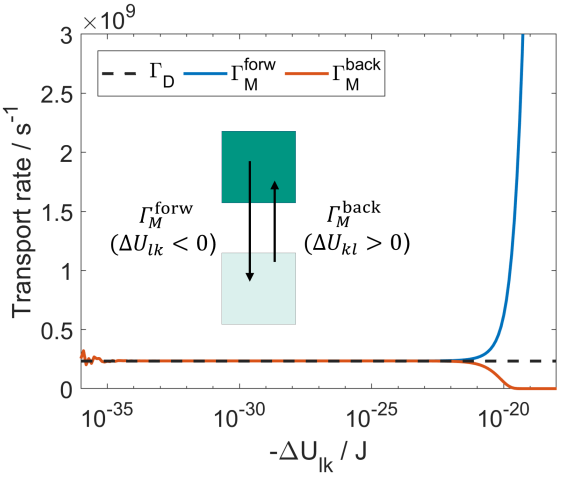

Figure 5.1: Forward and reverse transport rates as a function of the local potential energy difference and in comparison with the potential independent diffusion rate.

5.2.2 Definition of Electrostatic Interaction Models

After the derivation of potential energy dependent transport rates, the next step is to calculate the local potential energy based on coulomb interactions between charged particles in the electrolyte solution. According to Equation 5.5 this energy difference directly depends on the local potential difference $\Delta\varphi_{lk}$ between two neighboring sites l and k. In the following, different approaches to calculate the local potential based on coulomb interactions are introduced. These approaches are subsequently compared and discussed in Section 5.3.

In general, the coulomb potential φ_m caused by a point charge m can be calculated based on the following equation:

$$\varphi_m(r) = \frac{1}{4\pi\varepsilon_0\varepsilon_r} \cdot \frac{q_m}{r} \tag{5.12}$$

where ε_0 represents the permittivity of the vacuum, ε_r the dielectric constant of the solvent, q_m the charge of the considered point charge and r the distance to the considered point charge.

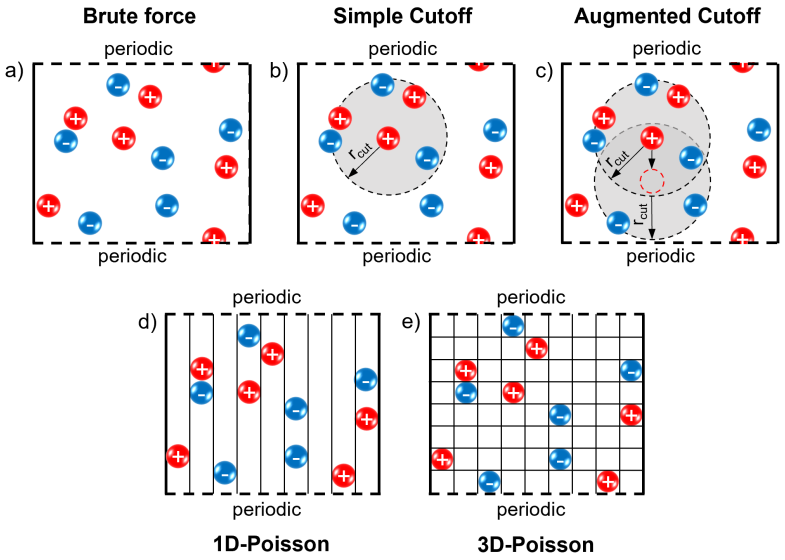

Figure 5.2: Schematic illustration and comparison of electrostatic interaction models. a) Brute force. b) Simple Cutoff. c) Augmented Cutoff. d) 1D-Poisson. e) 3D-Poisson.

Since the superposition principle applies to Coulomb interactions, the most straightforward approach is to sum up the potential contribution of all charge carriers m for each individual lattice site according to Equation 5.13.

$$\varphi_{\text{total}}(\mathbf{r}) = \sum_{m=1}^{n_{\text{cc}}} \frac{1}{4\pi\varepsilon_0\varepsilon_r} \cdot \frac{q_m}{|\mathbf{r} - \mathbf{r}_m|} \tag{5.13}$$

In this approach the contribution of each charge carrier within the simulation box or its periodic image is considered once based on the shortest distance. All other periodic images are neglected. Moreover, the self-contribution of the charge carrier present at the site itself is excluded to prevent divergence due to self-interaction (cf. Section 5.2.4.1). The concept of this modeling approach is visualized in Figure 5.2 a). It will hereafter be referred to as 'Brute force' approach. The

computational cost of this approach increases rapidly with the size of the kMC box and the number of charged species, making it very computationally expensive for larger systems.

To save computational time, it is therefore common in literature to apply a cutoff radius r_{cut} [135, 192–195, 198, 202, 204, 205]. As shown in Figure 5.2 b), in this case, only charged species which are present within the predefined cutoff radius $|\mathbf{r} - \mathbf{r}_m| < r_{\text{cut}}$ are considered for the local potential calculation. This reduces the computational cost, but neglects the long-range electrostatic interactions and hence also reduces the accuracy of the result. Typical cutoff radii vary between 1 - 1.5 nm in molecular dynamic simulations [193] and between 10 - 16 nm in kMC simulations of charge transport in organic semiconductors, where they are usually chosen to be larger than twice the Debye length [135, 193–195, 204]. Due to the higher ionic strength of the concentrated liquid electrolytes investigated here, the Debye length is only 0.135 nm. The cutoff radius can hence be chosen smaller than in the solid-state kMC models. To ensure that it remains significantly larger than the size of the single lattice sites it is set to 4.5 nm by default for this study. This approach is in the following referred to as 'Simple Cutoff'.

More recently, Pippig et al. [135] introduced a variation of this approach called 'Augmented Cutoff'. In contrast to the Simple Cutoff approach, they define a common cutoff for the origin and destination site. This way the potential difference between origin and destination site is evaluated based on the same charge carriers, which significantly improves the accuracy of the calculated potential differences. For this study, this common cutoff is defined as the union of the cutoffs around the origin site l and the destination site k (cf. Figure 5.2 c)). To ensure good comparability with the Simple Cutoff, the cutoff radius around each individual site is chosen such that the union of both cutoff volumes encloses the same volume as in the Simple Cutoff case. This leads to an individual cutoff radius of 4.31 nm. It should be noted, that in this approach the calculated potential of the sites depend on the direction of move. Hence, for each lattice site on the cubic lattice used in this study, local potentials must be calculated for all 26 neighboring sites accessible via hopping.

Another approach that, in contrast to the Cutoff approaches, allows to consider long-range forces is to directly solve the Poisson equation:

$$\Delta\varphi(\mathbf{r}) = -\frac{\rho(\mathbf{r})}{\varepsilon_0\varepsilon_r} \tag{5.14}$$

In literature numerous kMC studies have employed one-dimensional discretizations of the Poisson equation or similar planar approximations following the work of Pornprasertsuk et al. [200]. These approaches have been applied primarily in the context of solid-oxide fuel cells [199–201] and organic semiconductors [196, 216]. The 1D-Poisson approach is particularly effective when the charge gradient is expected predominantly along the discretized dimension. The general modeling idea is depicted in Figure 5.2 d). Its implementation is based on the approach of

Pornprasertsuk et al. [200]. First, the areal charge density per layer ρ_p^A is calculated following Equation 5.15.

$$\rho_p^A = \frac{1}{n_x \cdot n_y \cdot \Delta L^2} \sum_{k}^{n_x \cdot n_y} q_k \tag{5.15}$$

Based on this, the electric field E_p induced by each layer p can be calculated following Gauss's law:

$$E_p = \frac{\rho_p^A}{2\varepsilon_0 \varepsilon_r} \tag{5.16}$$

Eventually, the local potential of each layer is calculated by the summation of the contributions of the individual electric fields of each layer:

$$\varphi_p(z) = \sum_{i=1}^{n_{\text{layers}}} -E_i \cdot |z - z_i| \tag{5.17}$$

Few studies in literature also apply the solution of 2D-Poisson approaches [190, 191, 206]. However, in the here investigated 3D-system the x- and y- direction equally contribute to the local potential. Hence, a 3D-discretization is more appropriate, and the last considered approach is the solution of the 3D-Poisson equation (cf. Equation 5.18) by the finite difference method.

$$\frac{\partial^2 \varphi}{\partial x^2} + \frac{\partial^2 \varphi}{\partial y^2} + \frac{\partial^2 \varphi}{\partial z^2} = -\frac{\rho^V(x,y,z)}{\varepsilon_0 \varepsilon_r} \tag{5.18}$$

This approach is illustrated in a simplified manner in two dimensions in Figure 5.2 e). To the best of the authors knowledge, the 3D-discretized Poisson equation is being coupled with kMC simulations for the first time in this work. The local volumetric charge density ρ_l^V is calculated individually for each lattice site by Equation 5.19.

$$\rho_l^V = \frac{q_l}{\Delta L^3} \tag{5.19}$$

The corresponding boundary conditions are set to periodic boundaries in x- and y-direction. In order to represent a connection to an electroneutral bulk phase at both boundaries in z-direction, two different sets of boundary conditions are implemented and tested. The first set of boundary conditions (BC1) sets the potential at $z = 0$, i.e. at the lower boundary, to 0 V ($\varphi(x,y,0) = 0$ V) and the electric field on the upper boundary to 0 V m^{-1} ($\varphi(x,y,n_z+1) = \varphi(x,y,n_z)$). The second set of boundary conditions (BC2) follows the publications of Koster et al. [216] and Meng et al. [196] and defines $\varphi(x,y,n_z+1) = \Delta\varphi_{ext}$ and $\varphi(x,y,0) = 0$ V with the external potential difference $\Delta\varphi_{ext}$ set to 0 V.

In literature further approaches to treat electrostatic interactions in kMC such as the Ewald sum [135, 193] or the domain-based Fast Multipole Method [208, 211] have been reported. However, due to the expected high computational cost of the Ewald sum [135, 193, 211] and the computational complexity of the Fast Multipole Method they are not part of this comparative study.

5.2.3 Example System and Performed Simulations

To test and compare the previously introduced approaches, they are applied to a physical model system within the scope of this study. This model system is the common battery electrolyte EC/EMC 3:7 by wt. with dissolved $LiPF_6$ which has already been studied in Chapter 3. Here, only the dissociated salt ions are treated explicitly in the kMC model and no electrode surface and reaction processes are considered. Transport properties such as the diffusion coefficients of PF_6^- and Li^+ and the dielectric constant of the studied EC/EMC mixture are parameterized based on literature values (cf. Table 5.1). The MD-derived diffusion coefficient is adjusted as $D_{\mathrm{KMC}} = \frac{D_{\mathrm{MD}}}{1-\theta}$, where $\theta = \frac{n_{\mathrm{cc,init}}}{n_{\mathrm{total}}}$ represents the fraction of occupied sites in the kMC simulation box. This correction accounts for the reduction of molecular transport caused by physical blocking from other molecules, which is already accounted for in the MD derived diffusion coefficient. Thus, it prevents underestimation of transport rates in the applied kMC model, where transport into occupied sites is prohibited. Additionally, the degree of salt dissociation α is newly introduced in this chapter and set to 50 %, which falls within the range of values reported in the literature [217, 218]. The dimensions of the 3-dimensional box are set to $15 \times 15 \times 25$ cubic sites with an edge length of 0.8 nm, respectively and the boundary conditions of the simulation box are set to be periodic in the x- and y-directions.

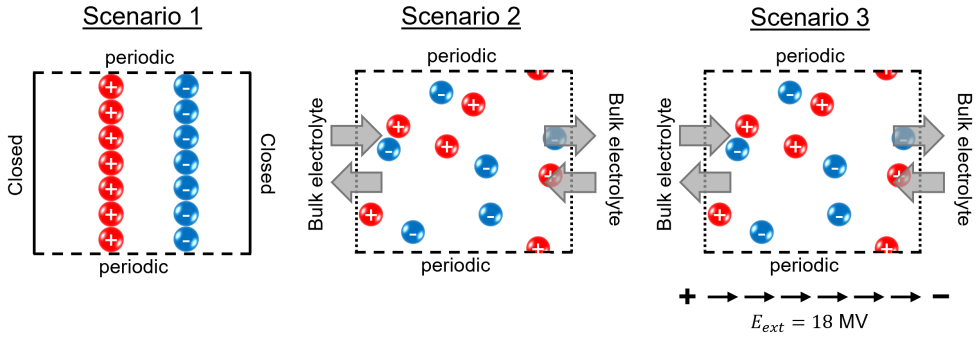

Figure 5.3: Schematic illustration of the applied test scenarios.

Table 5.1: Summary of physical parameters of the $LiPF_6$ in EC/EMC 3:7 by wt. model system.

Parameter	Description	Value	Unit
c_{salt}	Salt concentration	1 [a]	M
$D_{PF_6^-,\,MD}$	Diffusion coefficient PF_6^-	1.8 x 10^{-10} [b]	$m^2\ s^{-1}$
$D_{Li^+,\,MD}$	Diffusion coefficient Li^+	1.5 x 10^{-10} [b]	$m^2\ s^{-1}$
$\varepsilon_{EC/EMC}$	Relative permittivity	18.5 [c]	[-]
α	Degree of dissociation	50 [d]	%
n_x	No. of sites in x-direction	15 [a]	[-]
n_y	No. of sites in y-direction	15 [a]	[-]
n_z	No. of sites in z-direction	25 [a]	[-]
ΔL	Distance of lattice sites	0.8 [a]	nm
T	Temperature	300 [a]	K

[a] Chosen
[b] Parameter value adopted from Ringsby et al. [215]
[c] Parameter value adopted from Hall et al. [219]
[d] Chosen in the range of reported literature values [217, 218]

To evaluate the feasibility, accuracy and computational effort of the various methods, they are compared as follows: Three different test scenarios are defined and tested for each of the introduced electrostatic interaction models. An overview of the scenarios is provided in Figure 5.3. In scenario 1, two parallel layers extending in the x- and y-directions are completely filled with either positively (for $z = 9.2$ nm) or negatively (for $z = 14$ nm) charged ions, resulting in the placement of 225 positive and 225 negative charge carriers, respectively. In this case, closed boundaries are applied in z-direction preventing ions to enter or leave the simulation box. This initialization corresponds to the charge distribution in a parallel-plate capacitor and is used to qualitatively test and demonstrate the capability of the investigated models to account for electrostatic interactions and ensure local electroneutrality. In scenario 2, the impact of the different models on a homogeneous electrolyte system with a salt concentration of 1M is tested. The dissociated ionic species are initially randomly distributed in the simulation box. Moreover, open boundary conditions are applied in z-direction, connecting the simulation domain to an electrically neutral bulk phase on both sides. This test case is used to quantify the effects of the different electrostatic interaction models in a realistic electrolyte system and to evaluate their associated computational cost. Eventually, in scenario 3 an external field E_{ext} of 18 MV m^{-1} is applied in z-direction to the homogeneous electrolyte system, to verify the predictive capability of the models for ionic mobility. The external field is chosen such that the resulting potential differences are of a similar magnitude to those induced by Coulomb interactions (cf. Section C.1.1). For comparison, all defined test cases are also calculated using the conventional kMC transport rate

equation which does not account for electrostatic interactions (cf. Equation 5.1). This approach is in the following referred to as 'Diffusion only' case.

5.2.4 Strategies for Addressing Systematic Modeling Errors

A direct implementation of the electrostatic interaction models and potential energy dependent transport rate as introduced in Sections 5.2.1 and 5.2.2 might lead to unexpected and nonphysical results. This arises from several numerical challenges that require careful consideration. Specifically, these include self-interaction errors, the choice of kMC boundary conditions and the treatment of the solvation shell. This section discusses each of these aspects in detail along with appropriate strategies to mitigate their impact.

5.2.4.1 Handling of the Self-Interaction Error

The self-interaction error refers to the artificial influence of the electric field generated by a charge carrier on its own transport rate. Both, the potential at the origin and destination site, are directly affected by the electric field of the moving particle itself and change due to the transport process. This leads to nonphysical effects, where the moving ion interacts with itself, resulting in an overestimation of the transport rates.

This error has been previously addressed by Li et al. [191] in the context of organic semiconductors. They reported that the error increases with the dimensionality of the discretization and observed deviations of up to 400 % in their modeled current compared to the exact solution. Furthermore, they suggested efficient strategies to prevent this systematic error. In the following, their so-called 'Exclusion method' is applied in which the potential contribution of the ion moving from site l to site k is removed from the calculation of the local potential energy difference ΔU_{lk} following Equation 5.20.

$$\Delta U_{lk} = q \cdot [(\varphi_k - \varphi_k^{(l)}) - (\varphi_l - \varphi_l^{(l)})] \tag{5.20}$$

In this notation φ_l and φ_k represent the overall electric potentials at sites l and k, respectively and the terms $\varphi_l^{(l)}$ and $\varphi_k^{(l)}$ refer to the potential contribution of the ion located at site l on the respective overall potential. These terms are precalculated and depend on the chosen electrostatic interaction model. In case of all Coulomb-based approaches (Brute force, Simple Cutoff and Augmented Cutoff), the correction factor $\varphi_k^{(l)}$ is calculated based on Equation 5.12 with $r = \{\Delta L, \sqrt{2}\Delta L, \sqrt{3}\Delta L\}$ depending on the distance between the neighboring sites (face, edge, corner). The self-contribution of charges to the local potential at the same site has already been excluded in the definition of the Brute force and Cutoff approaches (cf. Section 5.2.2). Hence,

$\varphi_l^{(l)}$ is set to 0 for these approaches. For the 1D-Poisson approach, the electric field caused by a single charge E_{sc} is calculated according to Equations 5.15 and 5.16. Based on this, the correction factor for site k is computed as $\varphi_k^{(l)} = -E_{\mathrm{sc}} \cdot \Delta L$. In contrast, the self-contribution to the potential on site l is automatically excluded, since the distance $|z - z_i|$ is zero. Hence, $\varphi_l^{(l)}$ is set to 0 for this approach, too. In case of the 3D-Poisson approach, Equation 5.18 is initially solved for all possible configurations of only one point charge in the entire system and for the same boundary conditions. The resulting correction factors are applied in the computation of the local potential energy difference following Equation 5.20 during runtime.

5.2.4.2 KMC Boundary Conditions at the Bulk Electrolyte Interface

Where required, boundary conditions for the potential calculation of the electrostatic interaction models have been defined in Section 5.2.2. Additionally, in the case of open boundary conditions in z-direction, transport processes from and to the electroneutral bulk electrolyte phase must be considered. For simplicity, these processes are in the following referred to "disappear" (towards the bulk-phase) and "appear" (towards the simulation domain). The most straightforward approach to implement these boundary transport processes is to define a potential for each bulk phase and to calculate the boundary transport processes according to Equations 5.9 and 5.10 based on the local potential energy difference. In order to consider an electroneutral bulk phase, a simplistic approach would be to define the bulk potential as the average potential of the first or last kMC-layer, respectively (cf. Equations 5.21 and 5.22). This results in no potential difference between the bulk phase and the boundary layer on average and thus leads to purely diffusive transport across the boundary.

$$\varphi(x,y,0) = \frac{\sum_{i_x=1}^{n_x}\sum_{i_y=1}^{n_y}\varphi(i_x,i_y,0)}{n_x n_y} \tag{5.21}$$

$$\varphi(x,y,n_z+1) = \frac{\sum_{i_x=1}^{n_x}\sum_{i_y=1}^{n_y}\varphi(i_x,i_y,n_z)}{n_x n_y} \tag{5.22}$$

The quality of these kMC boundary conditions was tested for all electrostatic interaction models as well as for the Diffusion only case for a homogeneous electrolyte with randomly distributed charges, which is connected to an electroneutral bulk phase through open boundary conditions in the z-direction (test scenario 2, cf. Section 5.2.3). In this scenario, proper boundary conditions should ensure that the overall ion concentration remains consistent with the bulk concentration over time. Therefore, Figure 5.4 a) compares the ion concentration as a function of the number of iterations for all investigated models. This representation is more consistent than physical time in this context due to varying time step sizes across the different approaches. For reference, the corresponding data plotted against physical time is provided in Figure C.2 in the appendix.

The results clearly show that the ion concentration significantly increases over the number of iterations for all approaches except for the 1D-Poisson model and the Diffusion only case. This indicates that the boundary conditions for the 3D-Poisson approaches, the Cutoff approaches and the Brute force method are poorly defined.

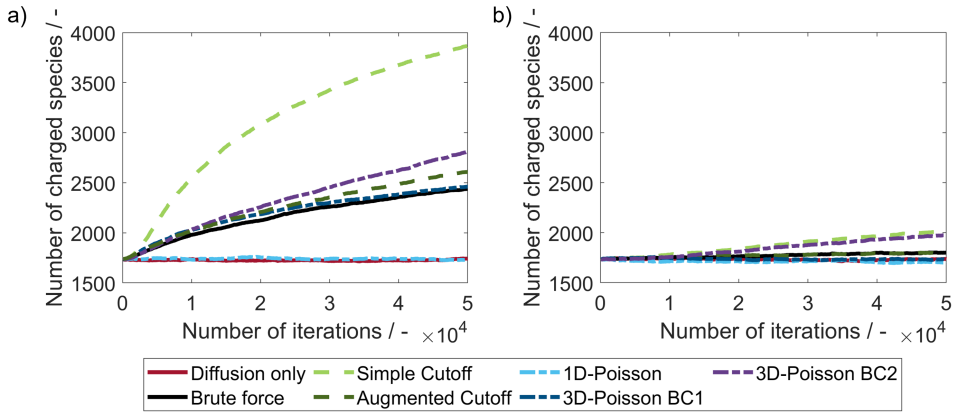

Figure 5.4: Comparison of the impact of different boundary conditions on the number of charged particles in the simulation domain over 50,000 time steps. a) Simplistic implementation without correction for lateral interactions. b) Advanced implementation with correction for lateral interactions.

The major reason for this is, that the ionic transport in these 3D approaches is decelerated by lateral electrostatic interactions, that are not considered in the bulk phase. Therefore, on average the appear process is faster than the disappear process. To mitigate this artifact, the boundary conditions of these approaches must include the average electrostatic interactions within the simulation box. These average interactions can be effectively quantified through the resulting average local energy differences. Based on this idea, an alternative advanced approach for the boundary condition, i.e. modeling the appear and disappear processes, can be defined as follows: After a predefined number of kMC iterations which is here set to 100, the direction-dependent appear and disappear rates are updated to match the latest average transport rates within the simulation box. For this purpose, in a first step, the local coulomb potential energy differences $\Delta U_{lk}^{\mathrm{clb}}$ between all sites covered with ions and their free neighboring sites are computed following Equation 5.20. Next, all direction-dependent overall potential energy differences are computed as the sum of Coulomb and external potential energy differences caused by e.g. external electric fields:

$$\Delta U_{lk} = \Delta U_{lk}^{\mathrm{clb}} \pm q_l \cdot E_{\mathrm{ext}} \cdot \Delta L \tag{5.23}$$

Based on all local potential energy differences, the average positive ($\langle \Delta U \rangle_+^{j,\mathrm{dir},z^\pm}$) and negative ($\langle \Delta U \rangle_-^{j,\mathrm{dir},z^\pm}$) potential energy differences are calculated separately for each ionic species j, transport direction $z^\pm$ (along or opposite to z-direction) and neighbor-type dir (face, edge, corner) according to Equations 5.24 and 5.25.

$$\langle \Delta U \rangle_+^{j,\mathrm{dir},z^\pm} = \frac{1}{n_+} \sum_{\Delta U_{lk}^{j,\mathrm{dir},z^\pm} > 0} \Delta U_{lk}^{j,\mathrm{dir},z^\pm} \tag{5.24}$$

$$\langle \Delta U \rangle_-^{j,\mathrm{dir},z^\pm} = \frac{1}{n_-} \sum_{\Delta U_{lk}^{j,\mathrm{dir},z^\pm} < 0} \Delta U_{lk}^{j,\mathrm{dir},z^\pm} \tag{5.25}$$

Here, n_+ and n_- represent the number of positive and negative potential energy differences, respectively. The resulting average positive and negative potential energy differences are used to calculate the corresponding average forward and reverse transport rates, as described by Equations 5.9 and 5.10 for each considered ionic species, direction and neighbor-type. The respective overall average transport rate is calculated by a weighted average of the corresponding average forward and reverse rates:

$$\Gamma_M^{j,\mathrm{dir},z^\pm} = \frac{n_+ \cdot \langle \Gamma_M^{\mathrm{rev}} \rangle^{j,\mathrm{dir},z^\pm} + n_- \cdot \langle \Gamma_M^{\mathrm{forw}} \rangle^{j,\mathrm{dir},z^\pm}}{n_+ + n_-} \tag{5.26}$$

Based on this, the average transport rates of each ionic species in the positive (z^+) and negative (z^-) z-directions are calculated by summing all relevant transport contributions in the respective direction. The contributions are weighted by the respective number of neighbors in z-direction (1 face neighbor, 4 edge neighbors, 4 corner neighbors).

$$\Gamma_M^{j,z^\pm} = \Gamma_M^{j,\mathrm{face},z^\pm} + 4 \cdot \Gamma_M^{j,\mathrm{edge},z^\pm} + 4 \cdot \Gamma_M^{j,\mathrm{corner},z^\pm} \tag{5.27}$$

Depending on the direction of motion across the boundary, the appear rate on an empty boundary site is subsequently defined as $\Gamma_{\mathrm{ap}}^j = \Gamma_M^{j,z^\pm} \cdot N_A \cdot \Delta L^3 \cdot c_j$ and the total disappear rate of an ion on a boundary site is defined as $\Gamma_{\mathrm{dis}}^j = p_0 \cdot \Gamma_M^{j,z^\pm}$ with $p_0 = 1 - N_A \cdot \Delta L^3 \cdot \sum_j c_j$. This accounts for the probability of coverage of the bulk site depending on the bulk concentrations c_j. In the appear process this is explicitly accounted for by the ions in the simulation box.

Figure 5.4 b) demonstrates that the application of these boundary conditions for the Brute force, Cutoff and 3D-Poisson approaches effectively mitigates the artifact. The advanced boundary conditions are especially well defined for the Brute force, Augmented Cutoff and 3D-Poisson BC1 approaches, while there is still a slight increase of charge carriers in the other approaches. This could potentially be improved by further tuning the boundary conditions, for example

through more frequent updates of the boundary rates. For this study the kMC appear and disappear rates are defined following the advanced approach outlined in this section.

5.2.4.3 Consideration of Solvation Effects

The third important aspect that needs to be accounted for to ensure accurate results is the shielding of charges by the solvation shell. In a liquid electrolyte system, this refers to the layer of solvent molecules that surrounds ions and stabilizes them. It further shields ions of opposite charge from each other, keeps them at a certain distance and therefore prevents frequent recombination and strong coulombic interactions. Since the solvation shell is not explicitly modeled in kMC, it has to be implicitly accounted for to prevent overestimation of the electrostatic interactions. This is done by setting the lattice site distance ΔL to the average distance of the considered ionic species in the investigated electrolyte chemistry. In the case of $LiPF_6$ in 3:7 EC/EMC, this distance was reported to fluctuate around 0.8 nm [220]. Hence, ΔL is set to 0.8 nm in the following analysis. The strong effect of this parameter on the simulation results has been revealed at the example of the 3D-Poisson BC2 approach. The results can be found in Figure C.1 in the appendix.

5.3 Assessment of Electrostatic Interaction Models

This section presents a qualitative and quantitative comparison of the previously introduced electrostatic interaction models. The analysis focuses on model accuracy without (cf. Section 5.3.1) and with (cf. Section 5.3.2) the influence of external fields, as well as on computational cost (cf. Section 5.3.3). In conclusion, the advantages and limitations of each method are discussed, and the most suitable approach for implementation into the previously discussed SEI models presented in Chapter 3 and Chapter 4 of this thesis is identified (cf Section 5.3.4).

5.3.1 Model Accuracy without External Fields

To highlight the similarities and differences between the modeling approaches, Figure 5.5 compares their resulting electrostatic potentials under the predefined initial conditions (cf. Section 5.2.3). The potential is plotted along the z-dimension of the kMC simulation box, with each data point representing the average potential within a z-layer. The configuration in Figure 5.5 a) corresponds to scenario 1 (cf. Section 5.2.3), featuring two oppositely charged planes in a parallel-plate capacitor setup.

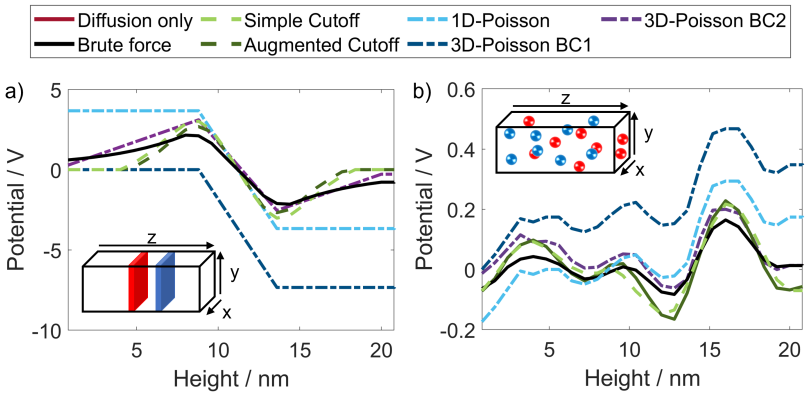

Figure 5.5: Comparison of average electrostatic potential per layer in z-direction (x-y plane) for two different initial charge distributions observed for the different electrostatic interaction models. a) Two parallel and oppositely charged planes (test scenario 1). b) Random distribution of ions (test scenario 2).

The 1D-Poisson and 3D-Poisson BC1 models yield a potential profile that matches the analytical solution for an ideal parallel-plate capacitor, with a linear potential drop between the charged planes and a constant potential outside. The two profiles of the 1D-Poisson and 3D-Poisson BC1 approaches are vertically offset due to the definition of 0 V at the lower boundary in the 3D-Poisson approach. However, the potential difference across the z-direction is identical, which results in the same accelerated ion transport between the planes and purely diffusive behavior outside.

The Simple Cutoff, Augmented Cutoff, Brute force and 3D-Poisson BC2 methods as well show a parallel-plate capacitor-like drop with reduced magnitude in the interplane region. However, towards the system boundaries they predict a potential decay towards 0 V, leading to overall potential profiles with pronounced extrema at the locations of the charged planes. In the case of the Brute force and the Cutoff approaches, this behavior results from the localized point-charge representation and the neglect of periodic images in x- and y-direction, causing the field strength to decrease with distance. For the cutoff-based methods, the potential reaches 0 V beyond the cutoff radius, as expected. In case of the 3D-Poisson BC2 method the potential is forced back to 0 V at the boundaries due to the applied boundary conditions. This effectively corresponds to an opposed electric field in the bulk phase that neutralizes the potential.

Overall, only the 1D-Poisson and the 3D-Poisson BC1 approaches reproduce the potential distribution of a parallel-plate capacitor in a physically consistent manner, while the remaining models exhibit artifacts under this configuration. However, since this scenario represents an extreme case that is unlikely to occur in a realistic electrolyte system, the other models may still provide sufficient accuracy for practical applications.

In scenario 2 (cf. Section 5.2.3), which is presented in Figure 5.5 b), the positively and negatively charged ions are randomly distributed throughout the box, representing a homogeneous electrolyte system. Overall, the potential profiles for all approaches have a similar shape. The profiles for the 1D-Poisson and 3D-Poisson BC1 models are again identical except for an offset: Both show a potential increase with height, which is a result of the specific random charge distribution and is not observed in the output of the other approaches. Moreover, it can be observed that the potential curves of the Brute force and the 3D-Poisson BC2 method are flatter than those of both Cutoff approaches. The resulting larger potential energy differences in case of the Cutoff approaches cause larger ionic transport rates and hence a comparatively strong impact of electrostatic interactions.

The effect of the different potential calculations on the distribution of charge carriers after 40 ns is presented in Figure 5.6. In order to qualitatively evaluate the ability of the different approaches to achieve local electroneutrality, all simulations were initialized with two oppositely charged planes, analogous to a parallel-plate capacitor, following test scenario 1 as described in Section 5.2.3. An additional Diffusion only case without electrostatic interactions is considered to represent purely diffusive behavior for comparison. The corresponding results are presented in Figure 5.6 a) and d). The model reproduces the expected diffusive behavior, with charge carriers spreading uniformly in all directions without compensating for the charge difference. Hence, after 40 ns there are still two distinct peaks observable at the initial positions of the charged planes (cf. Figure 5.6 d)), and local electroneutrality is not ensured. In contrast, all implemented electrostatic interaction models lead to a thorough mixing of the charged species after 40 ns. Instead of two separate concentration peaks for positive and negative ions, only one peak in the middle between the initially charged layers has formed. Moreover, the number of both charge carriers over height is identical with only small statistical deviations. Overall, this shows that all implemented electrostatic interaction models succeed in ensuring local electroneutrality over the height of the box within the first 40 ns.

However, there are some important differences to note: First, spreading of the charge carriers along the height varies depending on the applied electrostatic interaction model. This indicates varying ionic mobility in z-dimension, which is further evaluated in Section 5.3.2. In the tested approaches, the 1D-Poisson shows the broadest charge distribution, which is similar to the Diffusion only case. This can be explained by the neglected electrostatic interactions in the x- and y-directions. Hence, once electroneutrality in z-direction is reached, the ionic transport resembles diffusive behavior since it is not affected by local attractive or repulsive forces. The Augmented Cutoff approach exhibits a similarly broad distribution, despite accounting for electrostatic interaction in the x- and y-directions. This behavior results from the chosen cutoff radius, which is smaller than the distance between the charged layers. As a consequence, the charge carriers initially distribute uniformly and quickly in all directions without an impact of

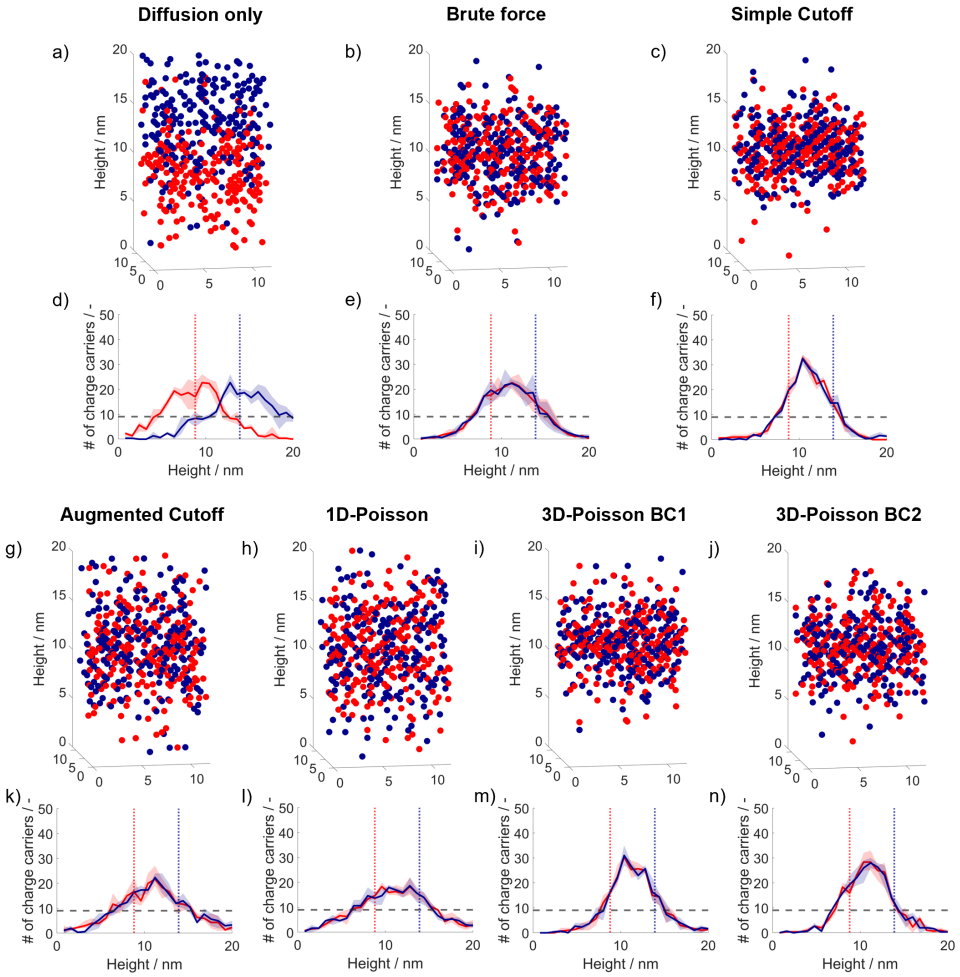

Figure 5.6: Qualitative comparison of electrostatic interaction models for initialization with two parallel and oppositely charged planes (scenario 1). (a) – (c) and (g) – (j) Box configuration after 40 ns. (d) – (f) and (k) – (n) Species distribution over the height of the box after 40 ns. The results represent the mean values from three simulations conducted with identical parameter settings. The shaded areas indicate the deviations observed among the individual runs.

mutual attraction. Only once local electroneutrality is achieved, the transport slows down due to local attractive forces. In comparison, the charge distributions of the remaining approaches are less broad and are similar in their characteristics. Additionally, it should be noted that in the Simple Cutoff case (cf. Figure 5.6 c)), artifacts in the form of periodic patterns start to form. This becomes particularly evident at longer simulation times, which can be found in Figure C.3 in the appendix. These patterns can be interpreted as the formation of charged clusters within

the electrolyte phase. Since this is not observed in any other approach and not expected in the studied electrolyte system [221], it can be concluded that the Simple Cutoff approach with the chosen cutoff radius of 4.5 nm overestimates the local electrostatic attraction between the charge carriers. Similar cluster formation is observed for all investigated cutoff radii up to 5.5 nm (cf. Figure C.5). Thus, significantly larger cutoff radii would be required to achieve a physically meaningful representation of the electrostatic interactions. However, this would substantially increase the simulation time. Overall, based on this analysis the Brute force and the 3D-Poisson BC1 and BC2 seem most accurate, since they slow down the transport in z-direction due to ionic attraction, while not promoting artifical cluster formation.

For a quantitative comparison of the electrostatic interaction models three quality measures are used: The first measure is the average potential energy per ion based on coulombic interactions of all charge carriers. This metric provides insight into the electrostatic stability of the system configuration resulting from the different approaches. Lower values indicate stronger ionic interactions and a more energetically favorable configuration, whereas higher values suggest that the ions move more independently within the electrolyte phase. This measure is defined by Equation 5.28, where n_{cc} denotes the total number of charge carriers.

$$U_{\mathrm{ion}} = \frac{1}{n_{\mathrm{cc}}} \sum_{m=1}^{n_{\mathrm{cc}}-1} \sum_{n=m+1}^{n_{\mathrm{cc}}} \frac{1}{4\pi\varepsilon_0\varepsilon_r} \frac{q_m q_n}{r_{mn}} \tag{5.28}$$

Secondly, the standard deviation of the charge per layer along the z-direction is evaluated to assess the homogeneity of the charge distribution resulting from the investigated approaches. A smaller standard deviation indicates a more uniform distribution of charge across the layers and hence a higher degree of local electroneutrality. The standard deviation is defined following Equation 5.29 with n_z being the number of layers in z-direction, Q_p denoting the overall charge of layer p and $\overline{Q}$ representing the average charge of all layers along z-direction.

$$\sigma = \sqrt{\frac{1}{n_z} \sum_{p=1}^{n_z} (Q_p - \overline{Q})^2} \tag{5.29}$$

The third quality measure is the radial distribution function $g(r)$, which quantifies the density of positively charged ions around a negatively charged ion as a function of distance. This provides insights into the ionic structure induced by the different electrostatic interaction models. For the investigated liquid electrolyte, a pronounced first peak, is expected representing short-range ordering due to electrostatic interactions [221]. In contrast, no long-range ionic order is anticipated, and thus no additional peaks at larger distances are expected. The radial distribution function is defined by Equation 5.30. Thereby, $n_+(r)$ represents the number of positively charged species at a distance r to any negatively charged ion in the box, $V(r)$ describes the shell volume

of the respective discrete element, n_- is the total number of negatively charged ions, and $\rho_{0,+}$ denotes the average density of positively charged ions in case of an ideal gas. In order to avoid double-counting of ions due to periodic boundaries, $g(r)$ is evaluated up to a maximum distance of 5.33 nm in 21 discrete elements in this study.

$$g(r) = \frac{n_+(r)}{n_- V(r) \rho_{0,+}} \tag{5.30}$$

The quantitative evaluation of the electrostatic interaction models is carried out for test scenario 2 (cf. Section 5.2.3), which represents a homogeneous electrolyte system. For each electrostatic interaction model, the simulation is executed for 50,000 iterations. The potential energy per ion and the standard deviation of charge are shown as a function of iteration count in Figure 5.7 a) and b). Due to differing time step sizes among the approaches, this representation offers a better comparability than the time-dependent representation, which is provided in the appendix (cf. Figure C.4). Based on both quality measures, it can be observed that all modeling approaches reach equilibrium within less than 20,000 iterations. Accordingly, the radial distribution function is evaluated at 30,000 iterations for all approaches, as equilibrium is reliably established by this point. The results are presented in Figure 5.7 c).

The analysis of the results reveals that the Brute force, Augmented Cutoff and 3D-Poisson methods exhibit very similar behavior across all evaluated quality measures. They quickly reduce the average potential energy per ion within approximately 4000 kMC iterations and subsequently equilibrate at similar magnitudes between -0.05 and -0.06 eV, which is significantly lower than the potential energy of the Diffusion reference case (cf. Figure 5.7 a)). Thereby, the equilibrium potential energies of the 3D-Poisson methods lie slightly below those of the Brute force and Augmented Cutoff approaches. Overall, this suggests that all of these approaches promote an initial rearrangement of charge carriers, leading to an energetically more favorable configuration compared to the Diffusion only case. The resulting configurations are thus dominated by attractive particle interactions. Similarly, in case of the Brute force, Augmented Cutoff and 3D-Poisson approaches, the standard deviation of charge quickly drops below the value of the Diffusion only reference case within the first few thousand iterations. Subsequently, the respective standard deviations remain constant, aside from statistical fluctuations (cf. Figure 5.7 b)). This demonstrates, that all of these approaches induce a quick initial charge compensation in z-direction and then maintain the achieved level of local electroneutrality throughout the remaining simulation. The respective radial distribution functions (cf. Figure 5.7 c)) peak at a distance of 0.8 nm, which corresponds to the shortest distance between two sites. This peak is slightly larger in case of the 3D-Poisson approaches. With increasing distance, the radial distribution functions of the Brute Force, Augmented Cutoff and both 3D-Poisson methods converge toward the radial distribution function of the Diffusion only case, which represents a random particle distribution throughout

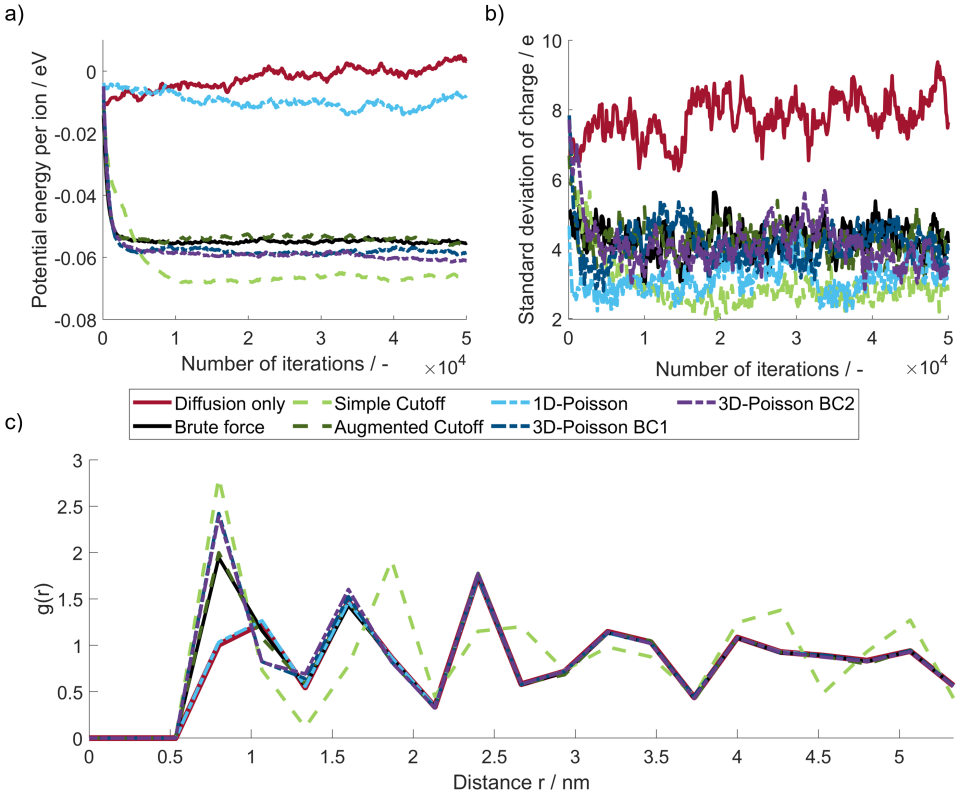

Figure 5.7: Quantitative comparison of electrostatic interaction models. a) Average coulomb potential energy per ion. b) Standard deviation of charge per layer. c) Radial distribution function of PF_6^- ions around Li^+ ions after 30,000 kMC iterations.

the cubic lattice. Beyond a distance of 1.87 nm, no significant deviation from this random particle distribution is observed. This suggests that all of these methods induce a short-range ionic order within up to 1.87 nm around a charge carrier but do not result in a long-range ionic order beyond that distance. This effect is slightly more pronounced for the 3D-Poisson approaches. Overall, the Brute force, Augmented Cutoff and 3D-Poisson methods all reproduce the expected behavior of charge carriers in liquid electrolytes.

In contrast, the 1D-Poisson approach differs particularly in the average potential energy per ion and the radial distribution function. It does not exhibit a substantial initial drop in potential energy per ion and thus its equilibrium energy is significantly higher than in the other approaches and close to the values of the random distribution of the Diffusion only case (cf. Figure 5.7 a)). Hence, the 1D-Poisson approach leads to a significantly less energetically favorable ion configuration. This can mainly be attributed to the fact that electrostatic interactions in this approach are

considered only along one of the three spatial directions. The same limitation causes that the radial distribution function of the 1D-Poisson approach equals the Diffusion only case. This means that this approach does neither induce a short-range nor a long-range ionic structure and that no increase in next-neighbor interactions compared to a random ion distribution may be observed. This differs from the expected behavior of ions in a liquid electrolyte. The standard deviation of charge exhibits a similar behavior as for the previous approaches but reaches slightly smaller values. It can thus be concluded that the 1D-Poisson approach successfully ensures a uniform charge distribution in z-direction but underestimates local interparticle interactions due to its 1D approximation.

The Simple Cutoff method behaves differently compared to the other electrostatic interaction models. It requires more time steps to reduce the average potential energy per ion as well as the standard deviation of charges per layer, indicating a longer time to reach local electroneutrality. At the same time, the final values of both metrics are smaller compared to the other approaches. This indicates a more energetically favorable ionic configuration and a better charge compensation in z-direction. The radial distribution function of the Simple Cutoff approach exhibits the highest peak of all approaches at the next-neighbor distance of 0.8 nm. This reveals a strong local interparticle interaction, which results in a pronounced short-range ionic order. Additionally, it is the only approach that deviates from the random distribution beyond 1.87 nm and does not fully match the random distribution up to the maximum investigated distance of 5.33 nm. This suggests a long-range regular ionic structure, which aligns well with the previously observed periodic patterns (cf. Figures 5.6 c) and C.5). However, such formation of long-range ionic structure is not expected in the studied liquid electrolyte system [221]. Hence, the Simple Cutoff approach with the applied cutoff radius of 4.5 nm fails to reproduce realistic ionic transport in the investigated liquid electrolyte. The same is true for further investigated cutoff radii up to 5.5 nm (cf. Figure C.5).

5.3.2 Model Reliability for Ionic Mobility Prediction

Subsequently, an external field E_{ext} is applied according to test scenario 3 (cf. Section 5.2.3) to evaluate the predictive reliability of the electrostatic interaction models with respect to ionic mobilities. According to the Nernst-Einstein equation $\mu = \frac{q}{k_B T} D$ and the diffusion parameters given in Table 5.1, the expected ideal mobilities of the Li^+ and PF_6^- ions are in the order of 5.8×10^{-9} m^2 $V^{-1}s^{-1}$ and 7×10^{-9} m^2 $V^{-1}s^{-1}$, respectively. Since the Nernst-Einstein equation describes an ideal, diluted electrolyte solution without interparticle interactions, these values should be considered as an upper limit for the expected mobilities, which are reduced by electrostatic interactions. In literature, mobility values are reported in a similar range. Experimental studies for Li^+ ions suggest mobilities in the range of 3.6×10^{-9} m^2 $V^{-1}s^{-1}$ in a gel

electrolyte [222] to 7.2×10^{-9} $m^2\ V^{-1}s^{-1}$ in ethylene carbonate/diethyl carbonate [223]. Moreover, molecular dynamic calculations reported Li^+ mobilities ranging from 2×10^{-9} $m^2\ V^{-1}s^{-1}$ in EC/EMC [215] to 5.4×10^{-9} $m^2\ V^{-1}s^{-1}$ in pure EC [101] and PF_6^- mobilities of 3.6×10^{-9} $m^2\ V^{-1}s^{-1}$ in EC/EMC [215]. Since the electrolyte and salt concentration in the study of Ringsby et al. [215] match the conditions applied in this chapter, their results serve as a reference for subsequent comparisons.

The mobilities predicted by the investigated electrostatic interaction models are calculated using Equation 5.31. Here, Ψ_{j,z^+} and Ψ_{j,z^-} describe the number of performed transport steps of species j in and against the z-direction, respectively. t represents the simulated time and n_j is the number of species j in the simulation box.

$$\mu_j = \frac{(\Psi_{j,z^+} - \Psi_{j,z^-}) \cdot \Delta L}{t \cdot n_j} \cdot \frac{1}{E_{\text{ext}}} \tag{5.31}$$

The resulting mobilities are presented in Figure 5.8 and compared to the ideal values according to the Nernst-Einstein equation (solid lines) and the literature values of Ringsby et al. [215] (dashed lines). In all cases the absolute mobility of PF_6^- is predicted to be larger than that of Li^+, which is in accordance with the higher diffusion coefficient of the negatively charged ion (cf. Table 5.1). Moreover, all predicted mobilities are in the range of the previously discussed literature values and the ideal mobilities suggested by the Nernst-Einstein equation. Nevertheless, the magnitude of the computed mobility values varies between the approaches.

Both, the 1D-Poisson approach and the Diffusion only approach predict mobilities that are very close to the ideal mobilities. This is as expected, since both approaches neglect lateral electrostatic interactions in x- and y- directions, and hence approximate the ideal case without local coulombic interparticle interaction, which would otherwise reduce ionic mobility. All other approaches predict Li^+ mobilities smaller than the ideal value, appropriately capturing the hindering effect of local interparticle interactions on ionic mobility. The predicted Li^+ mobilities decrease in the following order: Brute force, 3D-Poisson BC1, Augmented Cutoff, 3D-Poisson BC2, Simple Cutoff, with the Simple Cutoff prediction being close to the literature value reported by Ringsby et al. [215]. With the exception of the 3D-Poisson BC1 approach the same sequence holds for the PF_6^- mobility, with the Simple Cutoff approach again yielding the lowest value, which is below the corresponding literature value. The comparatively low mobilities predicted by the Simple Cutoff approach are likely to be an artifact resulting from the previously discussed overestimation of local interparticle interactions, which also result in the nonphysical long-range ionic structure observed in Figure 5.6 c) and Figure 5.7 c). In contrast, the 3D-Poisson BC1 approach predicts a PF_6^- mobility that exceeds the ideal value and is significantly higher than the Li^+ mobility. Since this behavior is not observed for the 3D-Poisson BC2 approach, it is assumed

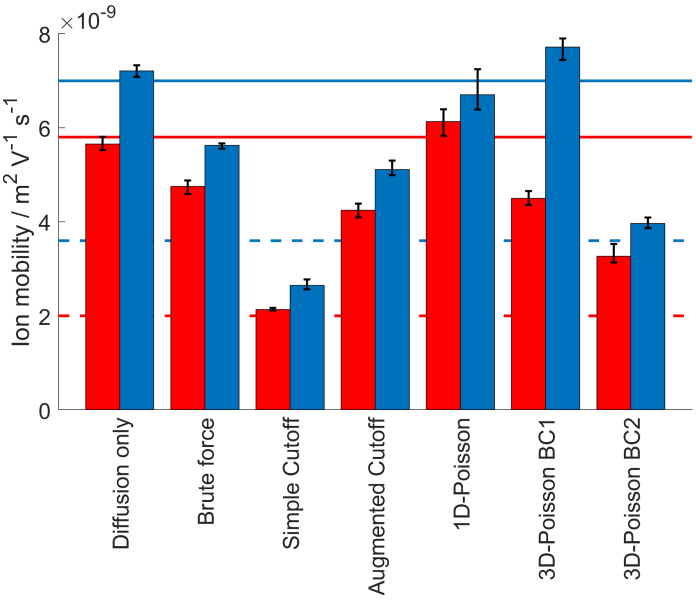

Figure 5.8: Comparison of predicted mobilities for Li^+ ions (red) and PF_6^- ions (blue) for different electrostatic interaction models for a 1M $LiPF_6$ in EC/EMC 3:7 by wt. electrolyte. The columns represent the absolute values of the average from three independent kMC runs with the same parameter set. The error bars indicate the maximum deviation among these runs. The dashed lines represent the results of Ringsby et al. [215] and the solid lines indicate the ideal mobilities following the Nernst-Einstein equation for comparison.

to be an artifact introduced by the applied boundary conditions, resulting in an overestimation of the PF_6^- mobility.

Overall, the Brute force, Augmented Cutoff and 3D-Poisson BC2 methods yield plausible estimates of the mobilities for both ion species. Their predicted Li^+ mobilities range from 3.3×10^{-9} m^2 $V^{-1}s^{-1}$ (3D-Poisson BC2) to 4.75×10^{-9} m^2 $V^{-1}s^{-1}$ (Brute force) and the predicted PF_6^- mobilities range from 4×10^{-9} m^2 $V^{-1}s^{-1}$ to 5.6×10^{-9} m^2 $V^{-1}s^{-1}$. These values are below the ideal mobilities as expected but exceed the literature values reported by Ringsby et al. [215]. A key reason for this deviation may be that only interactions between dissociated salt ions are considered in this study, whereas in real electrolyte systems, additional interactions with solvent molecules and associated ions could further reduce ion mobility. In contrast, the 1D-Poisson approach tends to overestimate mobility due to the lack of lateral interactions in x- and y-direction and the Simple Cutoff approach seems to underestimate the mobility due to an overestimation of local interactions. In case of the 3D-Poisson approach it is important to note that the boundary conditions highly impact the predicted mobility values. They should hence be carefully selected with respect to the investigated physical system.

5.3.3 Evaluation of Computational Cost

The selection of a modeling approach should not be based solely on the accuracy of the results. Computational efficiency is an equally critical factor for the applicability of any electrostatic interaction model in kMC, as it ensures reasonable computation times. To evaluate the computational cost of the electrostatic interaction models, each approach was executed three times for a minimum of 1 ns and for at least 1000 kMC iterations. The evaluation was conducted using test scenario 2, since it represents a realistic, homogeneous electrolyte system, which is comparable to the conditions under which a SEI on lithium metal commonly forms (cf. Section 5.2.3). All tests were executed on a computer with a Intel(R) Core(TM) i7-8700 processor with 3.20 GHz and 6 cores and 16 GB RAM using MATLAB 2024b. The resulting computational cost is then estimated as average computation time per kMC iteration and is summarized in Table 5.2.

Table 5.2: Comparison of computation time per iteration in ms.

Diffusion only	Brute force	Simple Cutoff	Augmented Cutoff	1D-Poisson	3D-Poisson BC1	3D-Poisson BC2
1.3	299.2	75.7	1145.1	3.1	183	189.5

The results demonstrate that the calculation of electrostatic interactions in kMC is associated with high computational cost – a challenge that has been previously discussed in the literature [135, 193, 206, 210]. The three-dimensional approaches including the 3D-Poisson, Brute force method and Cutoff approaches are particularly computationally expensive due to the high number of discrete elements caused by the three-dimensional discretization. Since a local potential needs to be calculated for each lattice site, the computation time per iteration is increased by several orders of magnitude compared to the Diffusion only case. The Augmented Cutoff approach is most computationally expensive, as it requires the calculation of separate local potentials for each combination of a lattice site and its immediate neighbors. Hence, in the investigated cubic lattice it requires the calculation of 26 different local potentials for each lattice site, which further increases the computational cost. In contrast, the 1D-Poisson approach exhibits a computational effort within the same order of magnitude as the Diffusion only case, increasing the simulation time by only a factor of 2.4. This comparatively low cost can be attributed to the reduced number of discrete elements resulting from the one-dimensional rather than three-dimensional discretization. Consequently, significantly fewer local potentials need to be computed and updated in each iteration.

5.3.4 Discussion

As a basis for the final discussion of the investigated electrostatic interaction models, Table 5.3 provides a summary of the performance of all models with respect to all previously discussed evaluation metrics. The symbols indicate the relative performance of each model in terms of either accuracy or computational efficiency: a "+" denotes good performance (e.g. high physical accuracy or low computational cost), "○" represents moderate performance (e.g. limited accuracy or average cost), and "-" reflects poor performance with respect to the respective metric.

This overview reveals a clear trade-off between physical accuracy and computational efficiency. In terms of accuracy, the Augmented Cutoff, 3D-Poisson and Brute force approaches exhibit the best overall performance, with only minor limitations. A shared drawback of the Brute force, Augmented Cutoff and 3D-Poisson BC2 methods is their inability to fully reproduce parallel-plate capacitor behavior. However, since this represents an artificial test scenario that is not expected to occur in real electrolytes, this limitation is not considered critical. In contrast, the 3D-Poisson BC1 approach successfully replicates parallel-plate capacitor behavior but introduces artifacts in the predicted PF_6^- mobility due to its boundary condition implementation. A major disadvantage of all these methods is their high computational cost, exceeding the Diffusion only case by two to three orders of magnitude.

In contrast, the 1D-Poisson approach is the most computationally efficient method evaluated, increasing the cost by only a factor of 2.4 compared to the Diffusion only case. It captures electrostatic interactions and maintains local electroneutrality along the z-direction comparably well, leading to similar standard deviation of charge in this direction as observed in the more

Table 5.3: Comparison of electrostatic interaction models with respect to all evaluated metrics.

Metric	Brute force	Simple Cutoff	Augmented Cutoff	1D-Poisson	3D-Poisson BC1	3D-Poisson BC2
Reproduction of parallel-plate capacitor	-	-	-	+	+	-
Electroneutrality in z-direction	+	+	+	+	+	+
Realistic potential energy	+	○	+	-	+	+
Realistic ionic structure	+	-	+	○	+	+
Mobility Prediction	+	○	+	-	-	+
Computational Cost	-	○	-	+	-	-

accurate methods. However, since lateral interaction in x- and y-direction are neglected, short-range ionic structuring is underestimated and ionic mobility is overestimated, which limits the overall accuracy of this approach.

The Simple Cutoff approach employing a cutoff radius of 4.5 nm is the second most efficient method in terms of computational cost. However, it performs worst with respect to physical accuracy. The cutoff of electrostatic interactions leads to an overestimation of local attractive forces, resulting in nonphysical long-range ionic structuring. While increasing the cutoff radius could partially mitigate these inaccuracies, it would also substantially raise the computational cost and thus eliminate the method's main advantage. As a consequence, the Simple Cutoff approach is not recommended for modeling electrostatic interactions in liquid electrolyte systems due to its poor physical reliability.

Overall, the 1D-Poisson approach represents a good compromise between accuracy and computational efficiency, particularly in cases where charge gradients predominantly occur in only one spatial direction and moderate overestimation of ionic mobilities is acceptable. For applications that require higher accuracy, the 3D-Poisson approach is the best alternative, since it is the fastest among the more physically accurate approaches. If this approach is selected, careful consideration must be given to the choice of appropriate boundary conditions and to an efficient implementation strategy.

In case of the 3D-kMC models for SEI formation which have been introduced in Chapter 3 and Chapter 4 of this thesis, a charge gradient is mostly expected in z-direction of the simulation box. This is since the lithium metal anode is initially placed in the bottom of the simulation box, while the top is connected to an electroneutral bulk phase. Therefore, the main transport direction of reactant and product species is in z-direction. Moreover, these models aim to increase the reachable timescale at molecular resolution, which requires high computational efficiency. Therefore, the 1D-Poisson approach is considered a good compromise for these models. It is thus selected for integration into the SEI model, which was previously presented in Section 4.3.1 in order to investigate the effect of different electrostatic interaction models on SEI formation in the following section.

5.4 Impact of Electrostatic Interaction Model on SEI Formation

In the SEI formation models introduced in the previous Chapters 3 and 4, electrostatic interactions were incorporated in a simplified manner using a next-neighbor approach. This approach accounts only for repulsive interactions, thereby avoiding the overestimation of local interactions and cluster formation, similar to what was previously observed for the Simple Cutoff method in Section 5.3. This simplification raises the question if and to what extent the choice of the electrostatic interaction model impacts the predicted SEI formation. To address this question, the SEI model from Chapter 4 was modified by replacing the transport equation in Table 4.1 with the selected 1D-Poisson approach for all charged species. Subsequently, the simulation of the primary SEI formation in an EC electrolyte with 1.2M $LiPF_6$ was repeated with the modified kMC model. The results of the original model from Chapter 4 and the extended model are compared in Figure 5.9.

The comparison of the SEI species distribution in the kMC boxes after 2 µs in Figure 5.9 a) shows no significant difference in the resulting SEI composition and morphology. This is confirmed by the comparison of the height dependent species distribution in Figure 5.9 b), which only exhibits slight deviations: The 1D-Poisson approach causes a minor shift of the maximum concentration of species towards the lithium metal anode. Thereby, the shape and height of the respective peaks remain largely unaffected. The temporal evolution of the SEI thickness in Figure 5.9 e) indicates that the 1D-Poisson approach leads to a slightly slower initial SEI growth compared to the simplified approach. However, the SEI thicknesses of both approaches converge over time and result in a very similar thickness after 2 µs. This suggests that the initial differences in growth dynamics have a limited impact on the long-time SEI formation. More significant differences are observed in the charge distribution over height after 2 µs in Figure 5.9 c) and in the temporal evolution of the potential energy per ion in Figure 5.9 d). In the original model, a surplus of positive charge is observed within the SEI between heights of 8 and 14 nm. In contrast, the 1D-Poisson maintains charge neutrality, with the charge per layer fluctuating around zero across the entire height of the simulation box. This indicates that the 1D-Poisson approach effectively enforces local electroneutrality along the z-direction, which is not achieved by the next-neighbor approach. Moreover, the 1D-Poisson approach leads to a significantly lower potential energy per ion, which remains constant over time and indicates an energetically favorable ionic configuration. In contrast, the potential energy in the next-neighbor coulomb approach increases over time and becomes largely positive, suggesting an unstable ionic configuration and underestimation of electrostatic interaction. This demonstrates the superior capability of the 1D-Poisson method to ensure consistent local electroneutrality throughout the simulation. However, this improved accuracy comes at the cost of a runtime increase of approximately 89 %.

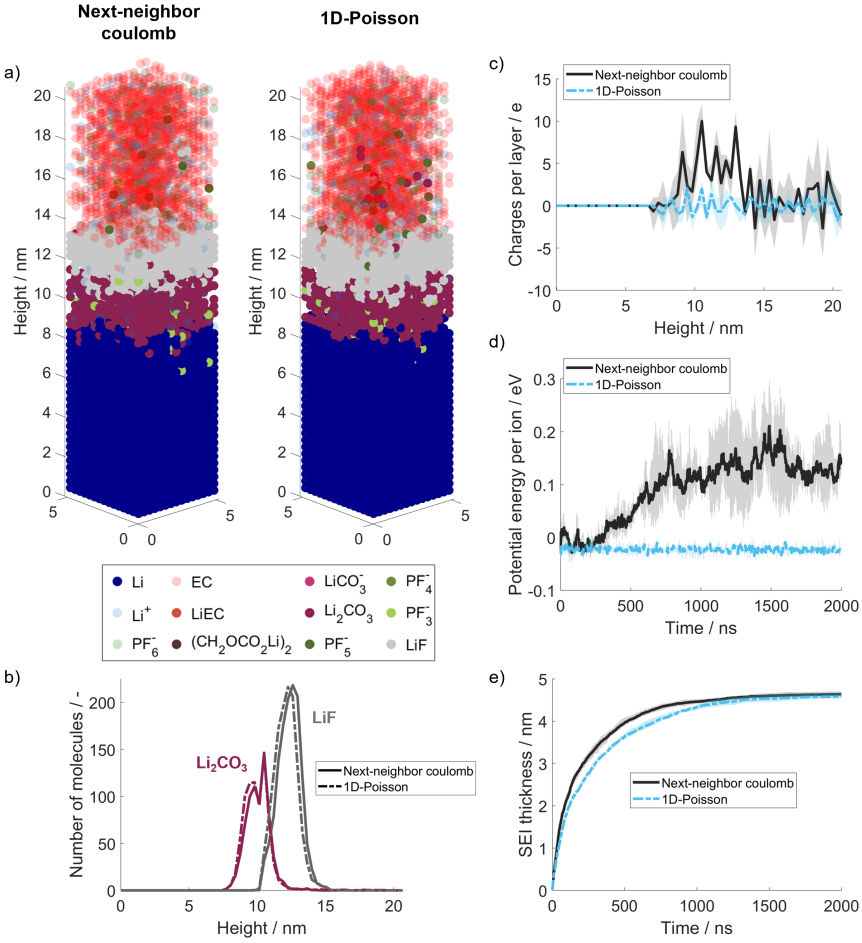

Figure 5.9: Impact of the 1D-Poisson approach on SEI formation in EC + 1.2M $LiPF_6$ up to 2 µs. a) SEI composition and morphology resulting from the next-neighbor Coulomb approach (left) and the 1D-Poisson approach (right) after 2 µs. b) SEI distribution over height after 2 µs. c) Charge distribution over height after 2 µs. d) Coulomb potential energy per ion over time. e) SEI thickness over time. Dash-Dotted lines indicate results based on the 1D-Poisson approach and solid lines refer to results based on the next-neighbor Coulomb approach. The results presented in b) to e) are the average of three independent kMC runs with the same parameter set, and corresponding shadings in c) to e) show the maximum observed deviation within these runs.

Overall, while the simplified next-neighbor Coulomb approach does not fully maintain local electroneutrality, this does not appear to significantly affect the final SEI composition or morphology in the investigated scenario. To verify that this also holds for higher salt concentrations, the same comparison was made for an EC:EMC (3:7 by wt.) electrolyte with 3M $LiPF_6$. The corresponding results are presented in Figure C.6 in the appendix. As in the low-concentration case presented in Figure 5.9, no significant effect on the SEI formation is observed. However, the

1D-Poisson approach again significantly improves local electroneutrality along the z-direction. Thus, it can be concluded that there is only a minor effect of the simplified electrostatic interaction model on the results presented in the previous Chapters 3 and 4. Nevertheless, the 1D-Poisson approach enables a more physically accurate representation of electrostatic interactions. This could lead to more accurate SEI predictions in other scenarios, e.g. if external potential is applied. Additionally, the efficient and precise consideration of electrostatic interactions in kMC models provides the foundation for resolving phenomena such as the electrical double layer between the electrode and the SEI, and between the SEI and the electrolyte in future kMC models.

5.5 Concluding Remarks

The presented work discussed the implementation of electrostatic interactions into kMC models of liquid electrolytes, focusing on suitable rate equations, electrostatic interaction models and numerical challenges. First, consistent potential-energy-dependent transport rate equations were successfully transferred from external potential energies in fluid dynamics to electrostatic interactions in liquid electrolytes. The derived transfer rates ensure that the total drift rate is maintained, while also preserving microscopic reversibility. In terms of numerical aspects, the study identified three potential challenges: The self-interaction error, the kMC boundary conditions and the impact of the solvation shell. All three issues were thoroughly analyzed and discussed. Furthermore, effective solution strategies were proposed and successfully implemented, ensuring accuracy in the kMC simulation of electrostatic interactions for liquid electrolyte systems.

Eventually, the study compares five electrostatic interaction models, ranging from the Brute force consideration of all interparticle interactions to Cutoff methods and the solutions of the 1D- and 3D-Poisson equation. These models are benchmarked against a Diffusion only reference case without electrostatic interactions, using an electrolyte composed of 1M $LiPF_6$ in 3:7 EC/EMC as example system. This investigation identifies the Brute force method, the 3D-Poisson and the Augmented Cutoff method as the most accurate approaches in terms of all investigated properties. However, at the same time they proved to be very inefficient, increasing the simulation time by two to three orders of magnitude. Moreover, in case of the 3D-Poisson approach, it was demonstrated that the careful selection of boundary conditions is crucial to ensure a high model accuracy. In contrast, the Simple Cutoff method proved to be comparatively efficient. However, the neglect of long-range electrostatic interactions resulted in an overestimation of local interaction effects, leading to unexpected ion clustering within the electrolyte phase. As a result, this approach was unable to maintain a homogeneous electrolyte phase for the investigated cutoff radii. The 1D-Poisson approach was identified to be by far the most efficient electrostatic interaction model. It provides a good representation of electrostatic interactions in the discretized

z-direction, ensuring accurate charge distribution along this dimension. However, due to its neglect of interactions in the x- and y-directions, it is slightly less accurate compared to the three-dimensional approaches. This is particularly reflected in the overestimation of mobility due to a lack of local interparticle interactions. Nevertheless, for applications in which charge gradients are mostly expected in one dimension, the 1D-Poisson approach offers the best trade-off between accuracy and computational cost. In case of the SEI model introduced in Chapter 4, the approach does not significantly impact the predicted SEI composition and morphology, proving the simplified interaction model applied in Chapters 3 and 4 to be sufficient for the investigated cases. Nevertheless, this could differ for further physical systems, e.g. if external potential is applied.

Overall, this comparative methodological study paves the way for reliably and efficiently accounting for electrostatic interactions in kMC simulations of liquid electrolytes. In the future, this could enable the explicit description of the electrical double layer in kMC models and allow for the prediction of ionic mobilities.

6 Conclusion and Outlook

The presented dissertation investigated the spontaneous formation of the SEI on lithium metal anodes. The stabilization of this interfacial layer is still an open challenge, but crucial to achieve sufficiently high Coulombic Efficiency and safety for the widespread adoption of the high energy-density lithium metal batteries. A targeted stabilization of the SEI requires a detailed understanding of its structure, the underlying formation mechanisms and macroscopic influencing factors. However, due to its low thickness in the nanometer range and fast formation processes that occur within timescales well below one second, a purely experimental characterization could not lead to a full understanding of spontaneous SEI formation on lithium metal, yet. Hence, advanced theoretical methods are required to complement experimental research and uncover underlying mechanisms of SEI formation. In this context atomistic simulation methods provide valuable insights, but are limited to simulation times of only a few nanoseconds. Thus, there is the need for mesoscale modeling approaches that bridge this gap between atomistic and macroscopic methods and enable a detailed understanding of the underlying mesoscale processes of SEI formation to allow for a knowledge-driven SEI design in future.

This work has therefore focused on three main objectives:

1. Development and application of *ab initio*-informed kMC models for spontaneous SEI formation on lithium metal.
2. Bridging the gap between atomistic simulations and technologically relevant timescales with a molecular resolution.
3. Mechanistic understanding of SEI formation on lithium metal and effect of macroscopic properties such as electrolyte composition on SEI formation.

Chapter 3 of this dissertation addressed all of these objectives. Building upon existing literature, an *ab initio*-informed kMC model of spontaneous SEI formation on lithium metal was developed (objective 1). This model accounts for specific characteristics such as the absence of a fixed anode surface and the spontaneous SEI formation, occurring without the application of external current. The physical plausibility of the model was ensured by a DFT-based parametrization, implementation of approaches to maintain local and global electroneutrality, and validation against ReaxFF MD simulations. Additionally, the accessible timescales were extended from

the nanosecond to the microsecond range, marking a first step towards objective 2 of reaching technologically relevant timescales. The model was subsequently applied to study the SEI formation in the standard electrolyte EC/EMC + $LiPF_6$, contributing to objective 3. The performed simulation studies predicted the formation of a layered inorganic SEI within the first microsecond after contact between lithium metal and liquid electrolyte, with the inner layer consisting of Li_2CO_3 and the outer layer consisting of LiF. Moreover, it was revealed that the local Li^+ ion concentration and the solvation environment have a significant impact on the SEI composition and morphology, potentially explaining ambivalent literature results. Ultimately, it was shown that, within solubility limits, the SEI formation is particularly affected by a variation in salt concentration, with higher concentrations resulting in faster passivation and a thinner SEI with increased LiF content.

The following Chapter 4 applied and extended the previously developed kMC model in order to investigate the impact of the film-forming additive VC. For this purpose, polymerization processes were added to the model. Moreover, the accessible timescales were increased up to the seconds range, thus meeting objective 2 of this work of achieving technologically relevant timescales. The application of the extended model revealed that VC does not significantly alter the very initial formation of the inorganic SEI layer close to the lithium metal. However, starting from the millisecond timescale, it leads to polymer formation. In contrast to the remaining SEI-forming reactions, which are based on the reduction of electrolyte components, this polymerization is, except for the initiation, a purely chemically driven process. This results in the formation of a passivating layer without the ongoing consumption of active lithium. The formed polymer layer further prevents the continuous degradation of solvent and conductive salt as well as the dissolution of SEI and intermediate products within a few hundred milliseconds. This overall mechanism is only hardly influenced by changes in the VC concentration or electrolyte composition. However, lower additive concentrations decelerate the polymer growth, and a larger proportion of the additive is consumed during the initial layer formation. Consequently, less additive remains in the electrolyte and is available for the formation of new passivation layers during operation. Hence, cell life could be extended by increased additive concentrations. Overall, these simulations provided important mechanistic insights and revealed how electrolyte composition may affect SEI formation, addressing objective 3 of this dissertation.

Chapter 5 took a step back and deep-dived into the consideration of electrostatic interactions in kMC models of liquid electrolytes, contributing to objective 1 of this dissertation. These long-ranging forces not only affect direct neighbours but in principle the transport rates of all charge carriers in the simulation box. For this reason, the complete consideration of all electrostatic interactions in kMC calculations is very computationally expensive and was drastically simplified in the previously developed SEI formation models. This chapter therefore investigated how these interactions can be efficiently incorporated into the kMC approach while still achieving accurate

results. Moreover, it was studied how the accurate consideration of electrostatic interactions impacts the predicted SEI formation. In a first step, consistent transport rates that consider the local potential difference were derived from literature. Subsequently, three obstacles were identified and discussed that must be considered during implementation to ensure accurate results, namely the self-interaction error, boundary effects and the impact of the solvation shell. Eventually, based on a comparison of five different electrostatic interaction models, the 1D-Poisson approach was selected as the most efficient and sufficiently accurate interaction model to be implemented in the previously developed SEI formation model. A comparison of the model output demonstrated that the 1D-Poisson approach succeeds in improving the local electroneutrality along the z-dimension of the simulation box. However, the predicted SEI does not significantly change, proving the previously applied simplified approaches to be sufficient in the investigated cases.

Overall, this dissertation accomplished to address the three defined objectives. All chapters contributed to the development and extension of the *ab initio*-informed kMC approach (objective 1), progressively increasing its functionality and accuracy. As a result, this thesis provides a kMC modeling framework for studying the spontaneous SEI formation on lithium metal based on atomistic input data. The developed framework allows to predict the time evolution, morphology and chemical composition of the SEI with three-dimensional resolution at the molecular level. Moreover, it succeeds to access technologically relevant timescales of seconds (objective 2). The application of the developed model on the example electrolyte system EC/EMC with $LiPF_6$ as conductive salt and VC as film-forming additive provided new mechanistic insights into SEI formation, including the identification of limiting processes and the operating principles of the film-forming additive. Moreover, the impact of changes in the electrolyte composition on the molecular SEI composition were revealed through parameter studies (objective 3).

These results represent an important step towards model-assisted SEI design and motivate a wide range of future research on model development and application. Promising research directions in terms of model development include the incorporation of more advanced electron-transport processes through the SEI. Replacing the lumped exponential decay function by the separate consideration of single electron transport processes could further enhance the model predictions. Additionally, based on the electrostatic interaction models presented in Chapter 5, the electrical double layer could be explicitly implemented into the kMC framework, allowing for a more accurate prediction of ionic concentrations close to the interface. In order to predict the long-term stability of the SEI during cycling, it would be of high interest to additionally extend the model to cover the effect of externally applied current. Eventually, experimental validation remains a critical step to assess the accuracy of the model predictions and should be an important focus of future research.

In terms of application, the developed modeling framework can be adapted to a wide range of electrolyte chemistries beyond those investigated in this dissertation. This would allow to predict the effect of different electrolyte solvents, conductive salts, film-forming additives or impurities on SEI formation and to gain fundamental mechanistic insight into the underlying layer formation processes. Of particular interest are advanced electrolyte formulations, such as ether-based electrolytes, which are known for their potential to enhance lithium metal battery performance [53]. However, the greatest bottleneck in extending the model to new electrolyte systems is the limited availability of high-quality input data, as all relevant mechanisms and their kinetic parameters must be explicitly provided. Currently, these mechanisms are selected based on literature, *ab initio* MD simulations and manual DFT calculations, requiring an extensive and tedious search for transition states. An acceleration of this process could enable the modeling framework to serve as an electrolyte screening tool, quickly predicting SEI composition and morphology. When combined with an improved understanding of the relationship between SEI structure and cell performance [20], this approach promises to significantly advance model-assisted electrolyte design for LMB. First promising approaches in this direction apply chemical reaction networks combined with neural networks, in order to predict extensive reaction networks and related reaction energies [33, 127, 224, 225]. A combination of these approaches with the modeling framework developed in this work would be an exciting future research direction and might eventually pave the way to comprehensive model-derived design recommendation for the electrolyte of LMB. Apart from this, the developed modeling framework is not limited to SEI formation on lithium metal, but could also be adapted and applied to further battery systems. This could be of particular interest for next-generation batteries such as sodium-ion batteries, in which as well the interface is not yet fully understood and stabilized. In the long term, kMC models could serve as a fully integrated mesoscale link within multiscale modeling frameworks that bridge atomistic simulations and continuum cell models. This would allow for a consistent prediction of SEI formation across different scales and could be applied to optimize electrolyte composition as well as formation strategies and cell design for specific applications. Such approach could lead to an accelerated knowledge-based development of durable, safe and cost efficient battery cells.

Bibliography

[1] J. Wagner-Henke, D. Kuai, M. Gerasimov, F. Röder, P. B. Balbuena, and U. Krewer, "Knowledge-driven design of solid-electrolyte interphases on lithium metal via multiscale modelling," *Nature Communications*, vol. 14, no. 1, p. 6823, 2023.

[2] J. Wagner-Henke, D. Kuai, P. B. Balbuena, and U. Krewer, "Understanding the effect of vinylene carbonate on SEI formation, morphology and stability on lithium metal anodes," *Energy Storage Materials*, vol. 81, p. 104434, 2025.

[3] Copernicus Climate Change Service, "Global Climate Highlights 2024," 2025, [Online]. Available: https://climate.copernicus.eu/global-climate-highlights-2024. Accessed: Feb. 6, 2025.

[4] United Nations Framework Convention on Climate Change (UNFCCC), "The Paris Agreement," 2015, [Online]. Available: https://unfccc.int/sites/default/files/english_paris_agreement.pdf. Accessed: Feb. 6, 2025.

[5] European Commission, "The European Green Deal," 2019, [Online]. Available: https://eur-lex.europa.eu/legal-content/EN/TXT/?uri=celex:52019DC0640. Accessed: Feb. 5, 2025.

[6] Bundesministerium für Wirtschaft und Energie (BMWK), "Speicher für die Energiewende," 2024, [Online]. Available: https://www.bmwk.de/Redaktion/DE/Downloads/S-T/speicher-fuer-die-energiewende.pdf?__blob=publicationFile&v=8. Accessed: Feb. 5, 2025.

[7] Umweltbundesamt (UBA), "Klimaschutz im Verkehr," 2024, [Online]. Available: https://www.umweltbundesamt.de/themen/verkehr/klimaschutz-im-verkehr#undefined. Accessed: Feb. 5, 2025.

[8] V. B. F. da Costa, L. Bitencourt, B. H. Dias, T. Soares, J. V. B. de Andrade, and B. D. Bonatto, "Life cycle assessment comparison of electric and internal combustion vehicles: A review on the main challenges and opportunities," *Renewable and Sustainable Energy Reviews*, vol. 208, p. 114988, 2025.

[9] M. Winter, B. Barnett, and K. Xu, "Before Li ion Batteries," *Chemical Reviews*, vol. 118, pp. 11 433–11 456, 2018.

[10] M. Li, J. Lu, Z. Chen, and K. Amine, "30 Years of Lithium-Ion Batteries," *Advanced Materials*, vol. 30, 2018.

[11] D. Lin, Y. Liu, and Y. Cui, "Reviving the lithium metal anode for high-energy batteries," *Nature Nanotechnology*, vol. 12, no. 3, pp. 194–206, 2017.

[12] A. Bills, S. Sripad, W. L. Fredericks, M. Singh, and V. Viswanathan, "Performance Metrics Required of Next-Generation Batteries to Electrify Commercial Aircraft," *ACS Energy Letters*, vol. 5, pp. 663–668, 2020.

[13] B. Horstmann, J. Shi, R. Amine, M. Werres, X. He, H. Jia, F. Hausen, I. Cekic-Laskovic, S. Wiemers-Meyer, J. Lopez, D. Galvez-Aranda, F. Baakes, D. Bresser, C.-C. Su, Y. Xu, W. Xu, P. Jakes, R.-A. Eichel, E. Figgemeier, U. Krewer, J. M. Seminario, P. B. Balbuena, C. Wang, S. Passerini, Y. Shao-Horn, M. Winter, K. Amine, R. Kostecki, and A. Latz, "Strategies towards enabling lithium metal in batteries: interphases and electrodes," *Energy & Environmental Science*, vol. 14, no. 10, pp. 5289–5314, 2021.

[14] X. He, D. Bresser, S. Passerini, F. Baakes, U. Krewer, J. Lopez, C. T. Mallia, Y. Shao-Horn, I. Cekic-Laskovic, S. Wiemers-Meyer, F. A. Soto, V. Ponce, J. M. Seminario, P. B. Balbuena, H. Jia, W. Xu, Y. Xu, C. Wang, B. Horstmann, R. Amine, C.-C. Su, J. Shi, K. Amine, M. Winter, A. Latz, and R. Kostecki, "The passivity of lithium electrodes in liquid electrolytes for secondary batteries," *Nature Reviews Materials*, vol. 6, no. 11, pp. 1036–1052, 2021.

[15] E. Peled, "The Electrochemical Behavior of Alkali and Alkaline Earth Metals in Nonaqueous Battery Systems—The Solid Electrolyte Interphase Model," *Journal of the Electrochemical Society*, vol. 126, no. 12, pp. 2047–2051, 1979.

[16] E. Peled and S. Menkin, "Review—SEI: past, present and future," *Journal of The Electrochemical Society*, vol. 164, no. 7, pp. A1703–A1719, 2017.

[17] P. Verma, P. Maire, and P. Novák, "A review of the features and analyses of the solid electrolyte interphase in Li-ion batteries," *Electrochimica Acta*, vol. 55, no. 22, pp. 6332–6341, 2010.

[18] X. B. Cheng, R. Zhang, C. Z. Zhao, F. Wei, J. G. Zhang, and Q. Zhang, "A review of solid electrolyte interphases on lithium metal anode," *Advanced Science*, vol. 3, no. 3, pp. 1–20, 2015.

[19] H. Wu, H. Jia, C. Wang, J. Zhang, and W. Xu, "Recent Progress in Understanding Solid Electrolyte Interphase on Lithium Metal Anodes," *Advanced Energy Materials*, vol. 11, no. 5, p. 2003092, 2021.

[20] A. Wang, S. Kadam, H. Li, S. Shi, and Y. Qi, "Review on modeling of the anode solid electrolyte interphase (SEI) for lithium-ion batteries," *npj Computational Materials*, vol. 4, no. 1, p. 15, 2018.

[21] F. A. Soto, Y. Ma, J. M. Martinez De La Hoz, J. M. Seminario, and P. B. Balbuena, "Formation and Growth Mechanisms of Solid-Electrolyte Interphase Layers in Rechargeable Batteries," *Chemistry of Materials*, vol. 27, no. 23, pp. 7990–8000, 2015.

[22] D. Kuai and P. B. Balbuena, "Solvent Degradation and Polymerization in the Li-Metal Battery: Organic-Phase Formation in Solid-Electrolyte Interphases," *ACS Applied Materials & Interfaces*, vol. 14, no. 2, pp. 2817–2824, 2022.

[23] D. E. Galvez-Aranda and J. M. Seminario, "Li-Metal Anode in a Conventional Li-Ion Battery Electrolyte: Solid Electrolyte Interphase Formation using Ab Initio Molecular Dynamics," *Journal of The Electrochemical Society*, vol. 169, no. 3, p. 030502, 2022.

[24] D. Witt, F. Röder, and U. Krewer, "Analysis of Lithium-Ion Battery State and Degradation via Physicochemical Cell and SEI Modeling," *Batteries & Supercaps*, vol. 5, no. 7, p. e202200067, 2022.

[25] A. M. Colclasure, K. a. Smith, and R. J. Kee, "Modeling detailed chemistry and transport for solid-electrolyte-interface (SEI) films in Li-ion batteries," *Electrochimica Acta*, vol. 58, no. 1, pp. 33–43, 2011.

[26] B. Horstmann, F. Single, and A. Latz, "Review on multi-scale models of solid-electrolyte interphase formation," *Current Opinion in Electrochemistry*, vol. 13, pp. 61–69, 2019.

[27] P. J. Weddle, E. W. C. Spotte-Smith, A. Verma, H. D. Patel, K. Fink, B. J. T. de Villers, M. C. Schulze, S. M. Blau, K. A. Smith, K. A. Persson, and A. M. Colclasure, "Continuum-level modeling of Li-ion battery SEI by upscaling atomistically informed reaction mechanisms," *Electrochimica Acta*, vol. 468, p. 143121, 2023.

[28] E. M. Gavilán-Arriazu, M. P. Mercer, D. E. Barraco, H. E. Hoster, and E. P. M. Leiva, "Kinetic Monte Carlo simulations applied to Li-ion and post Li-ion batteries: a key link in the multi-scale chain," *Progress in Energy*, vol. 3, no. 4, p. 042001, 2021.

[29] R. N. Methekar, P. W. Northrop, K. Chen, R. D. Braatz, and V. R. Subramanian, "Kinetic Monte Carlo simulation of surface heterogeneity in graphite anodes for lithium-ion batteries: Passive layer formation," *Proceedings of the American Control Conference*, vol. 158, no. 4, pp. 1512–1517, 2011.

[30] F. Röder, R. D. Braatz, and U. Krewer, "Multi-scale simulation of heterogeneous surface film growth mechanisms in lithium-ion batteries," *Journal of the Electrochemical Society*, vol. 164, no. 11, pp. E3335–E3344, 2017.

[31] F. Röder, V. Laue, and U. Krewer, "Model Based Multiscale Analysis of Film Formation in Lithium-Ion Batteries," *Batteries & Supercaps*, vol. 2, no. 3, pp. 248–265, 2019.

[32] C. Shinagawa, H. Ushiyama, and K. Yamashita, "Multiscale Simulations for Lithium-Ion Batteries: SEI Film Growth and Capacity Fading," *Journal of The Electrochemical Society*, vol. 164, no. 13, pp. A3018–A3024, 2017.

[33] E. W. C. Spotte-Smith, R. L. Kam, D. Barter, X. Xie, T. Hou, S. Dwaraknath, S. M. Blau, and K. A. Persson, "Toward a Mechanistic Model of Solid–Electrolyte Interphase Formation and Evolution in Lithium-Ion Batteries," *ACS Energy Letters*, vol. 7, no. 4, pp. 1446–1453, 2022.

[34] R. Korthauer, *Lithium-Ion Batteries: Basics and Applications*, R. Korthauer, Ed. Springer Berlin Heidelberg, 2018.

[35] J. B. Goodenough and K.-S. Park, "The Li-Ion Rechargeable Battery: A Perspective," *Journal of the American Chemical Society*, vol. 135, pp. 1167–1176, 2013.

[36] N. Nitta, F. Wu, J. T. Lee, and G. Yushin, "Li-ion battery materials: present and future," *Materials Today*, vol. 18, pp. 252–264, 2015.

[37] W. Luo, S. Cheng, M. Wu, X. Zhang, D. Yang, and X. Rui, "A review of advanced separators for rechargeable batteries," *Journal of Power Sources*, vol. 509, 2021.

[38] Y. Liu, C. Zhao, J. Du, X. Zhang, A. Chen, and Q. Zhang, "Research Progresses of Liquid Electrolytes in Lithium-Ion Batteries," *Small*, vol. 19, 2023.

[39] J. Lu, Z. Chen, F. Pan, Y. Cui, and K. Amine, "High-Performance Anode Materials for Rechargeable Lithium-Ion Batteries," *Electrochemical Energy Reviews*, vol. 1, pp. 35–53, 2018.

[40] H. Zhang, Y. Yang, D. Ren, L. Wang, and X. He, "Graphite as anode materials: Fundamental mechanism, recent progress and advances," *Energy Storage Materials*, vol. 36, pp. 147–170, 2021.

[41] M. Shi, C. Song, Z. Tai, K. Zou, Y. Duan, X. Dai, J. Sun, Y. Chen, and Y. Liu, "Coal-derived synthetic graphite with high specific capacity and excellent cyclic stability as anode material for lithium-ion batteries," *Fuel*, vol. 292, 2021.

[42] S. Goriparti, E. Miele, F. D. Angelis, E. D. Fabrizio, R. P. Zaccaria, and C. Capiglia, "Review on recent progress of nanostructured anode materials for Li-ion batteries," *Journal of Power Sources*, vol. 257, pp. 421–443, 2014.

[43] J.-M. Tarascon and M. Armand, "Issues and challenges facing rechargeable lithium batteries," *Nature*, vol. 414, pp. 359–367, 2001.

[44] T. Placke, R. Kloepsch, S. Dühnen, and M. Winter, "Lithium ion, lithium metal, and alternative rechargeable battery technologies: the odyssey for high energy density," *Journal of Solid State Electrochemistry*, vol. 21, pp. 1939–1964, 2017.

[45] T. Placke and M. Winter, "Batterien für medizinische Anwendungen: Stand der Batterieforschung und Zukunftsaussichten," *Zeitschrift fur Herz-, Thorax- und Gefasschirurgie*, vol. 29, pp. 139–149, 2015.

[46] C. Fang, X. Wang, and Y. S. Meng, "Key Issues Hindering a Practical Lithium-Metal Anode," *Trends in Chemistry*, vol. 1, no. 2, pp. 152–158, 2019.

[47] S. Li, M. Jiang, Y. Xie, H. Xu, J. Jia, and J. Li, "Developing High-Performance Lithium Metal Anode in Liquid Electrolytes: Challenges and Progress," *Advanced Materials*, vol. 30, 2018.

[48] A. Fotouhi, D. Auger, L. O'Neill, T. Cleaver, and S. Walus, "Lithium-Sulfur Battery Technology Readiness and Applications—A Review," *Energies*, vol. 10, p. 1937, 2017.

[49] J.-G. Zhang, W. Xu, and W. A. Henderson, *Lithium Metal Anodes and Rechargeable Lithium Metal Batteries*. Springer International Publishing, 2017, vol. 249.

[50] P. G. Bruce, S. A. Freunberger, L. J. Hardwick, and J.-M. Tarascon, "Li–O_2 and Li–S batteries with high energy storage," *Nature Materials*, vol. 11, pp. 19–29, 2012.

[51] J. Janek and W. G. Zeier, "Challenges in speeding up solid-state battery development," *Nature Energy*, 2023.

[52] K. Yoon, S. Lee, K. Oh, and K. Kang, "Challenges and Strategies towards Practically Feasible Solid-State Lithium Metal Batteries," *Advanced Materials*, vol. 34, 2022.

[53] G. M. Hobold, J. Lopez, R. Guo, N. Minafra, A. Banerjee, Y. Shirley Meng, Y. Shao-Horn, and B. M. Gallant, "Moving beyond 99.9% Coulombic efficiency for lithium anodes in liquid electrolytes," *Nature Energy*, vol. 6, no. 10, pp. 951–960, 2021.

[54] X. B. Cheng, R. Zhang, C. Z. Zhao, and Q. Zhang, "Toward Safe Lithium Metal Anode in Rechargeable Batteries: A Review," *Chemical Reviews*, vol. 117, no. 15, pp. 10 403–10 473, 2017.

[55] D. Aurbach, "Review of selected electrode-solution interactions which determine the performance of Li and Li ion batteries," *Journal of Power Sources*, vol. 89, no. 2, pp. 206–218, 2000.

[56] E. Peled, D. Golodnitsky, and G. Ardel, "Advanced Model for Solid Electrolyte Interphase Electrodes in Liquid and Polymer Electrolytes," *Journal of The Electrochemical Society*, vol. 144, no. 8, pp. L208–L210, 1997.

[57] K. Kanamura, H. Tamura, and Z. ichiro Takehara, "XPS analysis of a lithium surface immersed in propylene carbonate solution containing various salts," *Journal of Electroanalytical Chemistry*, vol. 333, no. 1-2, pp. 127–142, 1992.

[58] K. Kanamura, H. Tamura, S. Shiraishi, and Z. I. Takehara, "XPS analysis for the lithium surface immersed in γ-butyrolactone containing various salts," *Electrochimica Acta*, vol. 40, no. 7, pp. 913–921, 1995.

[59] K. Kanamura, "Chemical Reaction of Lithium Surface during Immersion in $LiClO_4$ or $LiPF_6$ / DEC Electrolyte," *Journal of The Electrochemical Society*, vol. 144, no. 6, p. 1900, 1997.

[60] E. Peled, D. Bar Tow, A. Merson, A. Gladkich, L. Burstein, and D. Golodnitsky, "Composition, depth profiles and lateral distribution of materials in the SEI built on HOPG-TOF SIMS and XPS studies," *Journal of Power Sources*, vol. 97-98, pp. 52–57, 2001.

[61] W. Xu, J. Wang, F. Ding, X. Chen, E. Nasybulin, Y. Zhang, and J. G. Zhang, "Lithium metal anodes for rechargeable batteries," *Energy and Environmental Science*, vol. 7, no. 2, pp. 513–537, 2014.

[62] F. Schomburg, R. Drees, M. Kurrat, M. A. Danzer, and F. Röder, "Characterization of the Solid–Electrolyte Interphase Growth During Cell Formation Based on Differential Voltage Analysis," *Energy Technology*, vol. 11, no. 5, p. 2200688, 2023.

[63] N. Harting, N. Wolff, F. Röder, and U. Krewer, "Nonlinear Frequency Response Analysis (NFRA) of Lithium-Ion Batteries," *Electrochimica Acta*, vol. 248, pp. 133–139, 2017.

[64] A. Schechter, D. Aurbach, and H. Cohen, "X-ray photoelectron spectroscopy study of surface films formed on Li electrodes freshly prepared in alkyl carbonate solutions," *Langmuir*, vol. 15, no. 9, pp. 3334–3342, 1999.

[65] Y. Xu, H. Wu, H. Jia, J. G. Zhang, W. Xu, and C. Wang, "Current Density Regulated Atomic to Nanoscale Process on Li Deposition and Solid Electrolyte Interphase Revealed by Cryogenic Transmission Electron Microscopy," *ACS Nano*, vol. 14, no. 7, pp. 8766–8775, 2020.

[66] Y. Xu, H. Wu, Y. He, Q. Chen, J. G. Zhang, W. Xu, and C. Wang, "Atomic to Nanoscale Origin of Vinylene Carbonate Enhanced Cycling Stability of Lithium Metal Anode Revealed by Cryo-Transmission Electron Microscopy," *Nano Letters*, vol. 20, no. 1, pp. 418–425, 2020.

[67] S. P. Kühn, F. Pfeiffer, M. Bela, U. Rodehorst, D. Weintz, M. Stan, M. Baghernejad, M. Winter, and I. Cekic-Laskovic, "Back to the basics: Advanced understanding of the as-defined solid electrolyte interphase on lithium metal electrodes," *Journal of Power Sources*, vol. 549, no. June, p. 232118, 2022.

[68] B. von Holtum, M. Kubot, C. Peschel, U. Rodehorst, M. Winter, S. Nowak, and S. Wiemers-Meyer, "Accessing the Primary Solid–Electrolyte Interphase on Lithium Metal: A Method for Low-Concentration Compound Analysis," *ChemSusChem*, 2023.

[69] U. Krewer, F. Röder, E. Harinath, R. D. Braatz, B. Bedürftig, and R. Findeisen, "Review—Dynamic Models of Li-Ion Batteries for Diagnosis and Operation: A Review and Perspective," *Journal of The Electrochemical Society*, vol. 165, no. 16, pp. A3656–A3673, 2018.

[70] S. Shi, J. Gao, Y. Liu, Y. Zhao, Q. Wu, W. Ju, C. Ouyang, and R. Xiao, "Multi-scale computation methods: Their applications in lithium-ion battery research and development," *Chinese Physics B*, vol. 25, no. 1, p. 018212, 2016.

[71] A. A. Franco, A. Rucci, D. Brandell, C. Frayret, M. Gaberscek, P. Jankowski, and P. Johansson, "Boosting Rechargeable Batteries R&D by Multiscale Modeling: Myth or Reality?" *Chemical Reviews*, vol. 119, no. 7, pp. 4569–4627, 2019.

[72] G. D. Wehinger, M. Ambrosetti, R. Cheula, Z. B. Ding, M. Isoz, B. Kreitz, K. Kuhlmann, M. Kutscherauer, K. Niyogi, J. Poissonnier, R. Réocreux, D. Rudolf, J. Wagner, R. Zimmermann, M. Bracconi, H. Freund, U. Krewer, and M. Maestri, "Quo vadis multiscale modeling in reaction engineering? – A perspective," *Chemical Engineering Research and Design*, vol. 184, pp. 39–58, 2022.

[73] M. Bordonhos, T. L. P. Galvão, J. R. B. Gomes, J. D. Gouveia, M. Jorge, M. A. O. Lourenço, J. M. Pereira, G. Pérez-Sánchez, M. L. Pinto, C. M. Silva, J. Tedim, and B. Zêzere, "Multiscale Computational Approaches toward the Understanding of Materials," *Advanced Theory and Simulations*, vol. 6, 2023.

[74] G. Ning and B. N. Popov, "Cycle Life Modeling of Lithium-Ion Batteries," *Journal of The Electrochemical Society*, vol. 151, no. 10, p. A1584, 2004.

[75] T. F. Fuller, M. Doyle, and J. Newman, "Simulation and Optimization of the Dual Lithium Ion Insertion Cell," *Journal of The Electrochemical Society*, vol. 141, no. 1, pp. 1–10, 1994.

[76] M. Heinrich, N. Wolff, N. Harting, V. Laue, F. Röder, S. Seitz, and U. Krewer, "Physico-Chemical Modeling of a Lithium-Ion Battery: An Ageing Study with Electrochemical Impedance Spectroscopy," *Batteries and Supercaps*, vol. 2, no. 6, pp. 530–540, 2019.

[77] F. Single, B. Horstmann, and A. Latz, "Dynamics and morphology of solid electrolyte interphase (SEI)," *Physical Chemistry Chemical Physics*, vol. 18, no. 27, pp. 17 810–17 814, 2016.

[78] ——, "Revealing SEI morphology: In-depth analysis of a modeling approach," *Journal of the Electrochemical Society*, vol. 164, no. 11, pp. E3132–E3145, 2017.

[79] F. Baakes, M. Lüthe, M. Gerasimov, V. Laue, F. Röder, P. Balbuena, and U. Krewer, "Unveiling the interaction of reactions and phase transition during thermal abuse of Li-ion batteries," *Journal of Power Sources*, vol. 522, p. 230881, 2022.

[80] C. Kupper, S. Spitznagel, H. Döring, M. A. Danzer, C. Gutierrez, A. Kvasha, and W. G. Bessler, "Combined modeling and experimental study of the high-temperature behavior of a lithium-ion cell: Differential scanning calorimetry, accelerating rate calorimetry and external short circuit," *Electrochimica Acta*, vol. 306, pp. 209–219, 2019.

[81] P. Hohenberg and W. Kohn, "Inhomogeneous Electron Gas," *Physical Review*, vol. 136, pp. B864–B871, 1964.

[82] D. S. Sholl and J. A. Steckel, *Density Functional Theory*. Wiley, 2009.

[83] M. Orio, D. A. Pantazis, and F. Neese, "Density functional theory," *Photosynthesis Research*, vol. 102, pp. 443–453, 2009.

[84] Y. Wang and P. B. Balbuena, "Theoretical insights into the reductive decompositions of propylene carbonate and vinylene carbonate: Density functional theory studies," *Journal of Physical Chemistry B*, vol. 106, no. 17, pp. 4486–4495, 2002.

[85] Y. K. Han and S. U. Lee, "Performance of density functional for calculation of reductive ring-opening reaction energies of Li^+-EC and Li^+-VC," *Theoretical Chemistry Accounts*, vol. 112, no. 2, pp. 106–112, 2004.

[86] T. Li and P. B. Balbuena, "Theoretical studies of the reduction of ethylene carbonate," *Chemical Physics Letters*, vol. 317, no. 3-5, pp. 421–429, 2000.

[87] Y. Wang, S. Nakamura, M. Ue, and P. B. Balbuena, "Theoretical studies to understand surface chemistry on carbon anodes for lithium-ion batteries: Reduction mechanisms of ethylene carbonate," *Journal of the American Chemical Society*, vol. 123, no. 47, pp. 11 708–11 718, 2001.

[88] J. Yu, P. B. Balbuena, J. Budzien, and K. Leung, "Hybrid DFT Functional-Based Static and Molecular Dynamics Studies of Excess Electron in Liquid Ethylene Carbonate," *Journal of The Electrochemical Society*, vol. 158, no. 4, p. A400, 2011.

[89] K. Tasaki, "Solvent decompositions and physical properties of decomposition compounds in Li-ion battery electrolytes studied by DFT calculations and molecular dynamics simulations," *Journal of Physical Chemistry B*, vol. 109, no. 7, pp. 2920–2933, 2005.

[90] L. E. Camacho-Forero and P. B. Balbuena, "Elucidating electrolyte decomposition under electron-rich environments at the lithium-metal anode," *Physical Chemistry Chemical Physics*, vol. 19, no. 45, pp. 30 861–30 873, 2017.

[91] D. Kuai and P. B. Balbuena, "Inorganic Solid Electrolyte Interphase Engineering Rationales Inspired by Hexafluorophosphate Decomposition Mechanisms," *The Journal of Physical Chemistry C*, vol. 127, no. 4, pp. 1744–1751, 2023.

[92] S. Tan, D. Kuai, Z. Yu, S. Perez-Beltran, M. M. Rahman, K. Xia, N. Wang, Y. Chen, X. Q. Yang, J. Xiao, J. Liu, Y. Cui, Z. Bao, P. B. Balbuena, and E. Hu, "Evolution and Interplay of Lithium Metal Interphase Components Revealed by Experimental and Theoretical Studies," *Journal of the American Chemical Society*, vol. 146, pp. 11 711–11 718, 2024.

[93] F. Fasulo, A. B. Muñoz-García, A. Massaro, O. Crescenzi, C. Huang, and M. Pavone, "Vinylene carbonate reactivity at lithium metal surface: first-principles insights into the early steps of SEI formation," *Journal of Materials Chemistry A*, vol. 11, pp. 5660–5669, 2023.

[94] Y. Wang, S. Nakamura, K. Tasaki, and P. B. Balbuena, "Theoretical studies to understand surface chemistry on carbon anodes for lithium-ion batteries: How does vinylene carbonate play its role as an electrolyte additive?" *Journal of the American Chemical Society*, vol. 124, no. 16, pp. 4408–4421, 2002.

[95] K. Ushirogata, K. Sodeyama, Y. Okuno, and Y. Tateyama, "Additive effect on reductive decomposition and binding of carbonate-based solvent toward solid electrolyte interphase formation in lithium-ion battery," *Journal of the American Chemical Society*, vol. 135, no. 32, pp. 11 967–11 974, 2013.

[96] E. P. Kamphaus, S. A. Gomez, X. Qin, M. Shao, and P. B. Balbuena, "Effects of Solid Electrolyte Interphase Components on the Reduction of LiFSI over Lithium Metal," *ChemPhysChem*, vol. 21, no. 12, pp. 1310–1317, 2020.

[97] S. Perez Beltran and P. B. Balbuena, "SEI formation mechanisms and Li^+ dissolution in lithium metal anodes: Impact of the electrolyte composition and the electrolyte-to-anode ratio," *Journal of Power Sources*, vol. 551, no. September, p. 232203, 2022.

[98] J. M. Martinez De La Hoz, F. A. Soto, and P. B. Balbuena, "Effect of the electrolyte composition on SEI reactions at Si anodes of Li Ion batteries," *Journal of Physical Chemistry C*, vol. 119, no. 13, pp. 7060–7068, 2015.

[99] D. Bedrov, G. D. Smith, and A. C. Van Duin, "Reactions of singly-reduced ethylene carbonate in lithium battery electrolytes: A molecular dynamics simulation study using the ReaxFF," *Journal of Physical Chemistry A*, vol. 116, no. 11, pp. 2978–2985, 2012.

[100] F. Ospina-Acevedo, N. Guo, and P. B. Balbuena, "Lithium oxidation and electrolyte decomposition at Li-metal/liquid electrolyte interfaces," *Journal of Materials Chemistry A*, vol. 8, no. 33, pp. 17 036–17 055, 2020.

[101] N. Kumar and J. M. Seminario, "Lithium-Ion Model Behavior in an Ethylene Carbonate Electrolyte Using Molecular Dynamics," *Journal of Physical Chemistry C*, vol. 120, no. 30, pp. 16 322–16 332, 2016.

[102] S. P. Kim, A. C. Duin, and V. B. Shenoy, "Effect of electrolytes on the structure and evolution of the solid electrolyte interphase (SEI) in Li-ion batteries: A molecular dynamics study," *Journal of Power Sources*, vol. 196, no. 20, pp. 8590–8597, 2011.

[103] Y. Liu, P. Yu, Y. Wu, H. Yang, M. Xie, L. Huai, W. A. Goddard, and T. Cheng, "The DFT-ReaxFF Hybrid Reactive Dynamics Method with Application to the Reductive Decomposition Reaction of the TFSI and DOL Electrolyte at a Lithium–Metal Anode Surface," *The Journal of Physical Chemistry Letters*, vol. 12, pp. 1300–1306, 2021.

[104] F. Röder, R. D. Braatz, and U. Krewer, "Direct coupling of continuum and kinetic Monte Carlo models for multiscale simulation of electrochemical systems," *Computers and Chemical Engineering*, vol. 121, pp. 722–735, 2019.

[105] E. Engel and R. M. Dreizler, *Density Functional Theory*. Springer Berlin Heidelberg, 2011.

[106] D. Frenkel and B. Smit, *Understanding Molecular Simulation*, 2nd ed. Academic Press, 2002.

[107] M. E. Tuckerman, *Statistical Mechanics: Theory and Molecular Simulation*. Oxford University PressOxford, 2023.

[108] J. Newman and N. P. Balsara, *Electrochemical systems*, 4th ed. John Wiley & Sons, 2021.

[109] A. Jansen, *An Introduction to Kinetic Monte Carlo Simulations of Surface Reactions*. Springer Berlin Heidelberg, 2012, vol. 856.

[110] M. Andersen, C. Panosetti, and K. Reuter, "A Practical Guide to Surface Kinetic Monte Carlo Simulations," *Frontiers in Chemistry*, vol. 7, pp. 1–24, 2019.

[111] P. Kratzer, "Monte Carlo and kinetic Monte Carlo methods," in *Multiscale Simulation Methods in Molecular Sciences*, J. Grotendorst, N. Attig, S. Blügel, and D. Marx, Eds. Jülich Supercomputing Centre, 2009, pp. 51–74.

[112] K. Reuter, "First-Principles Kinetic Monte Carlo Simulations for Heterogeneous Catalysis: Concepts, Status, and Frontiers," *Modeling and Simulation of Heterogeneous Catalytic Reactions*, pp. 71–111, 2011.

[113] A. Chatterjee and D. G. Vlachos, "An overview of spatial microscopic and accelerated kinetic Monte Carlo methods," *Journal of Computer-Aided Materials Design*, vol. 14, no. 2, pp. 253–308, 2007.

[114] T. P. Schulze, "Kinetic Monte Carlo simulations with minimal searching," *Physical Review E - Statistical Physics, Plasmas, Fluids, and Related Interdisciplinary Topics*, vol. 65, no. 3, pp. 1–3, 2002.

[115] T. P. Schulze, "Efficient kinetic Monte Carlo simulation," *Journal of Computational Physics*, vol. 227, pp. 2455–2462, 2008.

[116] A. Bortz, M. Kalos, and J. Lebowitz, "A new algorithm for Monte Carlo simulation of Ising spin systems," *Journal of Computational Physics*, vol. 17, pp. 10–18, 1975.

[117] D. T. Gillespie, "A General Method for Numerically Simulating the Stochastic Time Evolution of Coupled Chemical Reactions," pp. 403–434, 1976.

[118] K. A. Fichthorn and W. H. Weinberg, "Theoretical foundations of dynamical Monte Carlo simulations," *The Journal of Chemical Physics*, vol. 95, pp. 1090–1096, 1991.

[119] H. Eyring, "The activated complex in chemical reactions," *The Journal of Chemical Physics*, vol. 3, pp. 63–71, 1935.

[120] Z. Liu and P. P. Mukherjee, "Mesoscale Elucidation of Surface Passivation in the Li-Sulfur Battery Cathode," *ACS Applied Materials and Interfaces*, vol. 9, no. 6, pp. 5263–5271, 2017.

[121] V. Thangavel, O. X. Guerrero, M. Quiroga, A. M. Mikala, A. Rucci, and A. A. Franco, "A three dimensional kinetic Monte Carlo model for simulating the carbon/sulfur mesostructural evolutions of discharging lithium sulfur batteries," *Energy Storage Materials*, vol. 24, pp. 472–485, 2020.

[122] W. Cistjakov, J. Hoppe, J. Jung, F. Röder, H. T. Kim, and U. Krewer, "Insight into the Impact of Electrolyte on Passivation of Lithium–Sulfur Cathodes," *Advanced Materials Interfaces*, 2024.

[123] Y. Yin, R. Zhao, Y. Deng, and A. A. Franco, "Compactness of the Lithium Peroxide Thin Film Formed in Li-O_2 Batteries and Its Link to the Charge Transport Mechanism: Insights from Stochastic Simulations," *Journal of Physical Chemistry Letters*, vol. 8, no. 3, pp. 599–604, 2017.

[124] G. Blanquer, Y. Yin, M. A. Quiroga, and A. A. Franco, " Modeling Investigation of the Local Electrochemistry in Lithium-O_2 Batteries: A Kinetic Monte Carlo Approach ," *Journal of The Electrochemical Society*, vol. 163, no. 3, pp. A329–A337, 2016.

[125] G. Ramos-Sanchez, F. a. Soto, J. M. Martinez De La Hoz, Z. Liu, P. P. Mukherjee, F. El-Mellouhi, J. M. Seminario, and P. B. Balbuena, "Computational studies of interfacial reactions at anode materials: Initial stages of the solid-electrolyte-interphase layer formation," *Journal of Electrochemical Energy Conversion and Storage*, vol. 13, no. 3, pp. 1–10, 2016.

[126] F. Hao, Z. Liu, P. B. Balbuena, and P. P. Mukherjee, "Mesoscale Elucidation of Solid Electrolyte Interphase Layer Formation in Li-Ion Battery Anode," *Journal of Physical Chemistry C*, vol. 121, no. 47, pp. 26 233–26 240, 2017.

[127] X. Xie, E. W. Clark Spotte-Smith, M. Wen, H. D. Patel, S. M. Blau, and K. A. Persson, "Data-Driven Prediction of Formation Mechanisms of Lithium Ethylene Monocarbonate with an Automated Reaction Network," *Journal of the American Chemical Society*, vol. 143, no. 33, pp. 13 245–13 258, 2021.

[128] M. Esmaeilpour, S. Jana, H. Li, M. Soleymanibrojeni, and W. Wenzel, "A Solution-Mediated Pathway for the Growth of the Solid Electrolyte Interphase in Lithium-Ion Batteries," *Advanced Energy Materials*, vol. 13, no. 14, 2023.

[129] M. Gerasimov, F. A. Soto, J. Wagner, F. Baakes, N. Guo, F. Ospina-Acevedo, F. Röder, P. B. Balbuena, and U. Krewer, "Species Distribution During Solid Electrolyte Interphase Formation on Lithium Using MD/DFT-Parameterized Kinetic Monte Carlo Simulations," *The Journal of Physical Chemistry C*, vol. 127, no. 10, pp. 4872–4886, 2023.

[130] S. Perez-Beltran, D. Kuai, and P. B. Balbuena, "SEI Formation and Lithium-Ion Electrodeposition Dynamics in Lithium Metal Batteries via First-Principles Kinetic Monte Carlo Modeling," *ACS Energy Letters*, vol. 9, pp. 5268–5278, 2024.

[131] K. Hankins, M. H. Putra, J. Wagner-Henke, A. Groß, and U. Krewer, "Insights on SEI Growth and Properties in Na-Ion Batteries via Physically Driven Kinetic Monte Carlo Model," *Advanced Energy Materials*, vol. 2401153, pp. 1–13, 2024.

[132] T. O. Drews, R. D. Braatz, and R. C. Alkire, "Coarse-Grained Kinetic Monte Carlo Simulation of Copper Electrodeposition with Additives," *International Journal for Multiscale Computational Engineering*, vol. 2, no. 2, pp. 313–327, 2004.

[133] J. Neuhaus, D. Bellaire, M. Kohns, E. von Harbou, and H. Hasse, "Self-Diffusion Coefficients in Solutions of Lithium Bis(fluorosulfonyl)imide with Dimethyl Carbonate and Ethylene Carbonate," *Chemie-Ingenieur-Technik*, vol. 91, no. 11, pp. 1633–1639, 2019.

[134] F. A. Soto and P. B. Balbuena, "Elucidating Oligomer-Surface and Oligomer-Oligomer Interactions at a Lithiated Silicon Surface," *Electrochimica Acta*, vol. 220, pp. 312–321, 2016.

[135] M. Pippig and F. Mercuri, "Efficient evaluation of Coulomb interactions in kinetic Monte Carlo simulations of charge transport," *The Journal of Chemical Physics*, vol. 152, no. 16, p. 164102, 2020.

[136] R. Callejas-Tovar, C. A. Diaz, J. M. De La Hoz, and P. B. Balbuena, "Dealloying of platinum-based alloy catalysts: Kinetic Monte Carlo simulations," *Electrochimica Acta*, vol. 101, pp. 326–333, 2013.

[137] L. Kolzenberg, A. Latz, and B. Horstmann, "Solid–Electrolyte Interphase During Battery Cycling: Theory of Growth Regimes," *ChemSusChem*, vol. 13, no. 15, pp. 3901–3910, 2020.

[138] D. Aurbach, B. Markovsky, a. Shechter, Y. Ein-Eli, and H. Cohen, "A comparative Study of Synthetic Graphite and Li Electrodes in Electrolyte Solutions Based on Ethylene Carbonate-Dimethyl Carbonate Mixtures," *Journal of the Electrochemical Society*, vol. 143, no. 12, pp. 3809–3820, 1996.

[139] D. Aurbach, A. Zaban, A. Schechter, Y. Ein-Eli, E. Zinigrad, and B. Markovsky, "The Study of Electrolyte Solutions Based on Ethylene and Diethyl Carbonates for Rechargeable Li Batteries I. Li Metal Anodes," *Journal of the Electrochemical Society*, vol. 142, no. 9, pp. 2873–2882, 1995.

[140] D. Aurbach, a. Zaban, Y. Ein-Eli, I. Weissman, O. Chusid, B. Markovsky, M. Levi, E. Levi, a. Schechter, and E. Granot, "Recent studies on the correlation between surface chemistry, morphology, three-dimensional structures and performance of Li and Li-C intercalation anodes in several important electrolyte systems," *Journal of Power Sources*, vol. 68, no. 1, pp. 91–98, 1997.

[141] R. Krishnan, J. S. Binkley, R. Seeger, and J. A. Pople, "Self-consistent molecular orbital methods. XX. A basis set for correlated wave functions," *The Journal of Chemical Physics*, vol. 72, no. 1, pp. 650–654, 1980.

[142] M. J. Frisch, G. W. Trucks, H. B. Schlegel, G. E. Scuseria, M. A. Robb, J. R. Cheeseman, G. Scalmani, V. Barone, and G. A. Petersson, "Gaussian 16 Revision C.01," p. Gaussian Inc.: Wallingford CT, 2016.

[143] A. V. Marenich, C. J. Cramer, and D. G. Truhlar, "Universal solvation model based on solute electron density and on a continuum model of the solvent defined by the bulk dielectric constant and atomic surface tensions," *Journal of Physical Chemistry B*, vol. 113, no. 18, pp. 6378–6396, 2009.

[144] F. Single, A. Latz, and B. Horstmann, "Identifying the Mechanism of Continued Growth of the Solid–Electrolyte Interphase," *ChemSusChem*, vol. 11, no. 12, pp. 1950–1955, 2018.

[145] P. Sayavong, W. Zhang, S. T. Oyakhire, D. T. Boyle, Y. Chen, S. C. Kim, R. A. Vilá, S. E. Holmes, M. S. Kim, S. F. Bent, Z. Bao, and Y. Cui, "Dissolution of the Solid Electrolyte Interphase and Its Effects on Lithium Metal Anode Cyclability," *Journal of the American Chemical Society*, vol. 145, no. 22, pp. 12 342–12 350, 2023.

[146] S. M. Wood, C. Fang, E. J. Dufek, S. C. Nagpure, S. V. Sazhin, B. Liaw, and Y. S. Meng, "Predicting Calendar Aging in Lithium Metal Secondary Batteries: The Impacts of Solid Electrolyte Interphase Composition and Stability," *Advanced Energy Materials*, vol. 8, no. 26, pp. 1–6, 2018.

[147] D. T. Boyle, W. Huang, H. Wang, Y. Li, H. Chen, Z. Yu, W. Zhang, Z. Bao, and Y. Cui, "Corrosion of lithium metal anodes during calendar ageing and its microscopic origins," *Nature Energy*, vol. 6, no. 5, pp. 487–494, 2021.

[148] H. Yang, G. V. Zhuang, and P. N. Ross, "Thermal stability of $LiPF_6$ salt and Li-ion battery electrolytes containing $LiPF_6$," *Journal of Power Sources*, vol. 161, pp. 573–579, 2006.

[149] Q. Wang, J. Sun, X. Yao, and C. Chen, "Thermal stability of $LiPF_6$/EC+DEC electrolyte with charged electrodes for lithium ion batteries," *Thermochimica Acta*, vol. 437, pp. 12–16, 2005.

[150] R. Jung, M. Metzger, F. Maglia, C. Stinner, and H. A. Gasteiger, "Oxygen Release and Its Effect on the Cycling Stability of $LiNi_xMn_yCo_zO_2$ (NMC) Cathode Materials for Li-Ion Batteries," *Journal of The Electrochemical Society*, vol. 164, pp. A1361–A1377, 2017.

[151] L. Suo, W. Xue, M. Gobet, S. G. Greenbaum, C. Wang, Y. Chen, W. Yang, Y. Li, and J. Li, "Fluorine-donating electrolytes enable highly reversible 5-V-class Li metal batteries," *Proceedings of the National Academy of Sciences of the United States of America*, vol. 115, no. 6, pp. 1156–1161, 2018.

[152] K. Xu, "Nonaqueous liquid electrolytes for lithium-based rechargeable batteries," *Chemical Reviews*, vol. 104, no. 10, pp. 4303–4417, 2004.

[153] S.-K. Otto, Y. Moryson, T. Krauskopf, K. Peppler, J. Sann, J. Janek, and A. Henss, "In-Depth Characterization of Lithium-Metal Surfaces with XPS and ToF-SIMS: Toward Better Understanding of the Passivation Layer," *Chemistry of Materials*, vol. 33, no. 3, pp. 859–867, 2021.

[154] D. Aurbach, K. Gamolsky, B. Markovsky, Y. Gofer, M. Schmidt, and U. Heider, "On the use of vinylene carbonate (VC) as an additive to electrolyte solutions for Li-ion batteries," *Electrochimica Acta*, vol. 47, no. 9, pp. 1423–1439, 2002.

[155] H. Ota, K. Shima, M. Ue, and J. ichi Yamaki, "Effect of vinylene carbonate as additive to electrolyte for lithium metal anode," *Electrochimica Acta*, vol. 49, no. 4, pp. 565–572, 2004.

[156] R. Mogi, M. Inaba, S.-K. Jeong, Y. Iriyama, T. Abe, and Z. Ogumi, "Effects of Some Organic Additives on Lithium Deposition in Propylene Carbonate," *Journal of The Electrochemical Society*, vol. 149, no. 12, p. A1578, 2002.

[157] F. M. Weber, I. Kohlhaas, and E. Figgemeier, "Tuning the Reactivity of Electrolyte Solvents on Lithium Metal by Vinylene Carbonate," *Journal of The Electrochemical Society*, vol. 167, no. 14, p. 140523, 2020.

[158] K. Ushirogata, K. Sodeyama, Z. Futera, Y. Tateyama, and Y. Okuno, "Near-Shore Aggregation Mechanism of Electrolyte Decomposition Products to Explain Solid Electrolyte Interphase Formation," *Journal of The Electrochemical Society*, vol. 162, no. 14, pp. A2670–A2678, 2015.

[159] S. J. An, J. Li, C. Daniel, D. Mohanty, S. Nagpure, and D. L. Wood, "The state of understanding of the lithium-ion-battery graphite solid electrolyte interphase (SEI) and its relationship to formation cycling," *Carbon*, vol. 105, pp. 52–76, 2016.

[160] D. R. D'hooge, P. H. M. Van Steenberge, P. Derboven, M.-F. Reyniers, and G. B. Marin, "Model-based design of the polymer microstructure: bridging the gap between polymer chemistry and engineering," *Polymer Chemistry*, vol. 6, no. 40, pp. 7081–7096, 2015.

[161] X. Q. Zhang, R. A. Van Santen, and A. P. Jansen, "Kinetic Monte Carlo modeling of silicate oligomerization and early gelation," *Physical Chemistry Chemical Physics*, vol. 14, no. 34, pp. 11 969–11 973, 2012.

[162] X.-Q. Zhang, T. T. Trinh, R. A. Van Santen, and A. P. J. Jansen, "Mechanism of the Initial Stage of Silicate Oligomerization," *J. Am. Chem. Soc*, vol. 133, pp. 6613–6625, 2011.

[163] F. J. Arraez, P. H. Van Steenberge, and D. R. D'hooge, "The competition of termination and shielding to evaluate the success of surface-initiated reversible deactivation radical polymerization," *Polymers*, vol. 12, no. 6, 2020.

[164] ——, "Conformational Distributions near and on the Substrate during Surface-Initiated Living Polymerization: A Lattice-Based Kinetic Monte Carlo Approach," *Macromolecules*, vol. 53, no. 12, pp. 4630–4648, 2020.

[165] D. Li, D. Danilov, Z. Zhang, H. Chen, Y. Yang, and P. H. L. Notten, "Modeling the SEI-Formation on Graphite Electrodes in $LiFePO_4$ Batteries," *Journal of The Electrochemical Society*, vol. 162, no. 6, pp. A858–A869, 2015.

[166] M. Tang, S. Lu, and J. Newman, "Experimental and Theoretical Investigation of Solid-Electrolyte-Interphase Formation Mechanisms on Glassy Carbon," *Journal of The Electrochemical Society*, vol. 159, no. 11, pp. A1775–A1785, 2012.

[167] M. Broussely, S. Herreyre, P. Biensan, P. Kasztejna, K. Nechev, and R. J. Staniewicz, "Aging mechanism in Li ion cells and calendar life predictions," *Journal of Power Sources*, vol. 97-98, pp. 13–21, 2001.

[168] S. Shi, P. Lu, Z. Liu, Y. Qi, L. G. Hector, H. Li, and S. J. Harris, "Direct calculation of Li-ion transport in the solid electrolyte interphase," *Journal of the American Chemical Society*, vol. 134, no. 37, pp. 15 476–15 487, 2012.

[169] E. Dologlou, "Self-Diffusion in solid lithium," *Glass Physics and Chemistry*, vol. 36, no. 5, pp. 570–574, 2010.

[170] L. D. Gibson and J. Pfaendtner, "Solvent oligomerization pathways facilitated by electrolyte additives during solid-electrolyte interphase formation," *Physical Chemistry Chemical Physics*, vol. 22, no. 37, pp. 21 494–21 503, 2020.

[171] Y. Kamikawa, K. Amezawa, and K. Terada, "First-Principles Study on the Mechanical Properties of Polymers Formed by the Electrochemical Reduction of Fluoroethylene Carbonate and Vinylene Carbonate," *Journal of Physical Chemistry C*, vol. 124, no. 37, pp. 19 937–19 944, 2020.

[172] L. El Ouatani, R. Dedryvère, C. Siret, P. Biensan, S. Reynaud, P. Iratçabal, and D. Gonbeau, "The Effect of Vinylene Carbonate Additive on Surface Film Formation on Both Electrodes in Li-Ion Batteries," *Journal of The Electrochemical Society*, vol. 156, no. 2, p. A103, 2009.

[173] A. L. Michan, B. S. Parimalam, M. Leskes, R. N. Kerber, T. Yoon, C. P. Grey, and B. L. Lucht, "Fluoroethylene carbonate and vinylene carbonate reduction: Understanding

lithium-ion battery electrolyte additives and solid electrolyte interphase formation," *Chemistry of Materials*, vol. 28, no. 22, pp. 8149–8159, 2016.

[174] M. Nie, J. Demeaux, B. T. Young, D. R. Heskett, Y. Chen, A. Bose, J. C. Woicik, and B. L. Lucht, "Effect of Vinylene Carbonate and Fluoroethylene Carbonate on SEI Formation on Graphitic Anodes in Li-Ion Batteries," *Journal of The Electrochemical Society*, vol. 162, no. 13, pp. A7008–A7014, 2015.

[175] B. Zhang, M. Metzger, S. Solchenbach, M. Payne, S. Meini, H. A. Gasteiger, A. Garsuch, and B. L. Lucht, "Role of 1,3-Propane Sultone and Vinylene Carbonate in Solid Electrolyte Interface Formation and Gas Generation," *Journal of Physical Chemistry C*, vol. 119, no. 21, pp. 11 337–11 348, 2015.

[176] H. Ota, Y. Sakata, A. Inoue, and S. Yamaguchi, "Analysis of Vinylene Carbonate Derived SEI Layers on Graphite Anode," *Journal of The Electrochemical Society*, vol. 151, no. 10, p. A1659, 2004.

[177] J. Wellmann, J. P. Brinkmann, B. Wankmiller, K. Neuhaus, U. Rodehorst, M. R. Hansen, M. Winter, and E. Paillard, "Effective Solid Electrolyte Interphase Formation on Lithium Metal Anodes by Mechanochemical Modification," *ACS Applied Materials and Interfaces*, vol. 13, no. 29, pp. 34 227–34 237, 2021.

[178] K. Thanner, A. Varzi, D. Buchholz, S. J. Sedlmaier, and S. Passerini, "Artificial Solid Electrolyte Interphases for Lithium Metal Electrodes by Wet Processing: The Role of Metal Salt Concentration and Solvent Choice," *ACS Applied Materials and Interfaces*, vol. 12, no. 29, pp. 32 851–32 862, 2020.

[179] M. He, R. Guo, G. M. Hobold, H. Gao, and B. M. Gallant, "The intrinsic behavior of lithium fluoride in solid electrolyte interphases on lithium," *Proceedings of the National Academy of Sciences of the United States of America*, vol. 117, no. 1, pp. 73–79, 2020.

[180] J. Genzer, "In silico polymerization: Computer simulation of controlled radical polymerization in bulk and on flat surfaces," *Macromolecules*, vol. 39, no. 20, pp. 7157–7169, 2006.

[181] H. Liu, Y. L. Zhu, J. Zhang, Z. Y. Lu, and Z. Y. Sun, "Influence of grafting surface curvature on chain polydispersity and molecular weight in concave surface-initiated polymerization," *ACS Macro Letters*, vol. 1, no. 11, pp. 1249–1253, 2012.

[182] E. Mastan, L. Xi, and S. Zhu, "Factors Affecting Grafting Density in Surface-Initiated ATRP: A Simulation Study," *Macromolecular Theory and Simulations*, vol. 25, no. 3, pp. 220–228, 2016.

[183] P. Polanowski, J. K. Jeszka, and K. Matyjaszewski, “Polymer brushes in pores by ATRP: Monte Carlo simulations,” *Polymer*, vol. 211, p. 123124, 2020.

[184] Y. N. Zhou, J. J. Li, T. T. Wang, Y. Y. Wu, and Z. H. Luo, “Precision polymer synthesis by controlled radical polymerization: Fusing the progress from polymer chemistry and reaction engineering,” *Progress in Polymer Science*, vol. 130, p. 101555, 2022.

[185] R. Stockhausen, L. Gehrlein, M. Müller, T. Bergfeldt, A. Hofmann, F. J. Müller, J. Maibach, H. Ehrenberg, and A. Smith, “Investigating the dominant decomposition mechanisms in lithium-ion battery cells responsible for capacity loss in different stages of electrochemical aging,” *Journal of Power Sources*, vol. 543, no. June, p. 231842, 2022.

[186] M. Leißing, F. Horsthemke, S. Wiemers-Meyer, M. Winter, P. Niehoff, and S. Nowak, “The Impact of the C-Rate on Gassing During Formation of NMC622 II Graphite Lithium-Ion Battery Cells,” *Batteries and Supercaps*, vol. 4, no. 8, pp. 1344–1350, 2021.

[187] Z. L. Brown, S. Jurng, and B. L. Lucht, “Investigation of the Lithium Solid Electrolyte Interphase in Vinylene Carbonate Electrolytes Using Cu|LiFePO$_4$ Cells ,” *Journal of The Electrochemical Society*, vol. 164, no. 9, pp. A2186–A2189, 2017.

[188] X. Ren, Y. Zhang, M. H. Engelhard, Q. Li, J. G. Zhang, and W. Xu, “Guided Lithium Metal Deposition and Improved Lithium Coulombic Efficiency through Synergistic Effects of LiAsF$_6$ and Cyclic Carbonate Additives,” *ACS Energy Letters*, vol. 3, no. 1, pp. 14–19, 2018.

[189] H. Ozaki, K. Kuratani, and T. Kiyobayashi, “Monte-Carlo Simulation of the Ionic Transport of Electrolyte Solutions at High Concentrations Based on the Pseudo-Lattice Model,” *Journal of The Electrochemical Society*, vol. 163, pp. H576–H583, 2016.

[190] H. Li, Y. Li, H. Li, and J. L. Brédas, “Organic Field-Effect Transistors: A 3D Kinetic Monte Carlo Simulation of the Current Characteristics in Micrometer-Sized Devices,” *Advanced Functional Materials*, vol. 27, no. 9, 2017.

[191] H. Li and J. L. Brédas, “Kinetic Monte Carlo Modeling of Charge Carriers in Organic Electronic Devices: Suppression of the Self-Interaction Error,” *Journal of Physical Chemistry Letters*, vol. 8, no. 11, pp. 2507–2512, 2017.

[192] F. Yang and S. R. Forrest, “Photocurrent generation in nanostructured organic solar cells,” *ACS Nano*, vol. 2, no. 5, pp. 1022–1032, 2008.

[193] M. Casalegno, G. Raos, and R. Po, “Methodological assessment of kinetic Monte Carlo simulations of organic photovoltaic devices: The treatment of electrostatic interactions,” *The Journal of Chemical Physics*, vol. 132, no. 9, p. 094705, 2010.

[194] R. G. Kimber, E. N. Wright, S. E. O'Kane, A. B. Walker, and J. C. Blakesley, "Mesoscopic kinetic Monte Carlo modeling of organic photovoltaic device characteristics," *Physical Review B - Condensed Matter and Materials Physics*, vol. 86, no. 23, pp. 1–9, 2012.

[195] P. K. Watkins, A. B. Walker, and G. L. Verschoor, "Dynamical monte carlo modelling of organic solar cells: The dependence of internal quantum efficiency on morphology," *Nano Letters*, vol. 5, no. 9, pp. 1814–1818, 2005.

[196] L. Meng, D. Wang, Q. Li, Y. Yi, J. L. Brödas, and Z. Shuai, "An improved dynamic Monte Carlo model coupled with Poisson equation to simulate the performance of organic photovoltaic devices," *Journal of Chemical Physics*, vol. 134, no. 12, 2011.

[197] J. J. Van Der Holst, F. W. Van Oost, R. Coehoorn, and P. A. Bobbert, "Monte Carlo study of charge transport in organic sandwich-type single-carrier devices: Effects of Coulomb interactions," *Physical Review B - Condensed Matter and Materials Physics*, vol. 83, no. 8, pp. 1–13, 2011.

[198] P. Hein, B. O. Grope, J. Koettgen, S. Grieshammer, and M. Martin, "Kinetic Monte Carlo simulations of ionic conductivity in oxygen ion conductors," *Materials Chemistry and Physics*, vol. 257, p. 123767, 2021.

[199] D. S. Gunn, N. L. Allan, and J. A. Purton, "Adaptive kinetic Monte Carlo simulation of solid oxide fuel cell components," *Journal of Materials Chemistry A*, vol. 2, no. 33, pp. 13 407–13 414, 2014.

[200] R. Pornprasertsuk, J. Cheng, H. Huang, and F. B. Prinz, "Electrochemical impedance analysis of solid oxide fuel cell electrolyte using kinetic Monte Carlo technique," *Solid State Ionics*, vol. 178, no. 3-4, pp. 195–205, 2007.

[201] M. Jaipal and A. Chatterjee, "Mesoscale understanding of ionic conduction in yttria stabilized zirconia: The nanoscale percolation network and its effect on O_2-ion movement," *Modelling and Simulation in Materials Science and Engineering*, vol. 27, no. 6, 2019.

[202] J. Koettgen, S. Grieshammer, P. Hein, B. O. Grope, M. Nakayama, and M. Martin, "Understanding the ionic conductivity maximum in doped ceria: Trapping and blocking," *Physical Chemistry Chemical Physics*, vol. 20, no. 21, pp. 14 291–14 321, 2018.

[203] B. J. Morgan, "Lattice-geometry effects in garnet solid electrolytes: a lattice-gas Monte Carlo simulation study," *Royal Society Open Science*, vol. 4, p. 170824, 2017.

[204] L. Meng, Y. Shang, Q. Li, Y. Li, X. Zhan, Z. Shuai, R. G. Kimber, and A. B. Walker, "Dynamic monte carlo simulation for highly efficient polymer blend photovoltaics," *Journal of Physical Chemistry B*, vol. 114, no. 1, pp. 36–41, 2010.

[205] R. A. Marsh, C. Groves, and N. C. Greenham, "A microscopic model for the behavior of nanostructured organic photovoltaic devices," *Journal of Applied Physics*, vol. 101, no. 8, p. 083509, 2007.

[206] H. Li and J. L. Brédas, "Developing molecular-level models for organic field-effect transistors," *National Science Review*, vol. 8, no. 4, 2021.

[207] L. Greengard and V. Rokhlin, "A fast algorithm for particle simulations," *Journal of Computational Physics*, vol. 135, no. 2, pp. 280–292, 1997.

[208] W. R. Saunders, J. Grant, and E. H. Müller, "A new algorithm for electrostatic interactions in Monte Carlo simulations of charged particles," *Journal of Computational Physics*, vol. 430, p. 110099, 2021.

[209] N. J. van der Kaap and L. J. Koster, "Massively parallel kinetic Monte Carlo simulations of charge carrier transport in organic semiconductors," *Journal of Computational Physics*, vol. 307, pp. 321–332, 2016.

[210] C. Groves, "Simulating charge transport in organic semiconductors and devices: A review," *Reports on Progress in Physics*, vol. 80, no. 2, 2017.

[211] W. R. Saunders, J. Grant, E. H. Müller, and I. Thompson, "Fast electrostatic solvers for kinetic Monte Carlo simulations," *Journal of Computational Physics*, vol. 410, pp. 1–32, 2020.

[212] P. Kordt and D. Andrienko, "Modeling of Spatially Correlated Energetic Disorder in Organic Semiconductors," *Journal of Chemical Theory and Computation*, vol. 12, no. 1, pp. 36–40, 2016.

[213] Y. K. Lee and T. Sinno, "Analysis of the lattice kinetic Monte Carlo method in systems with external fields," *Journal of Chemical Physics*, vol. 145, no. 23, 2016.

[214] K. J. Laidler, "A glossary of terms used in chemical kinetics, including reaction dynamics (IUPAC Recommendations 1996)," *Pure and Applied Chemistry*, vol. 68, pp. 149–192, 1996.

[215] A. J. Ringsby, K. D. Fong, J. Self, H. K. Bergstrom, B. D. McCloskey, and K. A. Persson, "Transport Phenomena in Low Temperature Lithium-Ion Battery Electrolytes," *Journal of The Electrochemical Society*, vol. 168, no. 8, p. 080501, 2021.

[216] L. J. Koster, E. C. Smits, V. D. Mihailetchi, and P. W. Blom, "Device model for the operation of polymer/fullerene bulk heterojunction solar cells," *Physical Review B - Condensed Matter and Materials Physics*, vol. 72, no. 8, pp. 1–9, 2005.

[217] S. A. Krachkovskiy, J. D. Bazak, S. Fraser, I. C. Halalay, and G. R. Goward, " Determination of Mass Transfer Parameters and Ionic Association of $LiPF_6$: Organic Carbonates Solutions ," *Journal of The Electrochemical Society*, vol. 164, no. 4, pp. A912–A916, 2017.

[218] Z. Feng, K. Higa, K. S. Han, and V. Srinivasan, " Evaluating Transport Properties and Ionic Dissociation of $LiPF_6$ in Concentrated Electrolyte ," *Journal of The Electrochemical Society*, vol. 164, no. 12, pp. A2434–A2440, 2017.

[219] D. S. Hall, J. Self, and J. R. Dahn, "Dielectric Constants for Quantum Chemistry and Li-Ion Batteries: Solvent Blends of Ethylene Carbonate and Ethyl Methyl Carbonate," *Journal of Physical Chemistry C*, vol. 119, no. 39, pp. 22 322–22 330, 2015.

[220] M. T. Ong, O. Verners, E. W. Draeger, A. C. Van Duin, V. Lordi, and J. E. Pask, "Lithium ion solvation and diffusion in bulk organic electrolytes from first-principles and classical reactive molecular dynamics," *Journal of Physical Chemistry B*, vol. 119, no. 4, pp. 1535–1545, 2015.

[221] B. G. Choobar, H. Modarress, R. Halladj, and S. Amjad-Iranagh, "Multiscale Investigation on Electrolyte Systems of [(Solvent + Additive) + $LiPF_6$] for Application in Lithium-Ion Batteries," *The Journal of Physical Chemistry C*, vol. 123, pp. 21 913–21 930, 2019.

[222] H. Kataoka, Y. Saito, T. Sakai, S. Deki, and T. Ikeda, "Ionic mobility of cation and anion of lithium gel electrolytes measured by pulsed gradient spin-echo NMR technique under direct electric field," *Journal of Physical Chemistry B*, vol. 105, pp. 2546–2550, 2001.

[223] Y. Saito, H. Kataok, and S. Deki, "Ionic Mobility Measurements Applying a Controlled Direct Electric Field on Pulsed Gradient Spin Echo Nuclear Magnetic Resonance," *Journal of The Electrochemical Society*, vol. 148, p. E382, 2001.

[224] S. M. Blau, H. D. Patel, E. W. C. Spotte-Smith, X. Xie, S. Dwaraknath, and K. A. Persson, "A chemically consistent graph architecture for massive reaction networks applied to solid-electrolyte interphase formation," *Chemical Science*, vol. 12, no. 13, pp. 4931–4939, 2021.

[225] D. Barter, E. W. C. Spotte-Smith, N. S. Redkar, A. Khanwale, S. Dwaraknath, K. A. Persson, and S. M. Blau, "Predictive stochastic analysis of massive filter-based electrochemical reaction networks," *Digital Discovery*, vol. 2, pp. 123–137, 2023.

[226] G. H. Wrodnigg, J. O. Besenhard, and M. Winter, "Cyclic and acyclic sulfites: New solvents and electrolyte additives for lithium ion batteries with graphitic anodes?" *Journal of Power Sources*, vol. 97-98, pp. 592–594, 2001.

[227] Y. Li, K. Leung, and Y. Qi, "Computational Exploration of the Li-Electrode|Electrolyte Interface in the Presence of a Nanometer Thick Solid-Electrolyte Interphase Layer," *Accounts of Chemical Research*, vol. 49, no. 10, pp. 2363–2370, 2016.

[228] L. Benitez, D. Cristancho, J. M. Seminario, J. M. Martinez De La Hoz, and P. B. Balbuena, "Electron transfer through solid-electrolyte-interphase layers formed on Si anodes of Li-ion batteries," *Electrochimica Acta*, vol. 140, pp. 250–257, 2014.

[229] I. Skarmoutsos, V. Ponnuchamy, V. Vetere, and S. Mossa, "Li^+ solvation in pure, binary, and ternary mixtures of organic carbonate electrolytes," *Journal of Physical Chemistry C*, vol. 119, no. 9, pp. 4502–4515, 2015.

[230] M. D. Bhatt, M. Cho, and K. Cho, "Interaction of Li^+ ions with ethylene carbonate (EC): Density functional theory calculations," *Applied Surface Science*, vol. 257, no. 5, pp. 1463–1468, 2010.

[231] S. Chen, C. Niu, H. Lee, Q. Li, L. Yu, W. Xu, J. G. Zhang, E. J. Dufek, M. S. Whittingham, S. Meng, J. Xiao, and J. Liu, "Critical Parameters for Evaluating Coin Cells and Pouch Cells of Rechargeable Li-Metal Batteries," *Joule*, vol. 3, no. 4, pp. 1094–1105, 2019.

[232] K. Hayamizu, "Temperature dependence of self-diffusion coefficients of ions and solvents in ethylene carbonate, propylene carbonate, and diethyl carbonate single solutions and ethylene carbonate + diethyl carbonate binary solutions of $LiPF_6$ studied by NMR," *Journal of Chemical and Engineering Data*, vol. 57, no. 7, pp. 2012–2017, 2012.

[233] T. Hou, G. Yang, N. N. Rajput, J. Self, S. W. Park, J. Nanda, and K. A. Persson, "The influence of FEC on the solvation structure and reduction reaction of $LiPF_6$/EC electrolytes and its implication for solid electrolyte interphase formation," *Nano Energy*, vol. 64, no. May, p. 103881, 2019.

[234] S. A. Delp, O. Borodin, M. Olguin, C. G. Eisner, J. L. Allen, and T. R. Jow, "Importance of Reduction and Oxidation Stability of High Voltage Electrolytes and Additives," *Electrochimica Acta*, vol. 209, pp. 498–510, 2016.

[235] P. Novák, F. Joho, R. Imhof, J.-C. Panitz, and O. Haas, "In situ investigation of the interaction between graphite and electrolyte solutions," *Journal of Power Sources*, vol. 81-82, pp. 212–216, 1999.

[236] A. Naji, J. Ghanbaja, B. Humbert, P. Willmann, and D. Billaud, “Electroreduction of graphite in $LiClO_4$-ethylene carbonate electrolyte. Characterization of the passivating layer by transmission electron microscopy and Fourier-transform infrared spectroscopy,” *Journal of Power Sources*, vol. 63, pp. 33–39, 1996.

List of Figures

List of Tables

List of Symbols and Abbreviations

Symbols

c	Concentration	mol m^{-3}
C^{DL}	Double layer capacitance	F m^{-2}
C_A	Surface specific capacity	Ah m^{-2}
D	Diffusion coefficient	m^2 s^{-1}
d	Thickness	m
$\hat{\mathbf{e}}$	Union vector	–
$\mathbf{E}$, E	Electric field	V m^{-1}
E_A	Energy barrier of reaction	J mol^{-1}
E_A^{bond}	Energy barrier of transport	J mol^{-1}
E_n	Electrostatic energy	J mol^{-1}
$\Delta G^{\ddagger}$	Activation energy	J mol^{-1}
$\Delta_R G$	Gibbs free energy of reaction	J mol^{-1}
$g(r)$	Radial distribution function	–
I	Applied current	A m^{-2}
J	Diffusion flux	mol m^{-2} s^{-1}
k	Reaction rate constant	mol s^{-1} m^{-2}
k_0	Frequency factor	s^{-1}
l	Diffusion length	m
ΔL	Distance between lattice sites	m
$\dot{m}_{el}$	Capacity specific mass	g $(Ah)^{-1}$
M	Molar mass	kg mol^{-1}
n	Number of distinct entities	–
P	Probability of kMC configuration	–
p	Site coverage probability, proportion	–

p_{e^-}	Electron probability	–
Q	Charge of layer	C
q	Charge	C
$Q^{\ddagger}$	Partition function of transition state	–
Q_α	Partition function of initial state α	–
$\mathbf{r}$	Position vector	–
r	Distance	m
T	Temperature	K
t	Zeit	s
U	Potential energy	J
ΔU	Local potential energy difference	J
V	Shell volume in radial distribution function	m^3
v	Reaction rate	mol m^{-2} s^{-1}
V_A	Surface specific electrolyte volume	m
x	Latitude in the Cartesian coordinate system	m
y	Depth in the Cartesian coordinate system	m
z	Height in the Cartesian coordinate system	m
α	Symmetry factor, degree of dissociation	–, %
β	Electron decay factor	m^{-1}
Γ	Transition rate	s^{-1}
ε_r	Relative permittivity	–
ζ	Random number	–
η	Potential difference	V
θ	Fraction of occupied sites	–
κ	Electron transport factor	–
μ	Ionic mobility	m^2 $V^{-1}s^{-1}$
$\boldsymbol{v}^*$	Average effective drift velocity	m s^{-1}
ν	Scaling factor	–
ρ	Charge density, density	C m^{-3}, kg m^{-3}
σ	Standard deviation	C
Φ_a	Anode potential	V

$\Delta\Phi_{Conti}$	Potential difference continuum	V
$\Delta\Phi_{KMC}$	Potential difference kMC	V
Φ_{red}	Reduction potential	V
φ	Local potential	V
Ψ	Number of executed kMC processes	–

Constants

ε_0	Permittivity of the vacuum, 8.854188×10^{-12}	A s V^{-1} m^{-1}
F	Faraday constant, 96485.332	C mol^{-1}
h	Planck constant, $6.62607015 \times 10^{-34}$	J s
k_B	Boltzmann constant, 1.380649×10^{-23}	J K^{-1}
N_A	Avogadro constant, 6.02214×10^{23}	mol^{-1}
R	Ideal gas constant, 8.314	J $mol^{-1}K^{-1}$
e	Elementary charge, 1.60217×10^{-19}	C

Indices

i	Process
j	Species
k	Lattice site
l	Lattice site
m	Charge carrier, species, process
n	Charge carrier, species
nn	Next neighbor
p	Layer, plane
α	kMC configuration
β	kMC configuration

Subscripts/Superscripts

+	Positively charged ion, positive
-	Negatively charged ion, negative

0	Ideal case, bulk
A	Areal
ap	Appear
bot	Bottom layer/direction
cc	Charge carrier
Cl	Clustering
clb	Coulomb
corner	Corner neighbor
cut	Cutoff
D	Diffusion
D/C	Transport of charged species
dir	Direction of reaction/transport
dis	Disappear
edge	Edge neighbor
el	Electrochemical
ext	External
face	Face neighbor
forw	Forward
init	Initial condition
ion	Per ion
KMC	Kinetic Monte Carlo
layers	kMC layer in z-direction
long	Long timescale simulation
M	Migration
max	Maximum
MD	Molecular Dynamics
min	Minimum
ox	Oxidation
R	Reaction
red	Reduction
rev	Reverse
salt	Conductive salt

sc	Single charge
SEI	Solid Electrolyte Interphase
seq	Sequence
short	Short timescale simulation
top	Top layer/direction
total	Total
TST	Transition state theory
V	Volumetric
x	In x-direction
y	In y-direction
z	In z-direction
z^+	Along z-coordinate
z^-	Against z-coordinate

Abbreviations

AFM	Atomic force microscopy
AIMD	Ab-initio molecular dynamics
BC1	Boundary condition 1
BC2	Boundary condition 2
cryo	Cryogenic
DFT	Density functional theory
EC	Ethylene carbonate
EDL	Electrical double layer
EMC	Ethyl methyl carbonate
FTIR	Fourier transform infrared spectroscopy
KIT	Karlsruhe Institute of Technology
kMC	Kinetic Monte Carlo
LIB	Lithium-ion battery
LiEDC	Lithium Ethylene Dicarbonate
LMB	Lithium metal battery
MD	Molecular Dynamics
PES	Potential energy surface

ReaxFF	Reactive force-field
SEI	Solid Electrolyte Interphase
SEM	Scanning electron microscopy
SHE	Standard hydrogen electrode
SMD	Solvation model based on density
TEM	Transmission electron microscopy
TS	Transition state
TST	Transition state theory
VC	Vinylene carbonate
w/	With
w/o	Without
XPS	X-ray photoelectron spectroscopy

A Additional Information Chapter 3[1]

A.1 Model Development and Parametrization

Derivation of electron transport factor κ:

- Probability of electrons is 1 in and directly on lithium metal surface. This leads to $z = 1$, for $z \leq z_{\mathrm{Li,max}} + \Delta L$
- There is no electron transport above the maximum electron transport distance $z_{\mathrm{e^-,max}}$. Therefore holds $z = 0$, for $z \geq z_{\mathrm{Li,max}} + \Delta L + z_{e^-,\mathrm{max}}$
- The electron probability at the maximum electron transport distance $z_{e^-,\mathrm{max}}$ is $p_{\mathrm{e^-}}$. An exponential decay in the form of $\kappa(z) = \exp(-\beta \cdot \Delta z)$ of the electron probability is assumed between the lithium metal surface and the maximum electron transport distance. Substituting $p_{\mathrm{e^-}}$ and $z_{e^-,\mathrm{max}}$ into this equation gives: $p_{\mathrm{e^-}} = \exp(-\beta \cdot z_{\mathrm{e^-,max}})$. Rearrangement leads to $\beta = \frac{\ln(p_{\mathrm{e^-}})}{z_{\mathrm{e^-,max}}}$. Substituting this into the exponential decay equation yields $\kappa(z) = \exp(\frac{\ln(p_{\mathrm{e^-}})}{z_{\mathrm{e^-,max}}} \cdot \Delta z)$

[1] Parts of this chapter have been published in the supporting information of the following article: J. Wagner-Henke et al., Nat. Commun. 14, 6823 (2023) [1], licensed under CC BY 4.0.

Table A.1: List of further model parameters in Chapter 3.

Parameter	Description	Value	Source
α	Symmetry factor	0.5	Chosen
k_0	Frequency factor	10^{13}	Chosen according to literature [110]
D	Diffusion coefficient	$2.27 \cdot 10^{-10}$ m^2 s^{-1}	Chosen according to literature [129, 133]
ΔL	Distance of lattice sites	$3.443 \cdot 10^{-10}$ m	Literature value [129]
C^{DL}	Double layer capacitance	0.2 F m^{-2}	Chosen according to literature [104]
T	Temperature	298.15 K	In accordance with DFT calculations
p_{e^-}	Eelctron probabilty at maximum electron transport distance	1 %	Chosen
$z_{\mathrm{Li,max}}$	Maximum height of lithium layers	$10.33 \cdot 10^{-9}$ m	Chosen
$z_{\mathrm{e}^-,\mathrm{max}}$	Maximum electron transport distance	$2 \cdot 10^{-9}$ m	Literature value [137]
R	Ideal gas constant	8.314 J mol^{-1} K^{-1}	-
F	Faraday constant	$9.648 \cdot 10^4$ C mol^{-1}	-
k_B	Boltzmann factor	$1.38 \cdot 10^{-23}$ J K^{-1}	-
N_A	Avogadro constant	$6.022 \cdot 10^{23}$ mol^{-1}	-
E_A^{bond}	Binding energy lithium metal	436.8 kJ mol^{-1}	Chosen[a]
n_x	Number of sites in x-direction	15	Chosen
n_y	Number of sites in y-direction	15	Chosen
n_z	Number of sites in z-direction	75	Chosen
ε_r	Relative permittivity of EC	90.36	Literature value [226]

[a] The binding energy is chosen in such a way that the oxidation probability of a lithium atom embedded in a smooth surface is 5 % compared to a lithium metal atom without lithium neighbors

A.2 Additional Results

A.2.1 Impact of Updated Transport Rates on SEI Formation

To evaluate the impact of the newly derived transport rates (cf. Section B.1.2) on the results presented in Chapter 3, the SEI formation in EC + 1.2M $LiPF_6$ was recalculated using the new transport rates. The temporal evolution of SEI formation within the first microsecond is shown in Figure A.1, and is compared to the original results in Figure 3.6. Overall, the SEI formation dynamics are not significantly impacted by the updated transport rates. In both cases, the simulations predict the development of a layered SEI structure with Li_2CO_3 forming close to the lithium metal anode and LiF forming above. This structure becomes apparent after 10 ns and the layers can be clearly distinguished after 100 ns. No organic species are formed within the simulated time. The models further consistently predict a rapid initial SEI formation within the first nanosecond, followed by continuous decrease of the growth rate. Moreover, the SEI density increases over time. The modified transport rates result in a slower transport of electrolyte species towards the electrode surface. Therefore, the updated model predicts a slightly slower SEI growth, which does not reach a constant thickness within the first microsecond and is slightly thinner. Despite these differences, the key mechanistic insights and structural characteristics of the predicted SEI remain consistent between both models.

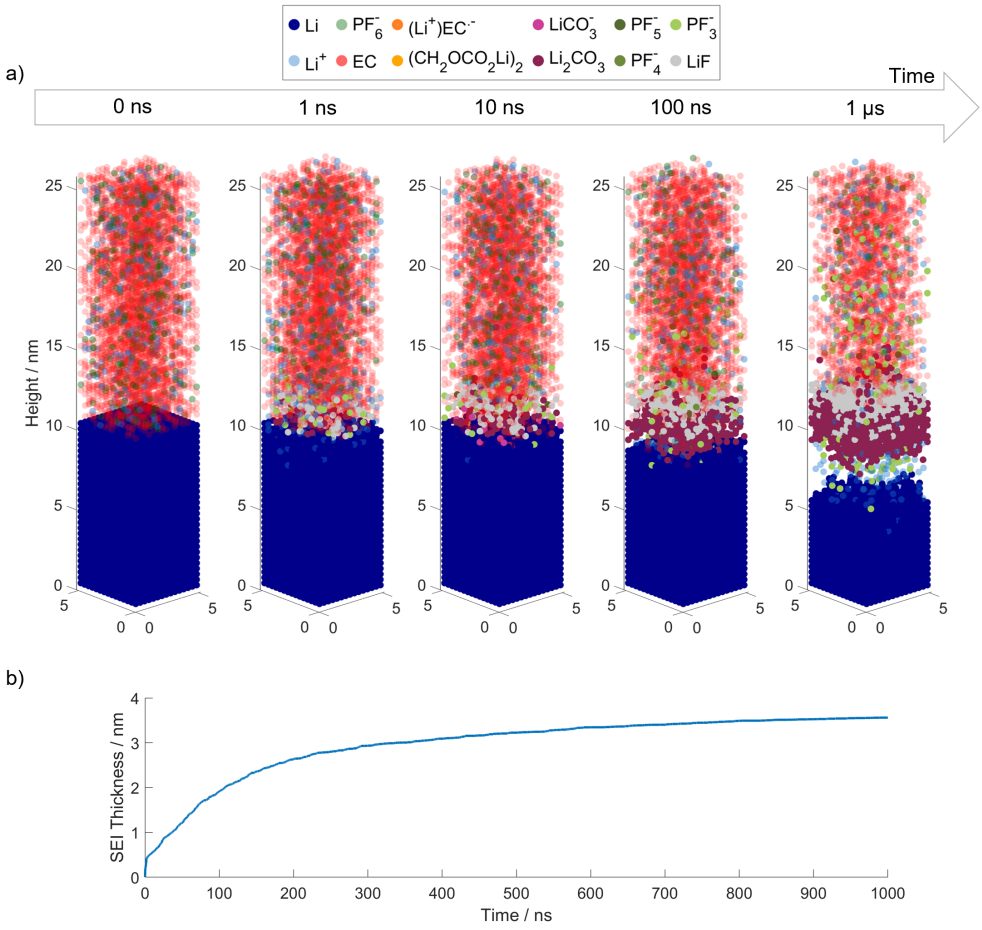

Figure A.1: Temporal evolution of SEI formation on lithium metal in EC + 1.2M $LiPF_6$ electrolyte for updated transport rates as derived in Section B.1.2. a) Resulting species distribution in kMC box at selected times and b) development of SEI thickness over time. Energy values comprise the case for EC reduction in the presence of Li^+.

A.2.2 Impact of Monolayer Step in the Lithium Metal Crystal Structure

In order to evaluate the effect of smaller inhomogeneities of the lithium metal surface morphology on the initial SEI formation, a monolayer step in the initial lithium metal crystal structure was introduced. Apart from this, the simulation was performed with the same parameters which were used for the results in Figure 3.6. The comparison between the final configuration after 1 µs with the monolayer step in Figure A.2 and without the monolayer step in Figure 3.6 demonstrates that

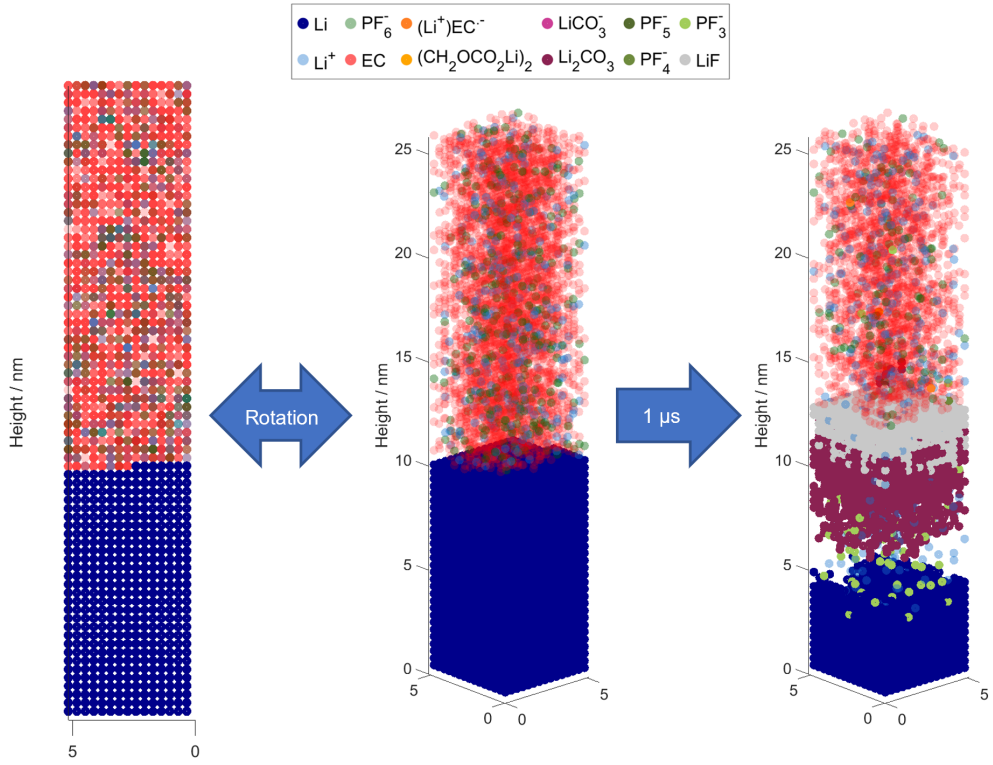

Figure A.2: SEI formation on a non-uniform lithium metal surface with an implemented step in the initial lithium metal crystal structure. Left: Initial kMC-box with step in the crystal structure in 2D. Center: Initial kMC-box with step in the crystal structure rotated in 3D. Right: Final kMC-box showing the SEI structure after 1 µs of simulated time.

there is – apart from stochastic variations – no significant difference in the formed SEI. In both cases, a Li_2CO_3-layer forms below the initial surface with a denser and thinner LiF-layer above. Moreover, the overall thickness of the initial SEI remains the same. Overall, the model suggests no major impact of small surface inhomogeneities on the investigated scale on the formed SEI within the first microsecond after the initial contact between the liquid electrolyte and the lithium metal anode.

A.2.3 Effect of the Electrical Double Layer on the SEI Formation in the Multiscale kMC/Continuum Model

The electrical double layer (EDL) has multiple effects on the formation of the SEI on lithium metal. First of all, it influences the ion distribution in the liquid electrolyte and hence the local

concentration of salt and Li^+ ions as well as charged intermediate species. Thereby, it impacts the availability of these species for reduction reactions. At the same time, the EDL is affected by the formed SEI, and therefore it is constantly changing during SEI formation [227]. Once stable SEI layers have formed, double layers are expected to form at the interface between electrode and SEI, as it is an ion conducting layer, and between SEI and liquid electrolyte - which has a different ion concentration as the SEI. Such a model with two double layers was able to reproduce experiments in Li-ion batteries including the two time semicircles in impedance spectra [24]. In addition, typical times for EDL charge/discharge in batteries are in the order of milliseconds to seconds [69], which is far beyond the here considered timescale.

The presented model considers electrostatic interactions in a simplistic way by considering the charge of the direct environment in the rate calculation of the transport of charged species (cf. Equation 3.6). Moreover, since the lithium metal atoms from the anode are oxidized during the simulation, there are many positively charged Li^+ ions available close to the surface. These implemented phenomena result in the accumulation of positive charges close to the lithium metal surface similar to an EDL within the first 100 ns as can be seen in Figure A.3. This vanishes after the first inorganic SEI has formed due to charge distribution and a decreasing number of lithium oxidation reactions. Hence, on larger timescales a more elaborate consideration of the EDL including the effect of the SEI might be required. A first important step in this direction has been done in Chapter 5 of this thesis, in which different electrostatic interaction models, which also include long-ranging interactions are compared.

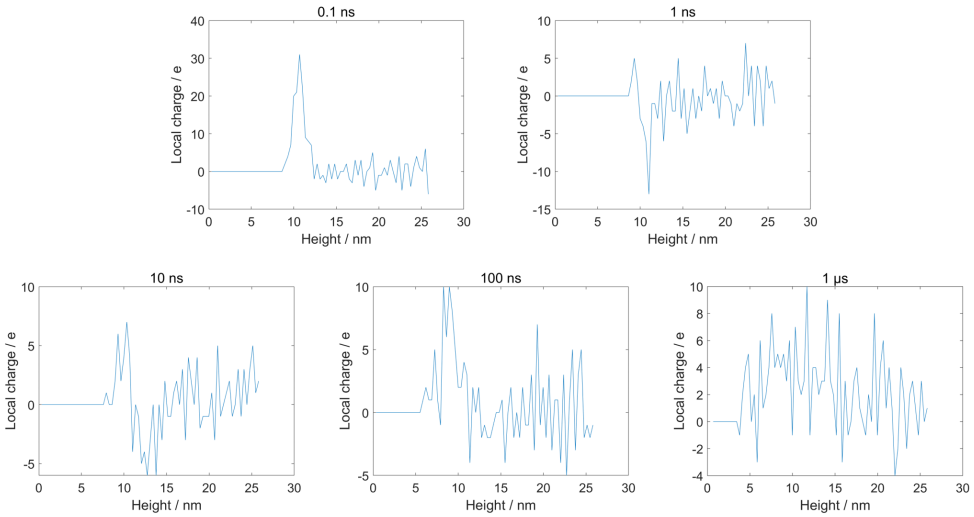

Figure A.3: Charge accumulation during SEI formation as function of height and time, showing the build-up of a double layer like charge distribution at the Li surface, which subsequently vanishes with SEI formation.

A.2.4 $LiPF_6$ Solubility in EC

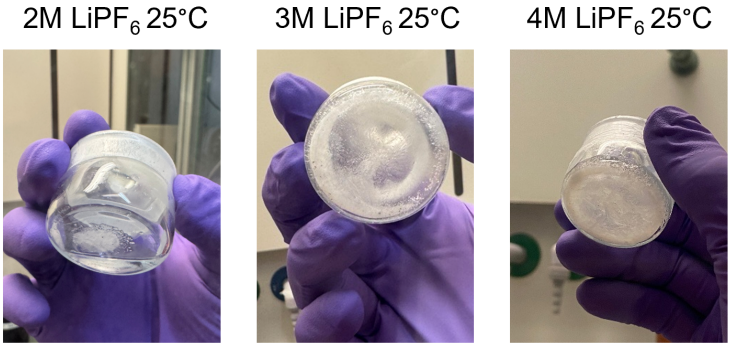

Figure A.4: Photographic documentation of $LiPF_6$ solutions in EC at room temperature for concentrations of 2M, 3M and 4M. Partial precipitation is visible at 2M, while complete solidification occurs at 3M and 4M. Measurements were performed by Leon Schmidt, IAM-ET, KIT.

A.3 Additional Tables

Table A.2: Summary of number of initially present EC molecules ($n_{EC,init}$) and salt molecules ($n_{salt,init}$) in the electron transport zone, number of overall consumed EC molecules ($n_{EC,total}$) and salt molecules ($n_{salt,total}$) and the respective ratio of initially present and overall consumed molecules for all conducted simulations.

Simulation	n_{EC}^{init}	n_{EC}^{total}	$\frac{n_{EC}^{init}}{n_{EC}^{total}}$	$n_{salt}{}^{init}$	n_{salt}^{total}	$\frac{n_{salt}^{init}}{n_{salt}^{total}}$
1M $LiPF_6$	505	1686	0.3	38	329	0.116
1.2M $LiPF_6$	534	1526	0.35	39	330	0.118
1.5M $LiPF_6$	534	1340	0.399	46	333	0.138
2M $LiPF_6$	431	937	0.46	78	353	0.221
30 wt.% EC	147	476	0.31	48	335	0.143
60 wt.% EC	264	832	0.32	51	324	0.157
100 wt.% EC	534	1526	0.35	39	330	0.118

Table A.3: Electronic energetics of structures in Table 3.1, computed at B3PW91/6-311G(3df) level of theory with SMD implemented. C, M represents the charge and multiplicity of the corresponding species, Pot. E. describes the potential energy, H, S and G stand for the enthalpy, entropy and free energy, respectively. The G1M column stands for the free energy value converted from 1 atm to 1 M at standard condition. All energy values are in hartree.

Structure	C, M	Pot. E.	H	S	G	G1M
Li^+	1,1	-7.42082	-7.41846	31.798	-7.43357	-7.43055
EC	0,1	-342.389	-342.309	69.277	-342.342	-342.339
EC^-[a]	-1,2	-342.434	-342.357	71.809	-342.391	-342.388
TS-R2 (w/o Li^+)[a]	-1,2	-342.437	-342.362	77.868	-342.399	-342.396
EC-R[a]	-1,2	-342.475	-342.400	81.669	-342.439	-342.436
$[EC\text{-}Li]^+$	1,1	-349.838	-349.755	75.223	-349.791	-349.788
$[EC\text{-}Li]^+ + e^-$	0,2	-349.894	-349.811	80.678	-349.849	-349.846
$[EC\text{-}Li]^0$	0,2	-349.911	-349.829	80.333	-349.867	-349.864
TS-R2 (w/ Li^+)	0,2	-349.888	-349.81	80.947	-349.848	-349.845
LiEC	0,2	-349.948	-349.87	88.085	-349.912	-349.909
C_2H_4	0,1	-78.5769	-78.522	52.297	-78.5468	-78.5438
TS-R3	0,3	-699.911	-699.753	132.139	-699.816	-699.812
LiEDC	0,1	-621.421	-621.313	112.859	-621.366	-621.363
$[LiEC]^-$	-1,1	-350.026	-349.952	75.253	-349.987	-349.984
TS-R4	-1,1	-350.121	-350.044	92.141	-350.088	-350.085
$LiCO_3^-$	-1,1	-271.502	-271.482	63.81	-271.513	-271.51
Li_2CO_3	0,1	-279.02	-278.995	74.181	-279.03	-279.027

[a] Energies adopted from Kuai and Balbuena [22].

B Additional Information Chapter 4[1]

B.1 Model Development and Parametrization

B.1.1 Size of Lattice Sites

The edge length of the voxel differs between the short and long scale simulations. In the short scale simulations, neutral lithium and Li^+ ions are explicitly considered and hence represent the smallest considered species. Therefore, to ensure a correct numerical representation for the short timescale simulations, the edge length of the voxels is set to 0.3443 nm, which stands for the average distance between two lithium atoms in a lithium metal crystal structure. In the longterm calculations, Li^+ is only implicitly considered. Hence, the voxel size is chosen based on the average size of the electrolyte molecules, which also allows a better size representation of the formed polymers. Thereby, the size of the lattice sites is calculated by an approach reported by Arraez et al. [164]. The EC, VC and $LiPF_6$ molecules are assumed to be perfect spheres that are closely adjacent to each other. The diameter of these spheres corresponds to the edge length of ΔL and can be calculated based on the molecular mass M_j and the density ρ_j of the respective species j according to Equation B.1.

$$\frac{\Delta L}{2} = \sqrt[3]{\frac{3}{4}\frac{M_j}{\pi \rho_j N_A}} \tag{B.1}$$

Table B.1 summarizes these properties and the resulting diameters of the electrolyte components. Since EC and VC are the two components with the smallest diameters, the edge length for simulations beyond the µs-scale is set to the concentration-weighted average diameter of both molecules, which is 0.595 nm.

[1] Parts of this chapter have been published in the supporting information of the following article: J. Wagner-Henke et al., *Energy Storage Mater.* 81, 104434, 2025 [2], licensed under CC BY 4.0.

Table B.1: Calculation of lattice size for simulations on extended timescale according to Equation B.1.

Species	**M / g mol^{-1}**	**ρ / g cm^{-3}**	**ΔL / nm**
EC	88.06	1.32 (40°C)	0.596
VC	86.05	1.355 (25°C)	0.586
$LiPF_6$	151.91	1.5 (20°C)	0.685

B.1.2 Derivation of Direction-Dependent Diffusion Rates

The following section extends the derivation of the diffusion rate equation for a two-dimensional square lattice by Drews et al. [132] to a three-dimensional cubic lattice as applied in this work. c_p denotes the concentration of a species in layer p of the kMC box along the z-direction, ΔL is the distance between two lattice sites and D is the diffusion coefficient. According to Fick's law, the particle flux J between to adjacent layers 1 and 2 is given by:

$$J = -D\frac{\partial c}{\partial z} = D\frac{(c1 - c2)}{\Delta L} \tag{B.2}$$

On a cubic kMC lattice this particle flux is represented by the sum of transport processes to the face , 4 edge and 4 corner neighbors along z-direction. This gives the following expression for the flux from layer 1 to 2:

$$J = (c_1 - c_2)(\Gamma_{D,\text{face}} + 4\Gamma_{D,\text{edge}} + 4\Gamma_{D,\text{corner}})\Delta L \tag{B.3}$$

The combination of Equations B.2 and B.3 leads to the following expression:

$$D = (\Gamma_{D,\text{face}} + 4\Gamma_{D,\text{edge}} + 4\Gamma_{D,\text{corner}})\Delta L^2 \tag{B.4}$$

The distance traveled in a single transport step is ΔL for face-directed transport, $\sqrt{2}\Delta L$ for edge-directed transport and $\sqrt{3}\Delta L$ for corner-directed transport. Since all transport steps contribute equally to the mean squared displacement over time, this gives the following relation between the direction-dependent transport rates:

$$\Gamma_{D,\text{face}} = 2 \cdot \Gamma_{D,\text{edge}} = 3 \cdot \Gamma_{D,\text{corner}} \tag{B.5}$$

Solving Equations B.4 and B.5 for the direction-dependent transport rates gives the following expressions:

$$\Gamma_{D,\text{face}} = \frac{3}{13}\frac{D}{\Delta L^2} \tag{B.6}$$

$$\Gamma_{D,\text{edge}} = \frac{3}{26}\frac{D}{\Delta L^2} \tag{B.7}$$

$$\Gamma_{D,\text{corner}} = \frac{1}{13}\frac{D}{\Delta L^2} \tag{B.8}$$

B.1.3 Electron Decay Factor β

The electron decay factor β is estimated based on literature data on the electron current at 2 V over the thickness of the SEI component LiF as published by Benitez et al. [228] and reproduced in Figure B.1 (left).

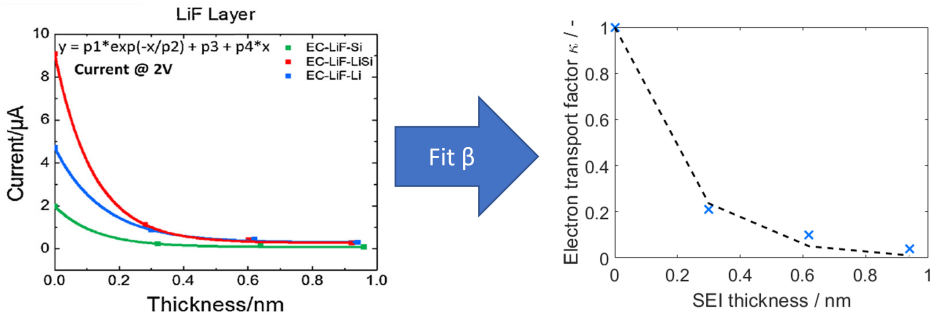

Figure B.1: Parameterization of electron decay factor based on literature data for LiF. Left: Original data on current vs. thickness (blue curve) [228]. Right: Fitting results of electron transport factor κ. Blue crosses represent the probabilities derived from literature data. Dashed line shows the fitting result.

Based on this, the current at the SEI-thickness of 0 nm is defined to correspond to a probability of 1. The remaining data points are relatively related to this maximum value. Thus, an exponential decreasing probability of electron transport at discrete SEI thicknesses is obtained (cf. Figure B.1, right). In order to obtain a continuous electron transport factor $\kappa(z)$, the exponential decay function in Equation B.9 is fitted to the literature data.

$$\kappa(z) = \exp\left(-\beta \cdot (z - z_{\text{Li,max}})\right) \tag{B.9}$$

Here, z represents the height variable of the kMC box, $z_{\mathrm{Li,max}}$ is the highest position in the kMC box in which metallic lithium is present and β is the electron decay factor which determines how fast the electron transport probability declines. For the fitting purpose $z_{\mathrm{Li,max}}$ is set to 0 nm. Based on this, the electron decay factor is estimated to be 4.81 $\mathrm{nm^{-1}}$.

B.1.4 Considered Reaction Processes

Only those chemical reactions are considered for kMC, which have a certain probability to happen during the simulated time. To identify reactions that are too slow to occur and can hence be neglected, the reaction time of chemical reactions is estimated as the inverse of its reaction rate. The corresponding rate equation is given in Table 4.1 in Chapter 4. Figure B.2 shows the inverse of the chemical reaction rate depending on the energy barrier for $k_{0,i} = 10^{13}$ and $p_j = 1$. Since an energy barrier above 21.8 kcal $\mathrm{mol^{-1}}$ results in reaction times of 1000 s and above, which are not reached by the kMC calculations in this work, all possible reaction pathways with higher energy barriers are neglected.

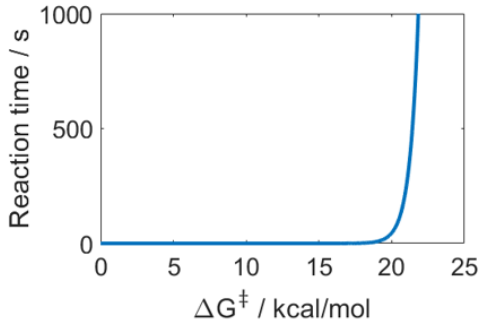

Figure B.2: Reaction time of chemical reactions depending on the reaction energy barrier.

B.1.5 Implemented Reaction Network

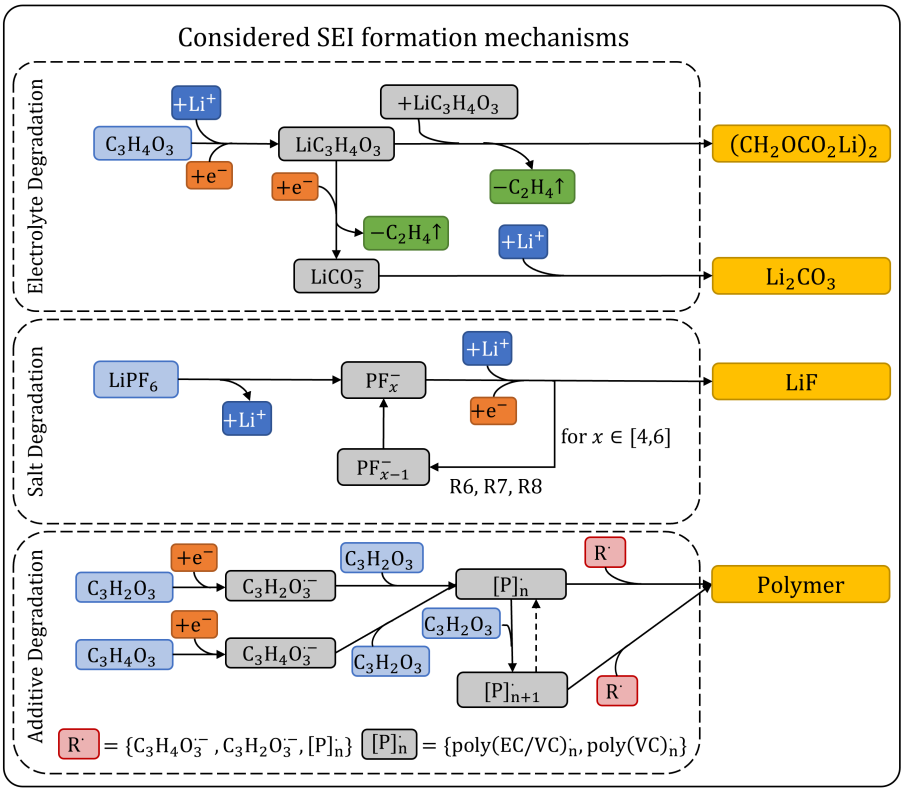

Figure B.3: Abstracted reaction network considered for kMC calculations subdivided into electrolyte degradation, salt degradation and additive degradation including polymerization mechanisms. Gaseous products are in green, electrons and Li^+ ions in orange and dark blue, respectively. Electrolyte components are in light blue, intermediate products in gray and radical species in red.

B.1.6 Assumptions for Long-Time Simulations

Mean-field approach: Figure B.4 a) and b) show the sum of the process frequencies of all transport and reaction processes for the VC-free and VC-containing electrolyte. In the vast majority of kMC steps, transport processes are selected instead of reaction processes. This effect even amplifies over the simulated time due to an increasing passivation of the surface. After 2 µs almost all selected processes are transport processes. Additionally, the reactant fraction over the height of the kMC box after 2 µs is shown in Figure B.4 c) and d). It corresponds to the ratio of the number of the respective electrolyte molecule per layer in the kMC box to the number

of free voxels per layer that are available to be occupied by electrolyte molecules. Above the densest SEI layer, there are still many voxels covered by SEI species. Hence, fewer free voxels are available, which causes the peak in EC reactant probability close to this layer. The reactant probabilities in the remaining electrolyte phase can be observed to be fluctuating around the bulk probability which shows a homogeneous distribution of the electrolyte phase. Consequently, a mean-field approximation can be applied to the electrolyte solvent, salt and additive, significantly reducing the computational cost, since electrolyte transport steps that move the system from one homogeneous electrolyte distribution to another are excluded.

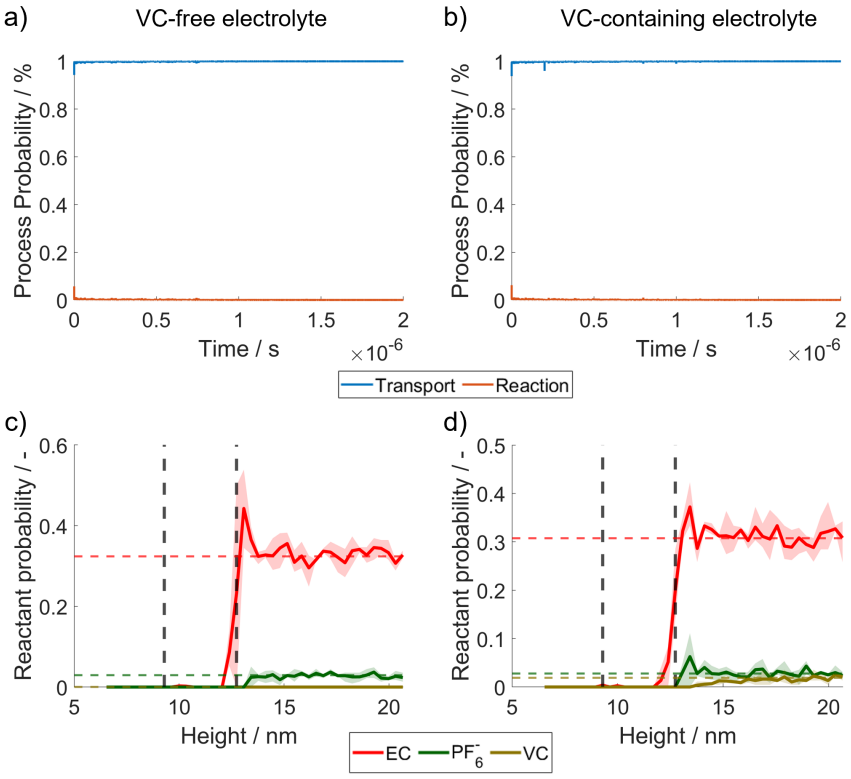

Figure B.4: Summary of observations that allow abstraction via mean field approach. Process frequency for all transport and reaction processes over time for a) VC-free (case 4) and b) VC-containing electrolyte (case 3), respectively. Reactant probability of electrolyte molecules over the height of the kMC box for c) VC-free (case 4) and d) VC-containing (case 3) electrolyte after 2 µs. The dashed lines represent the highest available metallic lithium (left) and the densest SEI layer (right), respectively. Solid lines represent the average of three independent kMC runs with the same parameter set and corresponding shadings show the maximum observed deviation within these runs.

Reaction energies: The proportion of non-lithiated EC and VC molecules in the bulk electrolyte phase is calculated under the assumptions of an ideal mixture, complete salt dissociation, a homogeneous electrolyte phase and an usual solvation shell of four coordinated solvent or additive molecules per Li^+ ion [95, 229, 230] according to Equation B.10.

$$p_{\mathrm{EC/VC}} = \frac{(c_{\mathrm{EC}} + c_{\mathrm{VC}} - 4 \cdot c_{\mathrm{LiPF_6}})}{c_{\mathrm{EC}} + c_{\mathrm{VC}}} \tag{B.10}$$

The resulting average share of non-lithiated EC/VC in a single-solvent EC electrolyte with 5 wt.% VC and for salt concentrations ranging from 0 to 4M is presented in Figure B.5 a). This demonstrates that, in the standard electrolyte used throughout Chapter 4 (1.2M $LiPF_6$ in EC + 5 wt.% VC), the majority of EC and VC molecules remain non-lithiated. Since non-lithiated species are significantly more prone to react according to the identified kinetic parameters (cf. Table 4.2) the SEI formation is expected to follow the dynamics of the non-lithiated parameter set for the standard electrolyte with a salt concentration of 1.2 mol l^{-1}.

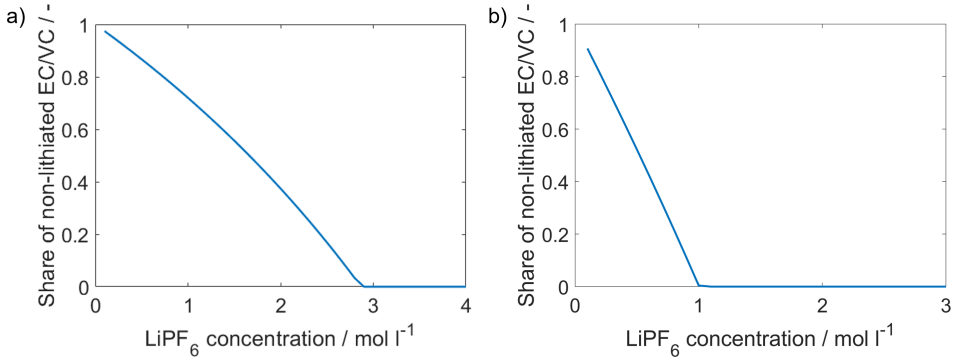

Figure B.5: Estimated proportion of unlithiated EC and VC molecules depending on the salt concentration (cf. Equation B.10. a) Single-solvent EC electrolyte. b) EC:EMC mixture (3:7 by wt.)

It should be noted, that the proportion of non-lithiated EC and VC molecules is strongly dependent on the electrolyte composition. In commercial electrolytes, EC is typically blended with other solvents such as EMC [152]. It has been reported that in EC:EMC (3:7 by wt.) mixtures, Li^+ ions preferentially coordinate with EC rather than EMC [220]. The share of non-lithiated EC and VC molecules in the mixed electrolyte is thus estimated based on the assumption of four coordinated EC or additive molecules per Li^+ ion following Equation B.10. The results are presented in Figure B.5 b) and indicate a significantly lower fraction of non-lithiated EC and VC molecules in the mixed electrolyte, which reaches zero at salt concentrations slightly above 1M. Consequently, the lithiated parameter set appears more appropriate in this case, particularly for highly-concentrated electrolytes. It has hence been applied to all simulations of the mixed

EC:EMC (3:7 by wt.) electrolyte with 1.2M and 3M $LiPF_6$ and 5 wt.% VC throughout the study presented in Chapter 4.

Simplified initial passivation layer: Figure B.6 shows an exemplary long-time calculation with direct input from the previous short-term calculations (cf. Figure 4.3). For this, the initial SEI structure and composition, the x- and y-dimensions of the kMC box as well as the size of the lattice sites were kept from the short-term calculation (case 1). Apart from this, the simulation represents the same case as the standard long-time parameter set (case 3) presented in Figure 2, including the average initial SEI thickness and electrolyte composition. Comparison between the results of both simulations demonstrates, that the exact composition of the initial SEI does not significantly affect the predicted long-time SEI growth, morphology and composition. In both cases the formation of an additional approximately 2 nm thick and dense passivation layer mostly consisting of dimers and trimers and some Li_2CO_3 clusters above on the sub ms-timescale is observed. Afterwards, one can observe that the actual polymerization starts on the ms-timescale and that a thick polymer layer grows up to 1 s. Importantly, the predicted overall thickness of the SEI after 1 s differs between both approaches, with the polymer layer being significantly thinner in the case presented in Figure B.6. This can be attributed to the smaller voxel size in the short-term input case. As discussed in Section B.1.1, due to the explicit consideration of Li^+ ions in the short-term calculations, the voxel edge length is set to the size of this smallest considered species. However, this approach underestimates the volume that the larger electrolyte and SEI species occupy and hence the thickness of the formed polymer layer. Moreover, the smaller voxel size leads to a smaller volume of the next neighborhood of a reactive chain end and hence reduces the monomer availability which slightly slows down the propagation rate and hence leads to shorter polymer chains after 1 s. Overall, in this study a simplified initial passivation is applied instead of the input of the actual predicted structure in the long-time calculations, since it allows for a better size representation of the formed SEI. Moreover, it allows to flexibly increase the studied dimensions of the kMC box and vary the thickness of the initial passivation to account for effects such as native or artificial passivation layers.

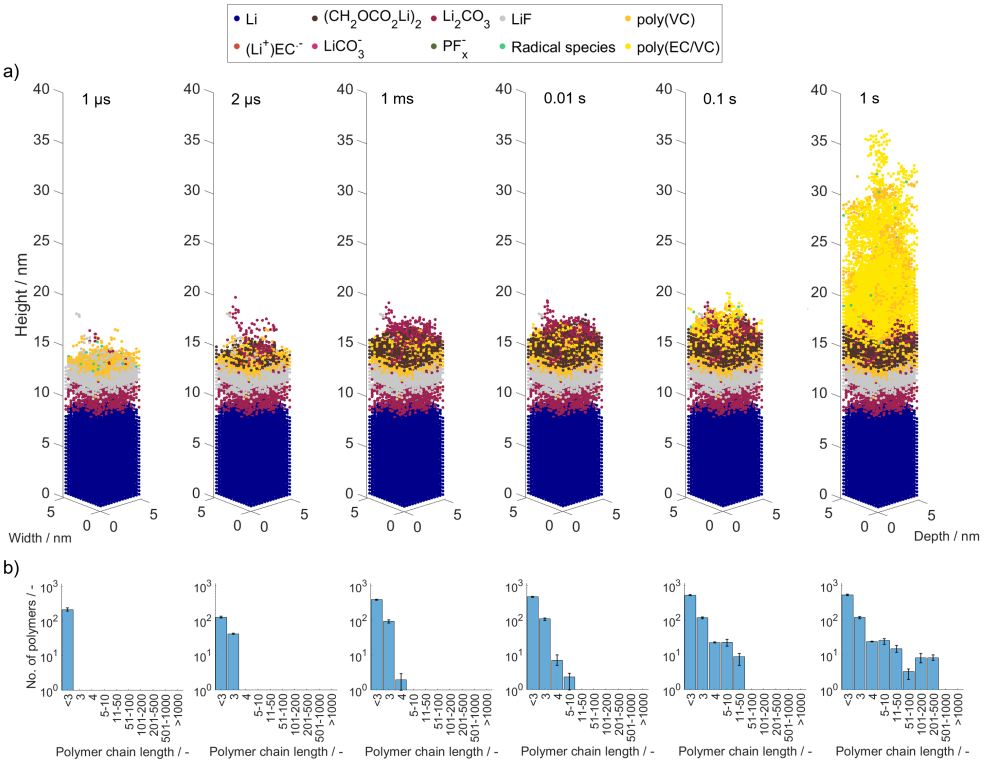

Figure B.6: Temporal evolution of SEI formation on lithium metal in EC + 1.2M $LiPF_6$ + 5 wt.% VC with direct input from short-term calculation (cf. Figure 4.3 a)). a) Spatial morphology and composition of the formed SEI at different times. b) Chain length distribution of the formed polymer species.

B.1.7 Estimation of Specific Electrolyte Volume

To estimate the amount of consumed additive the surface specific electrolyte volume is approximated as follows: Based on the study of Chen et al. [231], the example cell with the lowest applied electrolyte volume for lithium metal based coin cells is considered. This way, the amount of consumed additive rather tends to be over- than underestimated. In the selected case the authors used a capacity specific mass $\dot{m}_{\mathrm{el}}$ of 3 g electrolyte per Ah in coin cells with a cross sectional area of 1.27 cm^2 and a specific capacity C_A of 3.8 mAh cm^{-2}. Based on the density ρ_{EC} of EC (cf. Table B.1), the specific electrolyte volume V_{A} is calculated to be roughly 8.6 µl cm^{-2} following

$$V_{\mathrm{A}} = \frac{\dot{m}_{\mathrm{EC}} \cdot C_{\mathrm{A}}}{\rho_{\mathrm{EC}}} \tag{B.11}$$

B.1.8 Further Model Parameters

Table B.2: Gibbs free energies and energy barriers of considered solvent and salt degradation without polymerization processes.

Nr.	Reaction	$\Delta_R G$ / kcal mol^{-1}	$\Delta G^{\ddagger}$ / kcal mol^{-1}
I1a	$Li^+VC + e^- \rightleftharpoons Li^+VC^{\bullet-}$	-36.34[b]	0[b,d]
I1b	$VC + e^- \rightleftharpoons VC^{\bullet-}$	-18.5[b]	0[b,d]
I2a	$Li^+EC + e^- \rightleftharpoons Li^+EC^{\bullet-}$	-39.17[a]	12.05[a]
I2b	$EC + e^- \rightleftharpoons EC^{\bullet-}$	-30.43[a]	0[a]
R3	$2\ Li^+EC^{\bullet-} \rightarrow (CH_2OCO_2Li)_2 + C_2H_4$	-56.5[a]	2.93[a]
R4	$Li^+EC^{\bullet-} + e^- \rightarrow LiCO_3^- + C_2H_4$	-90.83[a]	0[a]
R5	$LiCO_3^- + Li^+ \rightleftharpoons Li_2CO_3$	-54.72[a]	0[a]
R6	$PF_6^- + Li^+ + e^- \rightleftharpoons LiF + PF_5^-$	-0.454[a]	3[a]
R7	$PF_5^- + Li^+ + e^- \rightleftharpoons LiF + PF_4^-$	-0.454[a]	3[a]
R8	$PF_4^- + Li^+ + e^- \rightleftharpoons LiF + PF_3^-$	-0.454[a]	3[a]
Cl1	$LiF + (n)LiF \rightarrow (n+1)LiF$	-	6.92[c]
Cl2	$Li_2CO_3 + (n)Li_2CO_3 \rightarrow (n+1)Li_2CO_3$	-	6.92[c]
Cl3	$(CH_2OCO_2Li)_2 + (n)(CH_2OCO_2Li)_2 \rightarrow (n+1)(CH_2OCO_2Li)_2$	-	6.92[c]

[a] Adopted from Chapter 3 (cf. Table 3.1)
[b] Adopted from Kuai et al. [22]
[c] Adopted from Esmaeilpour et al. [128]
[d] Manually set to 0 kcal mol^{-1} since the DFT calculations suggested negative values

Table B.3: Summary of binding energies between SEI intermediate species and solid SEI components. Energies are based on Röder et al. [30]. Binding energies of $(Li^+)VC^{\bullet-}$ and $(Li^+)EC^{\bullet-}$ are assumed to be identical. Binding energies with clustered LiF and polymer species are chosen. All energies are given in kJ mol^{-1}.

Species	Clustered LiF	Clustered Li_2CO_3	Clustered $(CH_2OCO_2Li)_2$	Polymer
$(Li^+)VC^{\bullet-}$	10	8	27	8
$(Li^+)EC^{\bullet-}$	10	8	27	8
$LiCO_3^-$	10	27	3	27

Table B.4: Summary of further model parameter.

Parameter	Description	Value	Unit	Source
α	Symmetry factor	0.5	[-]	Chosen
k_0	Frequency factor	10^{13}	[-]	Chosen according to literature [110]
D	Diffusion coefficient	2.27×10^{-10}	$m^2\ s^{-1}$	Chosen according to literature for EC [129, 133, 232]
ΔL_{short}	Distance of surface sites	3.443×10^{-10}	m	Literature value [129]
ΔL_{long}	Distance of surface sites	5.95×10^{-10}	m	cf. Section B.1.1
T	Temperature	298.15	K	In accordance with DFT calculations
ε_r	Relative permittivity of EC	90.36	[-]	Literature value [226]
η	Potential difference	-0.4	V	Chosen[a]
β	Electron decay factor	4.81×10^9	m^{-1}	Fitted (cf. Figure B.1)

[a] This assumption is discussed in Section B.2.5

B.1.9 Simulated Parameter Sets

Table B.5: Summary of performed simulations.

Case Nr.	Electrolyte	Initial SEI thickness / nm	VC concentration / wt.%	Salt concentration / mol l^{-1}	$\Delta G^{\ddagger}_{P3,P6}$ / kcal mol^{-1}
1	EC (explicit)	0	5	1.2	14
2	EC (explicit)	0	0	1.2	14
3	EC (implicit)	3.57	5	1.2	14
4	EC (implicit)	3.57	0	1.2	14
5	EC (implicit)	4.17	5	1.2	14
6	EC (implicit)	4.76	5	1.2	14
7	EC (implicit)	5.36	5	1.2	14
8	EC (implicit)	5.95	5	1.2	14
9	EC (implicit)	6.55	5	1.2	14
10	EC (implicit)	7.14	5	1.2	14
11	EC (implicit)	5.36	0	1.2	14
12	EC (implicit)	5.36	2.5	1.2	14
13	EC (implicit)	5.36	7.5	1.2	14
14	EC (implicit)	5.36	10	1.2	14
15	EC (implicit)	5.36	5	1.2	13
16	EC (implicit)	5.36	5	1.2	15
17	EC:EMC (implicit)	3.57	5	1.2	14
18	EC:EMC (implicit)	3.57	5	3	14

B.2 Additional Results

B.2.1 Temporal Evolution of SEI Formation on the Microsecond Timescale

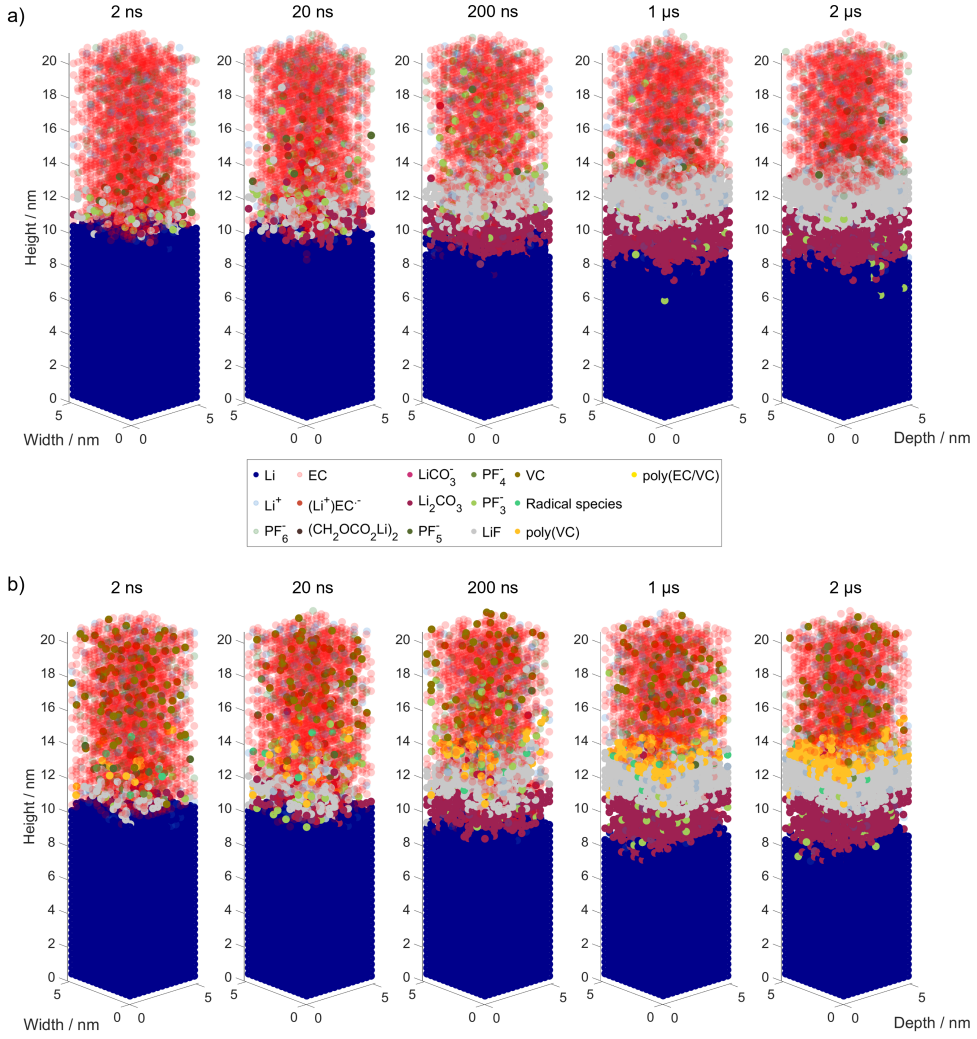

Figure B.7: Temporal evolution of SEI composition and morphology on lithium metal up to 2 µs. a) SEI formation in EC + 1.2M $LiPF_6$ (case 2). b) SEI formation in EC + 1.2M $LiPF_6$ + 5 wt.% VC (case 1).

B.2.2 Extended Timescale Results for the Mixed EC:EMC (3:7 by wt.) electrolytes

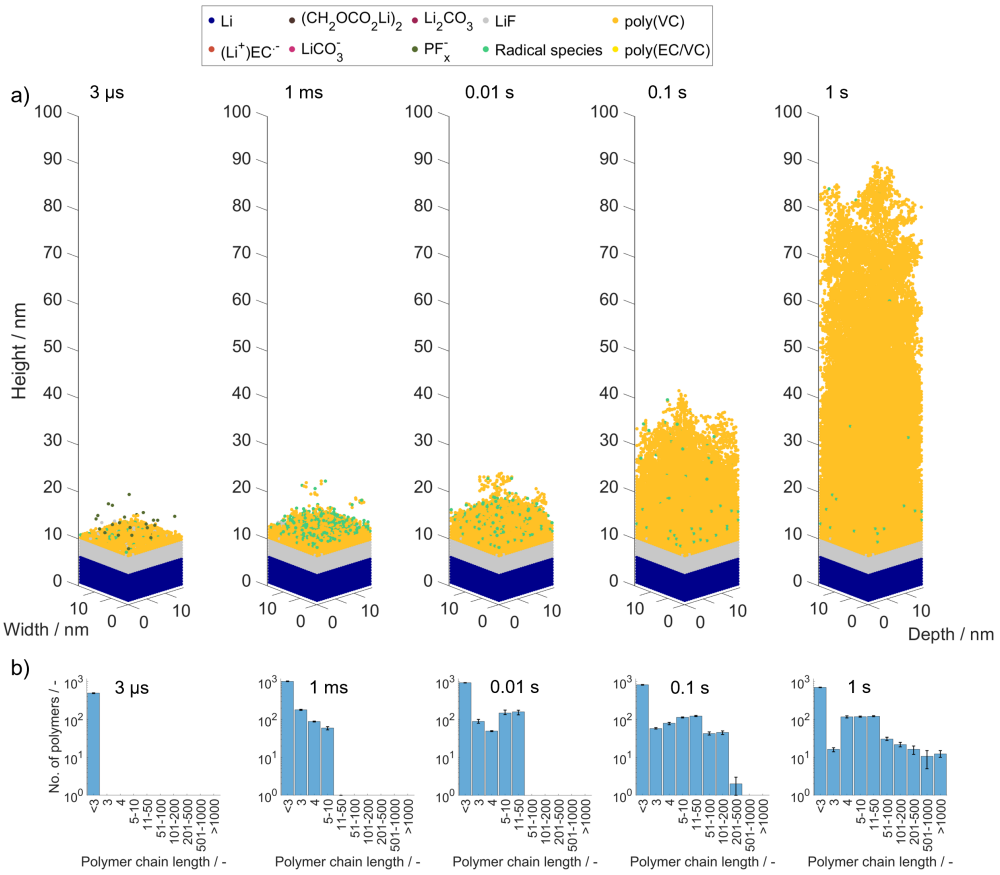

Figure B.8: Temporal evolution of SEI formation on lithium metal in EC:EMC (3:7 by wt.) + 1.2M $LiPF_6$ + 5 wt.% VC after formation of an initial 3.57 nm thick, dense LiF-based SEI at 2 µs (case 17). a) Spatial morphology and composition of the formed SEI at different times. b) Chain length distribution of the formed polymer species.

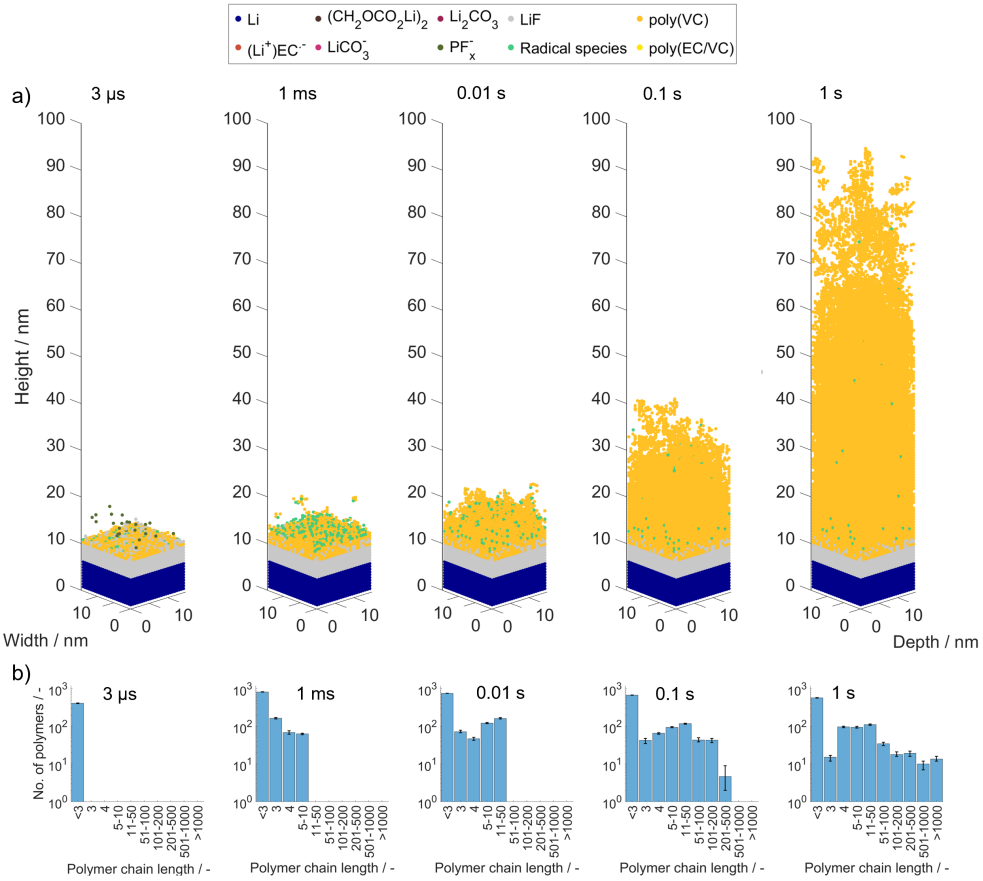

Figure B.9: Temporal evolution of SEI formation on lithium metal in EC:EMC (3:7 by wt.) + 3M $LiPF_6$ + 5 wt.% VC after formation of an initial 3.57 nm thick, dense LiF-based SEI at 2 µs (case 18). a) Spatial morphology and composition of the formed SEI at different times. b) Chain length distribution of the formed polymer species.

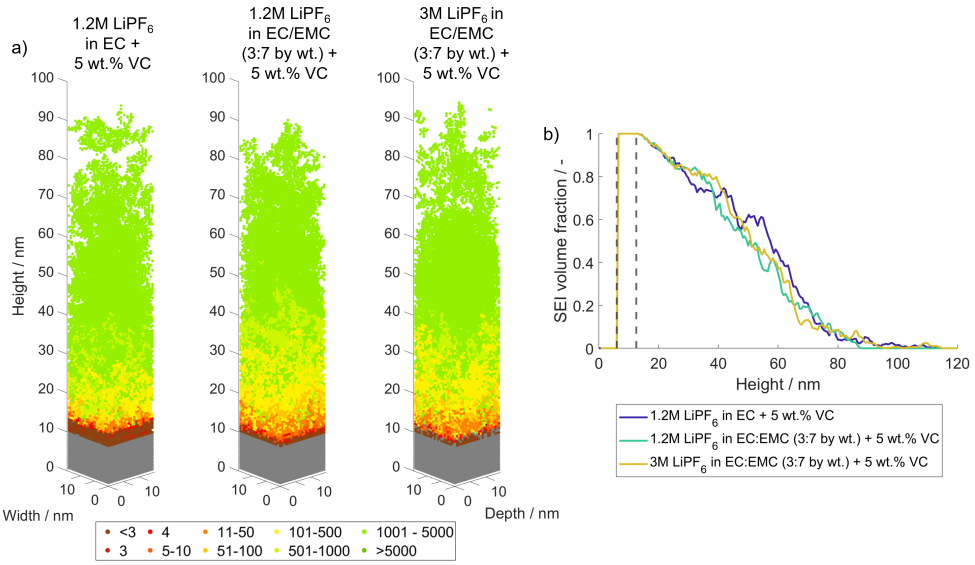

Figure B.10: Comparison of polymeric SEI layers formed after 1 s in the following electrolytes: EC + 1.2M $LiPF_6$, EC:EMC (3:7 by wt.) + 1.2M $LiPF_6$ and EC:EMC (3:7 by wt.) + 3M $LiPF_6$, each containing 5 wt.% of VC (cases 3, 17, 18). a) Spatial polymer chain length distribution. b) SEI volume fraction over height. The left dashed line represents the lithium metal surface and the right dashed line the highest completely dense passivation layer.

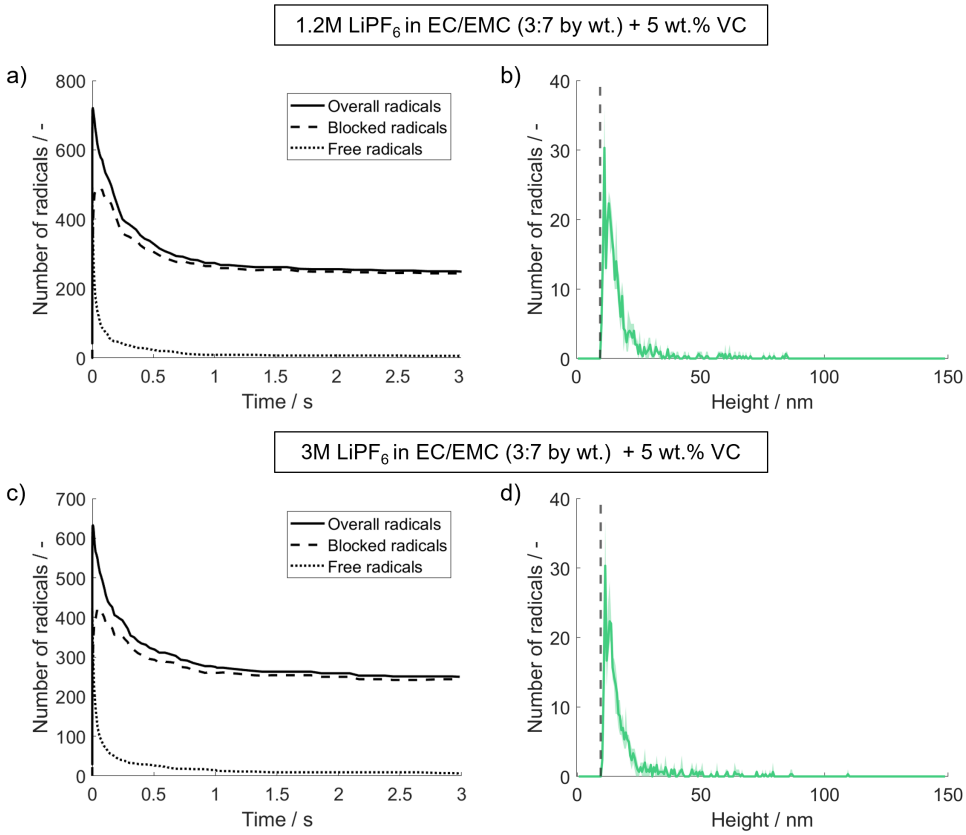

Figure B.11: Number of radicals and reactive chain ends over time and height for an initial SEI thickness of 3.57 nm in EC:EMC (3:7 by wt.) + 5 wt.% VC with 1.2M $LiPF_6$ and 3M $LiPF_6$, respectively (cases 17, 18). a) and c) Number of free and blocked radicals, and total number over time. b) and d) Distribution of radicals over the distance from the electrode after 1 s. The dashed line indicates the lithium metal surface.

B.2.3 Variation of VC Concentration

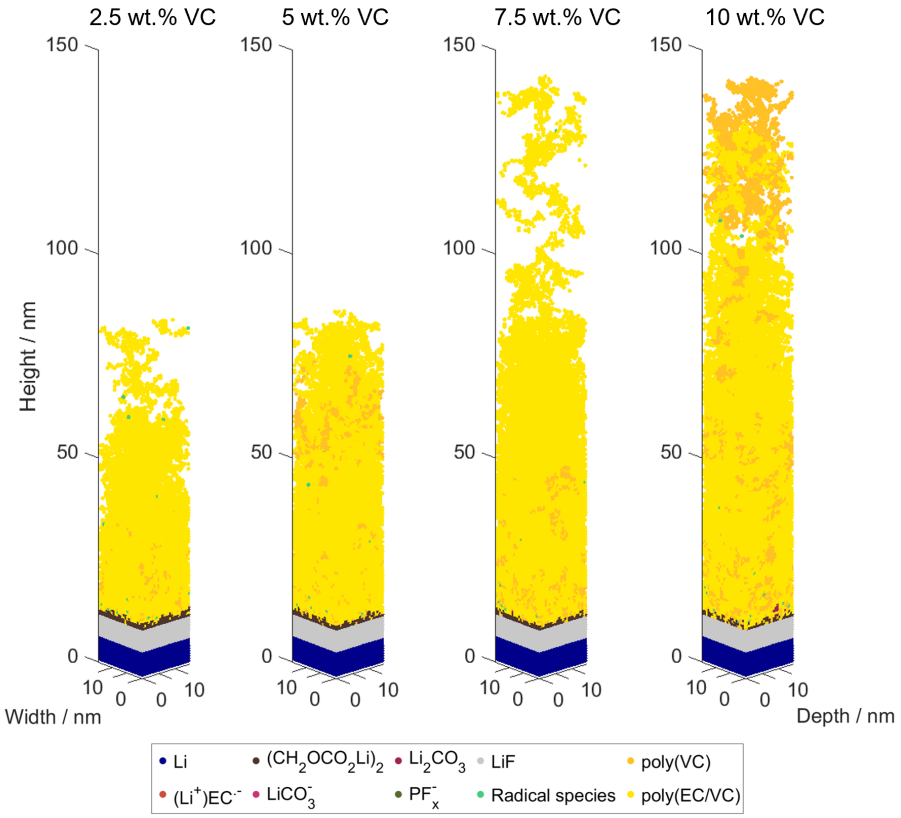

Figure B.12: Comparison of spatial chemical composition and morphology after 1 s for a variation of VC concentrations between 2.5 wt.% and 10 wt.% (cases 12, 7, 13 and 14).

B.2.4 Additional Results on Extended Timescales

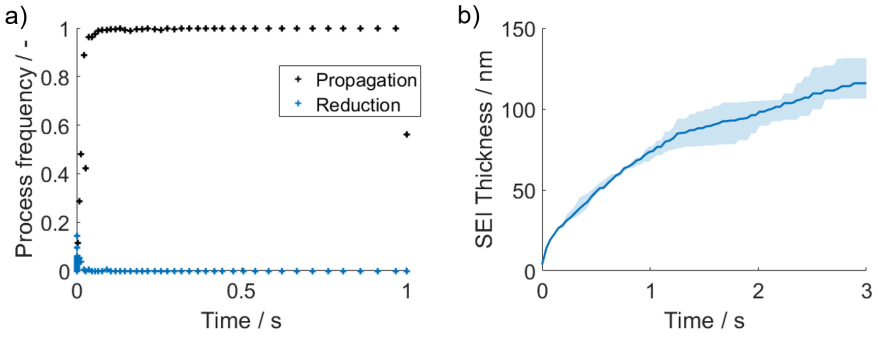

Figure B.13: Further properties of SEI formation in EC + 1.2M $LiPF_6$ + 5 wt.% VC (case 3). a) Frequency of polymer propagation reactions P3 and P6 and reduction reactions over time. Peaks at 0.01 s, 0.1 s and 1 s are computational artifacts due to intermediate saving of the results. b) Average SEI thickness over time. The maximum observed deviations from the average value are shown as blue shading.

B.2.5 Impact of Reduction Potential

In this study a uniform overpotential of SEI formation of -0.4 V was assumed for all electrochemical reactions. According to Equation B.12, this value results from the difference between the lithium electrode potential Φ_a of 0 V vs Li/Li^+ and a reduction potential of SEI formation Φ_{red} of 0.4 V vs. Li/Li^+, which is consistent with values used in similar models [29, 32].

$$\eta = \Phi_a - \Phi_{red} \tag{B.12}$$

In order to estimate the impact of this assumption on the predicted SEI formation, species-dependent reduction potentials are in the following derived from literature. In general, reported reduction potentials are very diverse, ranging between 0.21 V and 0.9 V vs. Li/Li^+ for EC [159, 233–236], 0.23 V and 1.4 V vs. Li/Li^+ for VC [159, 234] and are well above 1 V vs Li/Li^+ for $LiPF_6$ [159, 234]. Nevertheless, the following general order of reduction potentials is usually observed: $\Phi_{red,LiPF_6} > \Phi_{red,VC} > \Phi_{red,EC}$ [159, 233, 234]. Based on this, the reduction potentials were chosen within the reported ranges as $\Phi_{red,EC} = 0.6$ V, $\Phi_{red,VC} = 0.8$ V and $\Phi_{red,LiPF_6} = 1$ V and exemplarily applied to all reduction reactions of the respective species. Thereby, $\Phi_{red,LiPF_6}$ was chosen slightly smaller than reported to avoid unrealistically high reaction rates. It should be noted, that this is still a very rough estimate of the respective reduction potentials, but allows to assess the general impact of the reduction potential on SEI formation within the first microsecond and beyond.

Figure B.14 shows the results of SEI formation within 1 µs with the modified reduction potentials. Overall, the results are very similar to the predicted SEI with uniform reduction potentials in Figure 4.3. Both parameter sets predict a layered SEI consisting of Li_2CO_3 and LiF in the VC-free case and an additional organic/polymeric layer in the VC-containing electrolyte. In the case of the modified parameter set, a slightly higher amount of Li_2CO_3 is formed, and the mixing of the LiF and polymer phase is slightly increased. Additionally, the predicted SEI is slightly thicker, and the difference in SEI thickness between the VC-free and VC-containing electrolytes is less pronounced. The prediction of polymer chain length and number of polymer species is not significantly affected.

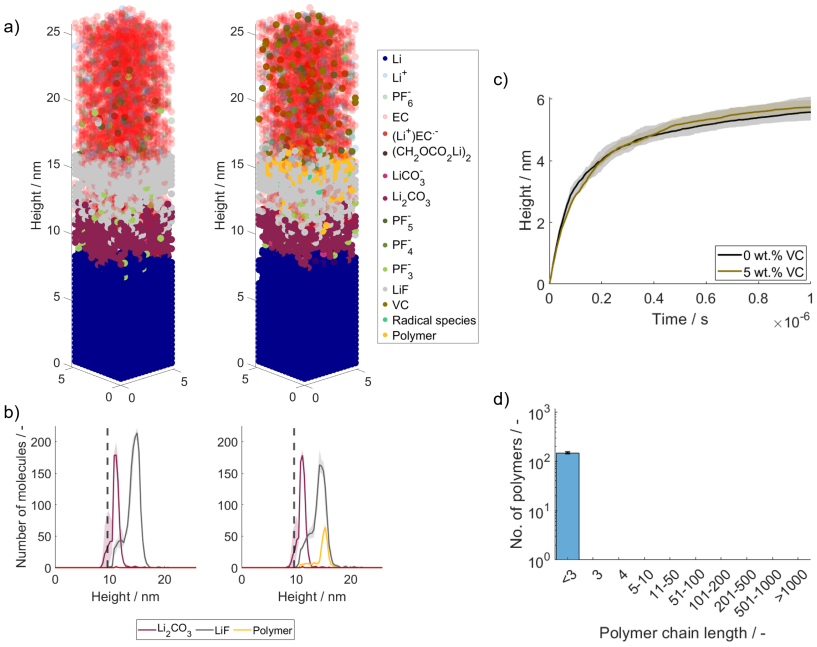

Figure B.14: Impact of reduction potential on SEI formation in carbonate-based electrolyte with and without 5 wt.% VC within the first µs. The results in a) are based on a single kMC run and the results in b)-d) display the average of three runs with the same parameter set. Deviations from the average are represented as shadings around the average in b) and c). In d), they are illustrated using error bars. a) SEI composition and morphology without (left) and with (right) VC. b) SEI species distribution over height without (left) and with (right) VC. The dashed line represents the upmost layer in which metallic lithium is present after 1 µs. c) Evolution of SEI height up to 1 µs for both cases. d) Polymer chain length distribution in SEI formed in VC-containing electrolyte after 1 µs.

The impact on SEI growth beyond the microsecond timescale is shown in Figure B.15. It may be observed that the polymer chain growth dynamics are very similar in both cases: Up to the millisecond timescale only very short oligomer species may be observed. Subsequently, longer

polymer chains form and grow a thick polymer layer consisting of a mixture of poly(EC/VC) and poly(VC) molecules after 1 s. The modified potentials shift the composition of this polymer layer from predominantly poly(EC/VC) polymers to a higher number of poly(VC) polymers. The most significant difference between both simulation results lies in the composition of the dense SEI close to the lithium anode. Since the modification of reduction potentials significantly favors salt decomposition over solvent decomposition, the composition of this layer is shifted from a mixture of solvent and additive decomposition products to a mixture of the salt decomposition product LiF and additive decomposition products.

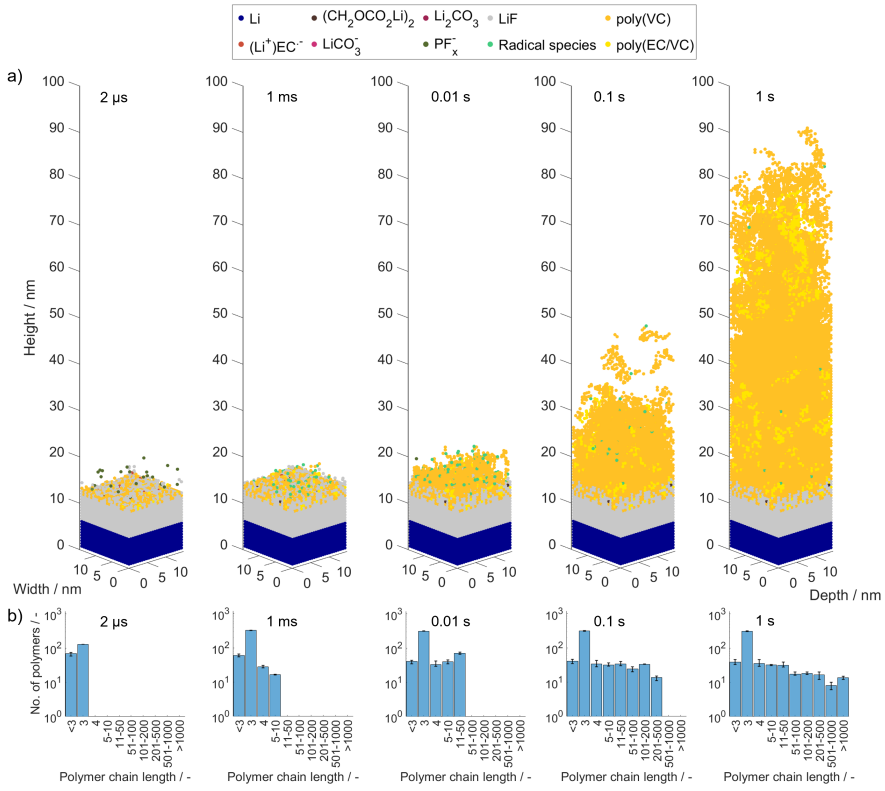

Figure B.15: Impact of reduction potential on temporal evolution of SEI growth on lithium metal in EC + 1.2M $LiPF_6$ + 5 wt.% VC until 1 s after formation of an initial 3.57 nm thick, dense LiF-based SEI at 1 µs. a) Spatial morphology and composition of the formed SEI at different times. b) Corresponding chain length distribution of the formed polymer species.

Overall, the short term SEI formation is only slightly impacted by the modified reduction potentials. On larger scales, the modified potentials lead to a shift from solvent to salt based SEI components. However, the conclusions on the impact of VC on SEI formation remain unchanged

independent of the used set of reduction potentials. Nevertheless, this case study shows that in order to refine the model and to further enhance its predictive power, future studies should focus on the DFT-based calculation of individual reduction potentials for each considered electrochemical reaction along with the other reaction energies.

B.2.6 Sensitivity Analysis of Propagation Barriers

The energy barriers of the long-chain propagation processes P3 and P6 could not be directly calculated from DFT. This is due to the high number of atoms in these large molecules and the corresponding high computational cost. Therefore, these parameters have been estimated based on the energy barriers of the short-chain propagation processes P2 and P5. In order to evaluate the effect of this assumption, a sensitivity analysis of the effect of these parameters on the SEI formation was performed. Figure B.16 a) demonstrates, that the decrease or increase of the barrier by 1 kcal mol^{-1} accelerates or slows down the SEI growth rate by multiple times. E.g. in the case of the decreased barrier, an average SEI thickness of 80 nm is reached after only 0.31 s, while it takes 8.53 s in the case of the increased barrier. From this it is concluded, that the time-dependent SEI thickness highly depends on these estimated parameters and their absolute values should hence be interpreted with caution. The analysis of the chemical SEI composition and the SEI morphology of the formed SEI-layers with an average thickness of 80 nm, is presented in Figure B.16 b). It reveals, that these properties are not highly affected by the variation of the propagation barriers. In all cases, a thin dense layer consisting of LiEDC, Li_2CO_3 and some polymeric species close to the initial LiF-layer and an increasingly porous polymer layer above can be observed. Thereby, this polymer layer consists of a mixture of poly(VC) and poly(EC/VC) with a greater proportion of poly(EC/VC) independent of the applied propagation barrier. The minor variations between the formed SEI layers are within the range of stochastic deviation. Based on this, it is concluded that although the overall growth rate is significantly affected by the tested parameters, the observed SEI characteristics are insensitive to the propagation barriers in the tested range. Hence, the estimated propagation barriers only cause uncertainties in the timescale but do not impact the presented results on the general effect of VC on SEI formation on lithium metal.

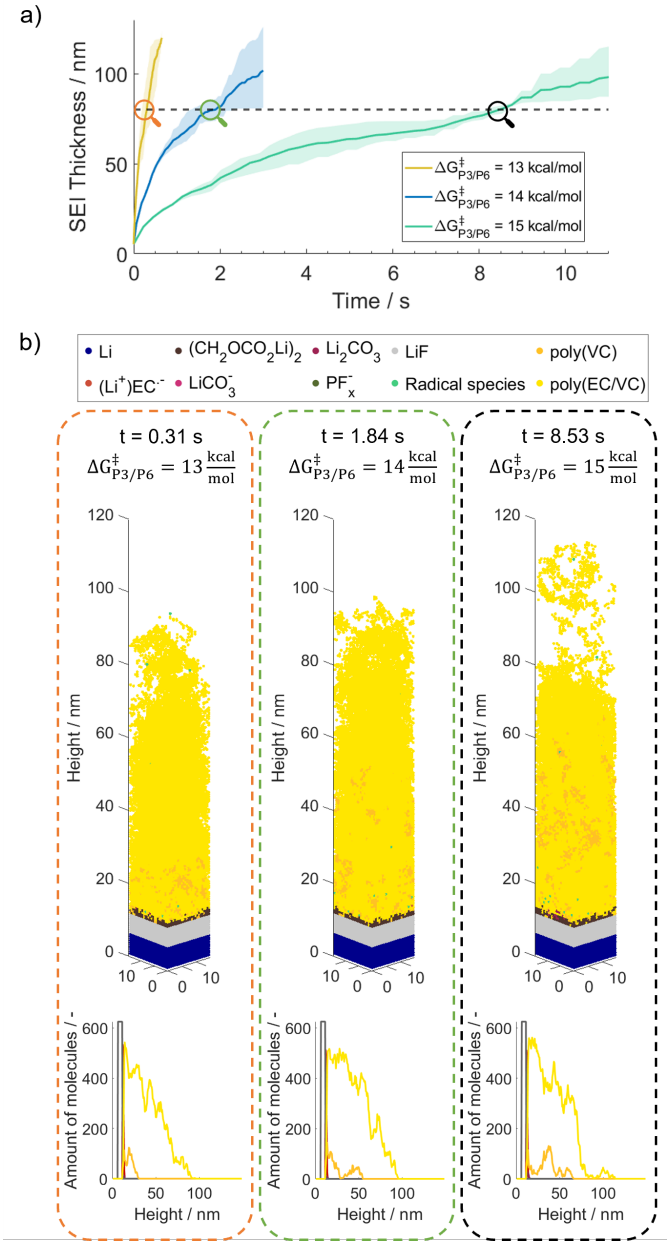

Figure B.16: Sensitivity analysis on the effect of the energy barriers of propagation (P3 and P6) on SEI formation. Barriers are varied between 13 and 15 kcal mol^{-1}, with 13 kcal mol^{-1} (case 15) being the fast, 14 kcal mol^{-1} (case 7) the standard and 15 kcal mol^{-1} (case 16) the slow polymerization. a) Comparison of time dependent SEI thickness for all investigated propagation barriers. Solid lines represent the average of three independent kMC runs with the same parameter set and corresponding shadings show the maximum observed deviation within these runs. b) SEI composition and morphology with an average SEI thickness of 80 nm for all investigated propagation barriers.

C Additional Information Chapter 5

C.1 Model Development

C.1.1 Choice of External Potential

In order to reduce the fluctuations in the predicted mobilities (cf. Figure 5.8), the applied external potential was chosen in a way that the induced potential difference between two neighbors in z-direction is of a similar magnitude like the potential differences that results from the Coulomb interactions. The applied external field E_{ext} leads to a potential difference of:

$$\Delta\varphi_{lk,\text{ext}} = E_{\text{ext}} \cdot \Delta L = 0.0144 \text{ V} \tag{C.1}$$

A single elementary charge induces a potential difference of:

$$\Delta\varphi_{lk,\text{clb}} = \frac{1}{4\pi\varepsilon_0\varepsilon_r}\left(\frac{e}{\Delta L} - \frac{e}{2\Delta L}\right) = 0.0486 \text{ V} \tag{C.2}$$

As shown in Figure 5.8, this choice of electric field strength results in a good reproducibility of mobility values.

C.1.2 Impact of Lattice Site Dimensions

In order to account for the average distance between dissolved Li^+ and $PF_6{}^-$ ions, the lattice site distance was set to $\Delta L = 0.8$ nm (cf. Section 5.2.4.3). Figure C.1 demonstrates the impact of this parameter choice by comparing the results of a lattice site distance of 0.8 nm and 0.5 nm. After 50,000 kMC iterations the charge carriers are well distributed throughout the simulation box with the larger site distance (cf. Figure C.1 b)). In contrast, in the case with the smaller site distance (cf. Figure C.1 a)), a clustering of charges is observed. Moreover, the peaks in the radial distribution function are significantly more pronounced for $\Delta L = 0.5$nm Overall, this suggests an overestimation of the local attractive forces due to the unrealistically small distances between the charge carriers.

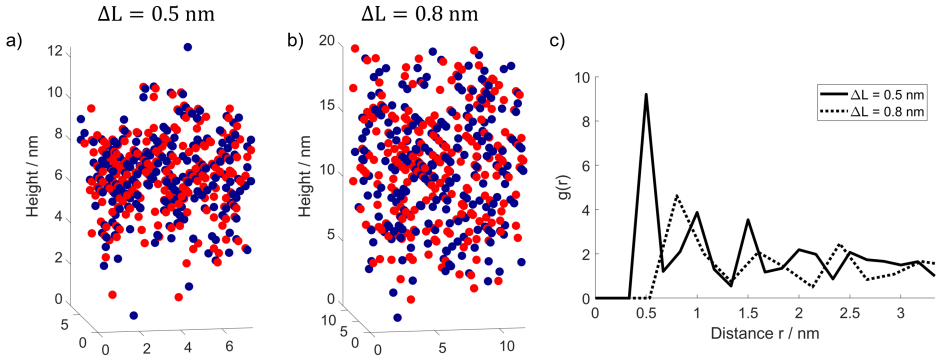

Figure C.1: Effect of the choice of the lattice site size ΔL on the example of the 3D-Poisson BC2 approach and an initialization with two charged planes (scenario 1). a) Final ion distribution after 50,000 kMC iterations for $\Delta L = 0.5$ nm. b) Final ion distribution after 50,000 kMC iterations for $\Delta L = 0.8$ nm. c) Comparison of radial distribution functions after 50,000 kMC iterations for $\Delta L = 0.5$ nm and $\Delta L = 0.8$ nm.

C.2 Additional Results

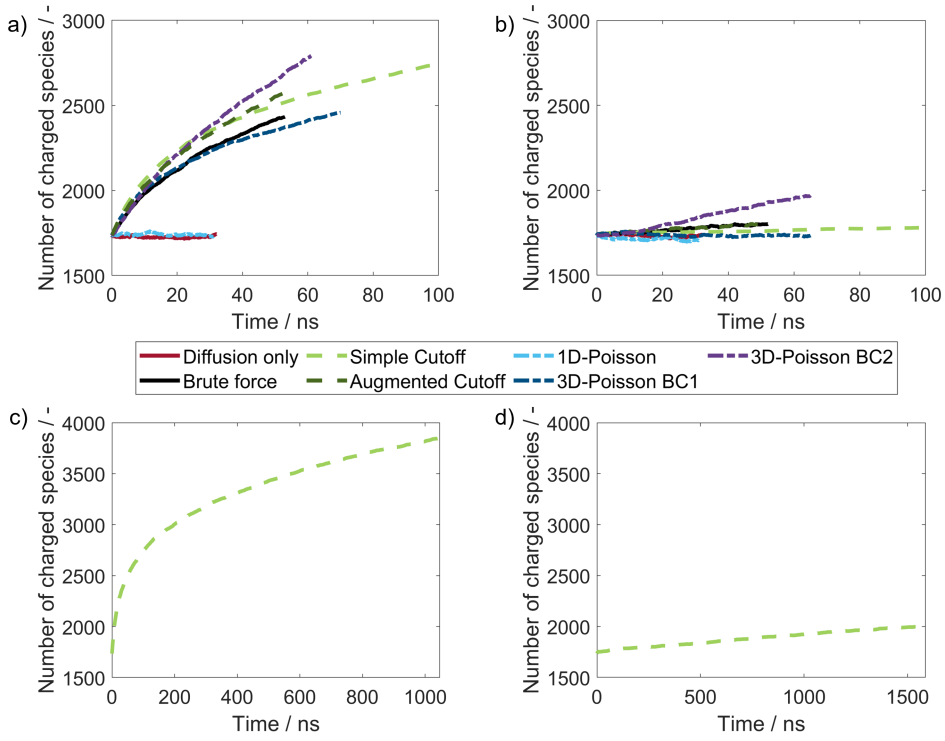

Figure C.2: Comparison of the impact of different boundary conditions on the number of charged particles in the simulation domain as a function of time. a) Comparison of electrostatic interaction models with simplistic implementation without correction for lateral interactions up to 100 ns. b) Comparison of electrostatic interaction models with advanced implementation including correction for lateral interactions up to 100 ns. c) Full simulated time for Simple Cutoff approach with simplistic implementation without correction for lateral interactions. d) Full simulated time for Simple Cutoff approach with advanced implementation including correction for lateral interactions.

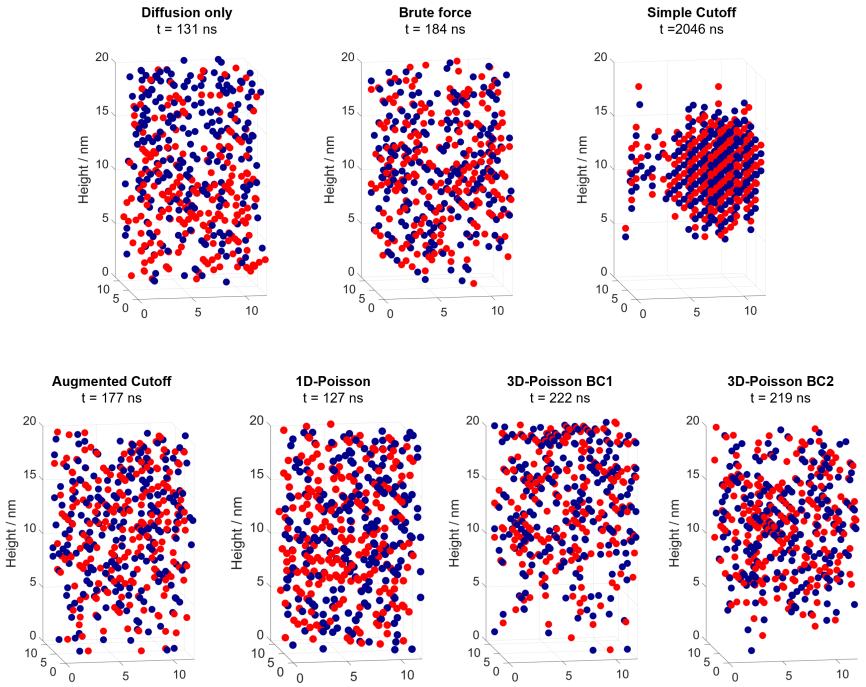

Figure C.3: Comparison of final ion distributions after 50,000 kMC iterations for initial conditions according to scenario 1 (parallel charged layers).

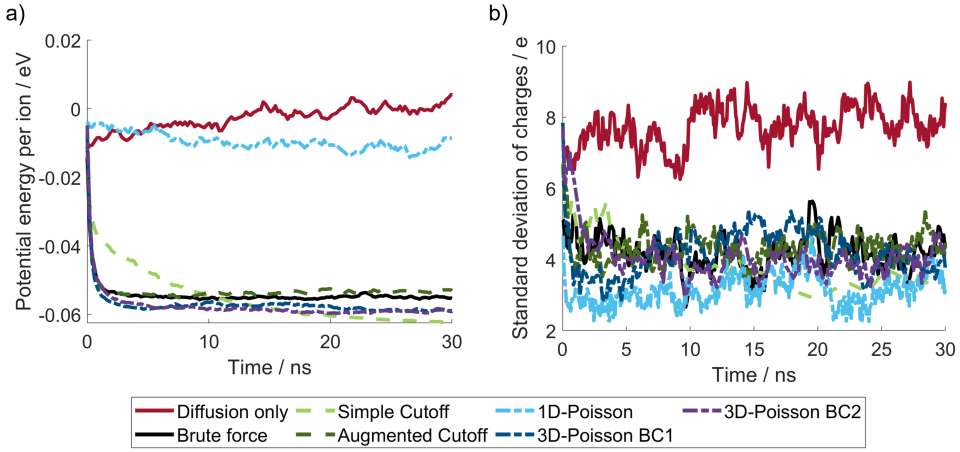

Figure C.4: Quantitative comparison of electrostatic interaction models over time. a) Temporal evolution of average coulomb potential energy per ion. b) Temporal evolution of standard deviation of charge per layer.

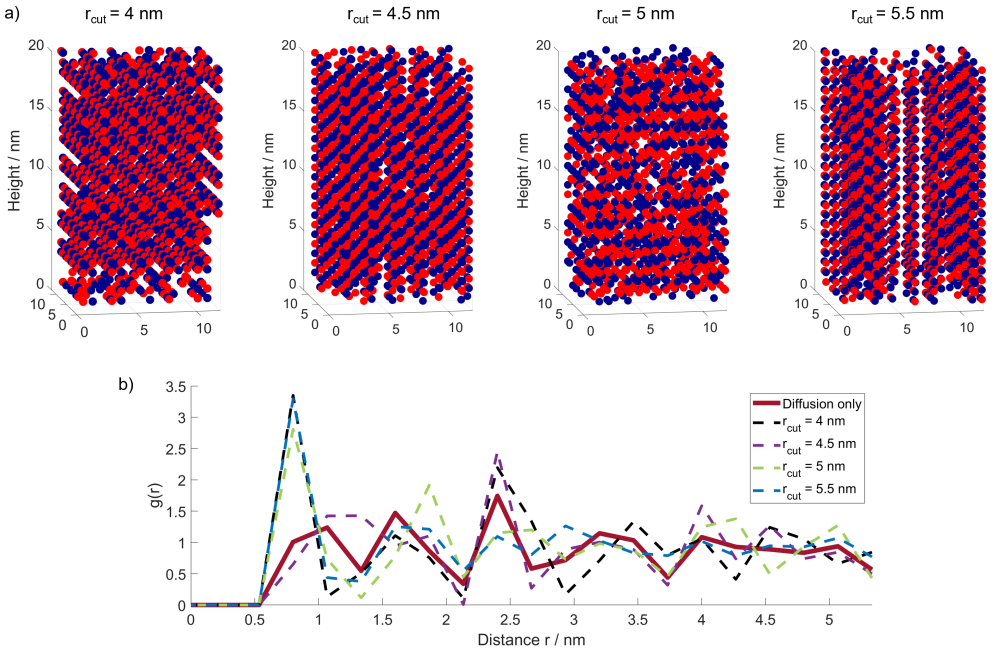

Figure C.5: Effect of different cutoff radii, ranging from 4 to 5.5 nm in the Simple Cutoff approach, on charge distribution in an initially homogeneous electrolyte phase (scenario 2). a) Final ion distribution after 50,000 kMC iterations. b) Radial distribution functions after 30,000 kMC iterations.

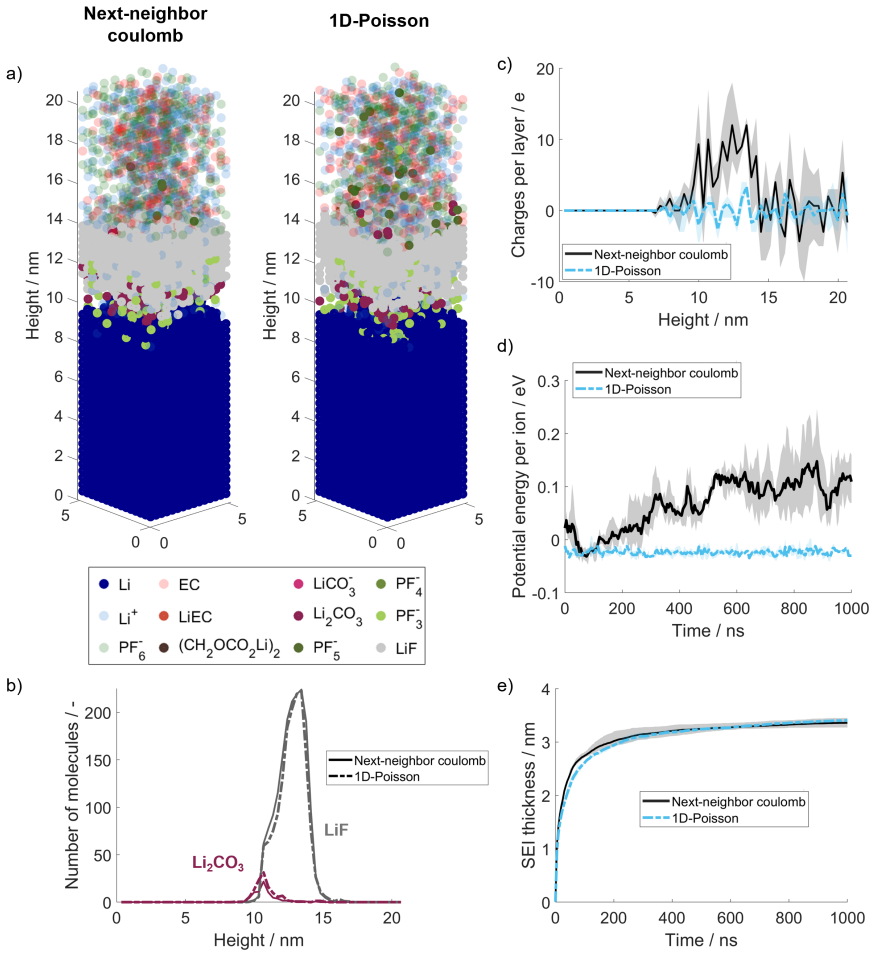

Figure C.6: Impact of the 1D-Poisson approach on SEI formation in EC:EMC (3:7 by wt.) + 3M $LiPF_6$. a) SEI composition and morphology resulting from the next-neighbor Coulomb approach (left) and the 1D-Poisson approach (right) after 1 µs. b) SEI distribution over height after 1 µs. c) Charge distribution over height after 1 µs. d) Coulomb potential energy per ion over time. e) SEI thickness over time. Dash-dotted lines indicate results based on the 1D-Poisson approach and solid lines refer to results based on the next-neighbor Coulomb approach. The results presented in b) to e) are the average of three independent kMC runs with the same parameter set, and corresponding shadings in c) to e) show the maximum observed deviation within these runs.